

# The University Of Sheffield.

# Doctoral Thesis

# Epitaxial Growth of Bismuth-Modified III-V Systems on 001 GaAs

## Author:

Matthew Carr

1<sup>st</sup> Supervisor: Dr Robert Richards 2<sup>nd</sup> Supervisor: Prof John David

A thesis submitted in fulfilment of the requirements

for the degree of Doctor of Philosophy

to the

Department of Electronic and Electrical Engineering

Submitted March 2024

## **Abstract**

Bandgap engineering of III-Vs with Bi has been a promising candidate for next generation infrared detectors and avalanche photo diode devices (APD). The large, induced change in bandgap, up to 78 meV per % Bi incorporated and the surfactant effect of Bi on the surface during epitaxial growth make it an attractive option. However, the application of Bi to III-V growth I nontrivial with low miscibility necessitating significantly reduced growth temperatures and narrow viable flux III-V flux windows. This necessitates careful optimisation and growth studies to produces device quality material with significant remaining challenges in the growth of Bi containing alloys.

The first chapter focuses on the surfactant effect of Bi on InAs quantum dot (QD) formation for infrared emission and detection in the O and C fibre communication attenuation windows. Bi fluxes between 0 to 3.5 nA were supplied to the surface during InAs QD formation at 480 °C at a rate of 0.01 atomic monolayers per second (MLs<sup>-1</sup>). The QDs were capped with 50 nm of GaAs and a further surface layer grown atop. The morphological changes and optical characteristics assessed by atomic force microscopy (AFM) and photoluminescence measurements (PL). QD height was found to vary between 3.8 to 10.1 nm in non-trivial relationship with supplied Bi flux. A critical threshold was observed were Bi initially enhanced QD formation up to 1.2 nA before the trend reversed and the level of enhanced QD height reduced. Supply at 3.5 nA was found to hinder the QD formation relative to no supplied Bi flux. The lowest energy emission was observed at 1.049 eV and 0.971 eV for PL measurements at 20 and 297 K respectively.

The second and third chapters investigate the growth and post-processing respectively of the quaternary alloy Al<sub>x</sub>Ga<sub>1-x</sub>As<sub>1-y</sub>Bi<sub>y</sub>. Of interest owing to the potential application as a next generation avalanche region in APD devices. Growth starts from optimised GaAsBi growth conditions with contents of Al between 0 to 15 at% grown. Further exploration of key growth parameters was conducted with Bi flux varied between 0.8 to 2.8 nA and growth temperatures between 280 to 340 °C. Sample were the analysed by XRD, PL and ion beam analysis to quantify crystalline, optical and compositional properties of the samples. The substitution of Ga for Al was found to introduce significant quantities of defects which acted as non-radiative recombination centres with 2-3 orders of magnitude decrease in PL brightness observed. Once Al was present the impact remained stable and insensitive to further increases in content between 2.5 to 15 at% Al. There was no indication the Al content affected the incorporation of Bi. Bi contents between 1.4 to 4.6 at% Bi and 0.9 to 6.2 at% for Bi flux and growth temperature control respectively with 5 at% Al. Sample grown for the ex-situ annealing suffered from degraded quality due to the cold capping layers. This overshadowed any indication that the material was degraded by the capping process or that it could be improved in quality by ex-situ annealing at temperatures between 400 to 650 °C for 30s. The viability of synthesis of this alloy was confirmed However there remains an

elevated quantity of unidentified compensation complexes within the material that degrade the optical quality.

## Acknowledgements

To my supervisors Dr Robert Richards and Professor John David for the continued patience and guidance during this PhD project through the highs and lows of semiconductor research on an MBE reactor.

I would also like to thank my colleagues within Nanoscience for their help and advice in all matters MBE and semiconductor related, Dr Edmund Clarke, Richard Frith, Dr Ian Farrer, Professor Mark Hopkinson and the technical staff.

To my fellow PhD students who have been supportive with advice and help throughout the PhD project irrespective of how many lunches have turned in research support group meetings.

My gratitude to my family for their continued unconditional support throughout my time studying at the University of Sheffield, Professor Mark Carr, Dr Hilary Carr and Dr Philippa Carr.

## **Publications**

- [1] N. J. Bailey, M. R. Carr, J. P. R. David, and R. D. Richards, "Growth of InAs(Bi)/GaAs Quantum Dots under a Bismuth Surfactant at High and Low Temperature," J. Nanomaterials., vol. 2022, no. 001, pp. 1–9, 2022.
- [2] S. Flores, D. F. Reyes, D, T. Ben, V. Braza, N. J. Bailey, M. R. Carr, R. D. Richards, D. Gonzalez, "Exploring the formation of InAs(Bi)/GaAs QDs at two growth-temperature regimes under different Bi supply conditions," Appl. Surf. Sci., vol. 607, p. 154966, Jan. 2023.

## **Oral and Poster Presentations**

- [1] Thomas B. Rockett, Nada A. Adham, Matthew Carr, John P. R. David & Robert Richards "GaAsBi light emitting diodes for 1050nm broadband light sources," Presentation in SPIE Photonics Europe, 2022.
- [2] M. R. Carr, N. J. Bailey, D. F. Reyes, S. Flores, V. Braza, J. P. R. David & R. D. Richards "Bi Flux Modification of Self Assembled InAs Quantum Dots, Grown on <001> GaAs by Molecular Beam Epitaxy," Presentation in SIOE 2022, 2022.
- [3] M. R. Carr, N. J. Bailey, J. Dulai, M. K. Sharpe, J. England, J. P. R. David & R. D. Richards "Development of Al<sub>x</sub>Ga<sub>1-x</sub>As<sub>1-y</sub>Bi<sub>y</sub> for the Next Generation of APDs," Presentation in UKNIBC User Day, 2022.
- [4] M. R. Carr, N. J. Bailey, J. V. D. Berg, A. Rossall, J. P. R. David & R. D. Richards "The Incorporation Of Bi into Al<sub>x</sub>Ga<sub>1-x</sub>As Between 30-80% Al Content By Molecular Beam Epitaxy on GaAs," Poster in UK Semiconductors Conference 22, 2022.
- [5] M. K. Sharpe1, M. R. Carr, N. J. Bailey, J. Dulai1, J. P. R. David & R. D. Richards "Time-of-Flight Elastic Recoil Detection Analysis and Rutherford Backscattering Spectrometry to Characterise Al<sub>x</sub>Ga<sub>1-x</sub>As<sub>1-y</sub>Bi<sub>y</sub> Avalanche Photodetectors," Poster in IBA & PIXE, 2023.
- [6] M. R. Carr, N. J. Bailey, J. P. R. David & R. D. Richards "The Incorporation Of Al into GaAs<sub>y</sub>Bi<sub>y-1</sub> By Molecular Beam Epitaxy For Next Generation APDs," Poster in EMRS 2023, 2023.
- [7] M. R. Carr, N. J. Bailey, M. K. Sharpe, C. Mcaleese, J. P. R. David & R. D. Richards "The Incorporation Of Al into GaAs<sub>y</sub>Bi<sub>y-1</sub> By Molecular Beam Epitaxy For Next Generation APDs," Poster in NAMBE, 2023.

- [8] M. R. Carr, N. J. Bailey, J. Dulai, M. K. Sharpe, J. England, J. P. R. David & R. D. Richards "Development of Al<sub>x</sub>Ga<sub>1-x</sub>As<sub>1-y</sub>Bi<sub>y</sub> for the Next Generation of APDs," Presentation in UK MBE workshop 2023, 2023.
- [9] M. R. Carr, N. J. Bailey, J. A. Van Den Berg, A. Rossall, J. Dulai, M. K. Sharpe, C. Mcaleese, J. England, J. P. R. David & R. D. Richards "Development of Al<sub>x</sub>Ga<sub>1-x</sub>As<sub>1-y</sub>Bi<sub>y</sub> for the Next Generation of APDs," Presentation in UKNIBC User Day, 2023.
- [10] M. R. Carr, N. J. Bailey, M. K. Sharpe, J. England, J. P. R. David & R. D. Richards "Influence of growth conditions on the structural and opto-electronic quality of Al<sub>x</sub>Ga<sub>1-x</sub>As<sub>1-y</sub>Bi<sub>y</sub>," Presentation in UK Semiconductors Conference 23, 2023.
- [11] S. Flores, D. F. Reyes, D, T. Ben, V. Braza, N. J. Bailey, M. R. Carr, R. D. Richards, D. Gonzalez, "Evaluation of the growth of quantum dots InAs(Bi)/GaAs under different Bi flow conditions.," Presentation in CNMAT2022, 2022.

# **Table of Contents**

1.Thesis Introduction	18
2.Literature Review	19
2.1 III-V Semiconductor Fundamentals	19
2.2 Epitaxial Growth of III-V Semiconductors	26
2.2.1 InAs QD Growth	26
2.2.2 GaAs <sub>1-x</sub> Bi <sub>x</sub> Growth	31
2.2.3 AlAs <sub>1-x</sub> Bi <sub>x</sub> & Al <sub>x</sub> Ga <sub>1-x</sub> As <sub>y</sub> Bi <sub>1-y</sub> Growth	35
3. Experimental Techniques	37
3.1 Molecular Beam Epitaxy	37
3.1.1 Molecular Beam Epitaxy System Overview	38
3.1.2 Pumping Systems	39
3.1.3 Effusion Cells	41
3.1.4 In situ Monitoring Systems	42
3.1.4.1 Ion Gauges	42
3.1.4.2 Wide Range Gauge	44
3.1.4.3 Reflection High Energy Electron Diffraction	44
3.1.5 Heater Stage and Flag Plate	48
3.2 MBE Operating Principles	52
3.2.1 Growth Modes	52
3.2.1.1 FvdM Growth	52
3.2.1.2 VW Growth	53
3.2.1.3 SK Growth	53
3.2.2 MBE Reactor Calibrations	54
3.2.2.1 Growth Rate	54
3.2.2.2 Substrate Temperature Calibration	55
3.2.2.3 Flux Calibrations	57
3.2.2.4 1:1 Calibration	57
3.2.2.5 Calibration Uncertainties	58
3.3 X-Ray Diffraction	59
3.4 Photoluminescence	61
3.4.1 Power Dependent PL	63
3.4.2 Temperature Dependent PL	64
3.5 Microscopy	64
3.5.1 Nomarski	64
3.5.2 Atomic Force Microscopy	65
3.5.3 Transmission Electron Microscopy	66

3.6 Ion Beam Analysis	67
3.6.1 RBS	67
3.6.2 ToF-EDR	69
4. Bi Surfactant Alteration of Self Assembled InAs QDs on 001 GaAs Substrates	71
4.1. Growth Methodology	72
4.2 QD Thickness Series	75
4.2.1 PL 20 K & 297 K	75
4.2.2 AFM	77
4.2.3 Power Dependent PL	83
4.2.4 Temperature Dependent PL	87
4.3 Growth Temperature	91
4.3.1 PL	91
4.3.2 AFM	93
4.3.2 Power Dependent PL	97
4.3.3 Temperature Dependent PL	100
4.4 Bi Flux Series	103
4.4.1 PL	104
4.4.2 AFM	106
4.4.3 Power Dependent PL	114
4.4.4 Temperature Dependent PL	116
4.5 QD Study Conclusions	119
5. Growth of Studies of Epitaxial Al <sub>x</sub> Ga <sub>1-x</sub> As <sub>y</sub> Bi <sub>1-y</sub> on 001 GaAs	120
5.1. Growth Methodology	122
5.1.2 Growth Study Subseries	125
5.1.2.1 Al Content Series	125
5.1.2.2 Growth Temperature Series	125
5.1.2.3 Bi Flux Series	125
5.2 PL 20 & 297 K	126
5.2.1 Al Content	126
5.2.2 Growth Temperature	131
5.2.3 Bi Flux	133
5.3 XRD	136
5.3.1 Al Content	136
5.3.2 Growth Temperature	138
5.3.3 Bi Flux	139
5.4 Nomarski Microscopy	140
5 / 1 Al Content	140

5.4.2 Growth Temperature	142
5.4.3 Bi Flux	143
5.5 Power Dependent PL	144
5.5.1 Al Content Series	144
5.5.2 Growth Temperature	147
5.5.3 Bi Flux	149
5.6 TD PL	152
5.6.1 AL Content	153
5.6.2 Growth Temperature	158
5.6.3 Bi Flux	162
5.7 Ion Beam Analysis	165
5.7.1 Al Content	165
5.7.2 Growth Temperature	170
5.7.3 Bi Flux	174
5.8 Conclusions	178
5.8.1 Al content Series Conclusions	178
5.8.2 Growth Temperature Series Conclusions	179
5.8.3 Bi Flux Sub Series Conclusions	180
5.8.4 AlGaAsBi Growth Study Conclusions & Final Thoughts	180
$ 6. \; Ex\text{-situ Annealing Studies of Epitaxially Grown } \qquad Al_xGa_{1\text{-}x}As_yBi_{1\text{-}y} \; on \; GaAs \; 001 $	182
6.1 Introduction	182
6.2 Growth Methodology	183
6.1 Unannealed Characterisation XRD and PL	185
6.2 Annealed Characterisation XRD and PL	188
6.5 Power Dependent PL	192
6.6 Ion Beam Analysis	194
6.7 Conclusions	204
7 Final thoughts & Future Works	205
9 Deferences	200

# **Contents of Figures**

Figure 1 Zinc blende crystal structure of GaAs [1].
Figure 2 A) Graph showing the relation between interatomic separation and energy gap
broadening. B) diagram showing the band broadening of the outer orbitals in GaAs. Adapted from [4]
Figure 3 Band diagrams illustrating the 3 classes of materials. Boxes denote the allowed
energy states within each band with grey denoting the level of occupied states within each band. The
dashed line represents the fermi level. Adapted from [5].
Figure 4 k space bandgap diagram for generalised semiconductor material showing a direct
semiconductor with indirect band gap shown with dashed line. Adapted from [6]2
Figure 5 Diagram of Auger recombination mechanisms: A) CHCC, B) CHSH & C)
Suppressed CHSH with increased $^{\Delta}$ so. Adapted from [9]
Figure 6 Binary semi-conductor alloys plotted with lattice constant against band gap with
effects of forming ternary alloys shown with interconnected lines between the constituent binaries
[12]
Figure 7 SK growth with 3D islands formed atop a wetting layer both composed from the
deposited material
Figure 8 Morphological map of the 25 GaAsBi samples growth at 325 °C under various flux
ratio profiles with the 4 droplet regimes shown. The colour of the data point represents the Bi
composition, and the size of the data points represents breadth of the peak. Taken from B. A. Carter
[58]
Figure 9 Omega 2 theta XRD scan of GaAs <sub>0.964</sub> Bi <sub>0.036</sub> sample with 3.6 at% Bi
Figure 10: 2D Schematic of OMICRON MBE reactor, with substrate holder shown at load
(solid) and growth height (dashed) with e-beam for RHEED (yellow dashed) shown. Additional cells
are present although not shown for ease of understanding.
Figure 11 schematic of the structure of an ion gauge, adapted from [72]
Figure 12 A) Diagram of construction of the ewald sphere and resultant diffraction pattern
from a crystalline substrate showing the first 2 laue zones from diffraction of $K_1$ and $K_2$ vectors. B)
Diagram of substrate surfaces and resultant impact on reciprocal space and observed RHEED pattern,
adapted from [74]4
Figure 13 A) Schematic diagram showing formation of kikuchi lines from inelastically
scattered electrons. B) Diagram of intensity showing kikuchi pattern formation. Adapted from [75]. 4
Figure 14 RHEED patterns take from on GaAs substrates. For C 2x4 the viewing orientation
are A) [110] and B) [110] with corresponding atomic arrangements for structures under low and
high As flux for $\alpha$ and $\gamma$ shown in B) and D) respectively. For C 4x4 the viewing orientations E)
[110] and B) [110] for the G) $\alpha$ structure and H) [110] and I) [110] for the J) $\beta$ structure. Adapted
from [76]4
Figure 15 Image of MBE STM heater stage taken during MBE maintenance. A) side on view
B) down up view C) top down view of Mo flag style sample plate holder4
Figure 16 Temperature profile as a function of time for an undoped GaAs wafer at 510 °C A)
raw temperature. B) Percentage of target temperature reached when power was restored5
Figure 17 Thermal image of GaAs wafer mounted in MBE system heater stages at 550 °C5
Figure 18 Schematic of surface interface free energies in MBE Growth on partially grown
epilayer5
Figure 19 FvdM growth with incident Ga atom migrating to step edge of incomplete epilayer
5
Figure 20 VW growth with 3D islands of deposited material atop the substrate5
Figure 21 SK growth with 3D islands formed atop a wetting layer both composed from the
deposited material.

Figure 22 RHEED intensity oscillations of a homoepitaxial growing GaAs surface measured
from the 2 brightest 1st order RHEED rods5
Figure 23 RHEEDof thermal desorption of the native surface oxide at 600 °C5
Figure 24 RHEED of $c(4x4) \rightarrow c(2x4)$ transition in the absence of an As flux at 400 °C 5
Figure 25 RHEED of the removal of an amorphous As capping layer by sublimation at 300
°C5
Figure 26 Image of RHEED from A) C 2x4 reconstruction on GaAs at start of 1:1 calibration
and B) post Ga droplet formation with additional spots due to Ga droplets highlighted within the
white squares5
Figure 27 Diagram of the diffraction of x-rays from the (004) plane of a crystalline sample.5
Figure 28 Diagram of basic XRD system6
Figure 29 Representative XRD scans of AlGaAsBi structure A) Reciprocal space map B)
Omega 2 theta scan C) and D) are rocking curves for the Bi peak at -700 arcseconds and AlGaAs at -
180 arcseconds respectively
Figure 30 Diagram of PL system setup6
Figure 31 Diagram of Nomarski microscopy system
Figure 32 Representative diagram of AFM system
Figure 33 Diagram of TEM system
Figure 34 A)Diagram of ion beam system setup for RBS measurements and B) an example
RBS measurement result for AlGaAsBi containing structure
Figure 35 Ion beam analysis of STM83 5 at% AlGaAsBi sample TOF ERD Histogram 6
Figure 36 A) diagram of ion beam setup for ToF ERD measurements B) 3D model of the
ToF ERD system utilised for measurement
Figure 37 RHEED reconstructions of GaAs surface from buffer through to InAs QD
formation
Figure 37 QD cross sectional sample structure with InAs QDs shown in blue7
Figure 39 QD growth procedure with substrate temperature and incident flux profiles for Bi
flux contain growth. Open cell shutters are represented as solid colour bars on the plot
Figure 41 Full width half maximum of PL taken at 297 K and 20 K for InAs QD grown with
deposition thicknesses between 2.2 to 3.1 ML.
Figure 40 Photoluminescence emission spectra at 100 mW excitation for InAs QD samples
with deposition thicknesses between 2.2 - 3.1 ML, measured at temperatures of A) 297 K and B)
20 K
Figure 42 A) Integrated PL spectra at 20 K and 300 mW with integration across full emission
spectra. B) QD ground state peak position of PL emission spectra at 100 mW excitation7
Figure 43 AFM images of InAs QDs grown with InAs deposition layer thicknesses between
2.2 to 3.1 ML. Where, A) 2.2 ML, B) 2.5 ML C) 2.7 ML D) 2.9 ML and E) 3.1 ML
Figure 44 QD density against InAs deposition thicknesses between 2.2 to 3.1 ML7
Figure 45 QD populations of height and aspect ratio for InAs QD samples with InAs
deposition layer thicknesses between 2.2 to 3.1 ML. Where A) QD height and B) QD aspect ratio7
Figure 46 QD height distributions for InAs QD samples with InAs deposition layer
thicknesses between 2.2 to 3.1 ML. Where, A) 2.2 ML, B) 2.5 ML C) 2.7 ML D) 2.9 ML and E) 3.1
ML8
Figure 47 QD aspect ratio distributions for InAs QD samples with InAs deposition layer
thicknesses between 2.2 to 3.1 ML. Where, A) 2.2 ML, B) 2.5 ML C) 2.7 ML D) 2.9 ML and E) 3.1
ML8
Figure 48 20 K PD PL of InAs QD on GaAs after A) 2.2. B) 2.7 and C) 3.1 ML of InAs
deposition8
Figure 49 Power dependent exponents for InAs QD samples with InAs deposition layer
thicknesses between 2.2 - 3.1 ML measured at 20 K.

Figure 50 A) Peak emission energies of ground, 1st and 2nd excited states, B) energy separation
between ground state (GS) and subsequent excited state (ES) emission
Figure 51 Normalised integrated photoluminescence vs excitation power for InAs QD
samples with InAs deposition thicknesses between 2.2 - 3.1 ML. Where, A) 2.2 ML, B) 2.5 ML C)
2.7 ML D) 2.9 ML and E) 3.1 ML
Figure 52 Non radiative recombination activation energies extracted from fitted temperature
dependent photoluminescence for InAs QD samples with InAs deposition layer thicknesses between
2.2 - 3.1 ML. A) Ea <sub>1</sub> B) Ea <sub>2</sub>
Figure 53 Non radiative recombination constants extracted from fitted temperature dependent
PL for InAs QD samples with InAs deposition layer thicknesses between 2.2 - 3.1 ML. A) C <sub>1</sub> B) C <sub>2</sub> 88
Figure 54 Temperature dependent PL of QD with 2.7 ML of InAs deposition at temperatures
between 20 K to 297 K
Figure 55 Normalised integrated photoluminescence vs temperature for InAs QD samples
with InAs deposition layer thicknesses between 2.2 - 3.1 ML. Where, A) 2.2 ML, B) 2.5 ML C) 2.7
ML D) 2.9 ML and E) 3.1 ML. Data is shown by blue triangle with the red line showing the fitting. 90
Figure 56 Photoluminescence emission spectra at 100 mW excitation for InAs QD samples
with InAs growth temperatures between 450 to 510 °C, measured at temperatures of A) 297 K and B)
20 K
Figure 57 Primary peak position of photoluminescence emission spectra at 100 mW
excitation for InAs QD samples with InAs growth temperatures between 450 to 510 °C93
Figure 58 Integrated Photoluminescence spectra at 20 K of for InAs QD samples with growth
temperatures between 450 to 510 °C.
Figure 59 QD populations of height and aspect ratio for InAs QD samples with InAs growth
temperatures between 450 to 510 °C.
Figure 60 Raw AFM of InAs QD samples with InAs growth temperatures between 450 to 510
°C, where A) 510 °C, B) 480 °C and C) 450 °C. Note the 450 °C image is of a comparatively larger
area95
Figure 61 QD Height distributions for InAs QD samples with InAs growth temperatures
between 450 to 510 °C, where A) 510 °C, B) 480 °C and C) 450 °C. Experimental data is indicated by
blue bars with gaussian fits shown by the red line
Figure 62 QD aspect ratio distributions for/ InAs QD samples with InAs growth temperatures
between 450 to 510 °C, where A) 510 °C, B) 480 °C and C) 450 °C. Experimental data is indicated by
blue bars with gaussian fits shown by the red line
Figure 63 QD densities for InAs QD grown between 450 to 510 °C.
Figure 64 Power dependent exponents for InAs QD samples with InAs growth temperatures
between 450 to 510 °C measured at 20 K
Figure 65 A) Representative power dependent PL at 20 K of sample grown at 480 °C. B)
Corresponding peak positions from QD emission.
Figure 66 Normalised integrated photoluminescence vs excitation power for InAs QD
samples with growth temperatures between 450 to 510 °C. Where, A) 510 °C, B) 480 °C and C) 450
°C
Figure 67 Normalised integrated photoluminescence vs temperature for InAs QD samples
with InAs growth temperatures between 450 – 510 °C. Where, A) 510 °C, B) 480 °C and C) 450 °C.
Experimental data is indicated by blue triangle with the fits shown by the red line
Figure 68 Non radiative recombination activation energies extracted from fitted temperature
dependent photoluminescence for InAs QD samples with growth temperatures between
450 to 510 °C
Figure 69 Non radiative recombination constants extracted from fitted temperature dependent
photoluminescence for InAs QD samples with growth temperatures between 450 to 510 °C 102
Figure 70 QD cross sectional sample structure with InAs QD shown in blue and bismuth
layers shown in purple.
, pw-p-w

Figure 71 Primary peak position of photoluminescence emission spectra at 100 mW	
excitation for InAs QD samples with Bi flux during QD Growth of between 0 to 3.5 nA	104
Figure 72 Photoluminescence emission spectra at 100 mW excitation for InAs QD samples	3
with Bi flux during QD Growth of between 0 - 3.5 nA, measured at temperatures of A) 297 K and I	B)
20 K	105
Figure 73 Integrated Photoluminescence spectra at 20k of for InAs QD samples with Bi	
fluxes of 0-3.5 nA	106
Figure 74 QD populations of height and aspect ratio for InAs QD samples with InAs QD	
samples with Bi flux during QD Growth of between 0 to 3.5 nA,	107
Figure 75 QD density for InAs QD samples with InAs QD samples with Bi flux during QD	)
growth of between 0 to 3.5 nA,	108
Figure 78 AFM Images of InAs QD samples with a Bi flux during QD growth between 0 to	С
3.5 nA. Where, A) 0 nA, B) 1.2 nA C) 2 nA D) 2.6 nA and E) 3.5 nA	109
Figure 77 QD height vs PL peak energy for Bi flux QD series with fluxes between 0 to 3.5	5
nA	110
Figure 78 QD volume density for InAs QD samples with InAs QD samples with Bi flux	
during QD growth of between 0 to 3.5 nA,	110
Figure 79 QD height distributions for for InAs QD samples with Bi flux during QD growth	ı of
between 0 to 3.5 nA. Where, A) 0 nA, B) 1.2 nA C) 2 nA D) 2.6 nA and E) 3.5 nA. Experimental	
data is indicated by blue bars with gaussian fits shown by the red line.	111
Figure 80 QD aspect tatio distributions for for InAs QD samples with Bi flux during QD	
growth of between 0 to 3.5 nA, Where A) 0 nA, B) 1.2 nA C) 2 nA D) 2.6 nA and E) 3.5 nA.	
Experimental data is indicated by blue bars with gaussian fits shown by the red line.	112
Figure 81 Power dependent exponents for InAs QD samples with InAs QD samples with B	i
flux during QD growth of between 0 to 3.5 nA, measured at 20 K.	114
Figure 82 PD PL of sample grown with 2 nA Bi flux.	114
Figure 83 Normalised integrated photoluminescence vs excitation power for InAs QD	
samples with Bi flux during QD growth of between 0 to 3.5 nA. Where, A) 0 nA, B) 1.2 nA C) 2 n	ıΑ
D) 2.6 nA and E) 3.5 nA.	115
Figure 84 Normalised integrated photoluminescence vs inverse temperature for InAs QD	
samples with Bi flux during QD growth of between 0 to 3.5 nA. Where, A) 0 nA, B) 1.2 nA C) 2 n	ıΑ
D) 2.6 nA and E) 3.5 nA.	
Figure 85 Non radiative recombination activation energies extracted from fitted temperatur	:e
dependent photoluminescence for InAs QD samples with Bi fluxes of 0-3.5 nA	
Figure 86 Non radiative recombination constants extracted from fitted temperature dependent	
photoluminescence for InAs QD samples with Bi fluxes of 0 to 3.5 nA	118
Figure 87 Comparative graph of α, β and k of GaAs & GaAs <sub>0.96</sub> Bi <sub>0.04</sub> [106]	
Figure 88 Diagram of the impact ionisation process and effect of Bi incorporation on band	
structure.	
Figure 89 Al <sub>x</sub> Ga <sub>1-</sub> yBi <sub>1-y</sub> series sample structure	
Figure 90 RHEED patterns of the sample surface A) post AlGaAs buffer growth and B) po	st
AlGaAsBi layer growth.	123
Figure 91 A) AlGaAs/GaAs QW sample structure B) Room temperature PL of control	
samples for AlGaAsBi growth study featuring a GaAs <sub>0.976</sub> Bi <sub>0.024</sub> and AlGaAs/GaAs QW sample	124
Figure 92 Photoluminescence emission spectra at 100mW excitation for AlGaAsBi sample	S
with Al content between 0-15 at% measured at temperatures of A) 297 K and B) 20 K	126
Figure 93 Photoluminescence emission spectra at 100 mW excitation for AlGaAsBi sample	es
grown between 280 -340 °C measured at temperature of A) 297 K and B) 20 K	131
Figure 94 Photoluminescence emission spectra at 100 mW excitation for AlGaAsBi sample	es
grown with Bi fluxes between $0.8 - 2.8$ nA measured at temperature of A) 297 K and B) 20 K	135

Figure 95 X Ray Diffraction for Al content series with fitted XRD data generated from layer
models. Where, A) 15 at%, B) 10 at%, C) 5 at%, D) 2.5 at% and E) 0 at%
Figure 96 X ray diffraction for Al content series with fitted XRD data generated from layer
models. Where, A) 340 °C, B) 320 °C, C) 300 °C and D) 280 °C
Figure 97 X Ray Diffraction for Al content series with fitted XRD data generated from layer
models. Where, A) 0.8 nA, B) 1.4 nA, C) 2.2 nA and D) 2.8 nA
Figure 98 Nomarski images of as grown sample surfaces. Where, A) 0 at%, B) 2.5 at%, C) 5
at%, D) 10 at% and E) 15 at%
Figure 99 Nomarski images of as grown sample surfaces. Where, A) 280 °C, B) 300 °C,
C) 320 °C and D) 340 °C
Figure 100 Nomarski images of as grown sample surfaces. Where, A) 0.8 nA, B) 1.4 nA,
C) 2.2 nA and D) 2.8 nA
Figure 101 Exponent values extracted from lines of best fit for normalised integrated
Photoluminescence vs excitation power at temperature of 20 K & 297 K for changing aluminium
contents between 0 to 15 at%
Figure 102 Power dependent PL of STM83 at 20K with excitation powers between 1000 to 0.
1 mW
Figure 103 Normalised integrated photoluminescence vs excitation power for changing
aluminium contents between 0-15 at%. Where, A) 0 at%, B) 2.5 at%, C) 5 at%, D) 10 at% and E) 15
at%
Figure 104 Exponent values extracted from lines of best fit for normalised integrated
Photoluminescence vs excitation power at temperature of 20 K & 297 K for varying growth
temperatures between 280 to 340 °C
Figure 105 Normalised integrated photoluminescence vs excitation power for growth
temperatures between 280 to 340 °C. Where, A) 280 °C, B) 300 °C, C) 320 °C and D) 340 °C 149
Figure 106 Exponent values extracted from normalised integrated photoluminescence vs
excitation power at temperatures of 20 K & 297 K for Bi fluxes between 0.8 to 2.8 nA
Figure 107 SEM image of metallic droplets present on surface of sample grown under 2.8 nA
of Bi flux
Figure 108 Int Pl Integrated Photoluminescence spectra at 20k of varying Bi fluxes between
0.8 to 2.8 nA
Figure 109 Normalised integrated photoluminescence vs excitation power for changing Bi
fluxes between $0.8$ - $2.8$ nA. Where, A) $0.8$ nA, B) $1.4$ nA, C) $2.2$ nA and D) $2.8$ nA
Figure 110 Integrated Photoluminescence spectra at 20k of varying Al contents between 0 to
15%
Figure 111 Non radiative recombination activation energies extracted from fitted temperature
dependent photoluminescence for aluminium contents between 0-15 at%. A) Ea <sub>1</sub> B) Ea <sub>2</sub> 154
Figure 112 Ratio of non-radiative recombination fitting coefficients from temperature
dependent photoluminescence for aluminium contents between 0 to 15 at%
Figure 113 Temperature dependent PL of STM 83 between 20 to 297 K at 100 mW optical
excitation
Figure 115 Integrated photoluminescence spectra at 20 K of varying growth temperatures
between 280 to 340 °C
Figure 116 Non radiative recombination activation energies extracted from fitted temperature
dependent photoluminescence for varying growth temperatures between 280 to 340 °C159
Figure 117 Temperature dependent PL of STM88 a sample grown at 280 °C and measured
between 20 to 297 K at 100 mW optical excitation
Figure 118 Normalised photoluminescence vs sample temperature at constant excitation for
growth temperatures between 280 to 340 °C. Where, A) 280 °C, B) 300 °C, C) 320 °C and D) 340 °C.
260 c, b) 300 c, c) 320 c and b) 340 c.

Figure 119 Ratio of non-radiative recombination constants extracted from fitted temperature
dependent photoluminescence for varying growth temperatures between 280 to 340 °C162
Figure 120 Non radiative recombination activation energies extracted from fitted temperature
dependent photoluminescence for Bi fluxes between 0.8-2.8 nA. A), Ea <sub>1</sub> and B) Ea <sub>2</sub> 163
Figure 121 Ratio of constants C1:C2 for Bi fluxes between 0.8 to 2.8 nA. A), Ea <sub>1</sub> and B) Ea <sub>2</sub> .
163
Figure 122 TD photoluminescence of STM 89 a sample grown with 2.2 nA of Bi flux at
temperatures between 20 to 297 K
Figure 124 A) Ion beam analysis of STM83 5 at% AlGaAsBi raw RBS spectra with
simulated fit B) Ion beam analysis of STM83 5 at% AlGaAsBi sample TOF ERD Histogram 165
Figure 125 Comparison of A) Bi contents as measured from PL XRD RBS and TOF ERD and
B) Al contents as measured from XRD and TOF ERD
Figure 126 Depth profile of 5 at% AlGaAsBi extracted from TOF ERD by Potku fitting 167
Figure 127 Cross section of STM83 as imaged by high-angle annular dark-field scanning
transmission electron microscopy
Figure 128 Substitutional contents for Bi and Al, Ga, As as measured by RBS
Figure 129 Comparison of A) Bi contents as measured from PL XRD RBS and TOF ERD
and B) Al contents as measured from XRD and TOF ERD
Figure 130 STM 88 280 °C Potku Profile extracted from Tof ERD fitting171
Figure 131 TOF ERD and RBS of Temperature Sub series shown with ascending
temperature.
Figure 132 Substitutional contents for Bi and Al,Ga, As as measured by RBS
Figure 133 Comparison of A) Bi contents as measured from PL XRD RBS and TOF ERD and
B) Al contents as measured from XRD and TOF ERD
Figure 134 TOF ERD and RBS of growth temperature sub series, shown in ascending order.
Figure 135 STM 89 Potku Profile of the sample grown under 2.2nA of Bi flux177
Figure 136 Substitutional contents for Bi and Al, Ga, As as measured by RBS
Figure 137 Al <sub>1-x</sub> Ga <sub>x</sub> As <sub>1-y</sub> Bi <sub>y</sub> annealing sample structure
Figure 138 RHEED patterns of the sample surface A) post Al <sub>0.3</sub> Ga <sub>0.7</sub> As buffer growth and B)
post Al <sub>1-x</sub> Ga <sub>x</sub> As <sub>1-y</sub> Bi <sub>y</sub> layer growth
Figure 139 Diagram of STM8F sample in sample holder. Cleaving lines used for sectioning of
the wafer for the annealing study with assigned annealing temperatures for each section185
Figure 140 X-ray diffraction for sections of STM8F as grown prior to the conduction of the
annealing study. Included are the fits to the XRD data used for extracting Bi contents and layer
thicknesses
Figure 141 Photoluminescence emission spectra at 300 mW excitation for AlGaAsBi
annealing sample sections as grown measured at temperatures of A) 297 K and B) 20 K187
Figure 142 Extracted value of Bi content prior and post annealing extracted by XRD and Pl.
Control values indicated by lines
Figure 143 X-ray diffraction for sections of STM 8F post a 30s anneal. Included are the fits to
the XRD data used for extracting Bi contents and layer thicknesses
Figure 144 Photoluminescence emission spectra at 300 mW excitation for AlGaAsBi
annealing sample sections post a 30 s anneal. Measured at temperatures of A) 297 K and B) 20 K. 190
Figure 145 PL Intensities relative to control for measurements at 297K and 20 K prior and
post 30 s annealing
Figure 146 Exponent values extracted from lines of best fit for normalised integrated
Photoluminescence vs excitation power at temperatures of 20 K & 297 K for varying annealing
temperatures between 400 to 650 °C. The control is also present at the in situ anneal temperature of
320 °C

Figure 147 Normalised Integrated Photoluminescence vs excitation power for ex-situ	
annealing 400 to 650 °C. Where, A) unannealed control, B) 400 °C, C) 500 °C, D) 550 °C E) 600 °C	
and F) 650 °C	3
Figure 148 ToF ERD and RBS results for the control sample STM 8FCC and equivalent	
sample grown with high temperature capping layers, STM 83 Al <sub>0.05</sub> Ga <sub>0.95</sub> As <sub>0.976</sub> Bi <sub>0.24</sub> 19	5
Figure 149 Potku and MCERD simulated composition of the control sample as fitted to the	
ToF ERD data shown in Figure 147.	6
Figure 150 Glancing angle RBS of control sample for annealing series and zoomed in	
subsection showing the magnified Bi peak	8
Figure 151 ToF ERD of sample annealed at 550 °C	9
Figure 152 Impurity atomic fractions of H, C and O as detected by ToF ERD in each	
epitaxial layer for samples annealed between 400 to 650 °C, with the control shown at 320 °C. Layers	;
are colour coded. With each impurity element point differentiated by shape20	0
Figure 153 III:V atomic ratio for samples annealed between 400 to 650 °C20	1
Figure 154 Bi contents as measured by RBS for each epitaxial layer for samples annealed	
between 400 to 650 °C, with the control shown at 320 °C	2
Figure 155 Substitutional percentages of Bi and group III elements within the structures for	
samples annealed between 400 to 650 °C.	3

# **Contents of Tables**

Table 1 Temperature ranges for different source effusion cells for Omicron MBE STM	42
Table 2 QD InAs deposition thickness series sample list	75
Table 3 Sample IDs of growth temperature optimisation samples.	91
Table 4 Sample ID for Bi flux QD series	. 104
Table 5 Energies of defects commonly observed with GaAsBi materials. Energy levels of	
majority-electron traps are relative values below conduction band minimum and majority-holes tra	aps
above valence band minimum	.129
Table 6 Bi contents calculated from RT PL of AlGaAsBi	.130
Table 7 Bi content extract from 297 K PL	.133
Table 8 Bi content extract from 297 K PL.	.134
Table 9 Al and Bi contents extract from XRD Fitting.	.138
Table 10 Al and Bi contents extract from XRD Fitting of sample grown between 280-340	°C.
	.139
Table 11 XRD fitting values from Bi flux series.	. 140
Table 12 Bi contents prior to annealing.	.186
Table 13 extracted Bi contents post annealing.	.188

## 1. Thesis Introduction

This thesis aims to extend the understanding of Bi as a constituent or modifying element within epitaxial growth of III-V semiconductor materials. Bi has many positive effects when incorporated into III-V semiconductors that make it well suited for engineering next generation materials for device applications. However, the parameter space for growing these potential next generation materials remains vastly unexplored. This thesis focuses on two potential new III-V materials for photovoltaic applications, InAs QDs modified by a Bi surfactant, with a view of offering a new mechanism to control QD morphology. Secondly the incorporation of Al into GaAs<sub>y</sub>Bi<sub>y-1</sub> to form and the quaternary alloy Al<sub>x</sub>Ga<sub>1-x</sub>As<sub>1-y</sub>Bi as a new material for the avalanche region of APD devices. Three chapters document the growth methodologies and ex-situ processing techniques utilised to synthesise these materials and map the available parameter space. Documenting the impact of growth conditions on the optical properties and crystalline structure of the materials. The ultimate goal is to provide the knowledge to make these materials accessible to the wider research community laying the groundwork for their adoption into consumer devices.

## 2.Literature Review

## 2.1 III-V Semiconductor Fundamentals

The III-V semiconductor gallium arsenide (GaAs) is the second most widely produced semiconductor on the planet after silicon (Si). However, despite the reduced cost of Si the indirect band gap makes it an ineffective material for optoelectronic devices, and within this field the use of III-V semiconductors has been widely adopted. GaAs is the most prominent of these with its direct band gap of 1.42 eV and high electron mobility of (~8500 cm2/Vs at 300 K), it's well suited to optoelectronic device applications. GaAs forms a zinc blend crystal structure with each atom forming 4 nearest neighbour bonds to produce a tetrahedral bonding structure within the lattice, shown in Figure 1 [1]. This produces 4 spin paired covalent bonds within the s and p orbitals. While the bonding in III-V is regarded as largely covalent there is a small component of ionic bonding present within the structure, this increases the bond strength within the crystal [2]. The lattice constant within the structure is 5.6533 Å with no impurity atoms present [3]. It is a member of the isometric crystal system with a cubic unit cell. The lattice constant and corresponding bond length can be altered by the inclusion of impurity or alloying elements. This results in an alteration of the electron orbital energies and the band gap of the crystal. The main attraction of GaAs is its ability to readily alloy with other group III and V elements providing access to an incredibly powerful mechanism to tailor the optoelectronic properties.

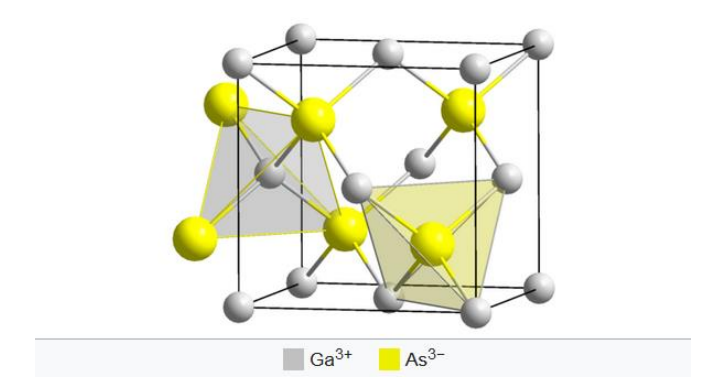


Figure 1 Zinc blende crystal structure of GaAs [1].

The band structure of III-V semiconductors and crystalline solids extends from the breakdown of the discrete energy levels of atoms due to the bonding electrons within the crystal. The outer electron orbitals overlap with the neighbouring orbitals of other atoms as the atoms are bought into proximity. As found within the environment of a crystalline solid. This results in the broadening of the electron orbital energies from discrete states into broad energy bands, as shown in Figure 2. In the case of GaAs and other III-V semiconductors, the bonding electron orbitals that contribute to the bands are the outer S and P orbitals. Group III element have a  $s^2$   $p^1$  configuration and the group V's a  $s^2$   $p^3$  outer shell electron configuration.

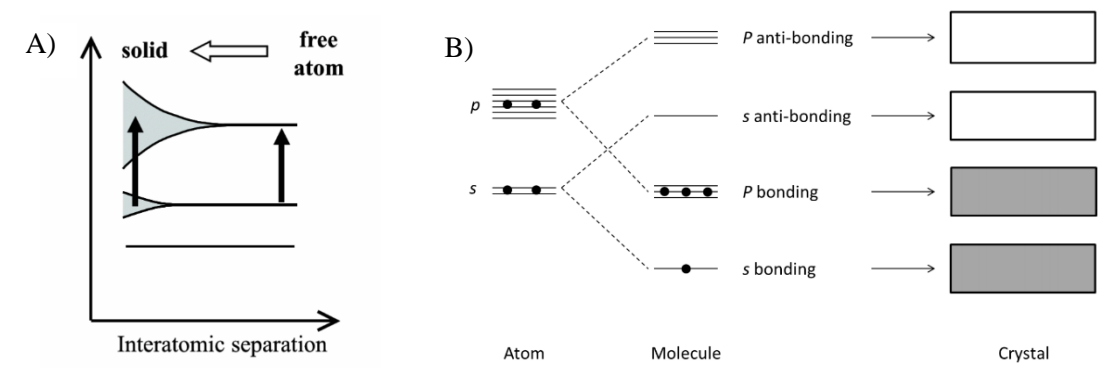


Figure 2 A) Graph showing the relation between interatomic separation and energy gap broadening. B) diagram showing the band broadening of the outer orbitals in GaAs. Adapted from [4].

The broadening of the electron orbitals into two bands, conduction and valence produces one of 3 types of band structures. These 3 cases are shown in Figure 3. The type of band structure is dependent on the atomic and electronic structure of the constituent atoms within the solid. Each atom contributes a state within each band to give the total number of states equal to the number of atoms. Each state can only be occupied by two electrons, spin up and spin down, in accordance with the Pauli exclusion principle. The states within each band are filled in order of increasing energy starting at the lowest energy states. However, above 0 K occupied energy states are influenced by the thermal excitation of electrons to higher energy states. Within a crystalline solid valence electrons are free to move with the provision that there are available uncopied states in which to migrate too. This necessitates that for electrons to move through the material the band must be partially occupied to provide unoccupied states for electron migration.

In the case of an insulator and semiconductor at 0 K the valence band is full, and the conduction band is empty. The distinguishing feature between these two classes is the energy gap between the conduction band and valence band, referred to as the band gap. The band gap is defined as the energy between the highest occupied state within the valence band and the lowest state within the conduction band. An intrinsic semiconductor is commonly regarded as having a small enough band gap that the thermal

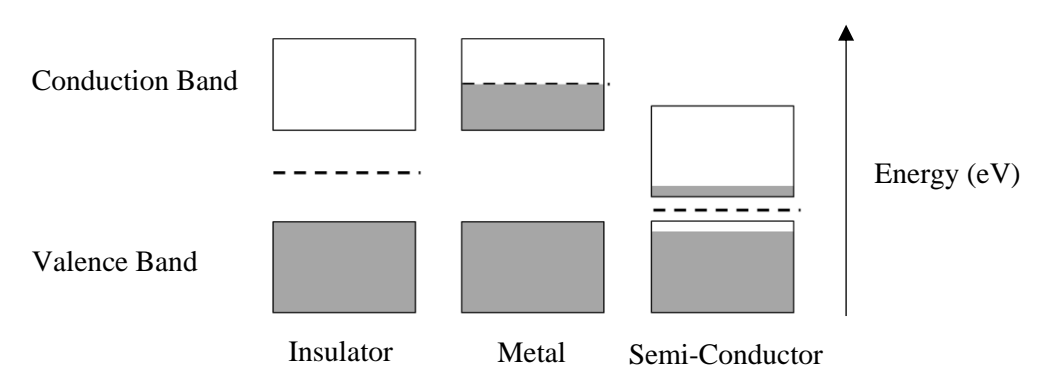


Figure 3 Band diagrams illustrating the 3 classes of materials. Boxes denote the allowed energy states within each band with grey denoting the level of occupied states within each band. The dashed line represents the fermi level. Adapted from [5].

excitation is enough to promote carrier up to the conduction band. However, while there is no exact cutoff between an insulator and a semiconductor, it is regarded that approximately 6 eV is a reasonable boundary. Conductivity within metals is independent of the thermal promotion of carriers into the conduction band, hence a band gap present within these materials. The conductivity instead originates from a permanent occupancy of electrons within the conduction band.

The promotion of carriers across the bandgap produces both a free electron within the conduction band and an empty state within the valence band. An electron is a fundamental subatomic particle with a negative charge and positive mass. However, the missing electron in the unoccupied valence state can be regarded for the sake of simplicity as a particle of positive mass and charge referred to as a hole. Within a band diagram, the energy of a hole is reduced as it increases in energy due to the opposite charge. Hence holes on a bandgap diagram rise as they minimise energy while electrons will fall back into the valence band. In intrinsic materials holes are produced only by the promotion of electrons hence, they can be regarded as an electron-hole pair. Both electrons and holes contribute to the conduction of current within a material. Responding to applied fields but moving in opposite directions due to the difference in charge.

Expanding on the previously 1D band diagram to include k space on the x-axis shows the relation of particle energy E against the momentum (wave vector) k of the electrons within the states. This is known as the dispersion relation and produces a plot such as that shown in Figure 4. Direct semiconductors such as GaAs have a conduction and valence band in which the maxima of the valence and minima of the conduction occur at the same momentum. This enables the radiative recombination of an electron-hole pair through the emission of a photon with energy equal to the difference between the initial state and the uncopied valence state. However, an indirect semiconductor shown by the dashed line in Figure 4 has a mismatch between the moment of the maxima and minima of the conduction and valence bands, respectively. This necessitates due to the low momentum of photons that a second interaction between the electron and a phonon must occur to allow for radiative recombination with a hole in the valence band. This second interaction greatly inhibits the promotion and recombination of carriers within indirect semiconductors. Hence, direct semiconductors are highly preferable for photovoltaic devices with absorption of photons with energy equal or greater than the band gap. However, carrier lifetimes are reduced by the ease of recombination within direct semiconductors. In contrast, indirect semiconductors are less efficient photon absorbers but have much longer carrier lifetimes.

The structure of the valence band within k space is also more complex, consisting of three sub bands: heavy holes (HH), light holes (LH) and a spin-orbit (SO) band. The holes with the HH band have a higher effective mass m\* than those within the LH band. This causes two different speeds of response for holes within an electric field. The spin-orbit band is a split-off band from one of the HH bands that

has mixed with a LH band to produce a SO split-off band. In the case of GaAs, the split-off energy ( $^{\Delta}$ so) is 3.4 meV below the HH band at the valence band maxima.

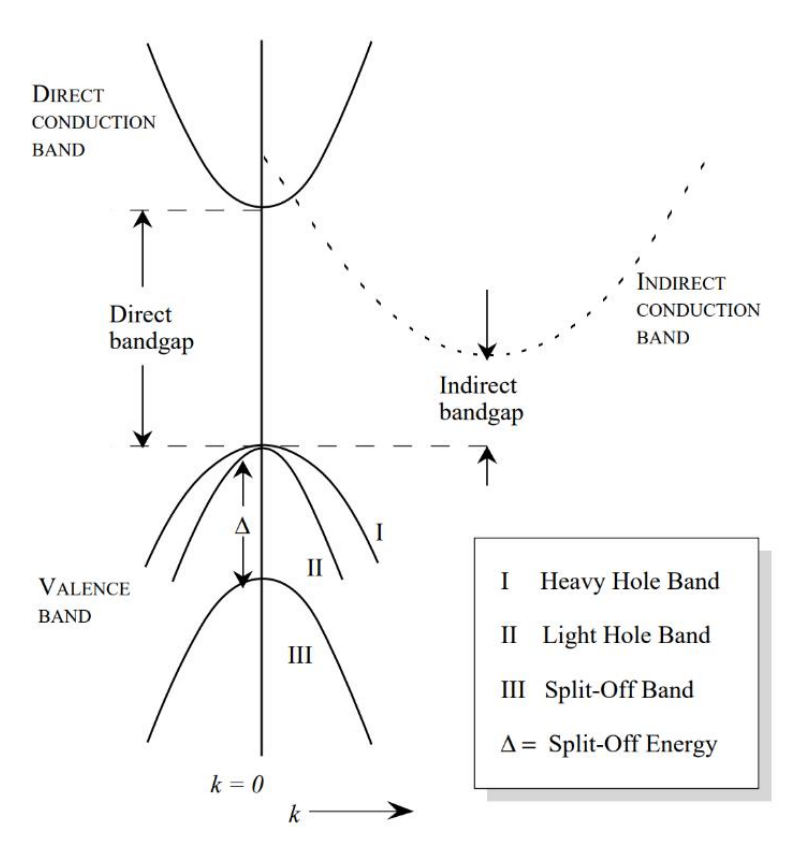


Figure 4 k space bandgap diagram for generalised semiconductor material showing a direct semiconductor with indirect band gap shown with dashed line. Adapted from [6].

Recombination of carriers though the loss of a photon is present in all semiconductor materials and is an unavoidable cause of loss within photovoltaic devices. However, non-radiative mechanisms for the recombination of carriers also exist and can be a further cause of undesirable carrier recombination. Recombination of carriers through trap states sitting at energies within the bang gap through the exchange of a phonon is one such mechanism. This is known as Shockley-Read-Hall (SRH) recombination. The trap states are the results of defects within the crystal structure or impurity elements. It is commonly defined that trap states with the thermal energy of the system to either the conduction or valence band are known as shallow traps and are easier to empty. States that are more deeply buried in the band gap are known as deep states and are more detrimental to the electrical properties. The ability of SRH recombination to absorb carriers with differences in momentum makes them the dominant process in indirect semiconductors. However, under very low carrier density or very high trap density, it can be dominant indirect semiconductors.

The second type of non-radiative recombination is Auger recombination. This process requires a third carrier and there are two main types. One involves two electrons and a heavy hole (CHCC) and the second involves two heavy holes and one electron (CHSH). The former is dominant in n-type and the latter in p-type GaAs[7]. In CHCC the energy is passed to a carrier within the conduction band exciting

it to a higher state and allowing the carrier to recombine with a hole in the valence band. Within the second subtype, the primary electron recombines and exchanges the energy with a HH promoting it into the SO band. The CHSH mechanism is sensitive to the SO split-off energy  $^{\Delta}$ so, hence it can be suppressed when  $^{\Delta}$ so exceeds the band gap. The alloying of Bi into GaAs can increase the  $^{\Delta}$ so value such that it exceeds the band gap, at Bi content above 10.5 at% [8]. This would suppress the CHSH auger recombination mechanism, shown in Figure 5C offering a potential way to reduce this loss mechanism [9]. However, there are additional considerations that arise with high Bi incorporation that will be discussed in later sections.

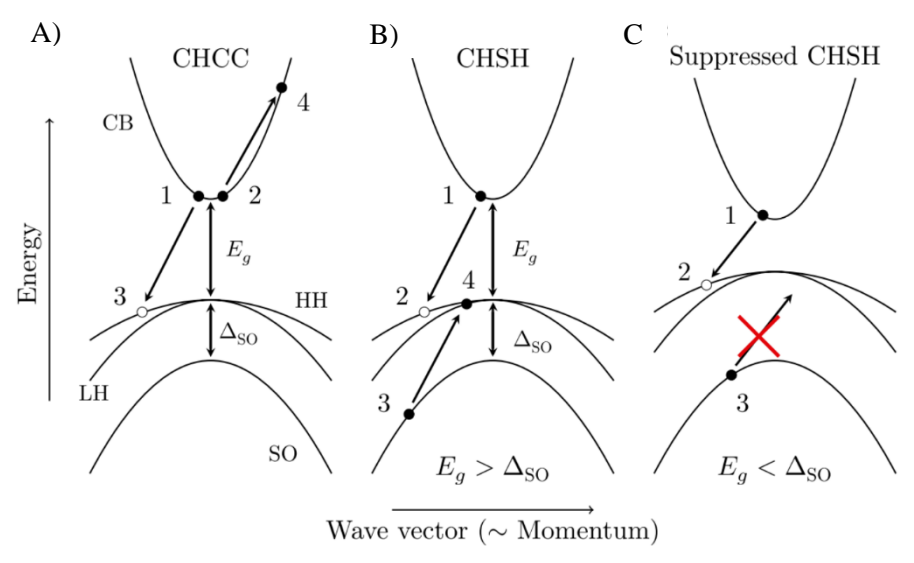


Figure 5 Diagram of Auger recombination mechanisms: A) CHCC, B) CHSH & C) Suppressed CHSH with increased \$^4\$so. Adapted from [9].

The carrier concentrations within pure semiconductors are prohibitively low for devices applications. Intrinsic GaAs crystals have a population of approximately 1.1x10<sup>6</sup> free electrons cm<sup>-3</sup> at 297 K and an equal number of holes, compared with a typical metal which has a free electron population of 10<sup>28</sup> cm<sup>-3</sup> [10]. Hence, pure semiconductors have a very high electrical resistance. The deliberate addition of impurity elements up to the 0.00001% limit with a higher or lower valence can significantly modify the carrier populations within a semiconductor material. The process of adding these elements is known as doping. An example would be the addition of the group V element P into the elemental semiconductor Si. With 5 valence electrons compared with Si's 4, this provides an additional electron that is weakly bound to the P. Bonding energies are of the order of 100ths of a typical electron, allowing them to be easily thermally promoted thermally into the conduction band. These are represented as a level just below the CB. This type of doping is called n-type as the majority of carriers carry a negative charge. Alternatively, through the addition of a lower valence atom such as the group III Al. With 3 valence one less than Si this introduces a potential electron acceptor site just above the VB. This type of doping produces holes with hen function as the majority carrier type. This is known as p-type owing to the positive charge of the majority carrier. This situation is complicated when considering compound semiconductors such as the III-V GaAs, as the effect of a dopant depends on the lattice site it occupies,

either a group III or V site. Group IV elements such as Si can act as either a donor or acceptor depending on which site the Si atom sits this is an example of amphoteric doping. In growth of GaAs by molecular beam epitaxy (MBE) controlling the Si site can be achieved by controlling the As:Ga flux ratio and growth temperature. Reducing the former and increasing the latter will lead to Si favouring the As site [11]. Within this study Si is used exclusively as an n-type dopant with the group II element Be used for p type doping when required. Doping is not without consequences or limits and the dopant species must be carefully selected to avoid creating unwanted defects within the lattice. The atomic species electronegativity and radii should be as similar as possible to the displaced atom to avoid distorting the lattice and introducing undesirable defects such as dislocation or interstitial atoms. Semiconductor materials that have been doped are known as extrinsic semiconductors.

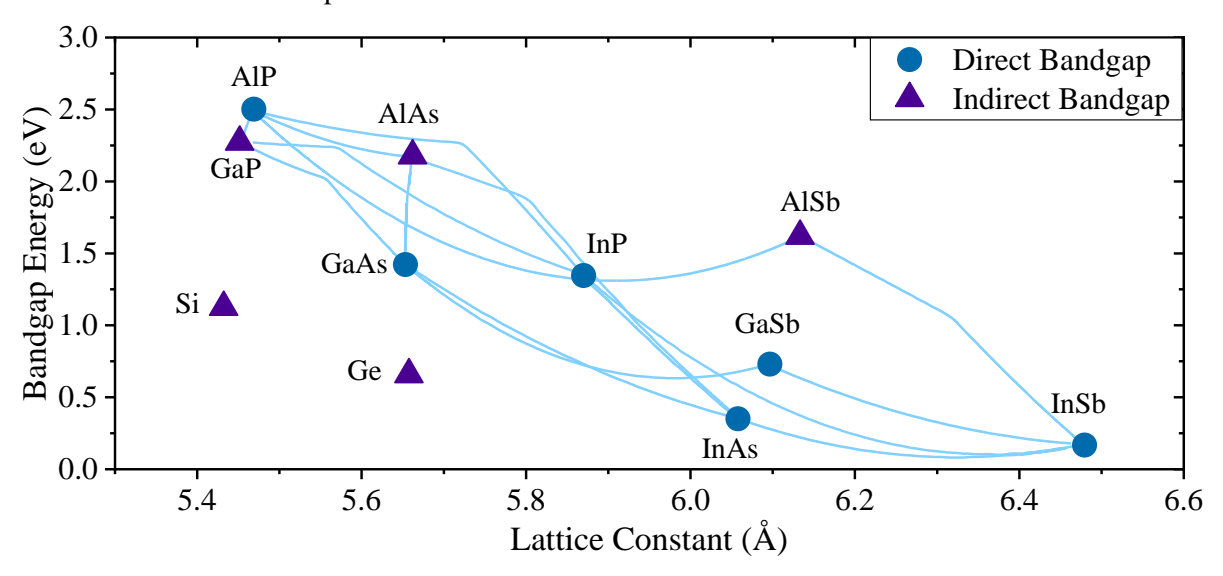


Figure 6 Binary semi-conductor alloys plotted with lattice constant against band gap with effects of forming ternary alloys shown with interconnected lines between the constituent binaries [12].

The properties of binary III-V semiconductor materials can be further modified and tailored through alloying with other III-V elements. Alloying provides the means to tune both the material band gap and the lattice constant through the inclusion of an additional atom species. This is differentiated from doping by the greater quantity of the atomic species present, typically in excess of 0.1%. Figure 6 shows how alloying between binary semiconductors to produce ternary alloys impacts both the lattice constant and the band gap [12]. Increasing the number of alloying elements from a ternary to a quaternary adds another dimension of freedom. Enabling tuning of bandgap and lattice constant within the area encompassed between the 3 constituent binaries Alleviating from the limitation of confinement of tuning along the conjoining line between the two binaries semiconductors. The research within PhD project will focus on alloying GaAs with primarily GaBi and AlBi in ternary and quaternary alloys. The impact of alloying with Al is fairly standard owing to the similar size and electronegativity of the atoms compared with the group III element it replaces within the lattice. The effect of alloying Al in GaAs is shown in Figure 6 along the line between AlAs and GaAs [12]. The addition of Al to GaAs, with AlAs

having a ~0.15% difference in lattice constant, enables the band gap to be tuned between 1.42 eV and 2.16 eV independently of lattice constant with a direct band gap at less than 40% Al content[13]. This can make the Al<sub>x</sub>Ga<sub>x-1</sub>As layer particularly useful for the confinement of electrons within GaAs layer within heterostructures. Indium on the other hand has a vastly different lattice constant to GaAs which allows for greater tuning of the lattice parameter. However, the strain induced when incorporating In into GaAs can change the growth mode and cause relaxation in the crystal. This is discusses in further details in the InAs QD growth sections. The band gap on InAs is 0.354 eV which makes it an effective element for alloying for decreasing the band gap of GaAs while maintaining a direct band gap [14]. Further discussion of the impact of alloying for the systems of interest in this thesis is presented later within this review.

The variation in lattice constant within alloys is dependent on the alloy composition, this relation is assumed to obey Vegard's law[15]. The law states that the lattice constant of a ternary compound can by determined from linear interpolation of the two binary component alloys that form the ternary alloy. This is expressed mathematically for a compound  $A_xB_{1-x}C$  in equation (1)(1. Where  $a_{ABC}$  is the lattice parameter of the ternary;  $a_{AC}$  and  $a_{BC}$  are the lattice parameters of alloys AC and BC respectively. The parameter x is the fractional composition of the binary AC in the ternary alloy ABC. This can be expanded for quaternary alloys by considering the alloy  $A_xB_{1-x}C_yD_{1-y}$  as the construct of is four binaries: AC, AD, BC, and BD. Hence the lattice constant  $A_{1-x}B_xC_{1-y}D_y$  can be constructed from the 4 binaries: AC, AD, BD, and BC which give rise to the interpolation in equation (2).

$$a_{ABC} = xa_{AC} + (1 - x)a_{BC} \tag{1}$$

$$a_{ABCD} = (1 - x)(1 - y)a_{AC} + (1 - x)ya_{AD} + x(1 - y)a_{BC} + xya_{BD}$$
(2)

The band gap of alloys can also be determined from interpolation however it is complicated as the dependence on the two the binary alloys is no longer a linear dependence. Equation (3) shows the interpolation for ternary alloys  $A_xB_{1-x}C$  with  $E_{AC}$  and  $E_{BC}$  are the band gaps of the binary components, note b the bowing parameter. The accounts for the curves observed in Figure 6, however of note there are some with abrupt changes in the curve owing to the transition from a direct to indirect semiconductors. The lines are in this case constructed by calculating the direct and indirect band gaps and taking the smallest value. The Interpolation can be expanded to a quaternary alloy of  $A_xB_{1-x}C_yD_{1-y}$  in which case the equation (4) is used in the calculation of the band gap. This interpolation is however incapable of accounting for large differences in the electronegativity of the component elements. This gives rise to bowing parameters b, which are themselves a function of composition.

$$E_{ABC} = E_{AC} + (1 - x)E_{BC} + x(1 - x)b$$
(3)

$$E_{ABCD} = (1-x)(1-y)E_{AC} + (1-x)yE_{AD} + x(1-y)E_{BC} + xyE_{BD} + bxy(1-x)(1-y)$$
 (4)

The advent of Molecular Beam Epitaxy (MBE) technology and other epitaxial growth techniques have provided the ability to produce structures at the atomic scale. The simplest is a step change in the composition where you produce two stacked semiconductor materials. This forms a heterojunction which is the interface between two semiconductor materials. Devices with these junctions are referred to as heterostructures and this is one of the key strengths of epitaxial technologies such as MBE. The ability to produce these heterostructures enables us to create quantum structures within our materials and devices. This gives another dimension of control over material properties the confinement of carriers through a reduction in dimensionality. Altering the properties of the material compared to the bulk. The confinement energy becomes significant as the dimensionality approaches the same order as the exciton Bohr radius. This is the distance between an electron-hole pair, which results in significant quantum confinement when dimensions are below ~10 nm [16].

The principle of confinement can be further pushed by confining the electrons in additional dimensions. Quantum structures can therefore be divided into groups based on the available degrees of freedom  $D_f$ or alternatively directions of confinement  $D_c$ . Where equation (5) is satisfied and where  $D_f$  equates to 3 the situation refers to bulk materials with no confinement. Quantum wells (QW) provide 2 degrees of freedom with the thickness of a layer decreased to below the confinement freehold. Multiple quantum wells can be stacked, and this can form a structure known as a super-lattice where a continuous crystal structure is made from alternating layers of two semiconductor materials. It is not a requirement of a super lattice that the alternating layer form quantum wells. A further degree of confinement can be added by changing the structure to quantum wire which retains a single degree of freedom along the direction of the wire but confines across the cross section. Three degrees of confinement can be achieved by using a quantum dot (QD) structure in which all dimensions are below the confinement minimum of 10nm. The integration of these structures into device architectures can significantly impact the device properties and performance with InAs QDs being proposed as another potential route to producing 1 eV photovoltaic devices [17]. Thin layers of InAs grown on GaAs can owing to the drastically different lattice constants self-assemble into quantum dots to reduce the strain energy of the layer [16]. Quantum well structures have also found significant uses in increasing the optical performance of devices. The implementation has resulted in increased absorption coefficients and reduced dark currents achievable under refined device architectures [18]-[20].

$$D_f + D_c = 3 \tag{5}$$

## 2.2 Epitaxial Growth of III-V Semiconductors

### 2.2.1 InAs QD Growth

There has been prevalent interest in quantum dots (QD) since their initial proposal in 1982 by Yasuhiko Arakawa and Hiroyuki Sakaki [21]. The spontaneous formation of these dislocation free 3D islands

from a lattice mismatched epitaxial deposition, offered an easy growth mechanism to access the benefits of low dimensional quantum engineering. The 3-dimensional quantum confinement achieved in these structures has attracted large research attention across several material systems. Quantum dot self-assembly has been observed in several substrate/deposition systems these include Si/Ge , InP/InAs, GaAs/CdTe and GaAs/InAs to name but a few [22]. The key objective is to be able to customise and control the QD morphology, density, composition, and location. Enabling tunability of these systems for optical and electronics applications, from laser to single photon sources. The following section will focus on the InAs/GaAs system which is of particular interest due to its low band gap emission which makes it ideal for tuning to a range of optical applications in the near and mid-infrared. The investigation later reported within this document is also focused on InAs QDs grown on 001 GaAs and hence the review will concentrate on this self-assembled QD system.

Growth of QDs can be achieved by multiple self-assembly mechanisms, the first observed was the Stranski Krastanov (SK) growth mode [23], [24]. This is strain dependent growth mechanism and relies on the lattice mismatch between the substrate and epitaxial layer to achieve 3D growth. Briefly outlining the process for the chosen system; deposition of InAs initially forms a wetting layer up to a critical thickness of 1.5 monolayers (ML) of InAs atop the GaAs layer. Subsequent deposition past this thickness initialises the formation of 3D islands across the surface of the strained wetting layer. These islands then grow in size with material sourced from both the incoming atomic fluxes and the underlying wetting layer. A diagram of this growth mode is shown in Figure 7. The morphology, composition, dot density and positions are all dependent on the growth parameters or substrate preparations. This is further expanded on in the methodology chapter section 3.2.1.3.



Figure 7 SK growth with 3D islands formed atop a wetting layer both composed from the deposited material.

Droplet epitaxy of QDs was first proposed in 1991 by Koguchi et al and is an alternative strain independent growth mechanism for compound QDs [25]. In the case of InAs on GaAs it relies upon the spontaneous formation of indium metallic droplets under an isolated indium group III flux. Post the formation of metallic droplets on the surface a group V flux is introduced to subsequently crystalised the droplets. Metallic droplet formation under group V deficient growth conditions is very commonly observed in III-Vs. It is the result of surface energy minimisation of the metallic layer when excess material is unable to incorporate or desorb from the surface. The morphology, composition, dot density and locations are again all functions of the growth parameters and substrate preparations. There are key

differences in the critical parameters between these two techniques. However, for the investigation conducted within the thesis SK growth was selected to enable the application of the Bi surfactant.

Growth conditions used for InAs QDs on GaAs substrates by SK growth have some variance reported within the literature. This is to be expected with different morphologies and densities optimal for different applications. It should also be considered that there is variance in reported conditions between research groups and epitaxial systems. The typical epitaxial growth conditions fall within the following windows. Substrates temperatures of between 480-530 °C with either a c4x4 or 2x4 surface reconstruction present depending on exact temperature and As flux [26]–[28]. Both species of Arsenic flux As<sub>2</sub> and As<sub>4</sub> have been reported with group III:V flux ratios of between 20-100. However, As<sub>2</sub> is more standard with As<sub>4</sub> use generally reserved for growth investigations where a wider As flux window is desirable [29], [30]. Indium deposition rates range between 0.005-1 MLs<sup>-1</sup> with SK QD formation observed past the wetting layer critical thickness of 1.5 ML of InAs [31] . Post QD deposition in situ heat treatments or pauses in growth can be applied to the QD layer before the capping process as an additional mechanism for controlling QD morphology. It is worth noting here that these conditions are not always reported within studies and can extensively impact the QD morphology. QD capping is typically conducted at the growth temperature of the QDs between 480-530 °C [26]. This is assuming a GaAs cap is applied with a total thickness of 20-100 nm typical in reported growth structures. To mitigate intermixing often the first 5-20 nm of the capping layer is grown 10-20 °C below the QD growth temperature. This QD deposition and capping may be repeated multiple times to produce multilayered QD structures. However, inter-layer strain can begin to affect QD formation dynamics. It is also very commonly observed that a layer of uncapped QDs is deposited on the surface to enable AFM analysis. The morphologies observed by (atomic force microscopy), AFM analysis, of these surface QDs does not account for the changes in the morphology due to the capping process. Cross sectional TEM is required to analyse the morphology of buried QDs.

There are additional steps that may also be conducted during QD growth to provide further mechanisms for control over the QD formation. However, these are not required to achieve SK growth. These can include metamorphic buffer layers to change the underlying strain at the interface between the substrate and the wetting layer. Altering the critical thickness, diffusion rates and strain field experienced during QD formation [32]. Alteration of the capping layer conditions, varying one or all of; composition, thickness, temperature, growth rate and flux ratios[33]. In situ heat treatments can also be applied to alter the thermodynamics of post QD deposition, altering the conditions for coalescence or desorption of a species still present on the surface. Surface surfactants can also be deposited during QD formation to alter mobilities and strain at the interface [34]–[36]. This is further discussed in later sections. The degrees of freedom available in engineering QDs are extensive, which is what makes them so attractive for semiconductor engineering. However, the drawback is it has been widely reported that the QD growth dynamics are incredibly sensitive to the MBE growth conditions [26]. This manifests that even

studies with apparently minor dissimilarities in growth conditions can demonstrate dramatically different trends through variation of the same control parameter. It has been put that assessing growth studies within this field is akin to looking down a kaleidoscope, with every minorly varied angle giving a different overall picture. I would argue it is therefore advocated to report the initial growth optimisation in the variance of InAs deposition thickness and temperature to allow for some orientation when addressing the wider literature.

The wetting layer is formed on the surface of the GaAs to minimise the free surface energy during InAs deposition for QD growth. The atoms at the surface have already undergone a degree of atomic relaxation and deviate in position from the underlying lattice. This is observed as the surface reconstructions commonly C 4×4 and C 2×4 under typical QD starting growth conditions. Initial incident indium and arsenic atoms provided by the atomic flux adhere and react with the growth surface as in traditional heteroepitaxy. The incorporation of In under these reconstructions is initially favourable. However, due to the 7% lattice mismatch between InAs and GaAs the formation of the InAs crystal atop GaAs will cause large compressive strain within the InAs layer. This results in atoms in the lateral direction being squeezed close together, while the poisson's ratio dictates that in the direction normal to the surface bonds are tensely strained. This results in extensively weakened bonds owing to the highly directional and inflexible bonding of a III-V in the zinc blend structure. This situation is exacerbated with increased InAs layer thickness. Ultimately leading to the point where incident In and As can no longer strongly adhere to the surface and incorporate due to the distortion and extension of the zinc blend structure. This situation is the strain induced critical thickness limit at 1.5 ML of InAs on GaAs 001. This thickness would constitute a wetting layer with a thickness of approximately 4.5 Å due to the poisson's ratio effect on the lattice constant. Once this point is reached it is regarded that the wetting layer in completely formed. It would be expected that this state would be a quasi-stable state, and the wetting layer cannot be considered chemically inert under all conditions experienced in the subsequent QD formation.

Further adatoms supplied to the surface are only able to weakly bond or physisorb onto the surface. This precipitates the conditions for self-assembly with mobile species of both arsenic and indium present at the surface. It has been noted in previous studies that As<sub>2</sub> and As<sub>4</sub> molecules from an incident flux physisorb onto the surface as As\* precursors [37]–[39]. Indium and gallium incident flux behave in a similar fashion weakly adhering to the surface. Both elements remain separate from one another until incorporation into the lattice [40]–[43]. However, there is the possibility of these reacting together if mobile and weakly bound as the case would be atop the wetting layer.

It has been observed in different epitaxial systems that floating species on the surface will aggregate into crystalline nanoclusters atop an inert substrate [38]. The exact dimension and morphology are again strongly dependent on the experiment conditions observed. This would create the conditions for the

starting point of progressive epitaxial growth observed in QD formation [44]. Where QD height and density are functions of the effective surface InAs coverage with increasing coverage producing higher populations and size up to a critical coverage or deposition thickness. The initial nucleation and steady growth of QDs has been widely reported. It must be considered however that the wetting layer thickness constitutes a significant amount of the total InAs deposition thickness, with typical growth deposition of between 1.6-2.7 ML. It has been noted that remnants of the wetting layer continue to be present in QD samples as observed in cross sections TEM and luminescence measurements [27], [45]. The total thickness of the wetting layer is nominally reduced as the wetting layer also constitutes a material source for QD formation through segregation and diffusion mechanisms into the growing QDs. This is expected when considering the metastable nature of the formed wetting layer. Reducing its thickness will increase the stability and more favourable crystallographic environments are available once the formation of the QDs has been precipitated. It is also possible for Ga and In intermixing to occur in both the wetting layer and QDs formed. There have been many observations of Ga intermixing into InAs QDs. Further supporting that there is significant diffusion both through the wetting layer and the capping layer. Indicating that the constituent material is ultimately largely incorporated in the final QD composition [46], [47].

Surfactants in epitaxial growth are chemical species or elements present on the growth surface that aid in the diffusion or mobility of species present on the surface. The surfactant species may either be incorporated into the final composition or thermally desorb from the surface, depending on the species selected and designated experimental conditions. There are reported cases within the literature for the use of Bi & Sb as surfactants in both GaAsBi/Sb bulk and GaAs/InAs QD systems respectively [34]–[36]. In QD growth it has been observed that a Bi surfactant can alter QD dot densities, increase heights, reduce size distributions, impact aspect ratios and increase overall optical quality [29], [35], [48]. However, there is not a ubiquitous consensus on the observed or expected effects when a surfactant is applied to QD growth. Again, it falls into the kaleidoscope perspective of QD growth studies where minor differences in experimental conditions can significantly alter the effects observed.

Studies have reported that with the previously stated benefits come concessions and limitations not reported in other instances. These include reports of increased density at the expense of reduced heights and aspect ratio due to a suppression of surface In mobility[36]. Alternatively increased heights and homogeneity at the expense of reduced indium surface migration and desorption of In adatoms [36]. The application of Bi surfactant in QD growth and potential explanation for the lack of consensus in the literature is that it has been reported as extremely temperature sensitive. At the extreme low end of growth temperatures, at 380 °C it has been shown Bi can aid in surface nucleation of QD where SK growth is not observed in the absence of Bi [29]. Studies of the growth temperature dependence of InAs/GaAs QDs grown without a surfactant within the literature bottom out at lower limits between 440 °C - 480 °C [49], [50]. Blow this temperature threshold InAs/GaAs QDs are only reported in

surfactant assisted growth [29], [51]. Further increasing the supplied Bi flux at growth temperatures of 380 °C and 510 °C both showed increasing heights across the populations. On the other hand, studies ranging from 475-500 °C have reported different regimes of Bi surfactant behaviour with decreasing density up to 492 °C before a reversal in trend and rising QD density up to 500 °C [36]. This was attributed to a transition from a nucleation limited growth regime to a coalescence limited regime. A potential cause for this ever changing behaviour with temperature is that to my knowledge no study has considered the increased desorption rate of Bi at increased surface temperatures. It is therefore logical to assume that not only are we going to observe the effect of increasing indium mobility and desorption rate due to higher temperature but a competing effect of reduced surfactant layer thickness as the equilibrium shifts due to a constant source with increasing Bi desorption rate. The interplay here makes the determination and attribution of the observed behaviours difficult which could explain the lack of consensus within the literature.

It must also be considered the techniques for surfactant deployment and how their interaction with the growth surface can impact the outcome. With some studies opting for pre-deposition of a given thickness and then standard growth. While others opt for a co-deposition of surfactant species alongside In and As [29], [52]. The two options will alter the wetting layer formation by different mechanisms. Initial surfactant deposition while shown to improve surface morphology prior to QD growth will also alter the surface reconstruction. It may also, depending on experimental conditions, provide a substantial source for the incorporation of the surfactant species into the wetting layer. This will alter the critical thickness, strain environment and diffusion mechanism at play during QD formation. This has been proposed in the literature in which a Bi surfactant resulted in a thicker wetting layer subsequently creating a route for thermal carrier escape and reducing PL intensity [53], [54]. Deposition with the In and As will not alter the initial reconstruction until a monolayer of material has formed. However, the surfactant effect may not initially be felt until a critical thickness of Bi has built up. Again, it then may also alter the composition and formation of the wetting layer depending on the experimental conditions, at which point the onset of the surfactant effect will also be altered. This neatly summarises the complexities of QD growth even when considering how a single control parameter. The interplay with other conditions is unavoidable and can drastically alter the observed behaviour.

### 2.2.2 GaAs<sub>1-x</sub>Bi<sub>x</sub> Growth

The growth of GaAsBi was first achieved using a MOVPE on a GaAs substrate, Rutherford backscattering spectroscopy (RBS) confirmed the Bi atoms substituted onto the As lattice sites within the zincblende crystal structures. The band gap temperature coefficient was found to reduce with increasing Bi content with a reduction of  $1/3^{rd}$  the initial value of GaAs reported at -0.15 meVK<sup>-1</sup> with 2.6% Bi. The temperature insensitivity of GaAsBi was further demonstrated with photoluminescence studies in which the peak shift was reduced compared with GaAs. Growth of GaAsBi by MBE has since

been extensively demonstrated with studies in good agreement in regard to the material properties. However, for this study the increased kinetic control enabled by MBE is preferred for engineering of the quaternary alloy  $Al_xGa_{1-x}As_yBi_{1-y}$ .

MBE growth of GaAsBi on GaAs substrates has been reported on in several studies using solid source effusion cells for Ga, As and Bi. Growth has been successfully conducted on both static and rotated substrates and with both As<sub>2</sub> dimers and As<sub>4</sub> tetramers. Prior to the growth of a GaAsBi layer a homoepitaxial GaAs buffer layer is grown at the ideal substrate temperature of 560-580 °C under an excess of As<sub>2</sub> flux, The surface reconstruction of C 2×4 is observed using RHEED post the homoepitaxial GaAs buffer layer growth. Substrate temperature must be reduced for GaAsBi growth with a temperature of less than 400 °C required for effective incorporation. The reconstruction during GaAsBi growth changes to a C 2×1 indicating the existence of Bi-Bi and Bi-As dimmer on the growth surface. Oscillations in the RHEED intensity are also observed during growth confirming a layer-by-layer growth process.

The parameter space in which GaAsBi can be grown is significantly more confined than those of GaAs. Above a substrate temperature of 400 °C the incorporation of Bi atoms will rapidly decrease, as Bi atoms instead desorb from the surface. The evaporation temperature at which Bi rapidly desorbs from GaAs is reported at 450 °C. Under a constant substrate temperature within the optimum window of ~380 °C the Bi incorporation is dependent on Ga ,As and Bi fluxes. Increasing Bi flux linearly increases Bi content under constant supplies of Ga and As up to a saturation limit determined by substrate temperature and incident As flux. Growing under an excess As flux similar to GaAs will reduce the incorporation of Bi as the As out-competes the Bi for atomic sites. Deficiencies in the As flux have been shown to result in reduced material quality owing to droplet formation on the surface. This limits the operating window for the As<sub>2</sub>:Ga flux ratio, with the ideal a stoichiometric ratio. The practicality of  $GaAs_{1-x}Bi_x$  growth necessitates a slight As overpressure be applied to avoid the detriment to the material properties. Altering the As species from As<sub>2</sub> to As<sub>4</sub> can offer an increased range of As<sub>4</sub>:Ga flux ratios allowing for finer control and a reduced As overpressure as As<sub>4</sub> incorporates at half the rate of As<sub>2</sub>. The dependence on As species used in GaAsBi growth has been found to produce no notable differences in the optical quality of the material produced [55].

Within this window, the behaviour of Bi on the surface can vary from directly incorporating under low Bi fluxes or at very low substrate temperatures. Alternatively, prior to the onset of droplet formation, the Bi can form a wetting layer subject to the growth conditions. The less directional bonding of metals compared with covalent III-V semiconductors can with the presence of a metallic surface layer aid in the diffusion of species across the surface. This Bi wetting layer then serves as another source of Bi for incorporation and also as a surfactant which aids diffusion. This can offset the cost in material quality

that a reduced growth temperature can result in. Control over the flux must be maintained to ensure the wetting layer remains below the critical thickness for droplet formation.

The formation of metallic surface droplets can plague the MBE growth of GaAsBi, with their formation degrading device performance and introducing compositional inhomogeneities [56], [57]. Droplet formation and composition while influenced by growth rate and substrate temperature is most strongly dependent on the flux ratios. B. A. Carter demonstrated 4 potential zones that arise in GaAsBi growth with respect to droplet formation depending on the relative ratios of incident fluxes The four zones identified are; no droplets, Bi droplets, Ga droplets and biphasic GaBi droplets [58]. Experimental and theoretical studies have both been conducted in mapping the location of these 4 zones within the parameter space[58]-[60]. These zones as mapped by B. A. Carter are shown in Figure 8 The droplet free regime covers the optimised growth parameters where high quality GaAsBi can be successfully grown [58]-[61]. J. Puustinen et al demonstrated droplet formation occurs at As<sub>2</sub>:Ga flux ratios above and below unity with a droplet free window between 1 to 1.2 [59]. This is in agreement with A. J. Ptak et al who observed droplets appearing on the surface as the As<sub>2</sub>:Bi flux was increased. Both observations can be explained by a stronger affinity of As for Ga compared with Bi [60]. This results in Bi being outcompeted for available Ga sites and accumulating on the surface in high As:Ga flux regimes. It follows thusly that in the high As:Ga ratio the droplets formed are Bi. Vadar et al reported on droplet formation of both mixed GaBi droplets and Ga droplets [62]. With phase separated GaBi droplet observed within the Ga rich regime and pure Ga droplets observed at stoichiometric fluxes, which attributed to an anti-surfactant behaviour of unincorporated Bi. The anti-surfactant effect has not been

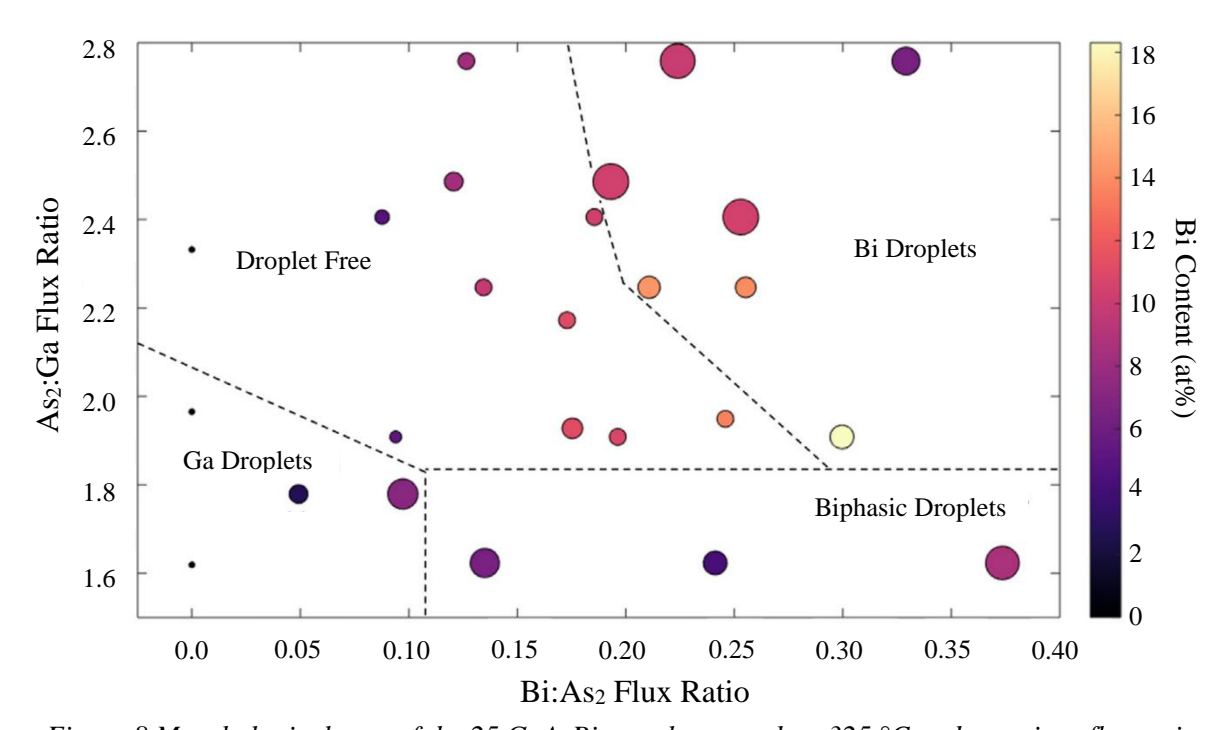


Figure 8 Morphological map of the 25 GaAsBi samples growth at 325 °C under various flux ratio profiles with the 4 droplet regimes shown. The colour of the data point represents the Bi composition, and the size of the data points represents breadth of the peak. Taken from B. A. Carter [58].

corroborated in other literature. However, quantities of Bi on the surface can be insufficient to form a metallic layer and will not act as a surfactant. Monte Carlo simulations of the GaAsBi system conducted by G. V. Rodriguez modelled the surface under various flux ratios to determine the droplet behaviour [63]. With an increasing Bi flux, the Ga droplet regime is moved further down until a critical limit where all droplets are a mixture of GaAsBi. Meanwhile above the stoichiometric flux within 10% we can observe two regimes a Bi droplet regime directly above the mixed droplet regime showing the saturation limit of Bi incorporation irrespective of As:Ga flux ratio. This Bi droplet regime also reduces in thickness when approaching stoichiometric fluxes presenting the narrow processing window for GaAsBi growth. The second is a low Bi flux regime above the stoichiometric flux, while Bi free in this study from other studies we can infer a low Bi incorporation due to the As outcompeting the Bi for available Ga sites [59], [64]. Increasing the growth rate has been shown to delay the onset of surface droplet formation, in line with the expectation that increasing the Ga and As flux to will produce a relatively lower Bi flux [65].

The XRD pattern of GaAsBi shows two peaks of interest the 004 GaAs peak at 66.5° on the 2-theta scan and 33.03° on the omega 2 theta scan. Types of XRD measurements are discussed in more detail in the XRD experimental section 3.3. The secondary GaAsBi peak is seen at lower angles with the angle dependent on the Bi content. Figure 9 shows an example omega 2 theta XRD scan of a GaAs<sub>x</sub>Bi<sub>1-x</sub> sample with ~3.6 at% Bi. Clear pendellösung interference fringes can be observed between the peaks indicating a smooth interface between the GaAs and layers. Composition determination of GaAs<sub>x</sub>Bi<sub>1-x</sub> from the lattice constant by Vegard's law requires both lattice constants of the constituent binaries to be known. GaBi is a theoretical alloy with an undermined lattice constant. The lattice constant has therefore been determined based on the RBS analysis of GaAs<sub>1-x</sub>Bi<sub>x</sub> samples with Bi content

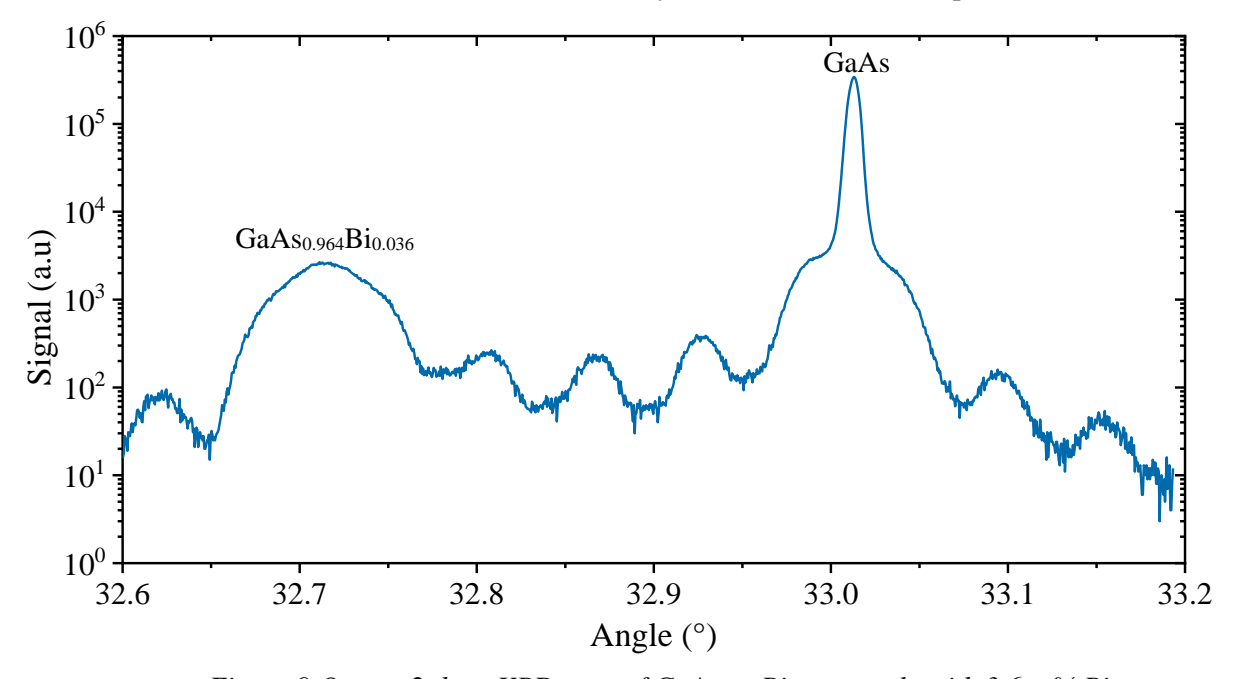


Figure 9 Omega 2 theta XRD scan of GaAs<sub>0.964</sub>Bi<sub>0.036</sub> sample with 3.6 at% Bi.

quantitively evaluated. This overlaid with the lattice constant determined from XRD allows the extrapolation of this data, with a determined lattice constant of 6.23 Å. In line with estimations of the GaBi lattice from simulations[66]. This can then be related back to the shift in XRD angular spacing to allow for compositional determination directly from XRD.

Device quality GaAsBi produced under optimised conditions will show a mirror surface finish free of droplets. Transmission electron microscopy (TEM) observations of samples of this quality reveal the remaining presence of structural defects including dislocation, dislocation loops and Bi precipitates. The presence of these below a certain threshold is tolerable and defects can never be totally eliminated within a material as it is not thermodynamically favourable. The quantities present however can be minimised through the optimisation of growth conditions. Photoluminescence analysis on GaAsBi samples has shown a broad PL peak at the band gap of GaAsBi. This is the result of high quantities of localised states present in GaAsBi containing samples. The PL peak energy is observed to decrease with increasing Bi content. The initial impact on peak shift is observed at between -78 to -62 me V/% Bi, between 0 to 4 at% Bi incorporated. The impact of each subsequent % Bi incorporated reduces down to 50 meV per % Bi at 20 at% [67]. Further increases in PL intensity can be achieved through the integration of MQW structures. GaAsBi contents with high quality PL have been achieved up to ~11 %. The temperature dependence of the PL spectra was also decreased with the presence of Bi. At a content of 2.5 at% Bi a temperature coefficient of -0.15 meV/K was reported with 0.23 meV/K reported for a content of 1.3 at% Bi. The direct relation between Bi content and the temperature coefficient through the Varshini equation is not conclusive with a range of coefficients reported. The consensus is the temperature coefficient has a strong dependence on the crystal quality of the samples.

#### 2.2.3 AlAs<sub>1-x</sub>Bi<sub>x</sub> & Al<sub>x</sub>Ga<sub>1-x</sub>As<sub>y</sub>Bi<sub>1-y</sub> Growth

Epitaxial growth of the Al ternary counterpart to GaAs<sub>x-1</sub>Bi<sub>x</sub>, AlAs<sub>1-x</sub>Bi<sub>x</sub> has been reported once within the wider literature. The study was published in 2019 and utilised growth conditions similar to GaAs<sub>x-1</sub>Bi<sub>x</sub>, with near unity III:V fluxes and growth temperatures between 270 °C to 310 °C [68]. Successful synestias of AlAs<sub>1-x</sub>Bi<sub>x</sub> with layer thicknesses of 400 nm and Bi content between 3-10.5 at% were reported. However, this was across a single statically grown 2 inch GaAs wafer with a range of flux conditions and temperature profiles across the sample depending on the position relative to the sources. Higher contents were reported in the region of higher Bi flux and As deficient flux, with content decreasing across regions as the Al:As flux shifted above unity to the value of 1:1.1. This was also aided by the relative Bi flux decrease. Metallic droplets were reported on the surface of the wafer in regions where the growth was either Al or Bi flux rich. This aligned with the previously described 4 droplet regimes of GaAsBi [58]. It would be likely therefore that the challenges observed in GaAsBi growth are also present in AlGaAs. Narrow group V flux ratio windows and limited growth temperature regimes are likely to be expected. However, from the available literature this can only be speculated on.

The higher strength of the Al bond due to its closer proximity to the atomic nuclei as compared with Ga could also infer that the process windows could be even narrower to achieve optical and device quality material [69]. The extracted lattice constant for AlBi was 6.23 Å slightly lower than values predicted from modelling which range from 6.266 to 6.460 Å [33], [66]. The observations of the study provided no indication that the growth significantly differed from GaAs<sub>x-1</sub>Bi<sub>x</sub>. Of note however is no optical measurements were reported of the material grown indicating the optical quality was likely very poor. No attempt at optimisation were reported beyond the flux variations of conditions observed across the wafer. From this, it remains that the unity III:V flux ratio are the optimised condition for Bi incorporation without metallic droplet formation. There have been to date publications reporting on the epitaxial growth of Al<sub>x</sub>Ga<sub>1-x</sub>As<sub>y</sub>Bi<sub>1-y</sub> experimental or simulated.

# 3. Experimental Techniques

# 3.1 Molecular Beam Epitaxy

Molecular beam epitaxy (MBE) is an ultra-high vacuum (UHV) deposition technique first developed in the 1970s [70]. It offers atomic level precision in the compositional control of materials. While this predominantly has been applied to research and industrial applications within semiconductors. The technology has been applied to a wide range of material systems limited only by the availability of elemental sources. The single crystal growth that can be achieved with discrete compositional differences has led to unprecedented advances in semiconductor technology [71]. This extended to opening up the world of quantum engineering within device structures and advanced materials research for next generation semiconductors. The technique that has been employed in the growth and discovery of semiconductor materials for the last 5 decades with an unparalleled level of control in the growth of materials. This results in the ability to produce; (1) single crystal materials with reduced concentration of thermodynamic defects, (2) atomic structures with abrupt or continuous changes in doping or composition profiles in the growth direction. This in turn opens up the ability to fabricate innovative devices, heterostructure and quantum structures inaccessible though other techniques. (3) Materials where immiscibility of the constituent atoms renders them synthesisable through non-epitaxial techniques such as GaAsBi. MBE remains a vital technology both within research but also increasingly scaling up for industrial applications. This section covers the experimental methods used in the epitaxial growth of samples by MBE as discussed within this thesis. Focusing on the growth of III-V semiconductors and extending to the idiosyncrasies of the Omicron MBE system used for this research.

The operating principles of MBE are deceptively simple for an epitaxial process conducted within a stainless-steel reactor under ultra-high vacuum conditions. New materials are grown on heated crystalline substrates which have been loaded into the reaction vessel, in the case of this study 001 GaAs was used. Elemental sources are then targeted at the substrate with their flux output varied through temperature control and the use of a shutter or needle valve. By controlling the ratio of element fluxes arriving at the substrate surface the composition of the new material can be controlled. To give an example if there are 3 fluxes present Al, Ga and As. Two of these are group III one is group V, for III-V growth the group V element is oversupplied and by altering the ratio of the group III fluxes the Al<sub>x</sub>Ga<sub>1-x</sub>As composition can be controlled. If they were equal the composition would be Al<sub>0.5</sub>Ga<sub>0.5</sub>As. The growth occurs layer by layer akin to atomic spray painting with atoms migrating across the surface until they interact in proximity of a suitable vacant lattice site in the case of III-Vs. The migration of elements across the surface is controlled by the substrate temperature and the substrate selection. The atoms bond to the substrate and adopt the same crystal structure as the substrate. This is then repeated layer by layer giving rise to epitaxial growth of a single crystal. The simplest growth is homogeneous growth when the same material as the substrate is grown atop, ie GaAs on GaAs. However, by altering

the ratio of fluxes the compositional profile of the sample can be abruptly changed and new materials can be grown atop the substrate. This on the assumption the lattice constant of the new material is compatible with the underlying substrate. One example would be changing the Ga;Al flux ratio from 1:0 for GaAs to 0.7:0.3 this allows you grow the ternary Al<sub>0.3</sub>Ga<sub>0.7</sub>As atop a GaAs substrate. From this you can construct device by adding doping sources and quantum structures such as quantum wells. This is where things get really interesting in epitaxial growth.

The previously described growth of GaAs and AlGaAs is a well behaving and understood III-V system for epitaxial growth with minimum additional considerations. The complexities of epitaxial growth expand considerably for different material systems as previously described in the literature review growth sections. However, all share the previously outlined fundamentals. To give a brief overview. These can include considerations such as immiscibility limits of various elements when incorporated into the single crystal. Leading to diffusion and segregation of consistent elements when exceeded. Altering the composition and structure of the sample from the intended design. The bonding between substrates and deposited elements must also be considered due to different lattice constants. Which gives rise to critical thickness of material before a change in how the growth proceed on the surface or layer relaxation. This is not always undesirable such as the transition from layer growth to island growth for instance in InAs which allows for QD deposition. The consideration of substrate temperature for element adhesion to the substrate. Different elements desorb at different rates from the substrate, this gives another consideration for targeting composition as the flux ratio form only part of the picture. The elements need to react on the substrate surface to incorporate and if their desorption rates are different then this must be accounted for in the supplied flux. This is exceptionally problematic in bismide containing materials where you are limited to substrate temperatures below 380 °C or else all Bi will desorb instead of incorporating. Considerations of lattice strains with a single crystal where eventually the structure may relax due to the in-built stresses. Then further how the stresses can lead to preferential growth sites at the growth surface. A particular issue in some QD growths where nucleation sites can be altered by underlying stresses in from previous layers This is by no means an exhaustive list, however it outlines how MBE is a deceptively simple technique that take years to learn.

## 3.1.1 Molecular Beam Epitaxy System Overview

The MBE system currently in use by the bismide research group at the University of Sheffield is an OMICRON MBE-STM system with Al, Bi, Ga and In effusion sources, along with a cracked As and dual dopant Si and Be effusion source. An annotated cross-sectional diagram of this system is shown in Figure 10. MBE systems are modular with standardised connections between components. The system is constructed from stainless steel with a main chamber onto which additional connecting sections of stainless steel are attached via CF flanges with copper gaskets. The flanges range in size depending on the component designed to attach in a designated position. These are 3 main structural

sections of this system. The fast entry load lock segment which is separated by a gate valve to the main chamber to allow this section to be isolated. This is due to function of this section which is utilised for loading and unloading of samples so is regularly exposed to atmosphere. It has an independent pumping system associated and a reduced volume to allow for rapid (within 30 minutes) pumping time from atmosphere to UHV conditions approximately  $2 \times 10^{-7}$  mbar. There is a nitrogen line in to repressurise the section when unloading and maintain positive pressure to keep the chamber clean. Connected to this is the main chamber to which the majority of components are attached directly, including all those associated with deposition and in situ monitoring. Finally, a T junction section for connection of the ion pump and turbo pump. The turbo pump connected to the main chamber is larger to account for the increased pumping volume and is also separate by a gate valve. The gate valves function to isolate the main chamber from pumping systems which connect to atmospheric pressure in case of component failure. These are required when pressuring for maintenance or in the event of a pump failure to protect the system from sudden pressurisation.

## 3.1.2 Pumping Systems

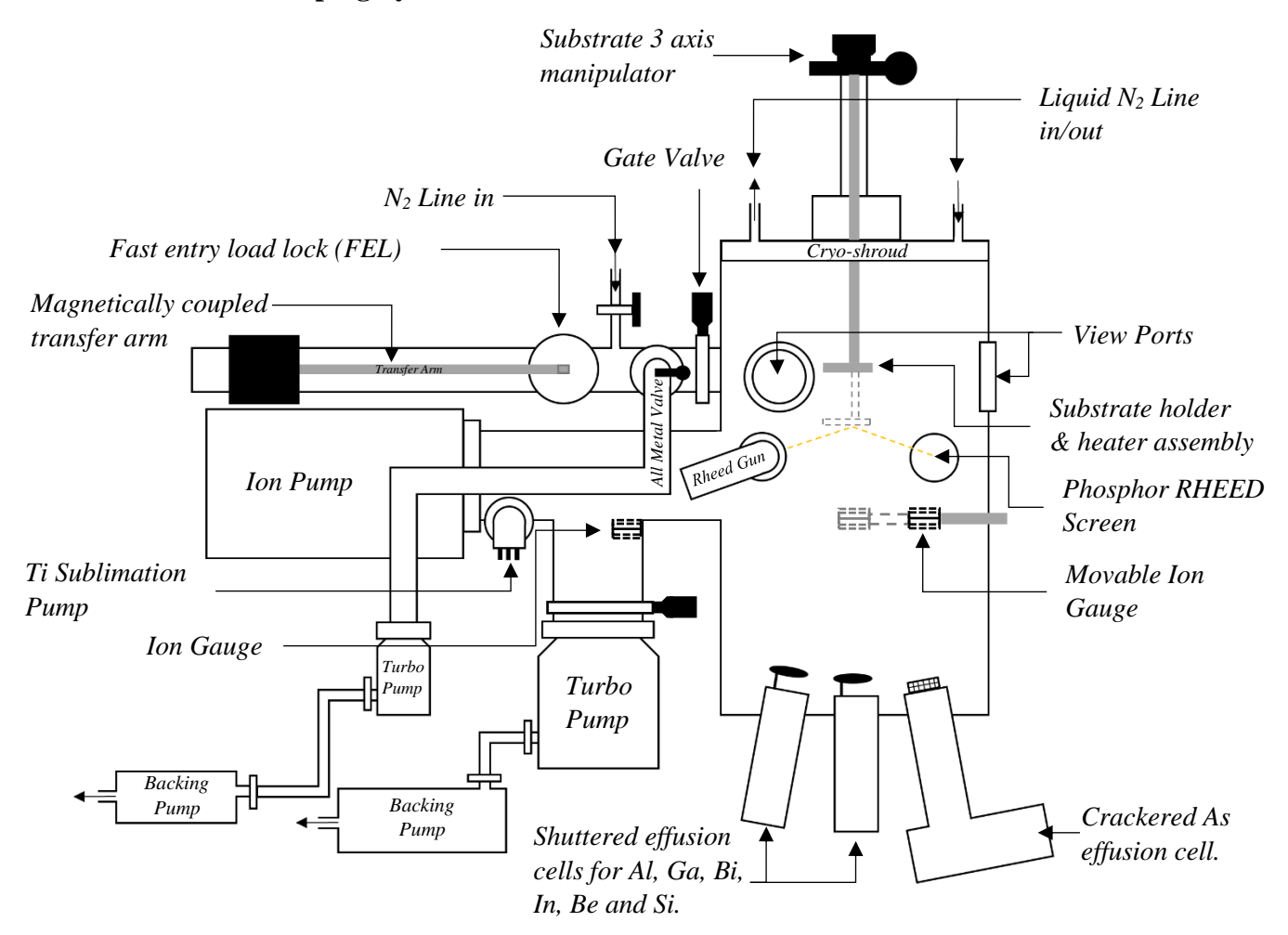


Figure 10: 2D Schematic of OMICRON MBE reactor, with substrate holder shown at load (solid) and growth height (dashed) with e-beam for RHEED (yellow dashed) shown. Additional cells are present although not shown for ease of understanding.

The constituent components attached to the MBE system can be broken down into groups related to their function. The most abundant of the components within the system are those utilised for pumping and maintaining the ultra-high vacuum (UHV). The pumping systems equipped to the MBE machine shown in Figure 10 include, 2 turbo molecular pumps with backing pumps, an ion pump, Ti sublimation pump and liquid  $N_2$  (LN<sub>2</sub>) cryoshroud. There are additional pumping technologies available however these are not present on this system, they include cryopump and oil diffusion pumps although the latter has mostly been surpassed with newer technologies. Ultra-high vacuum is achieved by the combination of all pumping technologies equipped. Pumping from atmosphere to low vacuum is achieved using scroll backing pumps capable of reaching ~1×10<sup>-2</sup> mBar. There are two of these pumps each one connected in series with one of the turbo pumps. One located on the FEL and the second on the main chamber. Once low vacuum is achieved the turbo pumps can be engaged and continue pumping the system from  $1 \times 10^{-2}$  to an ultimate pressure of  $\sim 1 \times 10^{-7}$  mBar. The turbo pumps function as a high-speed turbine operating at speeds between 30,000-90,000 rpm depending on size. This functions an accelerator for any molecules that come into contact with the blade forcing particles out through the backing pumps. At pressures below  $1 \times 10^{-6}$  mbar the Ion pump can also be activated with an effective pumping range of  $1\times10^6$  to  $1\times10^{-10}$  mbar. Operating at a high electric field 3-7 kV atoms are ionised and bound to cathode within the ion pump. Unlike the previously pumps this is a closed unit open only to the main chamber, functioning more like an elemental trap. The combination of these 3 pumping systems can reach UHV conditions however additional considerations need to be made when maintaining a UHV in a growing reactor.

The cryoshroud is a copper shroud sitting above the substrate heater assembly. Liquid nitrogen (LN<sub>2</sub>) is pumped through the shroud cooling it to between -80 to -120 °C. This functions similarly to the ion pump with particles binding to the cold surface and due to its placement, it also functions to effectively trap stray or reflected atomic fluxes from the source cells. Epitaxial growth is not conducted without an operational cryoshroud to prevent influence from indirect fluxes reflecting off the reaction chamber. The cryoshroud is typically engaged once pressures are lower than  $2\times10^{-7}$  mBar. Due to the location a significant quantity of material builds up on the cryoshroud during epitaxial growth. This material is released when the cryoshroud warms once the  $LN_2$  dewar is depleted. It is important to remove or protect a sample if it is in the chamber when this occurs. Samples can be protected by the application of an amorphous As cap which can be later removed. The final pumping system is the Ti sublimation pump system, used to remove reactive particles within the chamber. Ti is sublimated from a solid source coating a section of the internal stainless-steel wall with Ti. Elements particularly those such as  $O_2$  react with the Ti and are bound to the lining of the reaction vessel. In the case of this system, it is located in the T junction between the ion and Turbo pump so as not to contaminate samples with Ti.

#### 3.1.3 Effusion Cells

There are many technologies utilised in the production of an atomic flux for MBE growth. The technology selected is dictated by the material and flux requirements for the system. The most common source technologies employed are Knudsen effusion cells, electron beam cells, plasma sources and gas sources in some instances. Atomic fluxes for the growth within this study utilised Knudesen effusion cells. These operate by heating ultra-pure single elements contained within a pyrolytic boron nitride (PBN) crucible at temperatures up to 1400 °C. PBN is a III-V material used in this application for its temperature stability and chemically inert nature. The PNB crucible is suspended in the Knudsen effusion cell with a surrounding heating element and appropriately placed thermocouple. Temperature regulation is handled by a Proportional–integral–derivative (PID) controller to maintain the set temperature, by varying heater power against heat loss from the cell to the water-cooling loop. Depending on the location of the thermocouple the operating temperature can vary between different effusion cells even for the same source material. The temperature output required to maintain a set flux can also vary depending on material load remaining within the crucible, with higher temperatures required for a lower remaining charge.

The Al cell utilised was a single filament cold lip effusion cell with a heating coil surrounding the base of the crucible. The unheated upper section of the crucible is to counteract Al creeping up the crucible walls during growth. The Al is also the only cell with a double walled crucible, essentially a crucible within a crucible. This serves to protect the cell from the crucible cracking in the event the Al freezes and then remelts, due to Al expanding as it freezes. For the In and Ga sources a standard hot lip effusion cells were used where the filament starts part way up the crucible creating a temperature gradient down into the crucible. This prevents the In or Ga flux from condensing on the crucible walls during cell operation providing a more reliable and uniform flux output. The dopant sources Si and Be utilised single filament effusion cells however miniaturised on a dual source module which allowed for 2 sources to be fitted on the same flange of the MBE chamber. This was done to allow for a greater number of other sources to be fitted to the main chamber. The reduced volume of the crucibles is less of an issue for the doping source due to their reduced fluxes in operation. The final source is the Bi effusion cell which utilised a dual filament configuration. This allows for a controlled temperature gradient across the crucible with separately controllable heater filaments located in the lower and upper section of the crucible with corresponding thermocouples. These necessities 2 PID controllers for this cell however reduces spitting from the Bi source improving the flux uniformity in growth.

The As source is slightly different due to the sublimation nature of the As source material. It is supplied by a valved cracker cell. The fundamentals of this type of cell effusion cell still remain with the As contained within a PNB crucible surrounded by a single heater filament. However, the crucible is not open but sealed with a variable needle valve. Allowing for linear flux control through the adjustment

of the valve position without the need to alter the As bulk temperature. The thermal cracker functions to control the As species supplied to the sample through thermal cracking of the native  $As_4$  tetramers into  $As_2$  dimers. Structurally the cracker is a wire grid heated to between 650-1000 °C for  $As_4$  and  $As_2$  respectively. It is located at the output of the cell.

All cells with the exception of the As are shuttered by rotary shutters sitting between 5-7 cm above the lip of the crucible. These are integrated into the cell mechanisms on this reactor and used to block the flux as required. The temperature of each cell is adjusted for growth to control the atomic flux output, setting to a standby temperature for material conservation when not in use. The temperature is also adjusted to exceed the standard operating temperature by 30-50 °C to purify the materials by outgassing. Outgassing involves heating a cell above the growth temperature to preferentially evaporate the more volatile contaminants reducing their concentration in the subsequently grown samples, improving material quality. Source materials used within this study are as pure as possible to source, in excess of 5 nines. However, outgassing can improve this further, marked by a substantial improvement in the quality of material following outgassing of the cells. The standard temperature used for each cell is given in Table 1.

Cell	Operating (°C)	Standby (°C)	Outgassing (°C)
Al	1080-1150	800	1200
Ga	900-960	400	970
In	700-800	400	830
Bi	350-420	320	450
As Bulk	360-370	-	385
As Cracker	650-1000	-	1100

Table 1 Temperature ranges for different source effusion cells for Omicron MBE STM

## 3.1.4 In situ Monitoring Systems

The next category of components is those used for in situ monitoring of conditions within the MBE chamber. This includes vacuum gauges, flux monitoring gauges and analytical techniques to monitor the crystal growth. There are 3 main subcategories within the group.

#### **3.1.4.1 Ion Gauges**

Ion gauges comprise of a single collector filament surrounded by an electrically biased grid with a heated filament located 8 to 10 mm away, a schematic diagram is shown in Figure 11. The filament is heated with a low voltage high current supply at 50 V. This causes the emission of electrons from the filament which are then accelerated towards the grid biassed at 200 V. This is referred to as the emission current and is typically set to between 10 to 50 mA as regulated by the ion beam controller. If the

electrons encounter an atom, it is ionised and any ions are then attracted to the negatively biased collector held of 0 V. This current is typically between picoamps to microamps depending on pressure. The current in the collector is dependent on the number of ions produced, which with a fixed emission current is related to the number of ions and their ionisation energy. The ease of which different elements are ionised is referred to as the sensitivity s, this value is set by calibration within the ion gauge controller[72]. The formula for calculation of the pressure from the collector current Ic, emission current Ie and sensitivity s is given in (6). The operating range of an Ion gauge is limited to between  $3x10^{-11}$  to

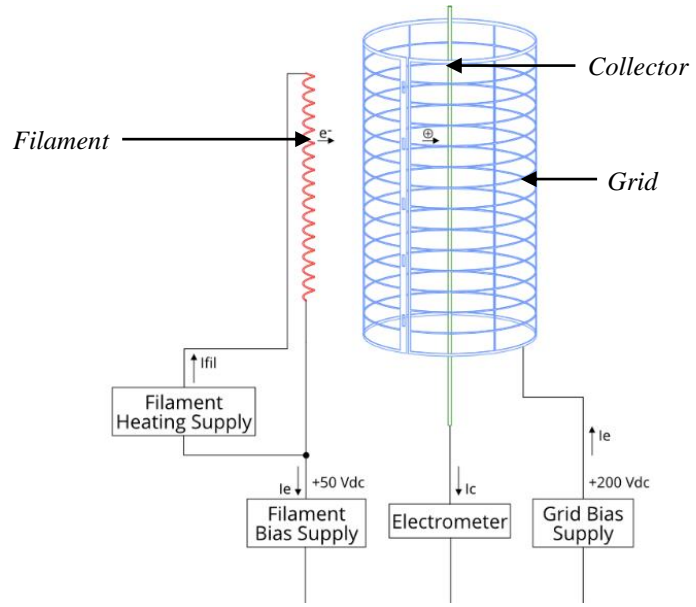


Figure 11 schematic of the structure of an ion gauge, adapted from [72].

$$1 \times 10^{-3} \text{ mBar.}$$
 (6) 
$$P = \frac{I_c}{s \times I_e}$$

There are two ion gauges present on the MBE STM system. The primary monitors the pressure at the junction between the Ion pump and turbo pump on the main chamber. The second is utilised as a retractable flux monitor, labelled as movable ion gauge (MIG) on Figure 10. This allows for the ion gauge which is mounted horizontally, to be moved into the path of the atomic fluxes produced by the effusion cells. The current can then be measured at different cell temperatures with the current dependent on the incident flux. Each effusion cell contains a different element with different ionisation sensitivity and incident angle to the gauge. Hence all the measurement of flux are only comparable for the same cell in the same position. The current though the gauge at each cell temperature is recorded into the MBE logbook and is typically in the range of 1 to 9 nA for Al, Ga, In and Bi while As is significantly higher at 20 to 80 nA in normal operation. This is a vital measurement for calibrating fluxes from the effusion cells as temperature changes can be equated to a proportional alteration of the atomic flux output. It is of note that latter within this study some fluxes are quoted in nA. Combined with additional calibration the relative fluxes of some species can be established between cells. This is

discussed later in section 3.2.2. When the second Ion gauge is retracted it functions as secondary measure of pressure within the MBE chamber. However, as it is located further from the pumping systems and so typically it reads  $4\times10^{-9}$  to  $6\times10^{-9}$  mBar higher at background pressure compared with the primary ion gauge. Background pressure is typically  $3\times10^{9}$  to  $6\times10^{9}$  mBar in the main chamber as measured by the primary ion gauge.

## 3.1.4.2 Wide Range Gauge

The wide range gauge, located on the FEL, is a combination of 2 gauges within a single unit. This includes a cold cathode gauge covering the pressure range of atmosphere to  $1\times10^{-3}$  mBar and a Pirani gauge covering  $1\times10^{-2}$  to  $1\times10^{-9}$  mBar. This allows for an operating range between atmosphere at 1000 to  $1\times10^{-9}$  mBar. The cold cathode gauge work by measuring anion current generated by ionising electrons, relating the current to pressure. While the Pirani gauge functions by comparing the current through two filaments. One is exposed to the conditions of the chamber and the other contained within a reference gas at fixed pressure and temperature. The relative current between the two can then be converted to a pressure [73].

This is used in the FEL to ensure the vacuum is sufficient before opening the gate valve between the FEL and main chamber post loading or unloading of a sample. The minimum acceptable pressure on this system within the FEL before opening to the main chamber for loading is  $5\times10^{-7}$  mbar. This is higher than the main chamber, however, in the absence of an ion pump installed on the FEL section and the pumping time of the FEL this is acceptable. The value is therefore a balance between pressure and pumping time which equates to loading and unloading time between growths. The absolute pressure reached in the FEL is  $6\times10^{-8}$  mBar hence the value previously stated strikes a good balance between limiting contaminant ingress into the main chamber and throughput of samples. Contamination is further reduced by a nitrogen gas supply line into the FEL which maintains a positive pressure when loading and unloading wafers.

#### 3.1.4.3 Reflection High Energy Electron Diffraction

Reflection high energy electron diffraction (RHEED) is an integral in situ monitoring technique used within MBE systems to observe the atomic arrangement of the surface atoms in real time. Sensitive to atomic positions of the upper few layers of atoms on the surface. RHEED is not only a monitoring technique used for substrate calibration but also a powerful analytical technique. Capable of showing how the surface atomic environment evolves with changes in temperature and supplied fluxes.

It operates by focusing a collimated electron beam that intersects the sample surface at a grazing incident angle of  $\sim$ 3° to produce a forward scattered diffraction pattern on a phosphorus screen. The electron beam is generated from filament with 1.42-1.49 A of current and an acceleration voltage of

15.5 KV. The beam passes through deflection coils, which collimate and allow for the beam to be deflected to focus on different areas of the sample surface. The refracted electron pattern is then visible on a phosphor screen located directly opposite the electron gun on the MBE system as shown in Figure 10. This screen is protected when not in use by a movable baffle to prevent build-up of material on the phosphor layer. A camera is attached to the RHEED screen to allow for viewing and analysis of the RHEED pattern through software. In the case of this system the software is used for growth rate calibrations. Due to the chamber view port positions RHEED along different crystallographic orientations is only possible by rotating the sample stage. However, due to a design oversight by Omicron, the heater stage on this system entirely blocks the electron beam in certain orientations when at growth height. This gives an ~50 ° window where the RHEED can be used for surface observations.

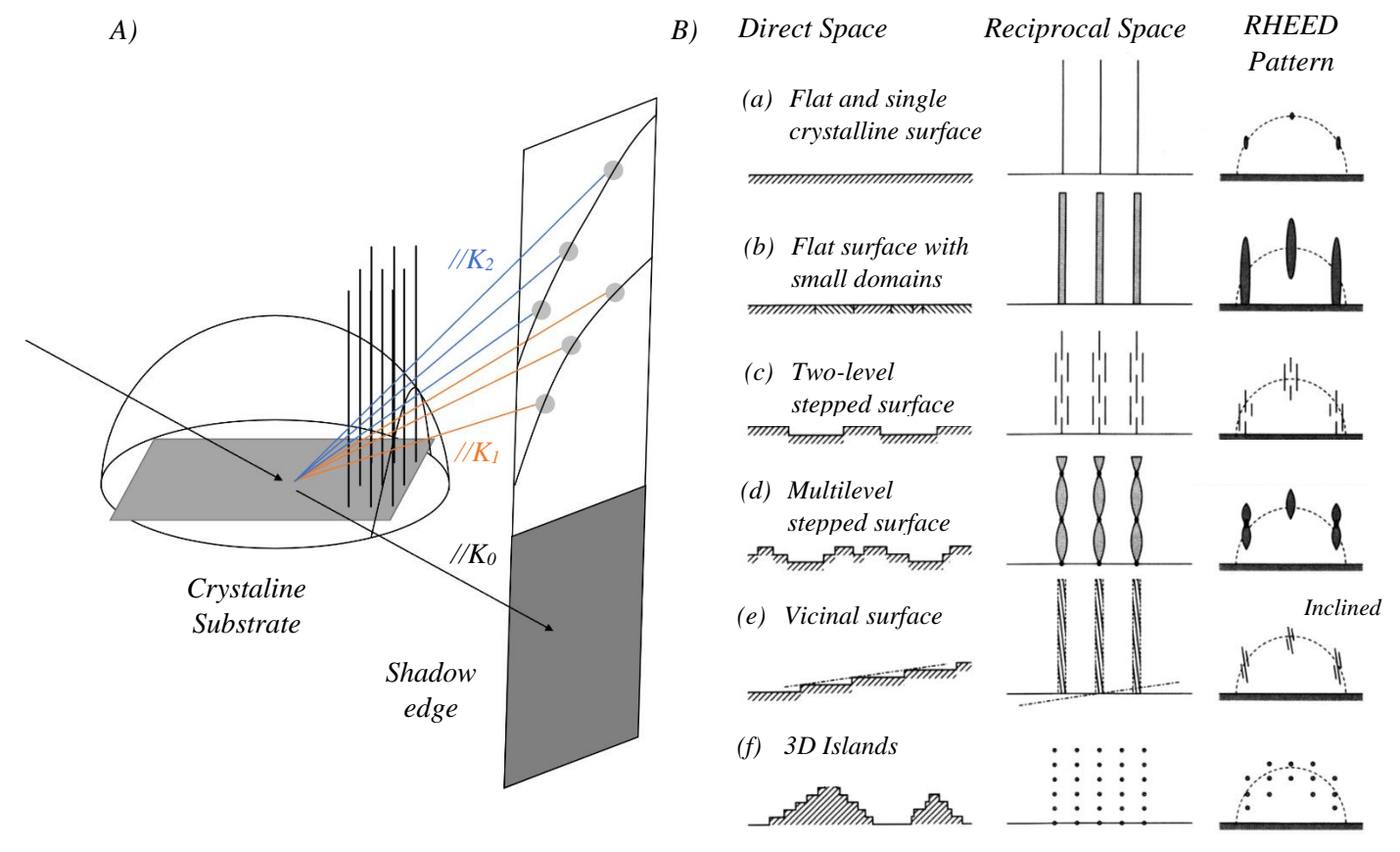


Figure 12 A) Diagram of construction of the ewald sphere and resultant diffraction pattern from a crystalline substrate showing the first 2 laue zones from diffraction of  $K_1$  and  $K_2$  vectors. B) Diagram of substrate surfaces and resultant impact on reciprocal space and observed RHEED pattern, adapted from [74].

Further due to non-rotating nature of the growth stage it is typical for RHEED observation on the system to be made from a single orientation along the  $[1\overline{1}0]$  for [001] GaAs substrates. Wafers are cleaved expressly so this orientation is aligned within the RHEED window of operation.

RHEED patterns have two primary features: the pattern of bright spots originating from elastic scattering and a series of bright and dark lines known as kikuchi bands originating from inelastic

scattering. The geometric arrangement of spots on the RHEED screen is determined by the reciprocal space (momentum space) of the substrate surface. This is why RHEED is sensitive only to the upper few layers of atoms on the substrate. The ewald sphere construction is the easiest way to visualise this arrangement. The vector K<sub>0</sub> is the wave vector of the incident electron beam which determines the radius of the ewald sphere. Additional vectors  $K_1$  and  $K_2$  represent elastically scattered wave vectors of equal magnitude. Therefore, all these vectors when drawn from the same origin (substrate surface) will fall on the ewald sphere. The reciprocal space of a crystalline surfaces such as GaAs, produces a reciprocal space lattice which consists of rods extending out of the 2D plane from the surface. The intersection of these rods and the vectors which fall on the ewald sphere produce the pattern of bright dots. With multiple vectors that satisfy the conditions to fall on the ewald sphere the pattern will show concentric circles with the smallest circle known at the 0<sup>th</sup> laue zone (L<sub>0</sub>) and the next the 1<sup>st</sup> laue zone (L<sub>0</sub>). This is shown in Figure 12A with Figure 12B showing the impact of surface morphology on the reciprocal space and subsequent RHEED pattern [74]. The intensity of these spots depends on the integrity of the surface with the brightest achieved on a perfectly flat surface. This effect can be utilised for monitor the completion of layer by layer growth with intensity oscillating as each layer reaches completeness, before a further layer begins to form atop. This effect is utilised in the calibration of growth rates which is discussed later in section 3.2.2.1.

Kikuchi bands are also strongly dependent on the surface. Sharp lines originate from perfect crystal structures, while broadening of the lines can indicate scattering from terraces and steps on the sample surface. These bands originate from inelastic scattering events in which electrons fly in all directions. Some of these will scatter in directions that satisfy the Bragg equation for a given lattice, in the vector  $P_1$ . This then forms a secondary suedo primary beam which in turn is diffracted producing a vector of increased intensity  $D_1$  and while the original incident vector of the beam is decreased in intensity. This is summarised in the schematics within Figure 13 [75]. The unrefracted pattern of kikuchi lines can be produced from bisecting the vector from origin to each reciprocal lattice points. Bands observed in real

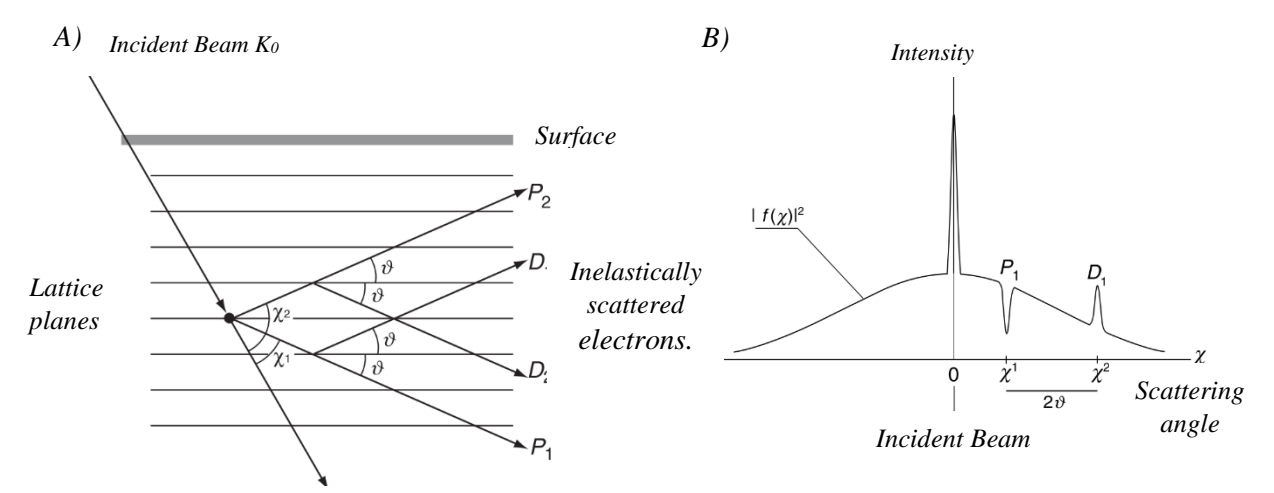


Figure 13 A) Schematic diagram showing formation of kikuchi lines from inelastically scattered electrons. B) Diagram of intensity showing kikuchi pattern formation. Adapted from [75].

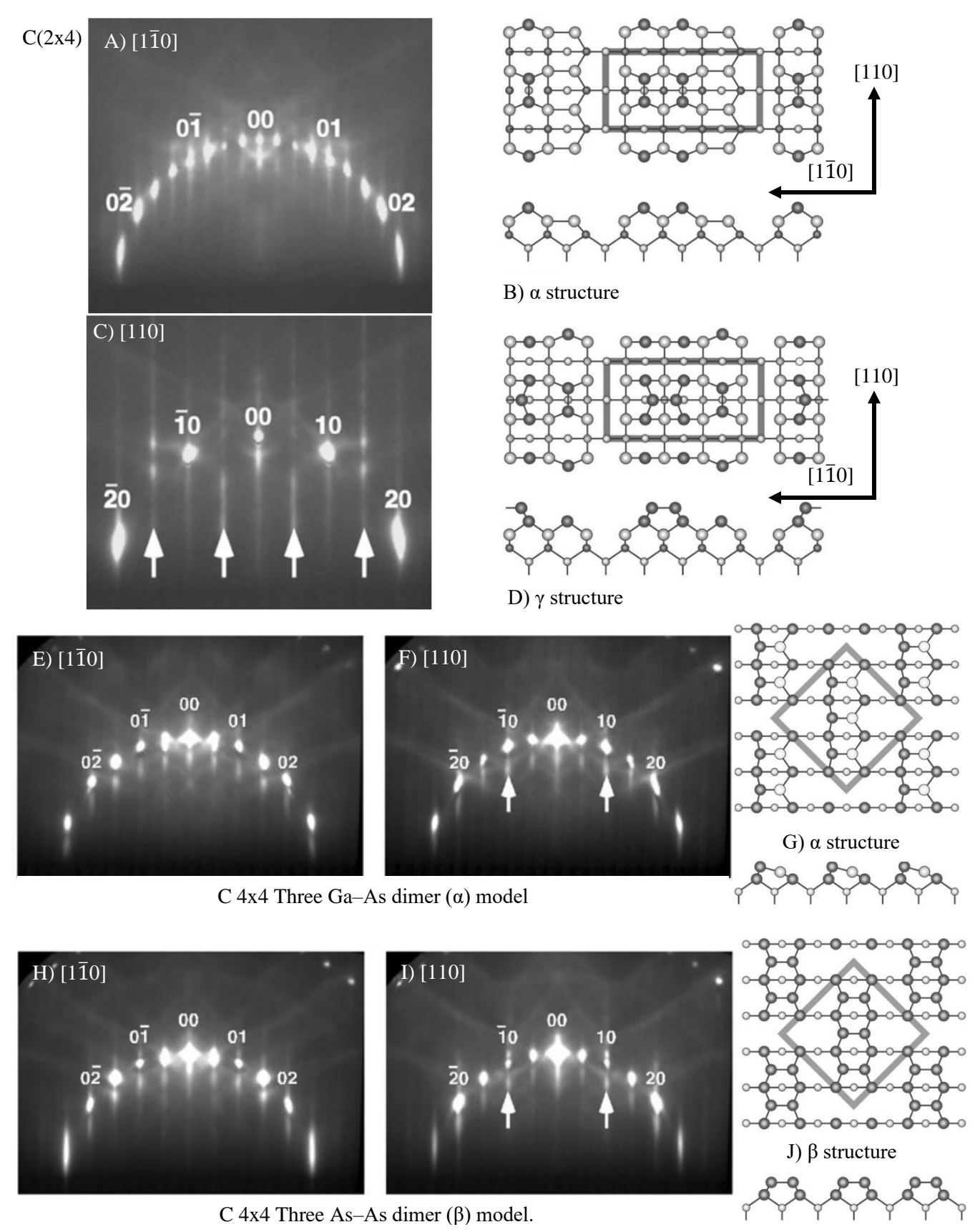


Figure 14 RHEED patterns take from on GaAs substrates. For C 2x4 the viewing orientations are A) [ $\overline{110}$ ] and B) [ $\overline{110}$ ] with corresponding atomic arrangements for structures under low and high As flux for  $\alpha$  and  $\gamma$  shown in B) and D) respectively. For C 4x4 the viewing orientations E) [ $\overline{110}$ ] and B) [ $\overline{110}$ ] for the G)  $\alpha$  structure and H) [ $\overline{110}$ ] and I) [ $\overline{110}$ ] for the J)  $\beta$  structure. Adapted from [76]

patterns are however refracted at the lower angles with the bands curving to the normal of the substrate surface as they approach and intersect with the 0<sup>th</sup> laue zone.

The reciprocal space rods position on a surface is dependent on the surface atomic positions. These deviate from the bulk crystal structure as atoms attempt to minimise the free surface energy. This results in a variety of observed RHEED patterns on the same material and bulk crystal structure, depending on the surface conditions. This can be utilised during growth to access how the surface reacts to the presence of a new element and shed light on the incorporation mechanism. However, to view and analyse a metastable reconstruction a more powerful and sensitive RHEED system is required than the one fitted in this instance. The RHEED can still however greatly inform on the growth such as giving structural information about the surface morphology as seen in Figure 12b and also identify stable reconstructions. Stable reconstructions are those that are achievable under a static surface, ie not growing surfaces.

In the case of GaAs this is useful effect as there are 2 stable reconstructions of note, the c2x4 and c4x4. The numbers refer to the number of atoms in the repeating unit cell of the surface structure. Examples of these surface reconstructions and the corresponding RHEED patterns for C 2x4 and C 4x4 on GaAs are shown in Figure 14 [76]. These are temperature and As flux dependent reconstruction with the transition between the two at 400 °C under no As flux. The transition point can be increased with increasing As flux limit A point used for temperature calibration of the GaAs substrate. Typically, the C 2x4 is observed post buffer growth as this is stable at optimised GaAs growth temperatures 560 to 580 °C under an As flux. This reconstruction can be observed across a wider range of temperatures depending on fluxes. There are sub variations of surface reconstructions with subtle difference in surface atomic arrangement that are not always apparent from the raw RHEED pattern. The transition from α to γ C 2x4 under increased As flux is one such example. The surface reconstruction is vital in growth as they affect the bonding availability for incident atoms as they adhere to the surface. In the case of  $\beta$  C 4x4 there is no Ga exposed any atom must be able to adhere to the exposed As. This is of less consequence as in III-V growth group III elements limit the growth rate so an entirely group V terminated surface is not an issue as Ga will adhere and As is supplied in excess. With all work within this study predicated on calibration by analysis of RHEED patterns to assess the buffer growth this is an essential technique to conduct epitaxial growth on an MBE system.

## 3.1.5 Heater Stage and Flag Plate

The sample heater stage within this system is a PNB resistive heater mounted into the support arm of the substrate holder assembly in the main chamber. This is directly attached the to 3 axis manipulator located at the top of the main chamber. The PNB is heated by passing a DC current supplied by a linear rail power up to 5 A with a 100 W power limit. The heater power wires are wrapped around the connecting rod between the upper manipulator and sample assembly. This limits this reactor to static

growth as rotating the stage more than  $\pm$  180 ° can cause the wires to strain against the connections causing them to detach from the heater contacts. Images of the heater assembly are shown in Figure 15A and B with the PNB resistive heater element seen in Figure 15B. The sample is loaded on a molybdenum flag plate holder secured underneath the heating element. The heat transfer is done radiatively from the heater element to the exposed back of the loaded wafer.

The molybdenum flag style sample plate is shown in Figure 15C and slots into the grooves highlighted by the green square shown at bottom of Figure 15A. Molybdenum is selected in this application due to its low thermal expansion coefficient and low outgassing at high growth temperatures. For this system the upper growth temperature is limited to 800 °C by the heater element. The flag style refers to the outer geometry of the sample plate. However, for the growth in this study a solid plate has been altered with a machined cutout in which the wafer sits atop small protruding tabs. The cutout within the sample plate is slightly rectangular measuring 11.4 x 11.8 mm in height and width, tabs protrude in by 1 mm from the inner edge. The depth is 1 mm through the plate with a tab thickness of 0.3 mm. This allows for wafers up to 700 µm in thickness with the wafer resting by gravity atop the tabs. This allows for sample to be cleaved from either 2 or 3 inch substrates. This slight rectangular nature to the sample holder is designed so wafers can be aligned for RHEED along a known crystallographic axis. Wafers are cleaved, depending on the orientation of the wafers as purchased, with the major cut aligned to the longer length 11.75 mm with the second 90 degree cut at 11.35 mm. This ensure the  $[1\overline{1}0]$  of the C 2x4 reconstruction is visible on the RHEED screen and eliminates the risk of misaligning the wafer in the holder. The small ring protrusion is referred to as the cold loop and is utilised to grip the sample holder for loading and unloading of wafers. The name is resultant from the impact the cold loop has on the thermal uniformity of a loaded wafer. It is also possible to load a solid flag and adhere a wafer of any geometry by using indium bonding. However, this wasn't conducted within this body of work.

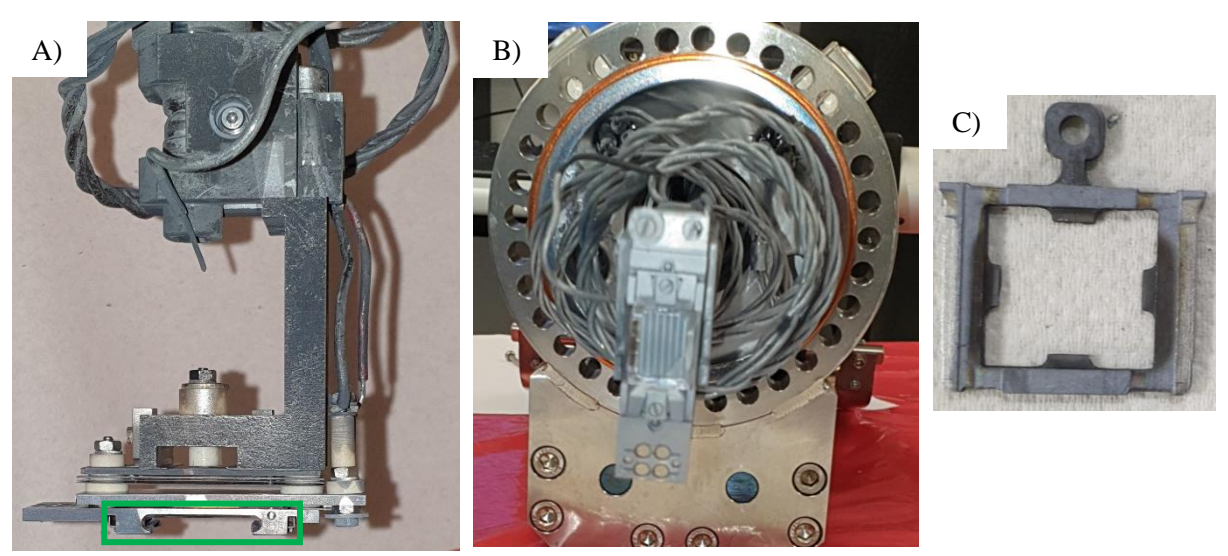


Figure 15 Image of MBE STM heater stage taken during MBE maintenance. A) side on view B) down up view C) top down view of Mo flag style sample plate holder

Substrate heating uniformity is a function of both the heater stage and sample plate used during growth. The temperature is calibrated to an individual flag plate and is recalibrated in the event a different flag plate has to be substituted in. However, all sample plates are machined to the same design so there should be minimal variation between those in circulation. Estimated at  $\pm$  10 °C based on shift in temperature calibration between plates. The variation in substrate surface temperature can be seen in the thermal image shown in Figure 17. This is an undoped 300 µm thick cleaved GaAs wafer held at 550 °C, according to the RHEED heater calibrations discussed in section 3.2.2.2. There is a slight disparity between the temperature measured by thermal imaging and the RHEED heater calibrations. Discussed in further detail later in section 3.2.2.2. This is attributed to the difficulties in measuring semiconductor temperatures by thermal imaging due to the high reflectance of the wafer. The key details shown here is the temperature delta of 35 °C observed between 1 mm above the tab closest to the cold loop and 1 mm below the adjacent tab. There is an increase rate of thermal loss due to the additional surface area of the loop. Heater calibrations by RHEED are conducted with the beam aimed at the centre of the wafer. The beam can be aligned to this position reliably as the tabs will shadow the electron beam depending which tab is blocking it, and so can be used to establish the beam's location on the sample surface. There is no way to mitigate the lack of temperature uniformity across the wafer However it does reduce at lower growth temperatures decreasing to 15 °C at 400 °C. This is approaching the lower limit where the camera used for these measurements can reliably operate. The thermal discontinuity across the wafer can lead to compositional changes, especially when working with bismides. The majority of analysis is conducted on the centre section of the wafer however some analysis necessitates sectioning a wafer and sending off quarters. In this case each quarter is measured individually to evaluate the uniformity of that sample. When a wafer is removed from the MBE machine it is scribed on the back in each corner with 3 digits to identify the wafer. The cold loop is the reference for the bottom each wafer with the text written in each corner as though on a single page. By comparison between the orientation of the text and tab position for each quarter the relative position of that quarter can be determined. This is a vital step in sample unloading and was employed to prevent any unfair comparisons across series due to measurements in different sections of the wafer.

The time taken for heater adjustment and subsequent substrate temperature stabilisation was also assessed for this system. This was conducted to inform the growth and evaluate the rate at which the substrate temperature can be changed. All temperatures given are measured from the thermal imaging camera. The undoped GaAs substrate was held at 510 °C for 30 s before heater power was cut. The heater power was then restored 30 s after the sample had cooled below the temperature detection limit of the thermal camera totalling 72 s. The temperature was then monitored for 210 s to assess how quickly the sample returned to the target temperature. This is thermal cycle is shown in Figure 16A and B. The sample took 42 s to reach the lower detection threshold of ~310 °C. This is a limit of the thermal

camera used in this investigation. Post the temperature set point being raised, it took 180 s to reach 99% completion in the transition from 310 °C to the 510 °C target temperature. Within the initial 30 s the substrate had reached 75 %, an additional 30 s later it reached 90 % of the target temperature. This informed us that it was quicker to lower growth temperature than raise. However, when raising the temperature, it would be expected that the lower the target temperature the shorter the rise time. Therefore, for the vast majority of growth a lower time limit of 120 s was set and adhered to for all temperature transitions between grown layers. This is for sample recipes which contained a growth

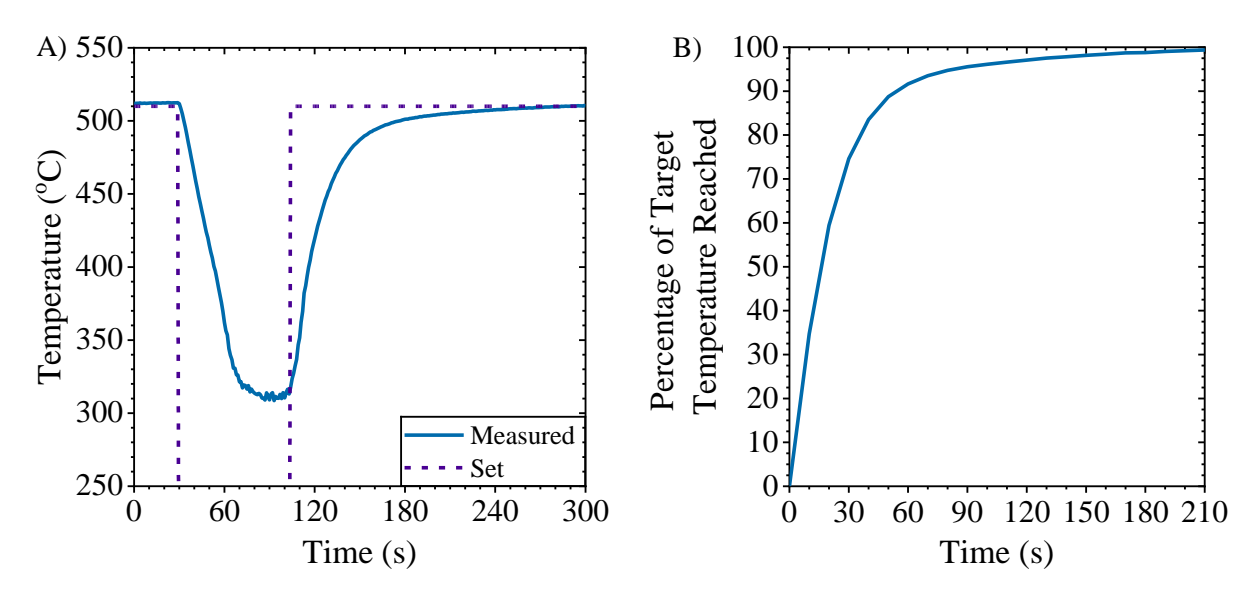


Figure 16 Temperature profile as a function of time for an undoped GaAs wafer at 510 °C A) raw temperature. B) Percentage of target temperature reached when power was restored.

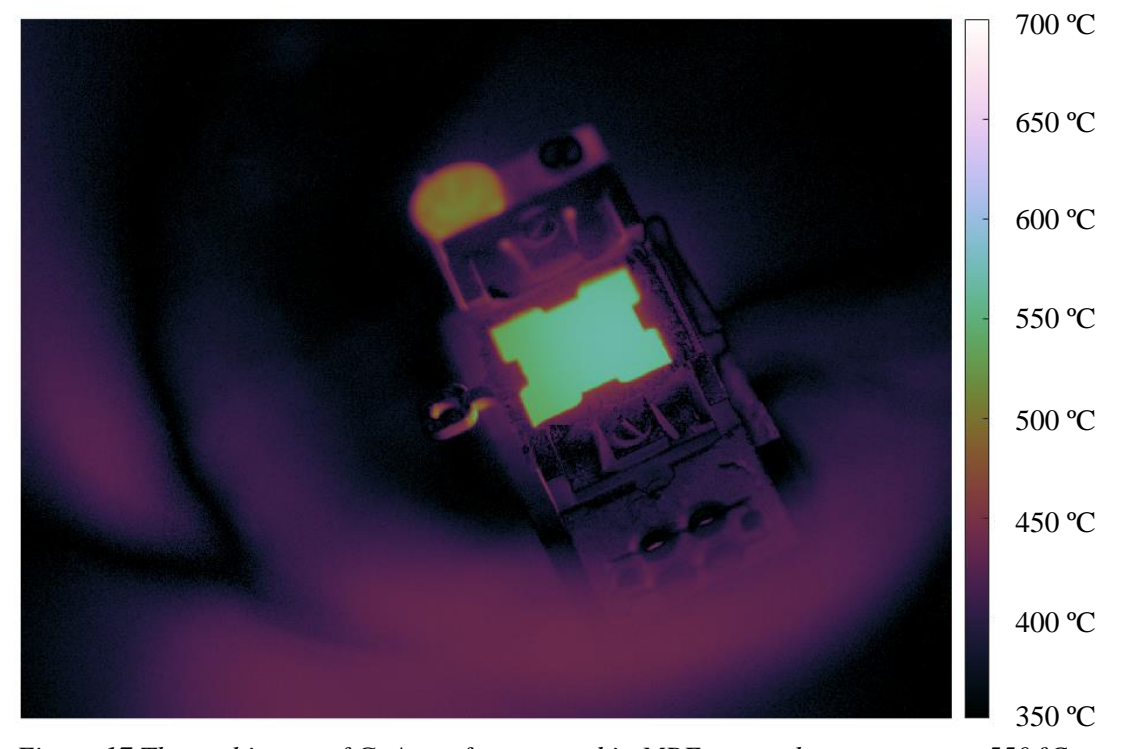


Figure 17 Thermal image of GaAs wafer mounted in MBE system heater stages at 550 °C.

interrupt to change the substrate temperature. The exceptions were for QD growth due to experimental difficulties associated with rapid InAs desorption from the surface. In this case a lower limit of 30 s was used in the temperature treatment. There were no negative effects observed in the QD sample due to this compromise. This lower 30 s limit was also used for samples where the temperature changes were minor such as switching between AlGaAs and GaAs where a 30 °C alteration was made during the layer growth. There was no negative effect observed in these samples due to this. In the cases presented within this work the temperature transition times are stated. Any deviation from the limits were based on preliminary growth of layers prior to commencement of series to ensure no adverse effects are present due to the heater transition time. It is also of note that the thermal images were taken with the effusion cells cold to prevent issues from reflected heat. This however means that the thermal camera cannot be used for temperature measurements during growth of any samples.

# 3.2 MBE Operating Principles

#### 3.2.1 Growth Modes

There are three main growth modes of epitaxial growth Frank-van der Merwe (FvdM), Volmer-Weber (VW) and Stransky-Krastanov (SK). The observed growth mode for a material system, substrate and deposition elements, is dependent on the relationship between the interfacial energies of that system [77]. There are 3 main interfaces for consideration in epitaxial growth, the epilayer/vacuum interface ( $\gamma_e$ ), the epilayer/substrate interface ( $\gamma_e$ ) and the substrate/vacuum interface ( $\gamma_e$ ). The location of the interfaces is shown in Figure 18 on a partially completed epilayer. The determination of the growth mode is dependent on the summation of  $\gamma_e$  and  $\gamma_i$  in relation to  $\gamma_s$ .

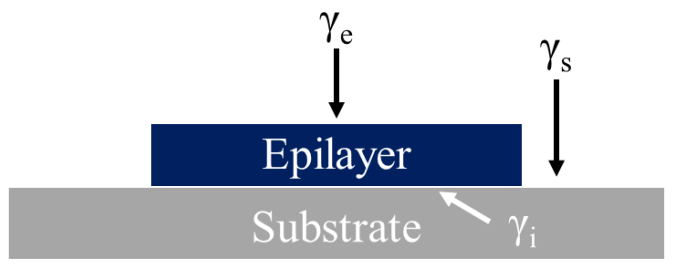


Figure 18 Schematic of surface interface free energies in MBE Growth on partially grown epilayer.

#### 3.2.1.1 FvdM Growth

The FvdM growth mode is energetically favourable when (7) is true. This equates to a material system that it is energetically favourable for deposited species to bind to the substrate rather than binding between the deposited species. The results in a 2D layer by layer growth mode in which a single mono layer of atoms is deposited before a subsequent monolayer forms atop the previous.

$$\gamma_e + \gamma_i < \gamma_s \tag{7}$$

This produces epitaxial growth of the highest quality. However, is limited to growth of the same material as the substrate (homoepitaxy) and growth of materials with very similar lattice constants to the substrates (hetroepitaxy). This growth is dependent upon atom migration across the growth surface to allow for layer completion, thus requiring high growth temperatures. This system can be described by incident atoms absorbing onto the surface and migrating until encountering a step edge of a partially complete epilayer. The atom is then incorporated into the lattice and the layer growth moves further to completion. It is common for substrates to have a fractional degree offcut to present step edges from

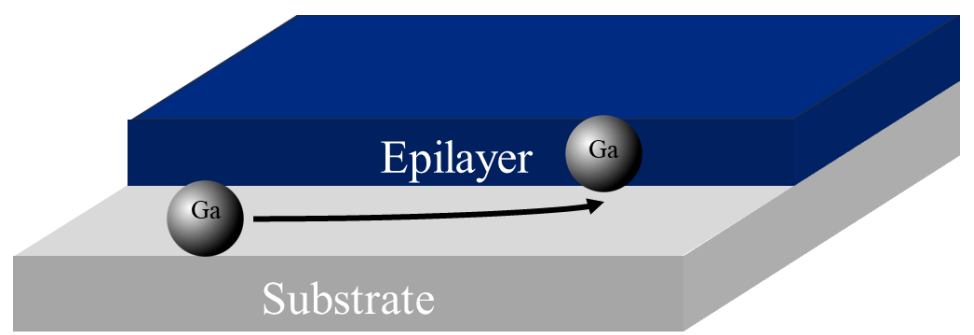


Figure 19 FvdM growth with incident Ga atom migrating to step edge of incomplete epilayer. the outset promoting this growth mechanism. A schematic of this growth mechanism is shown in Figure 19.

#### **3.2.1.2 VW Growth**

The VW growth mode is energetically favourable when equation (8) is true. Under this growth regime it is more energetically favourable for incident atoms to bind to one another, rather than bond with the substrate. This results in 3D islands of deposited material, growing in size with further disposition of material onto the substrate. Layers are completed by the coalescence of these islands. The growth regime may change upon the first layer completion as it then transfers to hetroepitaxy. However due to the random alignment of crystal structures within each islands this growth regime commonly results in polycrystalline films [78]. The interfaces between the crystal grains also contribute to poor quality material. The growth diagram for VW growth is shown in Figure 20.

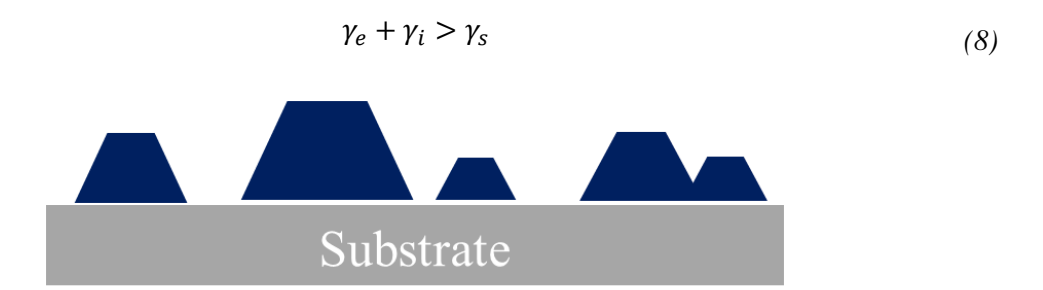


Figure 20 VW growth with 3D islands of deposited material atop the substrate.

#### **3.2.1.3 SK Growth**

SK growth, as previously touched on in the QD literature review is observed in material systems with a significantly large mismatch in the lattice spacing between the substrate and deposited material. This results in an initial growth frame where (7) is true up to a critical thickness of deposited material. The induced strain at this point exceeds a certain threshold and then growth proceeds via a 3D island mechanism. This creates a 3D island structure floating atop a wetting layer of deposited material. This growth regime is not advised for bulk film growth, due to defect propagation from the substrate wetting layer interface. The critical thickness of this transition is dependent on the lattice mismatch and relative



Figure 21 SK growth with 3D islands formed atop a wetting layer both composed from the deposited material.

bonding energies of the specific material system. This mechanism is discussed in further detail for the InAs/GaAs material system in section 2.2 Epitaxial Growth. The diagram for this growth mode is shown in Figure 21.

#### 3.2.2 MBE Reactor Calibrations

#### **3.2.2.1** Growth Rate

Growth rate calibrations were conducted by measuring the periodicity of growth rate oscillations as observed in RHEED on a growing surface. This was conducted on a stabilised C 2x4 reconstruction post oxide remove and deposition of 300nm of GaAs buffer. The surface was established at the growth temperature of 570 °C under a significant As flux, .This prepares an atomically flat surface giving the brightest intensity dots on the RHEED screen. Two dots are selected for intensity monitoring, commonly the brightest are two 0 order rods. These are highlighted within software growth oscillation software and the average intensity of the selected regions monitored against time. The Ga shutter is then opened initiating epitaxial growth. The roughening of the surface due to formation of an epilayer causes the brightness of RHEED to decrease. Reaching a lower limit at half completion of a single monolayer. Further growth improves the brightness as the epilayer completes and the surface approaches atomic smoothness. This progress then repeats as a new epilayer is formed atop the previous. This produces oscillations in the brightness of the RHEED proportional to the rate of completion of a singular monolayer. In the case of GaAs it is common to see the intensity of the oscillation decrease with time. This results from formation of the following mono preceding completion of the previous causing increased surface roughening with increased deposition time and thickness. This can be seen in the RHEED oscillations of a growing GaAs surface shown in Figure 22.

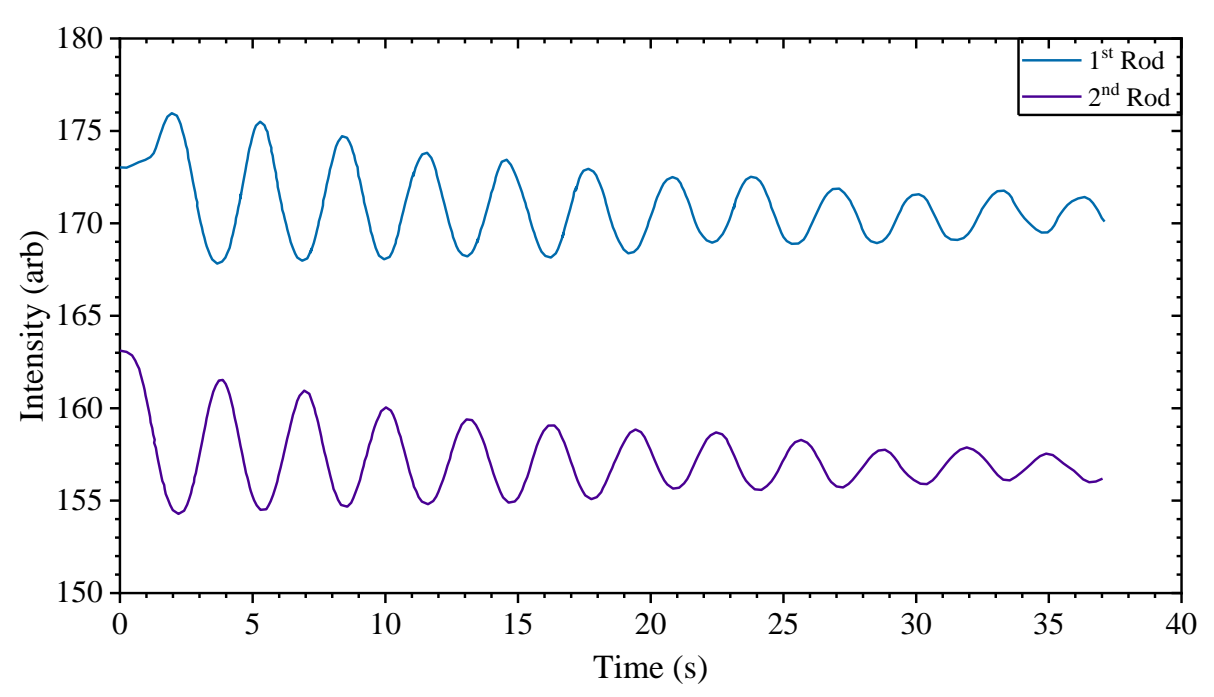


Figure 22 RHEED intensity oscillations of a homoepitaxial growing GaAs surface measured from the 2 brightest 1<sup>st</sup> order RHEED rods.

In the case of GaAs the zinc blende crystal structure unit cell contains 2 monolayers, with a lattice constant of 5.65 Å this equates to a monolayer thickness of 2.825 Å. The growth rate is extracted by measuring the time between peaks. In the case shown in Figure 22 there are 11 completed monolayers over a time span of 34.08 s for the 1<sup>st</sup> monitored rod and 34.27 s for the 2<sup>nd</sup> rod. The equates to a growth rate of 0.323 and 0.321 monolayers per second MLs<sup>-1</sup> respectively. The average is taken, and this is used to calculate the growth rate at a given Ga cell temperature. In this instance the growth rate would be 0.322 MLs<sup>-1</sup> or 0.910 Ås<sup>-1</sup>. For the case of ternary system such as AlGaAs the GaAs growth rate was measured and fixed followed by a separate measured of the combined AlGaAs growth rate. The Al growth rate was then calculated by subtraction of the GaAs from the combined AlGaAs growth rate.

This is however only possible for materials which grow in the FvdM growth mode. For the InAs/GaAs QD chapter the growth rate of In on a GaAs surface was assessed by another mechanism. Starting from the same C 2x4 stabilised surface, In flux was supplied along with an excess As flux and the RHEED monitored for the transition from a flat to 3D island surface. The theory is shown in Figure 12 with the experimental RHEED capture of this transition shown in the QD results chapter in Figure 37. The transition from flat to 3D islands occurs after 1.6 ML of In has been deposited on GaAs. This allowed for the growth rate to be calculated by division of the time taken to observe the transition divided by the required deposition thickness of 1.6 ML.

## 3.2.2.2 Substrate Temperature Calibration

Substrate temperature calibrations, as previously eluded to, were conducted using the RHEED systems targeted at the centre of the wafer. The RHEED system was utilised as the MBE system used was not

equipped with an optical thermometry system. There is a heater stage thermocouple however its location is too distance from the wafer, rendering it ineffective for reliable temperature measurements. The temperature of the GaAs wafers used within this study were calibrated using 3 well defined temperature transitions observable by Rheed. These in decreasing orders of temperature are:

• The thermal desorption of the native surface oxide at  $600 \pm 10$  °C [79]

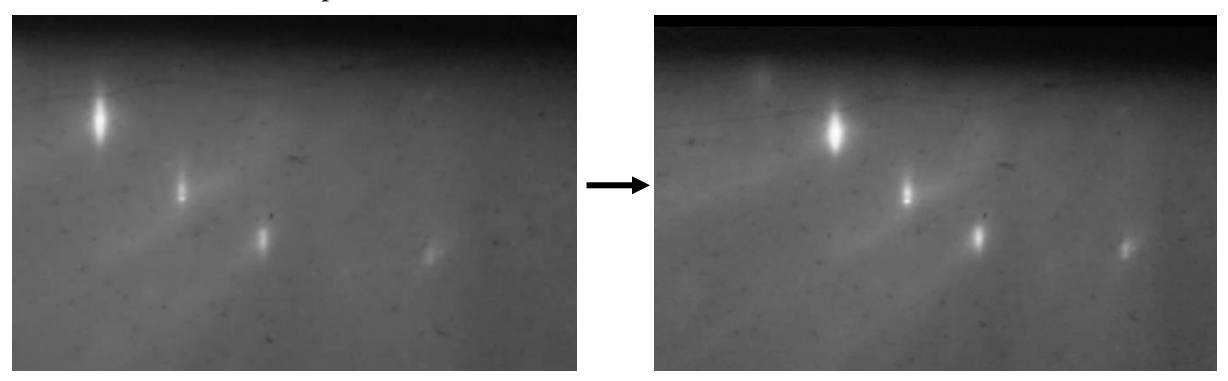


Figure 23 RHEED of thermal desorption of the native surface oxide at 600 °C.

• The  $c(4x4) \rightarrow c(2x4)$  transition in the absence of an As flux at  $400 \pm 10$  °C [80]

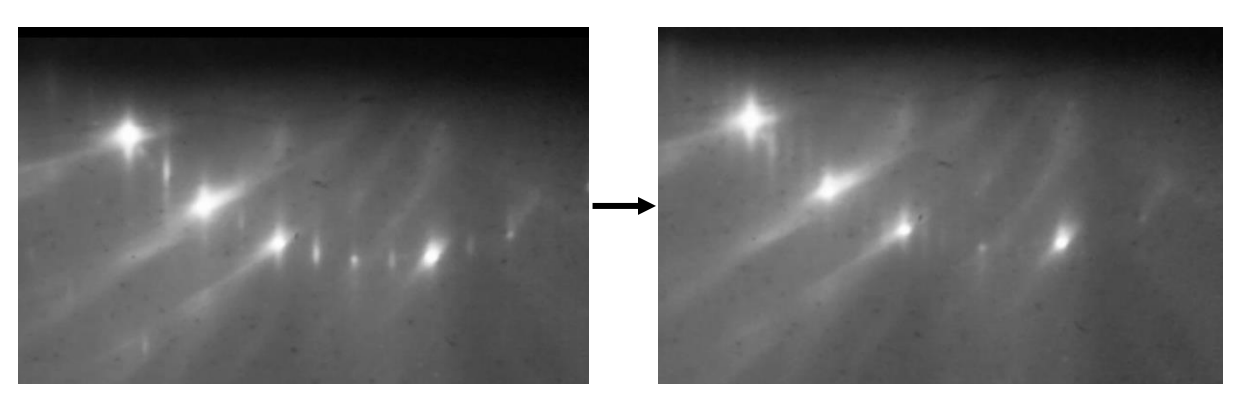


Figure 24 RHEED of  $c(4x4) \rightarrow c(2x4)$  transition in the absence of an As flux at 400 °C.

• The removal of an amorphous As capping layer by sublimation at  $300 \pm 20$  °C [81]

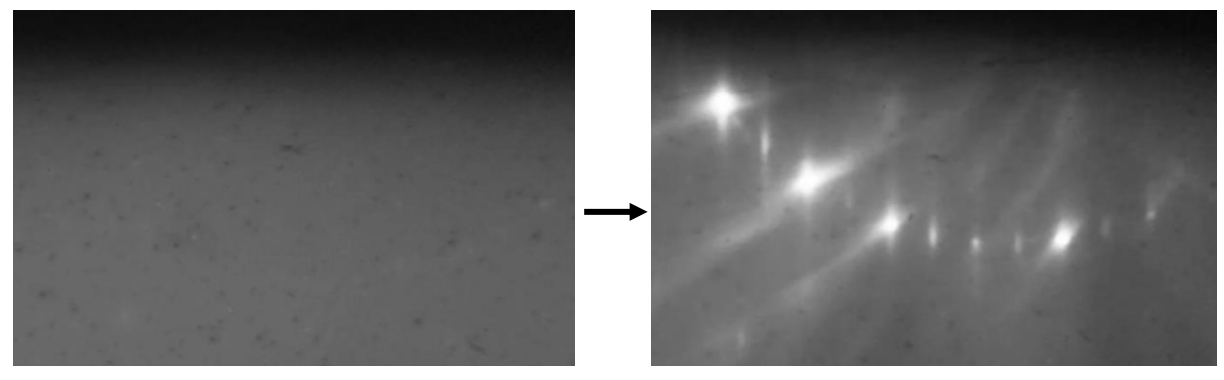


Figure 25 RHEED of the removal of an amorphous As capping layer by sublimation at 300 °C.

Examples of these transitions are shown in Figure 23, Figure 24 and Figure 25 for the 3 RHEED transitions at 600, 400 and 300 °C respectively. The heater current is recorded at each transition and with the 3 points fitted with a quadratic fit that best approximates the data. This allowed for calculation

of required heater current to reach a target temperature within the 300 to 600 °C range. This was then further extrapolated to allow for of the oxide remove at ~630 °C under an As flux.

#### 3.2.2.3 Flux Calibrations

Flux calibrations have been briefly touched on in the ion beam gauge section 3.1.4.1. They are used to calibrate the relationship between changing cell temperature and the atomic flux output for each cell. The flux calibrations are not comparable between cells due to the sensitivity difference of elements as measured by the ion gauge. The flux calibration was done by positioning the MIG below the sample stage and independently opening a single shutter for 300 s, closing the shutter and adjusting the temperature. Allowing for the cell temperature to stabilise before repeating. This was usually conducted at between 3 to 6 temperatures around the desired operating temperature of the cell with a typical range of  $\pm$  50 °C. The reading on the ion gauge was recorded as a function of temperature and fitted with an exponential relationship. This allowed for calculation of the atomic flux output in nA for each cell at a given temperature within the measured range. The As cell was slightly different as the bulk temperature was fixed and the needle valve varied to control the flux. In this case the ion gauge measurements were a function of needle valve position at a fixed As bulk temperature. These calibrations allowed for controlled adjustment of relative atomic fluxes. Particularly useful to account for flux drift with depleting source material.

Dopant fluxes are not measured in this way due to the significantly lower output required for doping. These fluxes when required, are calibrated by growing 1  $\mu$ m thick layers of Si or Be doped GaAs atop undoped wafers. The layers then had ohmic contacts added by diffusing small patches of indium into each corner of the wafer to allow for measurements by hall to calculate the doping density. This is conducted at 3 temperatures for each of the dopants and fitted with an exponential. This allowed the calculation of the doping density as a function of the Si/Be cell temperature for a fixed Ga growth rate.

#### 3.2.2.4 1:1 Calibration

This calibration is utilised to align the growth rate calibrations of the group III sources with the As flux calibration. This calibration provides the point at which the supplied group III fluxes to the surface

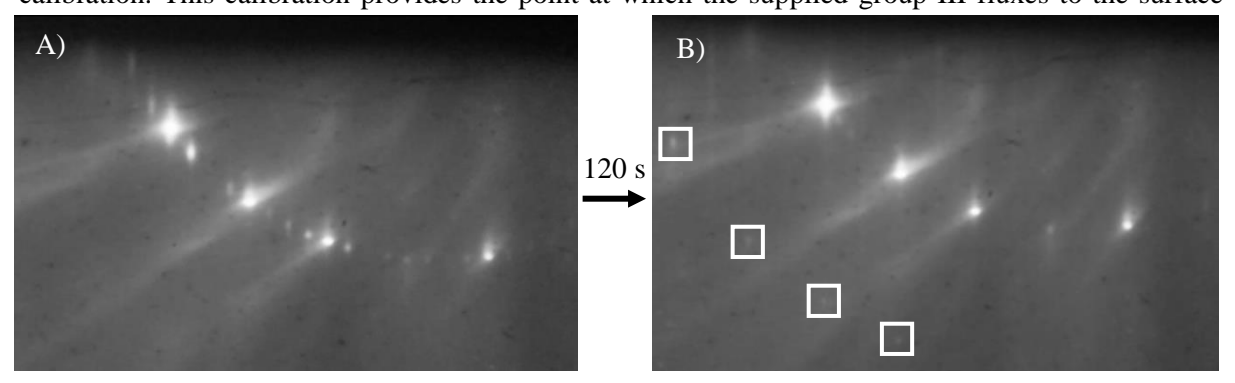


Figure 26 Image of RHEED from A) C 2x4 reconstruction on GaAs at start of 1:1 calibration and B) post Ga droplet formation with additional spots due to Ga droplets highlighted within the white

incorporate at unity with the As flux supply. Growth is group III limited with negligible desorption of the group III species under optimised growth. Therefore, the growth rate is fixed to the desired deposition speed typically 0.3 MLs<sup>-1</sup> for bulk layer growth and then the As valve position is varied. The valve position is systematically reduced, and the Ga shutter opened for 120 s. The RHEED is monitored for the formation of Ga droplets on the surface. The As flux is lowed until this is observed then slightly increased above this point and rechecked. The 1:1 point is the lowest As valve position at which Ga droplet formation is not observed within the 120 s timeframe. Figure 26 shows the C 2x4 reconstruction present at the start of a 1:1 calibration for GaAs with an example of Ga droplet formation as observed by RHEED.

#### 3.2.2.5 Calibration Uncertainties

The previously discussed calibrations have some inherent uncertainties in the values extracted. The highest contributing factor is the in interpretations of the RHEED patterns. This can be subjective in the determination of the exact temperature at which a transition is deemed to of occurred or fully transitioned. This places an inherent uncertainty on all temperature calibration estimated at  $\pm$  10 °C. This is based on of the temperature range at which consensus was achieved within the current growers within the research group when conducting temperature calibrations. This further impacts the 1:1 calibration as the formation of droplets is not always clear at very low droplet densities on the surface. The consensus amongst the present growers is within  $\pm$  2 mm on the As valve position which equates to  $\sim$  1%. This however is further increased by drift of flux outputs from the effusions cells over time which while corrected periodically will still alter the 1:1 point. This value is therefore estimated higher at  $\pm$  5% based on the typical values of the Ga flux drift between calibrations.

Uncertainties surrounding the flux calibrations are lower as the ion gauge reading is not open to interpretation. However, factors such as increased background pressure, unstable flux outputs or misaligned shutters can all cause issues. The repeatability of an accurately conducted flux check is within  $\pm$  5% when conducted back-to-back. This assumes the ion gauge is moved into the same position for flux checks as marked on the MBE system. However, the flux output of a given temperature will reduce as material is depleted from an effusion cell. Further uncertainties surrounding flux check have been discussed in the ion gauge and flux checks sections.

The growth rate calibration is the most accurate measurement for the flux output of the Ga and Al effusion cells. Well prepared growth surfaces for GaAs can give strong oscillations lasting up to 60 s. This allows for the growth rate to be extracted from an average period of over multiple monolayers of growth, increasing the confidence in the measurement. Further the measurements are taken from 2 rods on the RHEED pattern concurrently. There is some inherent noise in the brightness value from the RHEED spots. This can mostly be attributed to the camera used to measure which has a limited dynamic

range and high inherent noise. Its selection was based on cost and acceptable performance. The value of growth rate quoted is therefore accurate to  $\pm 3\%$ .

# 3.3 X-Ray Diffraction

X-Ray Diffraction (XRD) is a powerful non-destructive analytical technique for probing crystallographic structures of crystalline materials. The periodic structure and well-defined order within crystals allows for the diffraction of incident monochromatic x-rays in accordance with Braggs law of refraction[82]. The equation for which is given in equation (9). Here, the angle of diffraction is  $\theta$ , (9)th the x-ray wavelength  $\lambda$ , n denotes the integer order of the diffraction and d the lattice spacing.

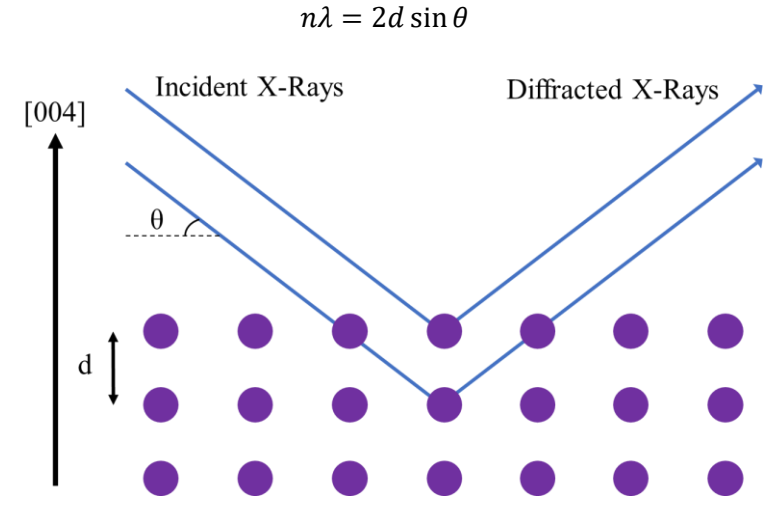


Figure 27 Diagram of the diffraction of x-rays from the (004) plane of a crystalline sample.

In an XRD system  $\lambda$  is fixed with a monochromatic x-ray beam utilised for the diffraction. In the case of the Bruker D8 XRD system utilised for measurements in this study, the source was a copper K- $\alpha$  with a wavelength of 1.5406 Å. Figure 27 shows a symmetric x-ray diffraction where the angle of diffraction is dependent on the d lattice spacing of the 004 plane . For GaAs this is only dependent on a single lattice constant  $\alpha$  with the spacing d a function of the 3 miller indices of the crystal plane h ,k and l, shown in equation (10). There are other orientations that satisfy the Bragg conditions for the GaAs crystal structure, the most common aside from [004] are [224] and [133].

$$d = \frac{\alpha}{\sqrt{h^2 + k^2 + l^2}}$$

Adjusting the scans for different crystal planes can be conducted by varying the operating parameters of the XRD system. With the angle of incident  $\omega$  variable alongside the angle of the detector relative to the incident beam given as 20. The orientations of the sample stage can then be controlled in 3 dimensions with 360 ° rotation relative to the x-ray beam along with x, y translation for alignment. This allows for all crystallographic orientation where the angle of diffraction 20 is less than 180° ie a hemisphere to be probed. However practically this is limited to 170° due to positional constraints where

the x-ray source can become blocked by the detector. A diagram of the basic XRD setup is shown in

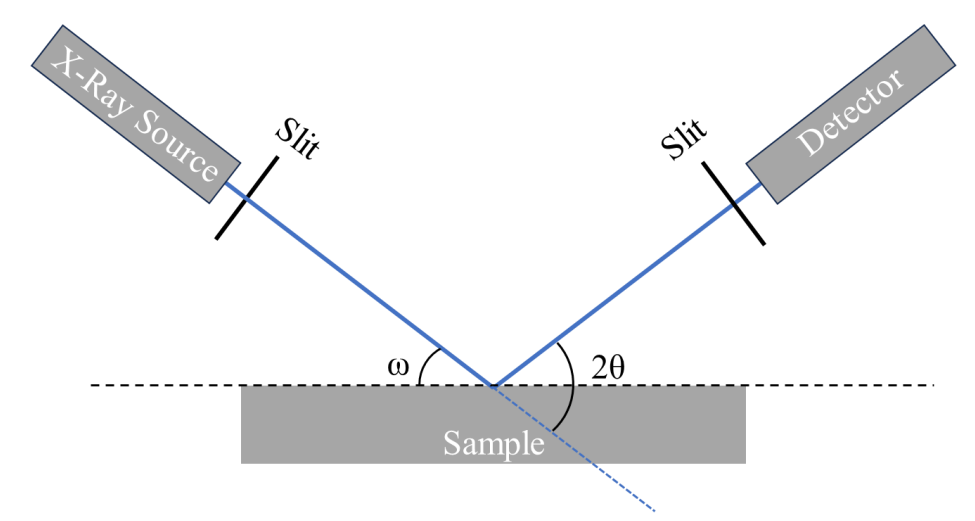


Figure 28 Diagram of basic XRD system.

Figure 28.

There are multiple possible measurements possible with an XRD system, each used to investigate different aspects of the crystal. The most common is the 2-theta scan which will detect all angles of diffraction over a range of  $2\theta$  values, typically over a  $60^{\circ}$  range. This can be used to identify single or multiple crystallographic structures within the sample by comparing with a database of known materials. Functioning similarly to a fingerprint for crystalline materials. This is less applicable in epitaxy as the crystal structure will align with the substrate.

Within this study the most common measurement is an omega 2 theta scan. This is a coupled scan where both the omega and 2 theta angles are adjusted simultaneously. This gives sensitivity to changing diffraction angles along a fixed orientation. Allowing for the change in a lattice spacing to be probed across epitaxial layers. This detects the change in the d spacing due to changing stresses within the same crystal structure. This is used in our case to identify the changing lattice constant due to Bi incorporation. In the case of 004 GaAs the omega angle was between 30.05 to 31.5° with a 20 between 59 to 61°.

Rocking curve XRD scans fix the  $2\theta$  angle and adjust the omega by tilting the sample stage this gives information over the range of d spacing at a specific diffraction peak. The tighter the d distribution spacing the thinner the rocking curve peak will appear. Conversely when there is a range of Bi contents within a layer the rocking curve will broaden significantly.

Reciprocal space mapping is another very useful XRD based technique it has the effect of concurrently doing both a rocking curve and omega 2 theta scan. Essentially stacking a series of omega 2 theta scans at slightly different omega offsets. This will reveal is there is any misalignment of the peak x-ray intensity for the changing d spacing detected. This can be immensely helpful in spotting relaxed layer

or layers which have grown at a slight tilt relative to the substrate. Examples of the three types of scans used within study are shown in Figure 29. The versatility of XRD is one of the key elements to its usefulness in crystallographic analysis.

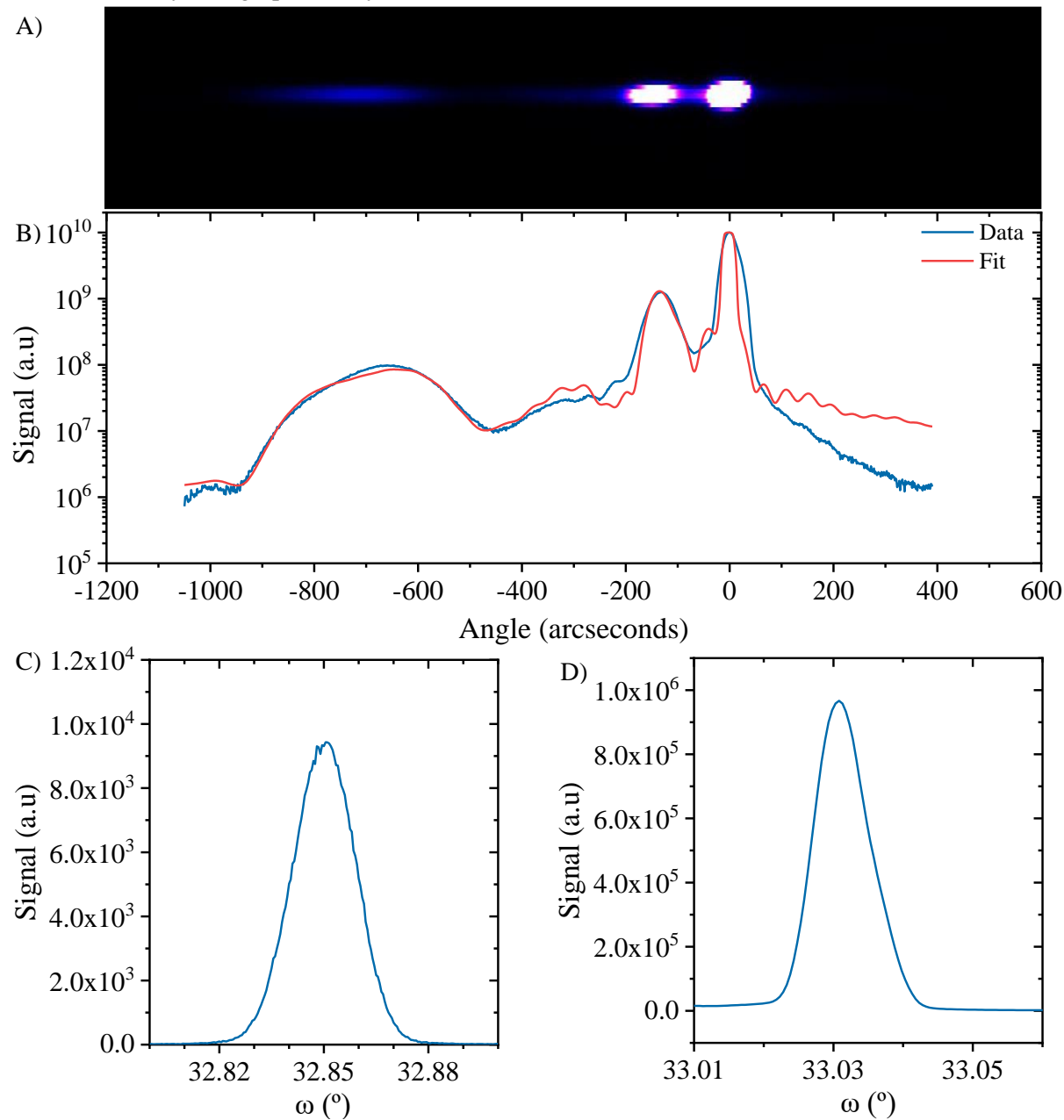


Figure 29 Representative XRD scans of AlGaAsBi structure A) Reciprocal space map B) Omega 2 theta scan C) and D) are rocking curves for the Bi peak at -700 arcseconds and AlGaAs at -180 arcseconds respectively.

## 3.4 Photoluminescence

Photoluminescence is a powerful non-destructive analytical technique for studying the band gap of semiconductors materials. The basic setup of a PL system is shown in Figure 30. This system contains multiple components some of which are interchanged depending on the measurement. The 532 nm continuous class 4 laser was used for all measurements in this study. The beam path intersects with an

optical chopper at ~180 Hz and a 380 to 550 nm band pass filter. This creates a pulsed beam while the band pass blocks any higher order harmonics of the laser output. The is then aligned using two mirrors onto the sample which is mounted to a 3-axis sample stage to allow for measurement of multiple areas and alignment. Carriers are injected into the wafer structure by the incident laser, provided the photon energy of the laser exceeds the semiconductor bandgap. The wafer is positioned at the focal point of the Cassegrain mirror to allow for the emitted luminescence from carrier recombination within the wafer to be captured. The Cassegrain mirror gathers the emitted radiation and focuses the beam to a point on the entrance slits of the monochromator. The beam intersects with 2 sets of filters. Firstly, a long pass filter both a 610 and 730 nm were used within this study to block laser light from entering the monochromator. Secondly a set of neutral density filters used to reduce the intensity of the radiation entering the monochromator to avoid saturation of the detector. This effect may also be achieved by reducing the slit width at either the entrance, exit or both. In addition to reducing the intensity, reducing the slit width improve the maximum resolution by further limiting the wavelength range that enters the detector. The monochromator contains an internal Bragg reflector where the angle of reflection is wavelength dependant. This allows for a single wavelength to be selected and sent down the optical path to the detector. A single pixel LN<sub>2</sub> cooled Ge detector was used in the measurements shown within this thesis, although this may be substituted to extend the detectable range of wavelengths. The output from the monochromator is focused onto the detector by a focusing mirror with an output voltage between 0 to 10 V recorded by the lock in amplifier.

The integration time for each measurement on the amplifier is 0.3 s this covers 54 pulses of laser light.

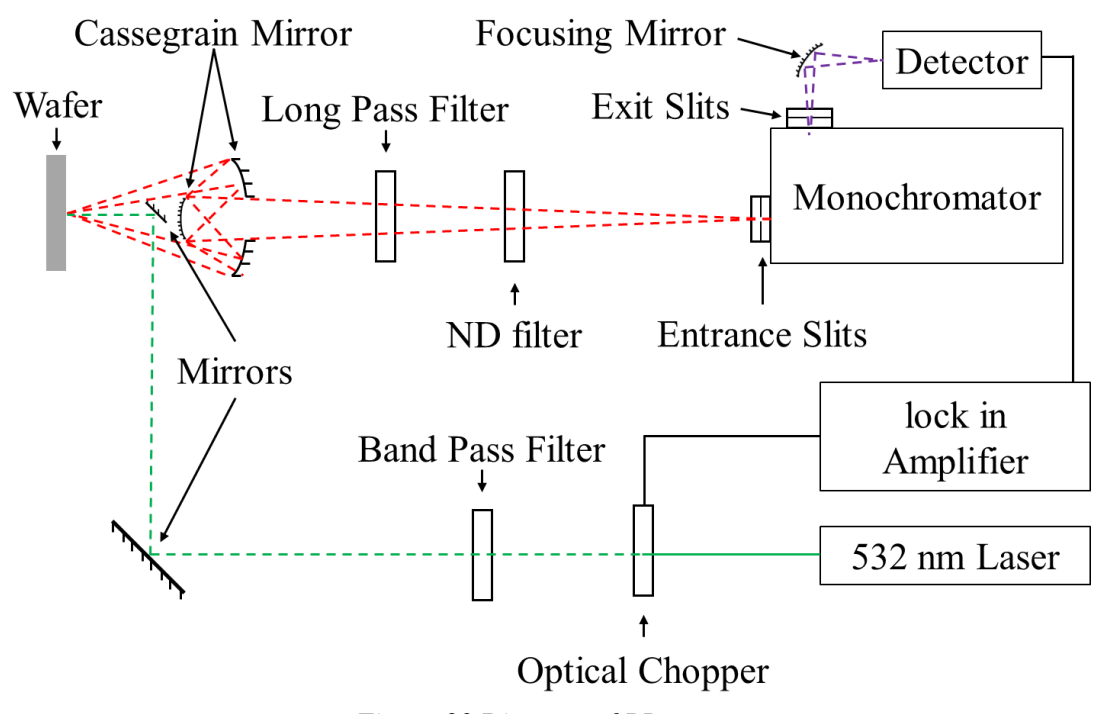


Figure 30 Diagram of PL system setup.

Measurements are therefore taken with the both the sample under excitation and ambient lighting

conditions. The lock in amplifier allows the real time comparison and deduction of the latter from the former. This removes the background noise due to lighting within the lab. It also allows for averaging of the signal over several measurements to reduce the noise for each measurement. PL scans are built up as the monochromator adjusts the Bragg reflectors angle relative to the incident beam, changing the output wavelength in synchronisation with the integration time. Typically, the step size is between 0.1 to 5 nm depending on the desired accuracy. The total range is limited by the excitation wavelength of the laser, the long pass filter used, the Bragg reflector selected and the Ge detector. For the setup used in this thesis measurements between 610 to 1550 nm can be produced accurately before encountering a limit of the system. This technique gives the emission intensity as a function of wavelength. The emitted wavelength from the wafer is dependent on the internal band structure, including defect levels and localised sates. There are variations of the PL measurement where additional information can be gained by systematically varying a control parameter. Two techniques employed within this study included variation of the laser excitation power and wafer temperature during PL measurements. The wavelength was calibrated using the emission laser line with the long pass filter removed and by taking measurements of internal GaAsBi reference sample. This allowed for drift of the monochromator and system to be accounted for or highlight any issues such a misaligned component.

## 3.4.1 Power Dependent PL

Adjusting the excitation power used in PL measurement can provide additional insights into the optical characteristics of the wafer. Increasing the concentration of carriers can show how the quantum efficiency is limited as well as revealing higher energy states within the system. If the quantum efficiency of a system is limited by a lack of carriers doubling the laser power and carrier injection should proportionally impact the total luminance. This can be extracted by integrating the PL emission, which in this thesis was done using the trapezium rule. However, if their material has significant quantities of active non radiative recombination centres then the behaviour will differ. The quantity of these centre is finite within a material at a fixed temperature. This creates an intrinsic limit at which point if reached these centres become saturated by the number of injected carriers. This changes the proportion of carriers recombining radiatively and non-radiatively within the material. This produces a disproportionately large increase in the integrated luminescence to the increase in excitation power. The power dependent PL measurements conducted within this thesis are fitted with equation (11). Where integral of PL (Int PL) is equal to a constant a multiplied by an optical power I to the power of the exponent k. Where the exponent k varies between 1 to 2. For values close to 1 the recombination is radiatively limited, while for values close to 2 it is limited by non-radiative recombination. This fitting is done in the linear region where log power is plotted again the log of the integrated PL. This prevents fitting to regions where the sample temperature increased due to the higher optical powers used. This measurement is taken at a single temperature, however, can be conducted at a range of fixed temperatures.

$$Int Pl = aI^k \tag{11}$$

## 3.4.2 Temperature Dependent PL

Adjusting the temperature of samples during PL measurements can also alter the emission by changing the active number of non-radiative defects. The majority of defects and traps states within semiconductor materials have an associated activation energy. By thermally quenching the material the underlying processes can be suppressed. This makes temperature dependent PL a powerful technique to investigate the defect activation energies and enable their attribution to physical processes within the material. The laser power is fixed with the excitation value being the lowest possible while still achieving a measurable single at the highest temperature tested. The temperature of the substrate is then adjusted with a fixed wavelength range used for the PL measurements conducted at each increment. Substrate temperature control is achieved by the use of a cryostat with He cooling and in-built heater with a PID temperature controller. This allows for a measurement temperature range between 12 to 400 K. The log of the integrated PL from each of these scans is then plotted against the inverse of measurement temperature. This allows for fitting with equation (12) a dual of Arrhenius formula with 4 fitting parameters. Two energies Ea<sub>1</sub> and Ea<sub>2</sub> which are related to the activation energies of the trap states and two constants of C<sub>1</sub> and C<sub>2</sub> which relate to the relative concentration of these defects. The number of energies fitted can be increased to investigate a higher number of underlying processes. However, to avoid the practical limitations of fitting with too many degrees of freedom the dual Arrhenius fit was selected. (12)

$$Int Pl = \frac{1}{1 + C_1 exp\left(-\frac{Ea_1}{K_h T}\right) + C_2 exp\left(-\frac{Ea_2}{K_h T}\right)}$$

## 3.5 Microscopy

#### 3.5.1 Nomarski

Nomarski microscopy is an optical microscopy technique sensitive to changes in thickness and refractive index across a sample surface. Also referred to as a reflectance differential interference contrast system. The arrangements of optical elements for a Nomarski microscope are shown in Figure 31. The tungsten filament bulb is used as a broad band light source of randomly polarised light. The light is then polarised and split into 0° and 90° polarised light by a Wollaston prism. There is a slight spatial separation between the orthogonally polarised beams of ~0.2 µm known as the sheer. This means the beam pass through the wafer at slightly different locations. If the refractive index or thickness is different between these two points the optical path length is unequal. The two beams are then recombined in the second Wollaston prism and will constructively or destructively interfere depending

on the relative optical path lengths taken. This modifies the output intensity at each point depending on the interference enhancing the contrast of the image by differences in thickness and refractive index.

This allows for visual study of the atomically smooth substrates and sample used in epitaxy. Both for surface and sub surface features which while not impossible are considerably more difficult when using a conventional optical microscope. One example of commonly observed feature is a cross-hatching pattern which is observed in Nomarski when there is strain relation of an epilayer. This is not seen within this study due to the low layer thicknessed used in the samples. Example of Nomarski images of AlGaAsBi can be seen in section 5.4.

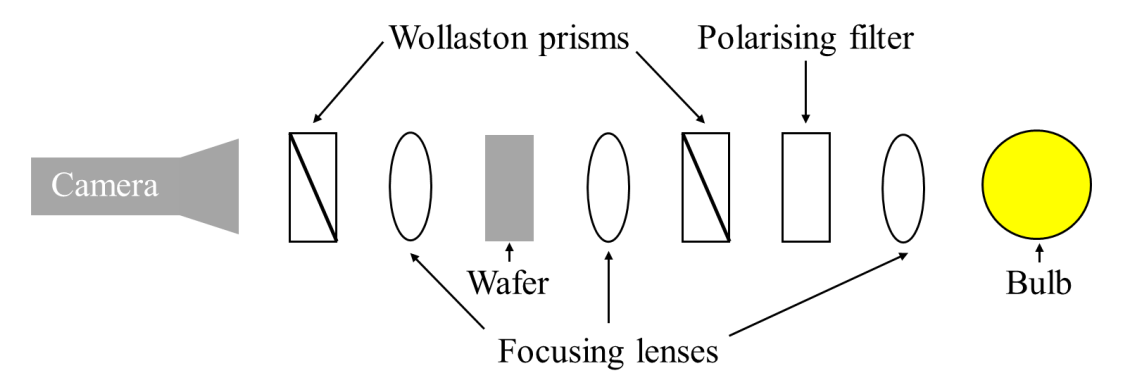


Figure 31 Diagram of Nomarski microscopy system.

## 3.5.2 Atomic Force Microscopy

Atomic force microscopy (AFM) is non-destructive technique used to analyse surface morphology at the nm resolution. The technique produces 3D topological data of the surface structure and was applied in this study to measure the morphology of surface QDs. AFM is a contact measurement where the tip attached to a cantilever is scanned across the sample surface by a transducer in x and y. The deflection

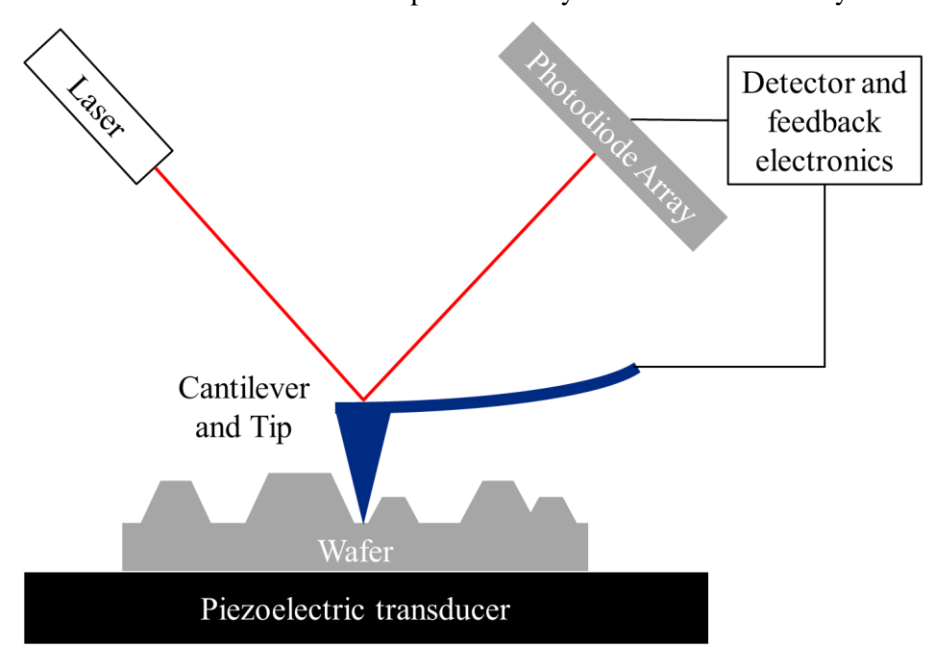


Figure 32 Representative diagram of AFM system.

of the cantilever in z as it encounters surface features is measured by the changing deflection of a laser focused above the tip. The force applied is also recorded through a piezoelectric transducer which can be located in the cantilever and or in the sample stage. The minimum resolvable feature is limited by the tip diameter and scanning speed. This can lead to vertical changes in morphology being recorded as a graded change depending on the angle of the tip and the speed of the scan. The broader the diameter of the tip the larger the area over which this averaging occurs. It is also not possible to measure overhanging features in AFM due to the top-down geometry of the tip. This can lead to inaccurate measurement of surface topology with a smoother surface recorded and small features missed. Figure 32 shows a representative diagram of an AFM system. AFM data presented within this study was kindly provided by Prof Mark Hopkinson due to a lack of AFM availability to the bismide research group.

The data provided was processed using the Gwydion software to level the background. This allowed for particle analysis by applying a thresholding height above the substrate. Typically, this threshold height was set to between 0.8 to 1.5 nm depending on the sample and typical size of the QDs. The particle analysis was conducted using a MATLAB code written by N. Bailey which allowed for checking of each separately detected particle from the thresholding. In the event multiple QD are incorrectly counter as 1 the particle can be manually split in the software. Every particle counted as part of this study was visually checked. This allowed for the extraction of topological information about each particle including height, area diameter and QD density. Droplets below 1 nm in height and agglomerates above 30 nm in height were disregarded from the fitting.

The extracted AFM results for particle properties of height and aspect ratio were fitted using a gaussian function to each population of QDs seen fit by the data. This allowed for extraction of number of QD populations and changes in QD distributions to be extracted from the AFM particle analysis. Most commonly this was a dual gaussian function which is shown in equation (13). The fitting parameters for the first gaussian are a, b and c which fit to the first population of QDs. Where a is the height of the curves peak, b is the position of the centre of the peak and c is the standard deviation of the distribution. The second gaussian uses m, l and p to fit to the second population which function identically for fitting to a, b and c respectively. Additional gaussians can be added if the data necessitates.

$$y = ae^{-\frac{(x-b)^2}{2c^2}} + me^{-\frac{(x-l)^2}{2p^2}}$$
(13)

## 3.5.3 Transmission Electron Microscopy

Transmission electron microscopy (TEM) is a non-contact non-destructive analytical technique in which a beam of electrons is transmitted through an ultrathin sample. Unlike previous microscopy techniques used within this thesis the sample must be prepared for TEM analysis. This was done using a focused ion beam to mill out a small section suitable for TEM analysis with a thickness below 100 nm.

The key advantage of this technique is the greatly increased resolution achievable owing to the reduce de Broglie wavelength of electrons comparatively to photons. This allows for resolution of individual atoms within a sample. In the case of this study samples were prepared to allow for the imaging of a cross section of the grown epilayers.

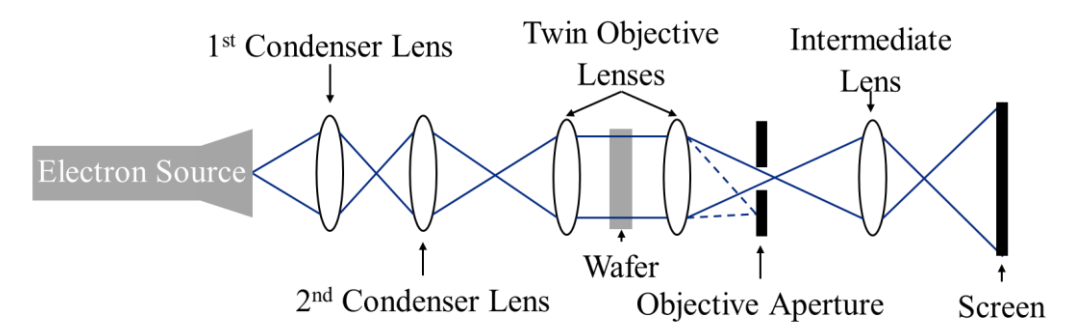


Figure 33 Diagram of TEM system.

The TEM analysis contained within this study was conducted by collaborators at the university of Cadiz. This was a part of a parallel TEM investigation in the materials grown as part of this project. Figure 33 show a representative diagram of components within a typical TEM setup. Conducted under UHV conditions an electron beam is focused by a series of lenses onto the prepared sample. The lens allows for adjustment of the beam focusing and position to image multiple areas of the wafer or multiple samples mounted on a single TEM grid. The transmitted electrons as shown by the solid blue lines. Once transmitted through the objective aperture the beam is focused by a final lens onto a screen or camera. A portion of the electron beam will interact and scatter as it transients through the sample these forward scattered electrons are blocked from the final image by the objective aperture. There are multiple configurations and imaging modes available in TEM analysis and multiple ways for contrast to be produced. This includes sensitivity to thickness, atomic number, crystal structure and crystal orientation. This is by no means exhaustive in the analysis modes possible. However, within this study the TEM is primarily used to assess the interface quality between the Bi containing epilayers. More in depth analysis will be reported in the parallel project run by Dr D. R. Reyes.

# 3.6 Ion Beam Analysis

Ion beam analysis contained within this study was conducted and the UK National Ion Beam Facility (UKNIBF) at the University of Surrey. Two techniques were employed to analyses the AlGaAsBi series Rutherford backscattering spectrometry (RBS) and time of flight elastic recoil detection (ToF ERD). All ion beam analysis is conducted in an UHV environment.

#### 3.6.1 RBS

RBS is a non-destructive technique using high energy ions typically alpha nuclei <sup>4</sup>He<sup>2+</sup> to probe the bulk crystallographic properties of materials. Figure 34A shows a diagram of a typical RBS measurement

setup. The incident ion beam, in the case <sup>4</sup>He<sup>+</sup> ion at 2.5 MeV, is targeted at the sample in either a randomly aligned orientation or channelling alignment. Channelling alignments are dependent on the crystal structure. However, the aligned orientation, can be thought of as any orientation that satisfied the condition that when looking down a crystal only the top unit cell of the structure can be seen with all subsequent atoms below shadowed by those above. There are multiple angles possible for the zinc blend structure of GaAs with the [100] geometry used for aligned scans shown later in this thesis. Random alignment is the antithesis of this case. In both cases as the ions transit through the material they have the potential to scatter from interactions with atoms within the sample. These can be inelastic from collision events between the ions and atoms of the host lattice or an electric scattering event. The elastic events involve the transfer of momentum between atoms of the host lattice and the ion as the direction of the ion is changed by attraction to host atoms. Depending on; the angle of incidence of the ion beam, the atomic number of the atom and the direction. The energy transferred during the scattering event can range significantly. However, by fixing the incident angle and scattering angle for detection, the energy of the ions scattering in a given direction provides valuable information about the host lattice. Generally, the larger the atoms for scattering the smaller the transfer of moment from the ion to the host lattice and the higher the energy of the back scattered ion. This is further dependent on the depth of the scattering within the material with deeper scattering event losing more energy as the ion transits back through the lattice. There is also the potentially for an ion to undergo multiple scattering events.

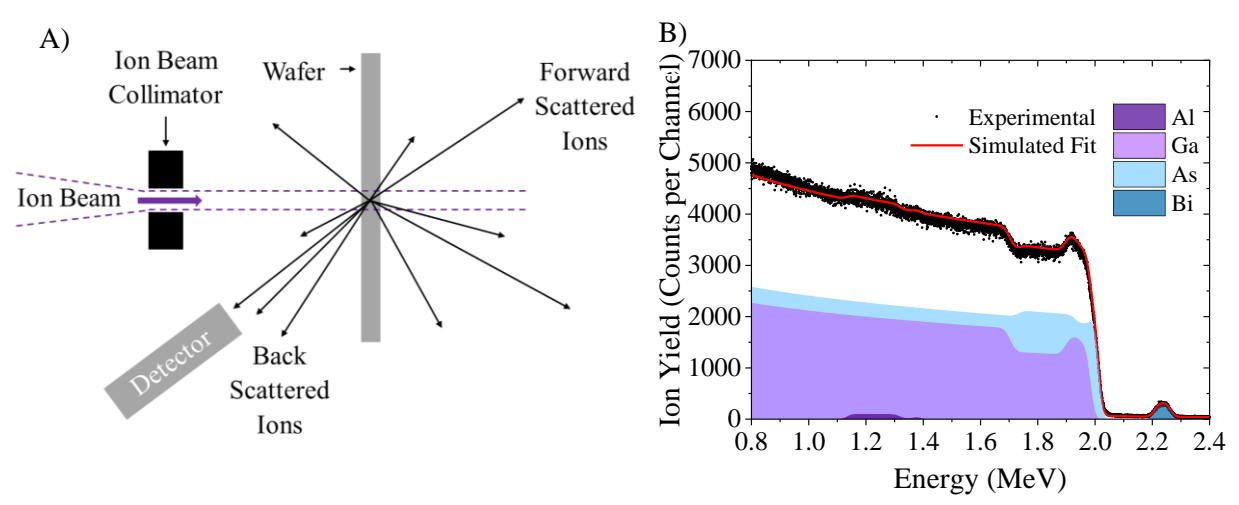


Figure 34 A)Diagram of ion beam system setup for RBS measurements and B) an example RBS measurement result for AlGaAsBi containing structure.

This produces an energy spectrum for a fixed scattering angle, an example of which is shown in Figure 34B. This is then fixed with a simulated back scattering based on the predicted sample structure with an iterative process to align the simulated to the experimental. The RBS data within this study was fitting using the software SIMNRA for both aligned and random scans. The basic experimental setup of the ion beam for RBS measurement is shown in Figure 34.

#### **3.6.2 ToF-EDR**

Time of flight elastic recoil detection (ToF ERD) is a partially destructive analytical technique for composition analysis of a sample as a function of depth. The incident ion beam of 16 MeV <sup>127</sup>I<sup>8+</sup> collides with the sample at a glancing angle knocking atoms out of the lattice. These forward recoiled atoms then pass through 2 sequential timing foils followed by a gas ionisation chamber where the energy of the ionised atom is measured. This produces a 2D heat map of energy against flight time with a count for each point. The fixed energy of the ions used to knock each element off its lattice site, results in the velocity of the forward recoiled atom being a function of the atomic mass and originating depth. Heavier elements take longer to transient through the timing foils than light element originating from the same depth within the sample, due to equal kinetic energy assuming an identical originating depth. This produces traces which curve down in energy with increasing originating depth, referred to as banana curves. Further separated in energy by the relative difference in atomic mass of each element species. The count rates for each point then correspond to the relative quantity of elements present within the sample. This can be seen in the example ToF ERD measurement of an AlGaAsBi sample is shown in Figure 35. The separation of Ga and As is only possible closer to the sample surface where the forward recoiled atoms have higher energy. This is due to the similar atomic masses of Ga and As at 69.73 and 74.92 AMU respectively.

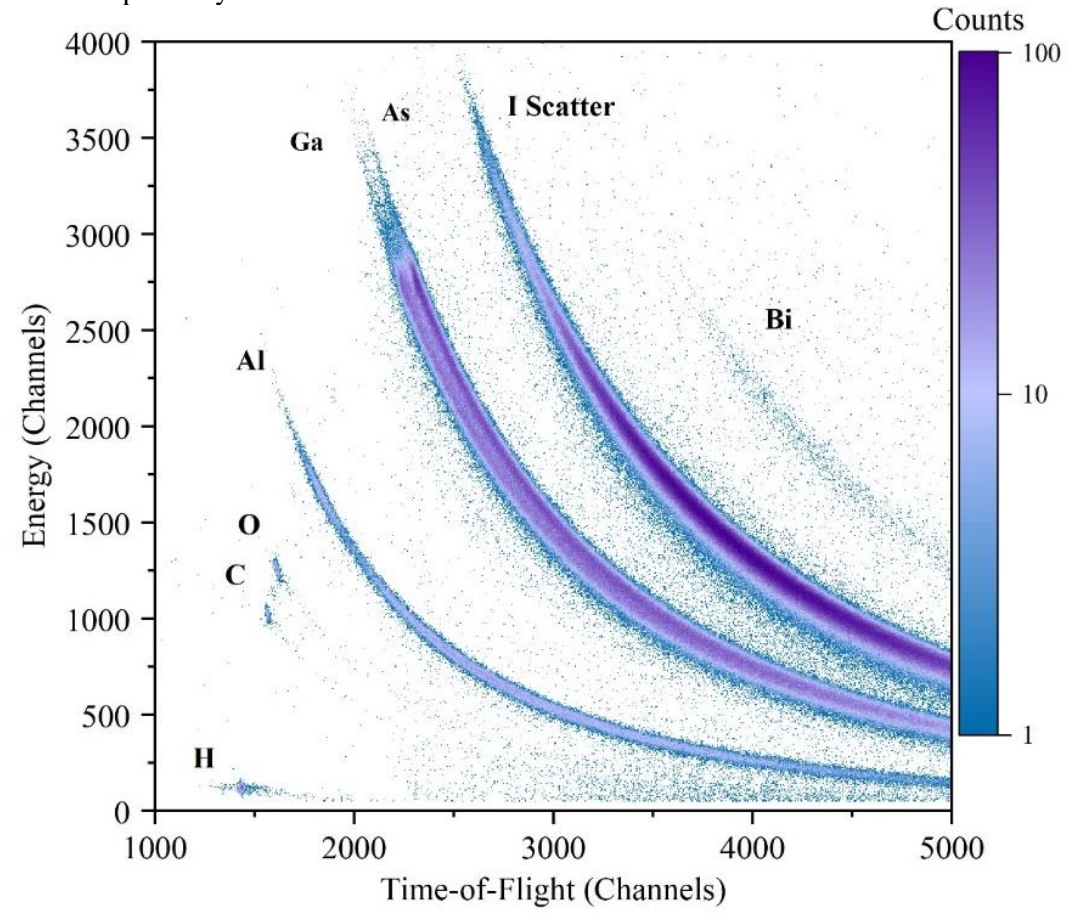


Figure 35 Ion beam analysis of STM83 5 at% AlGaAsBi sample TOF ERD Histogram

McERD. The later allowing for simulation of the predicted layer structure using the software potku and MCERD. The later allowing for simulation of multiple scattering events. The process is then an iterative adjustment the composition and layer thickness of the model to achieve a fit to the experimental data. This allows for extraction of elemental contents and conversion to a depth profile for of the detected elements. Elements with a mass exceeding the incident ions are harder to detect, due to the reduced velocity post collision between ion and atom. This accounts for the substantially reduced Bi count rate in comparison to the other elements. ToF ERD is however ideally suited for determination of lighter element contents within materials, in the case of the AlGaAsBi the Al content is of particular interest. The loss of energy due to depth places a fundamental limit on the maximum thickness that can be measured this is ~ 200 nm. The structure of samples measured with this body of work were designed to account this limit, as described in more detail in growth methodologies in sections 5.1 and 6.1. A diagram of the experimental setup for ToF ERD analysis by ion beam is shown in Figure 36.

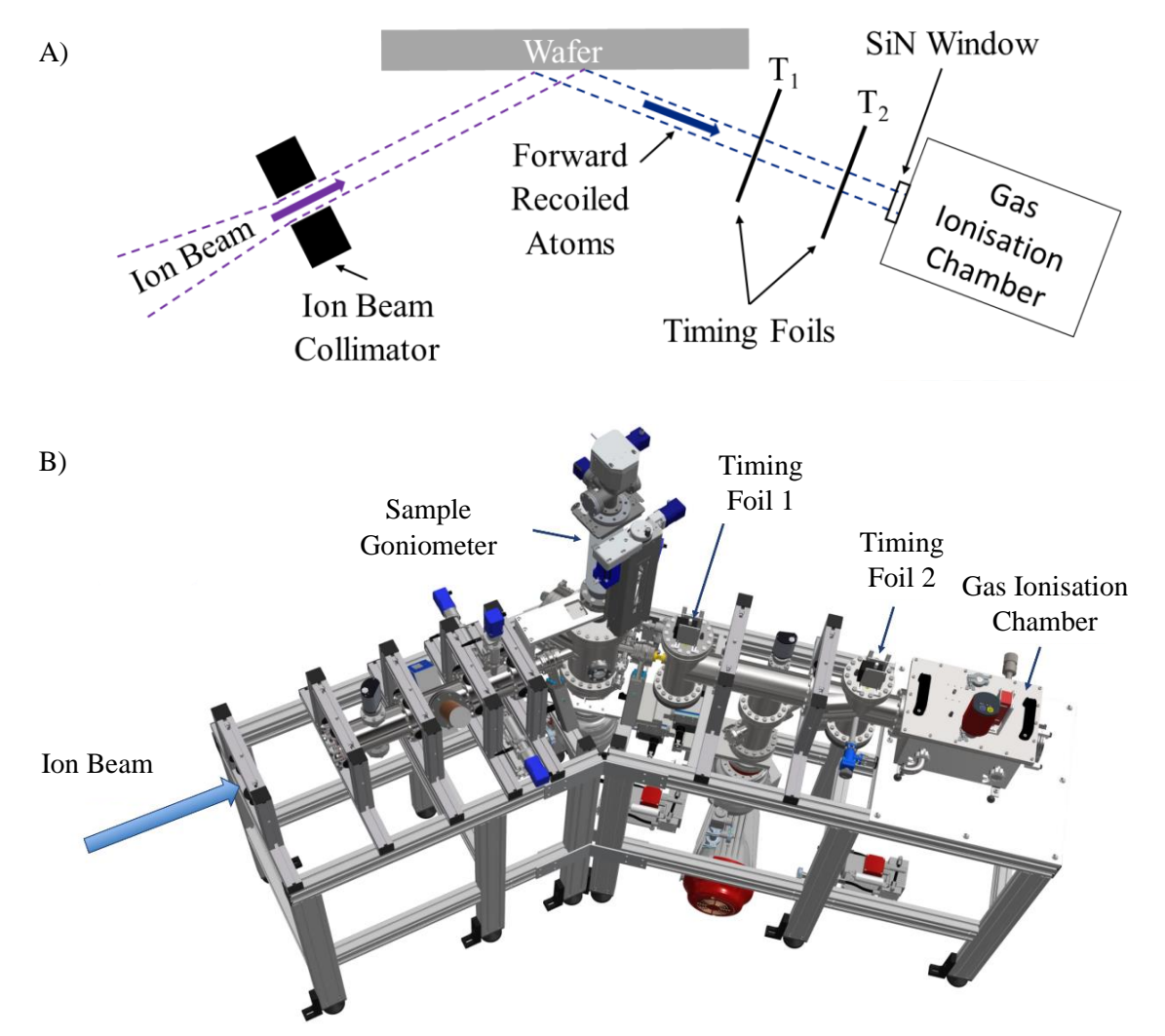


Figure 36 A) diagram of ion beam setup for ToF ERD measurements B) 3D model of the ToF ERD system utilised for measurement.

# 4. Bi Surfactant Alteration of Self Assembled InAs QDs on 001 GaAs Substrates

There has been prevalent interest in QDs since their initial proposal in 1982 by Yasuhiko Arakawa and Hiroyuki Sakaki [21]. The unique 3-dimensional quantum confinement achieved within these structures has attracted large research attention owing to a unique combination of properties and tunability available. Especially for optoelectronics where great efforts have been spent to optimise morphology and density for a variety of optoelectronic applications. Self-assembled InAs QDs on GaAs are of particular interest owing in part to their emission in the near and mid infra-red. This enables their emission to be tuned to align with the O and C band attenuation minimum in modern fibre optic cables. This is significant as these form the backbone of the 21<sup>st</sup> century telecommunications networks into which this device must integrate in order to achieve widespread adoption. This in culmination with compatibility to integration III-V substrates for epitaxial deposition process has opened the door to engineering of quantum structure for optoelectronic devices

Of particular interest is their possibility of using SK grown InAs QDs as single photon sources. The emerging fields of quantum cryptography and linear optic quantum computation. Where photons are used in place of electrons as the information carriers for the logic [83]. This is not a direct analogy with the underpinning logic of quantum computing not a direct translation from the classical. However, it is a novel approach uniquely suited to certain types of problems found in our world. This includes factoring large integer numbers, which form the backbone of modern encryption techniques. Presently their is no efficient solution to this on a classic computational system [84]. In addition to the ability of a quantum computer to more efficiently search through an unordered database with increased speed compared to the classical equivalent [85]. Linear optic quantum computation takes this a step further, by performing the quantum computations on optical qubits. This optical integration would enable a massive advantage in modular design and integration of quantum computing to wafer scales.

However, the continuing challenge in the development of these fields is the efficient generation of single photos. Without a reliable single photon source, these fields remain inaccessible and unviable to scale up to the levels required to greatly realise their benefits. QDs other a viable solution for reliable single photon generation. The demonstrated mechanism relies on the biexciton decay to the crystal ground state under specific excitation conditions confirmed theoretically and in practical studies [86][87]. Outlining the mechanism in further detail, the starting conditions required are a biexciton state where two electron hole pairs of equal energy and opposite spin coexist,  $\pm 0.5$  are generated. The hole spins are dictated by the HH valance band states and exist at  $\pm 1.5$ . Therefore, the polarisation of the emitted photon is dependent on the recombining electron-hole pair. This provides only two routes for optical emission with photon polarisation of  $\pm 1$ . Once a photon has been emitted by either pathway then the

second exciton pair can also decay. Ei, the two pathways will result in the emission of a single photon followed by a second decay and emission of a second oppositely polarised photon. Ie a photon of 1 then -1 polarisation or -1 then 1. But most crucially the mechanism does not allow for concurrent emission of two photons thus creating a reliable single photon source. Thus, by controlling the creation of the biexcitation state you can generate and regulate a predictable single photon source.

In order to achieve the required properties for engineering this state and emission wavelength of the QD growth be optimised and studied. The requirements for this application are a highly uniform QD population with similar morphology and composition. The exact parameters would be determined by the desired emission wavelength for the optical circuit. This would most likely fall within the O and C band to enable the integration of different optical components by current fibre optical cables. This work explores a potential route in which the morphological properties of self-assembled InAs QD on GaAs can be controlled. The key QD properties of size, density, aspect ratio and optical emission were investigated to study the impact of each parameter. This is further outlined in the InAs QD growth section 2.2.1. These include InAs deposition rates, thicknesses, growth temperatures, surfactants, capping conditions and substrate materials. SK growth was chosen for this study for 2 main reasons. Firstly, it would be expected the application of Bi as a surfactant would be more impactful on the strain dependent growth regime. Secondly, the strain induced morphology of the InAs QDs without additional tuning on GaAs is a desirable starting point when trying to redshift the QD emission to align with the 0.954 and 0.8 eV O and C band optical fibre attenuation minima.

The study presented within this body of work investigates the effect of Bi as a surfactant species on InAs SK QD growth on GaAs. Isolating the impact and limits of a Bi as a surfactant within the growth parameter space. In order to aid with placing the context of this work within the wider body of literature. The initial optimisations of InAs deposition thickness and QD growth temperature are also reported to underpin the basic framework of parameter space under investigation. This chapter was a photoluminescence directed study prioritising the decrease of emission energy targeting emission within the O or C band. Samples were analysed by photoluminescence at temperatures between 20 to 297 K with optical carriers injected by a 532 nm laser at optical powers between 0.1 mW to 1 W. Morphological analysis of the surface layers was conducted by AFM.

# 4.1. Growth Methodology

The sample architecture for all QD samples in this chapter is shown in Figure 38. Standard calibration techniques outlined in the MBE experimental section were used for determinations of substrate temperatures and fluxes. InAs growth rate was measured by recording the time to observe QD formation on the RHEED system. This transition occurred after the completion of the wetting layer and was assumed to be visible on the RHEED system after 1.6 ML of InAs deposition. Where each atomic monolayer is half of a zinc blende unit cell crystal, making the thickness equivalent to half the lattice

constant, 6.0583 Å. The growth rate was then determined by dividing the measured time to onset by 1.6 ML. Images of the RHEED at each stage of QD formation are shown in Figure 37. All sample within this chapter were grown on the Omicron MBE system described in section 3.1.1. Sample growth occurred over the span of 2 weeks, with temperatures calibrations conducted prior and post the series

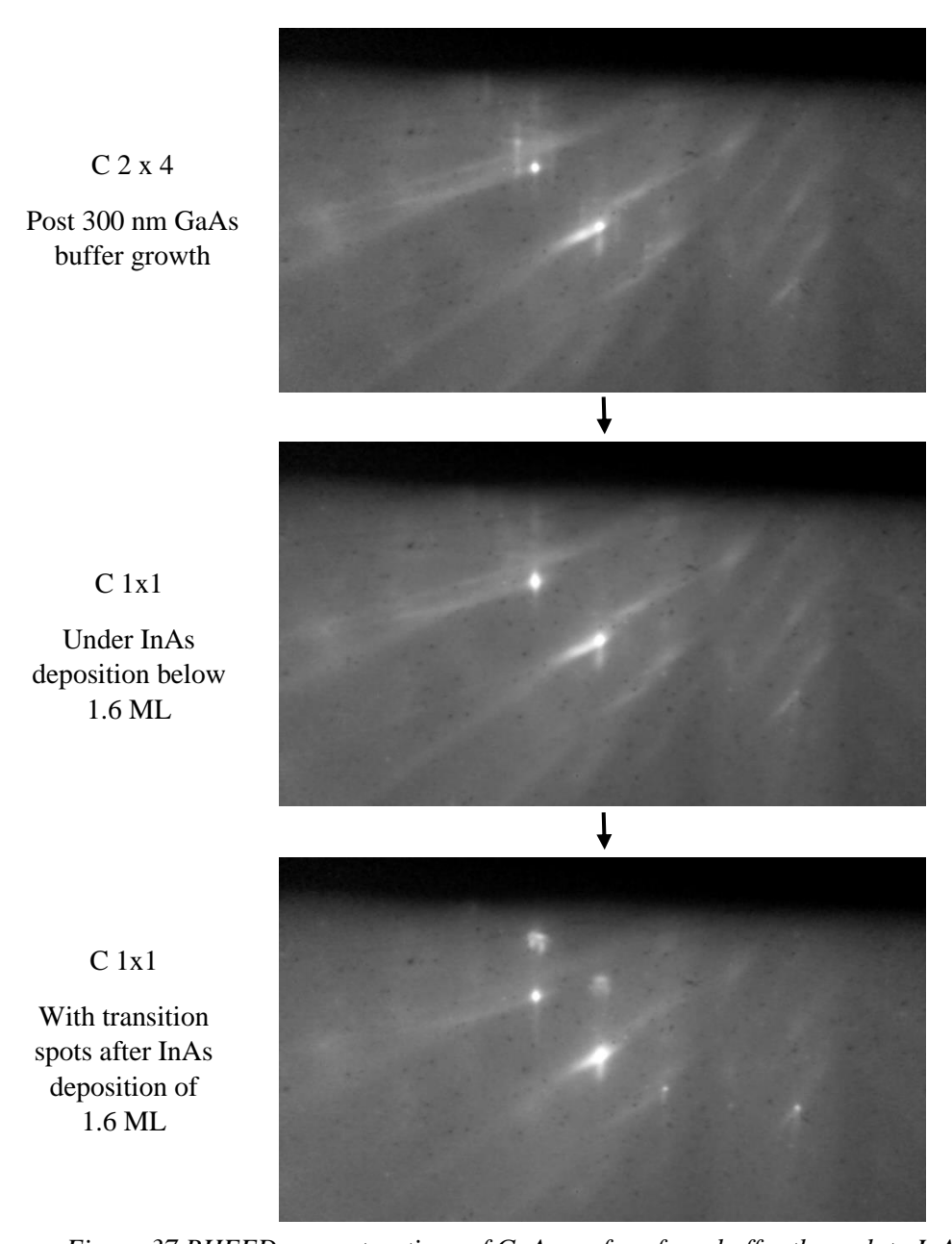


Figure 37 RHEED reconstructions of GaAs surface from buffer through to InAs QD formation.

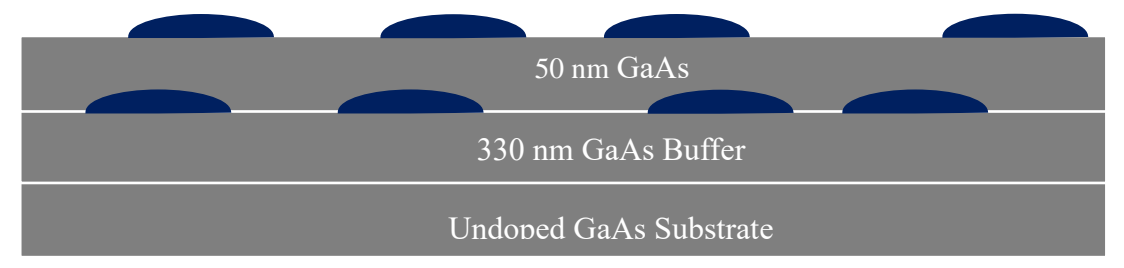


Figure 38 QD cross sectional sample structure with InAs QDs shown in blue.

completion. Calibration of growth rates and fluxes were conducted at the start of each week and drift accounted for in effusion cell temperatures as required.

Cleaved 11.8 x 11.4 mm undoped GaAs substrates were out gassed at 380 °C for 20 minutes followed by the removal of the native oxide at 620 °C under an As<sub>2</sub> flux for 40 minutes. The GaAs buffer was then grown at 570 °C at a rate of 0.3 MLs<sup>-1</sup> to a thickness of 330 nm. The Ga:As<sub>2</sub> flux ratio was 1:1.7. An allowance of 20 minutes was given following buffer growth to stabilise the surface and lower the temperature for QD growth. Temperatures between 450 to 510 °C were used within this study. This time was also used to adjust the As cracker temperature from 1000 °C to 650 °C changing the As species to As<sub>4</sub>. The C 4x4 reconstruction was stabilised during this time and is shown in Figure 37 prior to QD deposition. The QD growth rate was fixed at 0.01 MLs<sup>-1</sup> for 270 s with a concurrent Bi flux applied at levels between 0 to 3.5 nA. The In:As<sub>4</sub> flux ratio was 1:36 during QD growth. Post growth of the QD layer was followed by a 30 s anneal at the growth temperature then a 60s quench in which heater power was cut and final a 30 s rise to the QD growth temperature. This was conducted under a constant As<sub>4</sub> flux equal to that used during the QD growth. The GaAs capping was applied immediately following 30 s rise to the QD growth temperature. This was conducted at the QD growth temperature at a rate of 0.3 MLs<sup>-1</sup> to a thickness of 50 nm with a Ga:As<sub>4</sub> flux ratio of 1:2.4. 20 minutes was again allowed for flux equilibrium prior to deposition of the top QD layer. This was deposited under identical conditions to the buried QDs. Following the top QD layer a 30 s of anneal was applied at the QD growth temperature and a subsequent 60s quench then termination of the As<sub>4</sub> supply. The complete growth procedure is shown graphically in Figure 39.

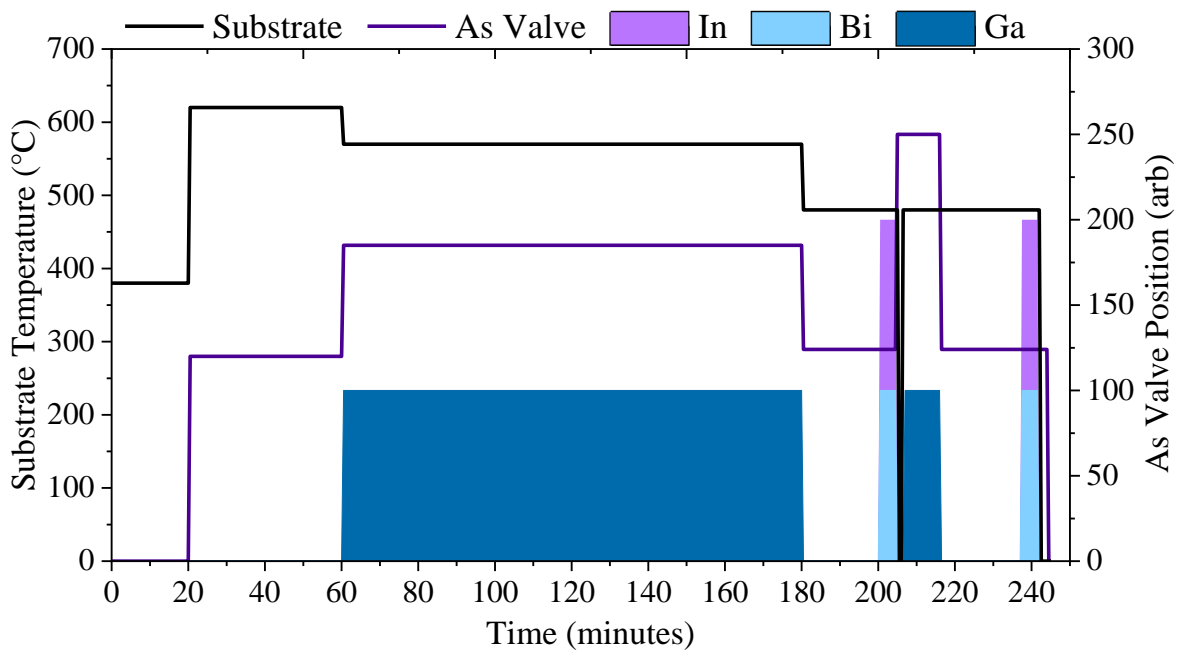


Figure 39 QD growth procedure with substrate temperature and incident flux profiles for Bi flux contain growth. Open cell shutters are represented as solid colour bars on the plot.

## 4.2 QD Thickness Series

To establish the underlying parameter space prior to conducting the Bi surfactant study the InAs deposition thickness was first optimisation. This is a key growth parameter in self-assembled InAs QD growth. The deposition controls the available quantity of material for self-assembled QD formation altering the final QD morphologies. QD Growth followed the experimental procedure are sample architecture outlined in section 4.1. InAs deposition was conducted at 510 °C with the deposition thickness varied between 2.2 - 3.1 ML across 5 samples at a constant growth rate of 0.01 MLs<sup>-1</sup>. These were then subsequently analysed using PL and AFM to determine the optimal thickness to carry forward within this study. The samples of the series are shown in Table 2 and are labelled chronologically. Samples were grown in a random order to mitigate the potential effects of drift.

Sample ID	QD Thickness (ML)
STL91	2.2
STL96	2.5
STL95	2.7
STL92	2.9
STL94	3.1

Table 2 QD InAs deposition thickness series sample list

#### 4.2.1 PL 20 K & 297 K

The photoluminescence spectra at room temperature show a close grouping of the ground state QD emission peaks. The variance in emission is 20 meV and 26 meV for measurements at 297 K and 20 K respectively, shown in Figure 42A. An emission energy minimum was seen in the centre of the series at InAs deposition thicknesses of 2.7 and 2.9 ML. The peak intensity at room temperature between these two samples is barely distinguishable. However, at 20 K a brighter luminescence from the 2.7 ML sample with clearer distinction between the 1st and 2nd excited states is observed. This is clearer at 20 K when comparing the integrated emission shown in Figure 42B. The 2.7 ML sample produces a markedly higher signal in comparison to the adjacent samples. This can also be seen in the FWHM data for the primary QD peak shown in Figure 40. This combined with the emission energy minima strongly suggests this is an optimal position in parameter space for InAs deposition thickness.

Decreasing the quantity of supplied InAs to the surface resulted in a minor blue shift of 10 meV for both 2.2 & 2.5 ML. With decreasing thicknesses, a reduction in the luminescence is also observed with a loss of approximately half the observed luminescence from 2.2 compared with 2.5 ML. The confinement within the peaks is also reduced in these samples with broader emission peaks at both

temperatures measured in Figure 41. This could be the result of a larger variance in QD sizes as more cross over in the emission energies between the ground state and 1<sup>st</sup> excited state is seen.

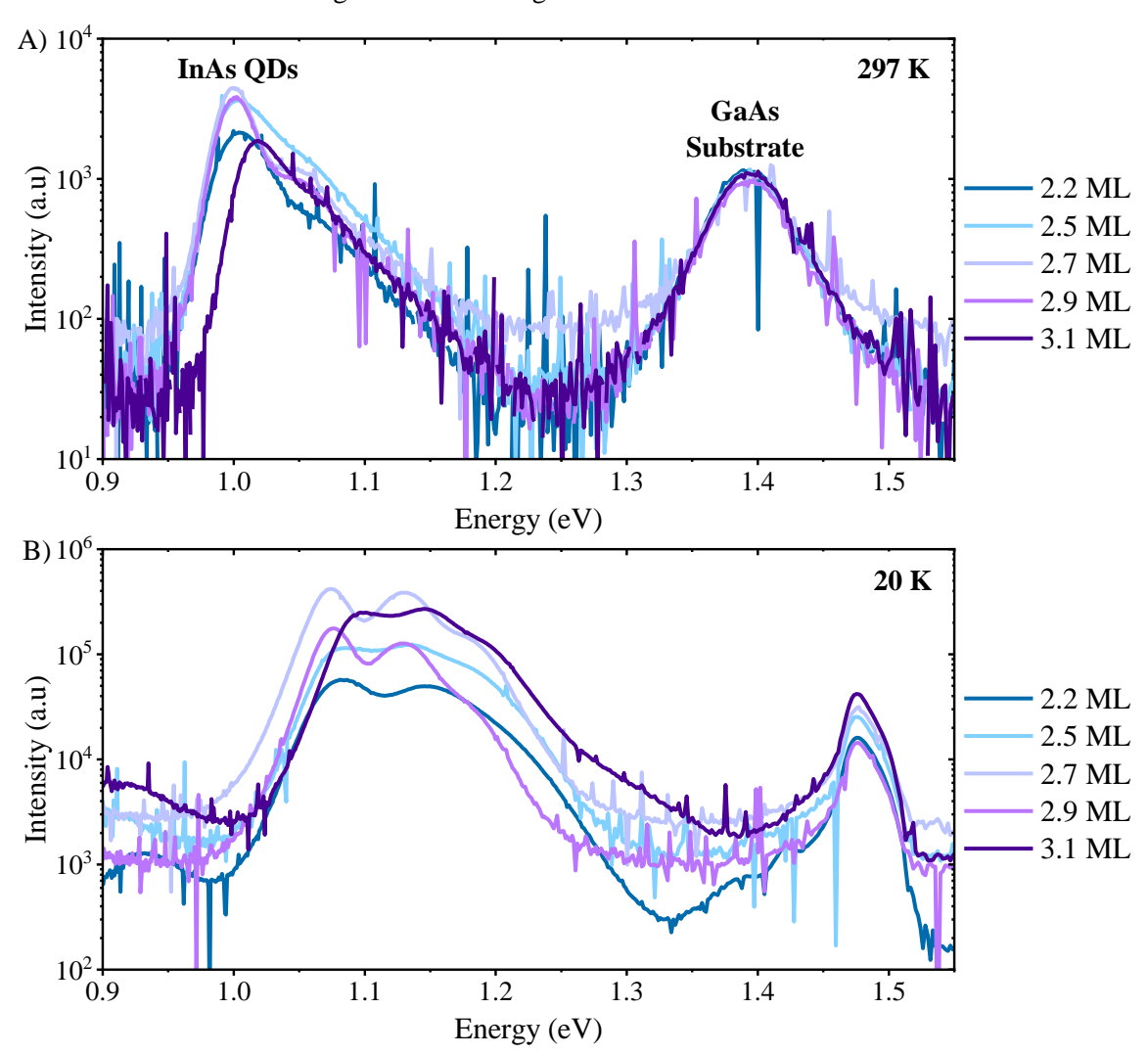


Figure 41 Photoluminescence emission spectra at 100 mW excitation for InAs QD samples with deposition thicknesses between 2.2 - 3.1 ML, measured at temperatures of A) 297 K and B) 20 K.

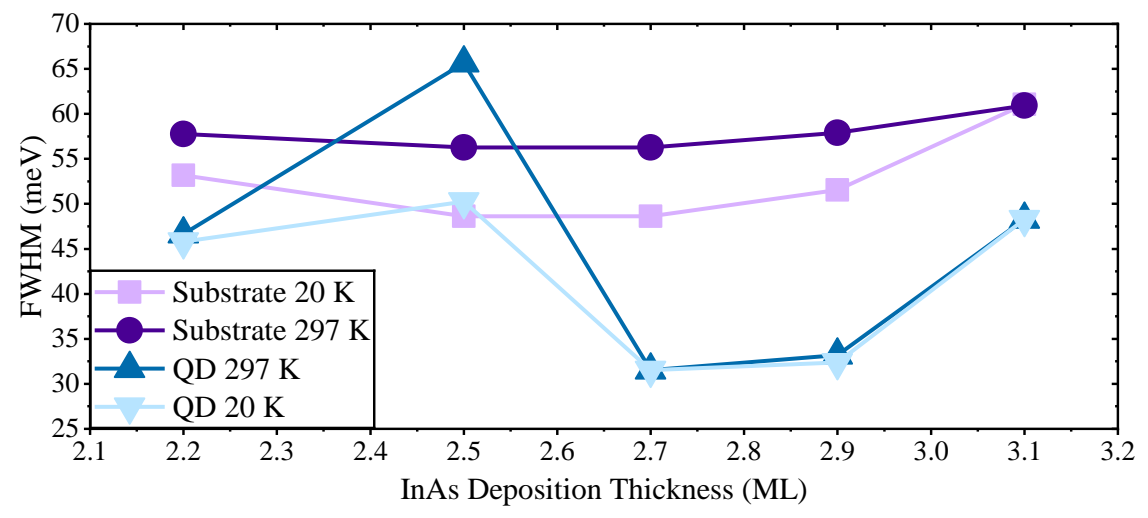


Figure 40 Full width half maximum of PL taken at 297 K and 20 K for InAs QD grown with deposition thicknesses between 2.2 to 3.1 ML.

Supplying InAs beyond a thickness of 2.9 ML to 3.1 ML yielded another significant blue shift of 20 meV. There is also evidence of reduced QD uniformity as the emission cross over between ground state and 1<sup>st</sup> excited state is increased. However unlike with lower thickness we do not see a significant penalty in reduced emission intensity. With the second highest emission of this series demonstrated at 3.1 ML of InAs deposition. There is evidence of and a positive correlation between layer thickness and luminescence, shown in Figure 42B. However, there is further scope for a reduced step size surrounding the 2.7 ML to access if this is an optimal optical growth quality window under the tested experimental conditions.

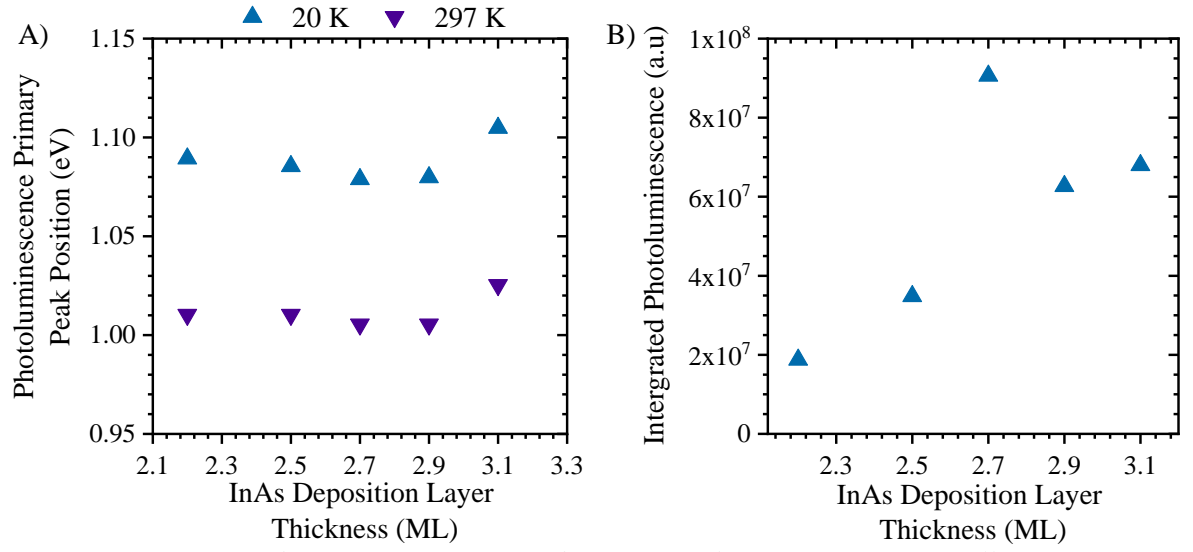


Figure 42 A) Integrated PL spectra at 20 K and 300 mW with integration across full emission spectra.

B) QD ground state peak position of PL emission spectra at 100 mW excitation.

## 4.2.2 AFM

The AFM images of the 5 samples in the QD deposition thickness series are shown in Figure 43. This provides an insight into the QD formation prior to growth of the capping layer with changing InAs deposition thicknesses. Analysis of the surface QDs shows a clear bimodal distribution of QD heights and aspect ratios in all samples within this series. This can be observed in Figure 45 where the peak values for the 2 populations are shown. The lowest thickness of InAs deposited 2.2 ML possessed a large proportion QDs with measure heights between 1 to 2 nm with a 2<sup>nd</sup> larger QD population centred around 7.7 nm with a standard deviation (SD) of 1.46. The larger QDs however dominate the contribution to the observed luminescence. This situation is improved by increased deposition to 2.5 ML of InAs. There remains a bimodal distribution but the coalescence of surface InAs into fully formed QDs is much more complete. There remains a small proportion of small but widely dispersed QDs with an average height of 7.3 nm and SD of 2.6. However, the bulk of the population is within a tighter distribution centred at 9 nm with a SD of 1.0. Further increases in deposition thickness increase the proportion of the taller QDs at the expense of marginally reduced average heights with 8.3 and 8.2 nm

for 2.7 and 2.9 ML of InAs deposition respectively. Both of these deposition thicknesses still retain a bimodal distribution with a second population of smaller QDs at 1.2 and 6.1 nm respectively. The loss of the 1 to 2 nm QDs is observed at deposition thicknesses above 2.9 ML. The highest tested deposition of 3.1 ML of InAs showed a regression in QD formation with dual populations of shorter QDs at 3.7 and 6.6nm. This could be caused by potential saturation of migration sites on the surface during QD formation, limiting the surface mobility of In and As. In two samples it was noted that formations of cluster far exceeding the QD size were observed. This was in the higher InAs deposition samples of 2.9 and 3.1 ML. These large clusters do not contribute to the PL however will of reduced the volume of material in the of remaining QDs on these sample as the clusters consumed the surface InAs.

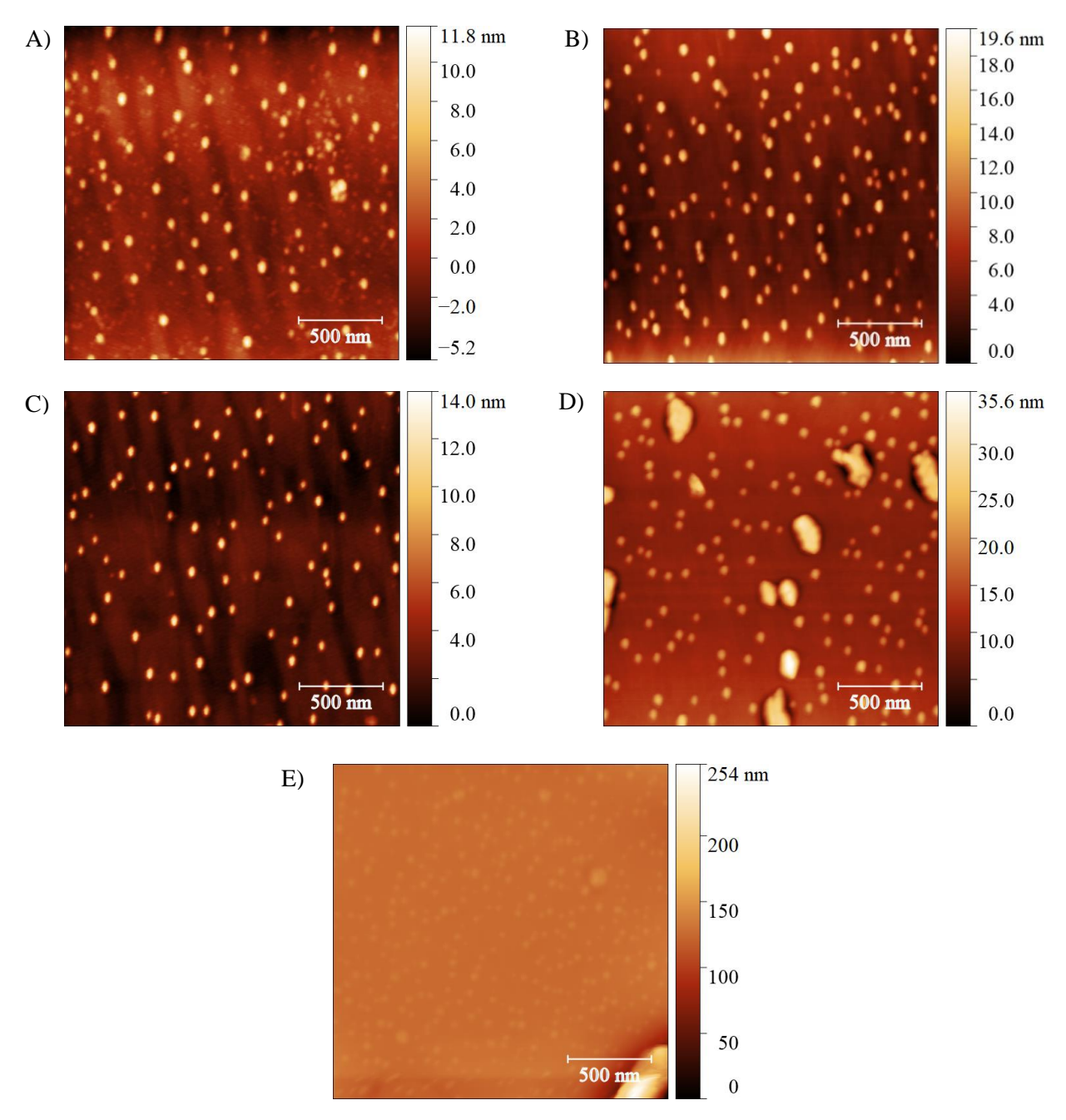


Figure 43 AFM images of InAs QDs grown with InAs deposition layer thicknesses between 2.2 to 3.1 ML. Where, A) 2.2 ML, B) 2.5 ML C) 2.7 ML D) 2.9 ML and E) 3.1 ML.

Observing the QD densities shown in Figure 44 it can be seen that for deposition past 2.9 ML the coalescence of QDs on the surface is hindered. There is a dramatic increase in the number of QDs with commensurate decrease in their size. From 2.2 to 2.9 ML a gradual decrease in the QD density is observed and corresponds to the increased average heights of the entire QD populations. Uncertainties in the QD densities are due to the random position of QD nucleation on the surface. The uncertainties were estimated based on the variance of QDs density in each quarter of the AFM images shown in Figure 43.

The aspect ratios follow a similar trend as previously described for the heights. The dual QD population were also observed in the aspect ratios, shown in Figure 47. The shorter QD population has a lower values aspect ratios across the full series. This trend follows the previously described relation for the heights with the exception at 2.9 ML of InAs deposition, which showed an unexpected high aspect ratio for the tallest population of QDs.

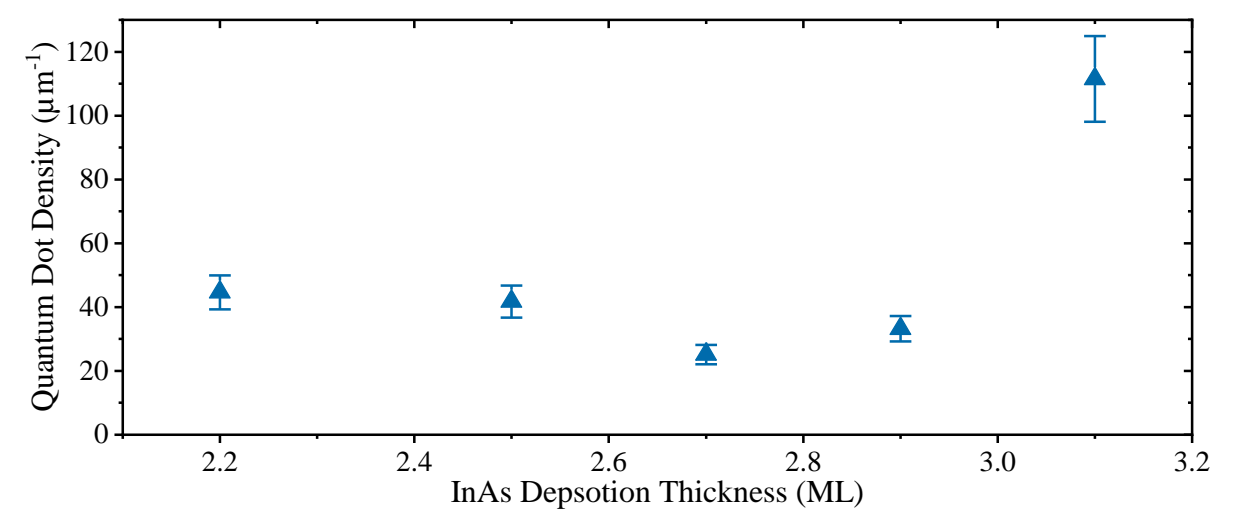


Figure 44 QD density against InAs deposition thicknesses between 2.2 to 3.1 ML.

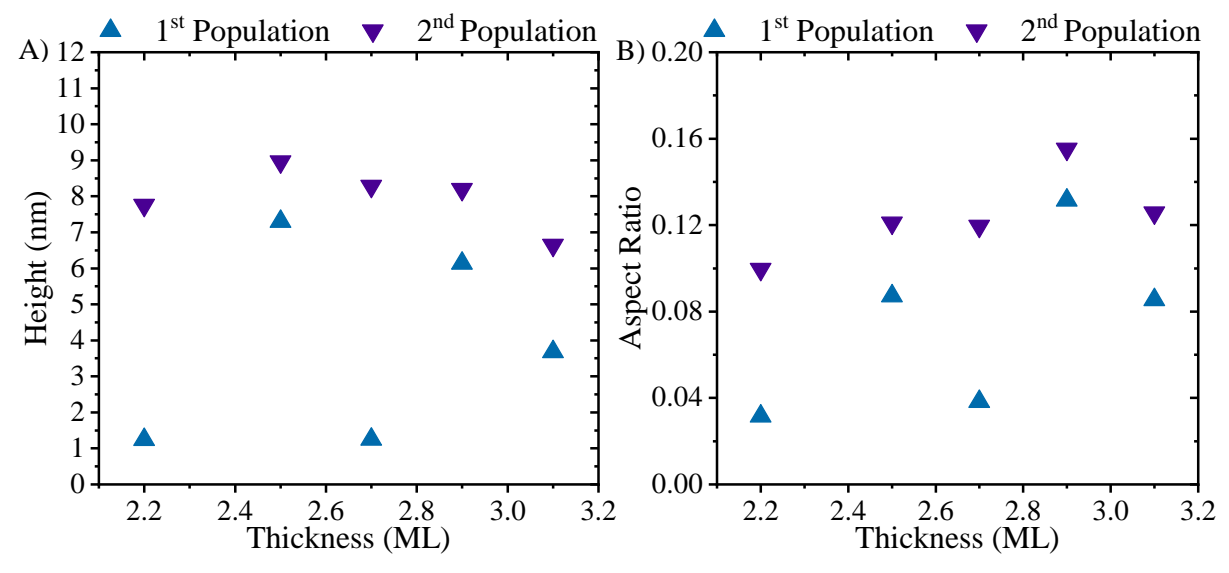


Figure 45 QD populations of height and aspect ratio for InAs QD samples with InAs deposition layer thicknesses between 2.2 to 3.1 ML. Where A) QD height and B) QD aspect ratio.

The centre of the thickness series again shows an inflection point, in this instance in the height and aspect ratio of QDs, shown in Figure 45A & B. The 3 centre samples 2.5, 2.7 & 2.9 have a bimodal distribution with primary population heights within a  $\pm$  0.5 nm variance. The difference between our 3 centre samples can be seen in the aspect ratio of the QDs, shown in Figure 45B. There are two case for comparison that can be drawn here. Firstly, is the same aspect ratio with a different QD height 2.5 v 2.7 ML. Secondly is the reverse the same height with a different aspect ratios, 2.7 v 2.9 ML with the most hemispherical shaped QDs observed at 2.9 ML across the entire series. Pushing beyond 2.9 ML a regression in overall QD size is observed with an equal bimodal distribution at 3.7and 6.6nm. Which corelates well to the observed blue shift in the PL emission and increased PL emission line width seen in Figure 41.

Contrasting the AFM of the centre samples with the PL results of the previous section, it is evident when optimised for longer wavelength emission a height and aspect ratio of 0.12 and 8.5 nm is best suited. This is seen in sample grown 2.7 ML of InAs deposition. However, in the second comparative instance the change in quantum confinement and associated bandgap shift is least affected by varying the aspect ratio of the QD. Deposition of 2.7 and 2.9 ML of InAs produced identical emission wavelengths at 1.0054 eV at 297 K, as seen in Figure 41A. Unexpectedly when contrasting 2.5 ML and 2.7 ML the increased QD heights of 2.5 ML sample correspond to a slight blue shift in emission of 4.9 meV at 297 K. This is the opposite of what would be anticipate as the reduced quantum confinement should cause a redshift. However, it may indicate a larger contribution to the PL from a close second population between 5 to 7 nm. This could also cause issue a with the least squared gaussian fitting due to the overlap between the populations that may misrepresent the true centre of both populations. It is also possible to attribute this blue shift to compositional differences which could also alter the bandgap of the QDs. Although isolation this from the changes in morphology requires further analysis. The AFM measurements presented have been taken on the uncapped surface QDs. Buried QDs will have been affected by the GaAs capping and overgrowth that may cause changes in morphology and composition. Analysis by cross sectional TEM and EDX could confirm these changes.

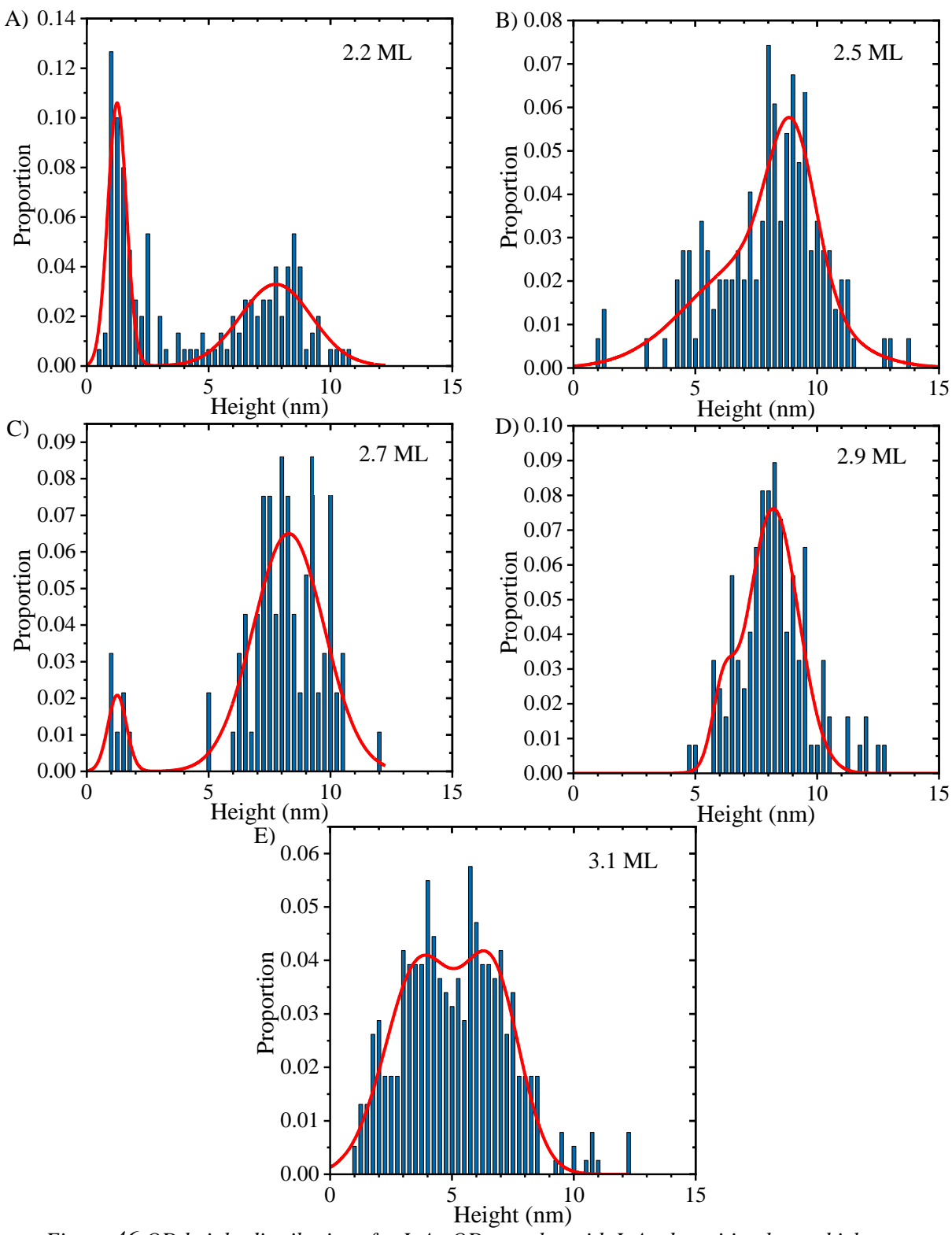


Figure 46 QD height distributions for InAs QD samples with InAs deposition layer thicknesses between 2.2 to 3.1 ML. Where, A) 2.2 ML, B) 2.5 ML C) 2.7 ML D) 2.9 ML and E) 3.1 ML.

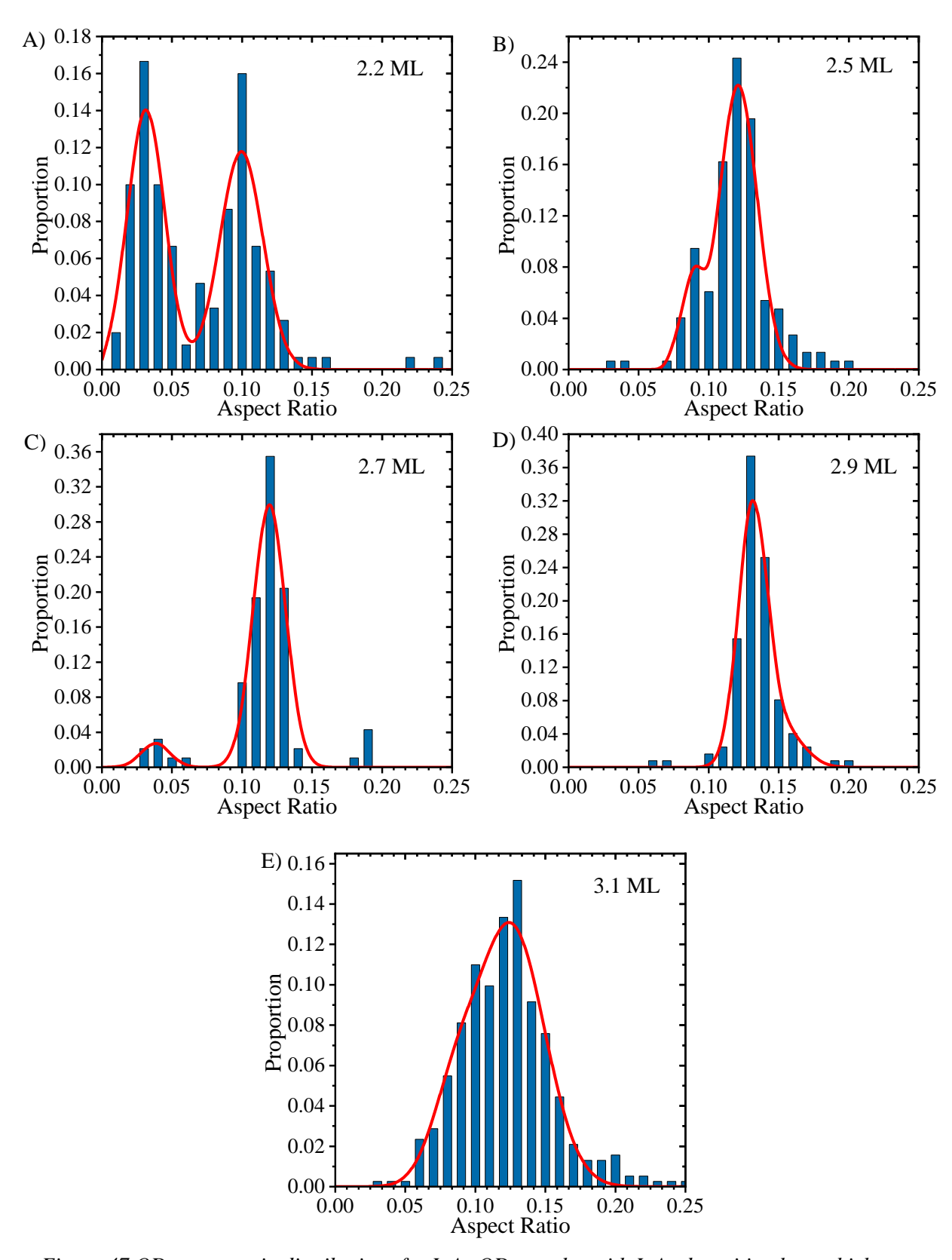


Figure 47 QD aspect ratio distributions for InAs QD samples with InAs deposition layer thicknesses between 2.2 to 3.1 ML. Where, A) 2.2 ML, B) 2.5 ML C) 2.7 ML D) 2.9 ML and E) 3.1 ML

# 4.2.3 Power Dependent PL

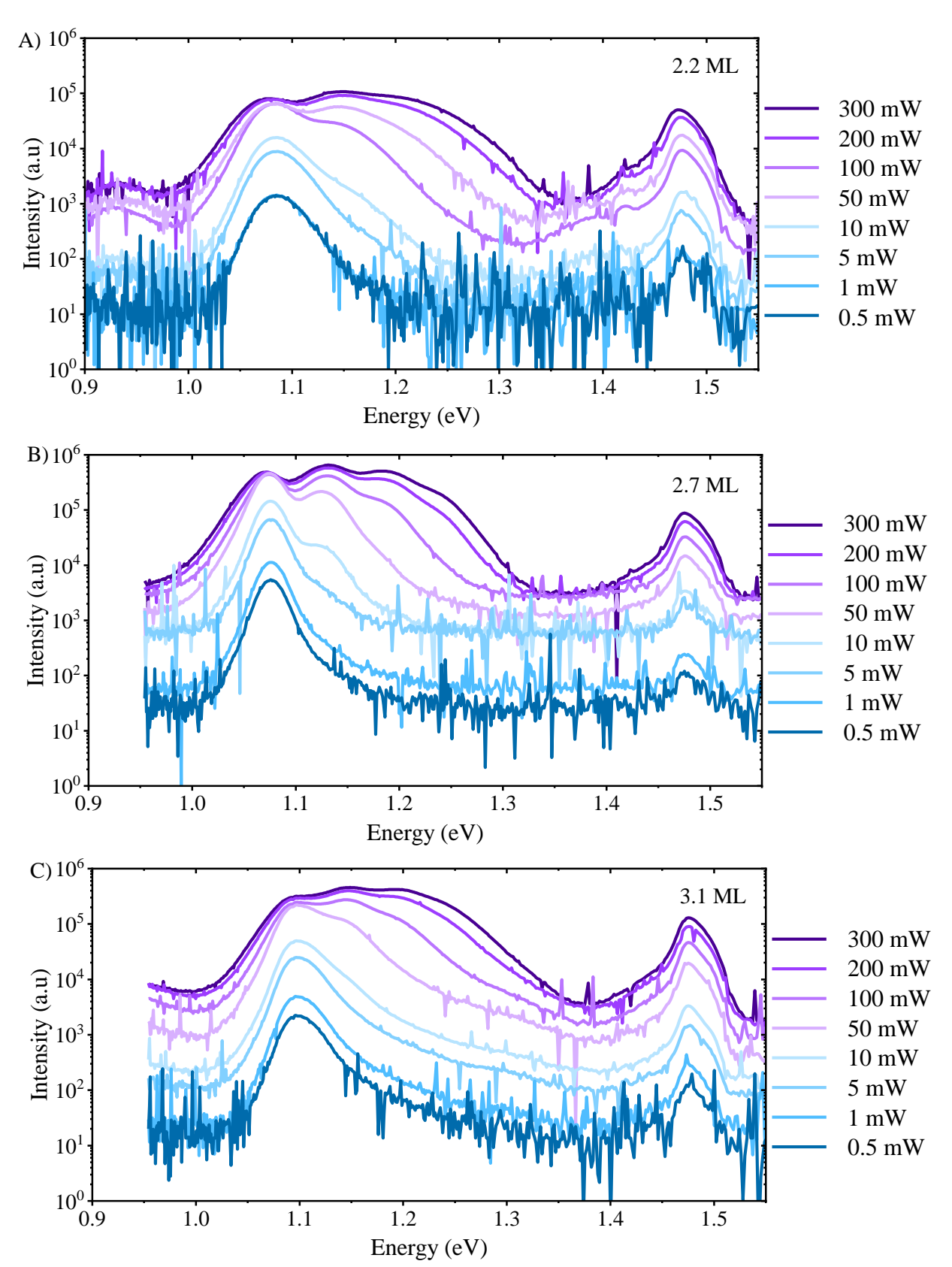


Figure 48 20 K PD PL of InAs QD on GaAs after A) 2.2. B) 2.7 and C) 3.1 ML of InAs deposition.

Representative PD PL measurements for the InAs deposition series are shown in Figure 48. These spectra, including for samples not shown, were integrated across the full range of emission energies measured. The integrated power dependent photoluminescence was then fitted with equation (11) as shown in Figure 51. The process is outlined in greater detail in section 3.4.1.

The values of the exponents extracted from the fitting are shown in Figure 49. Across the series the values all fall very close to 1 indicating a radiatively limited luminescence process in all samples. This corresponds to excitation limited luminescence, where if the excitation power is increased the luminesce increase will be directly proportional. Above 2.7 ML there is an observed slight increase in the measured exponent value. The slight increase with higher InAs deposition thicknesses could indicate there is a very minor contribution coming from non-radiative recombination pathways. This could be the result of increased carrier escape into the capping layer owing to the increasing populations of overlapping smaller QDs, seen in Figure 46C, D and E.

The raw PD PL for 2.2 and 2.7 ML of InAs deposition are shown in Figure 48A and B respectively. In both samples state filling with increased optical power is observed. However, the overlap between excited states is lower at 2.7 ML of InAs deposition. Asymmetry is seen in the GaAs peak at 1.48 eV in both samples, with a clear shoulder to the right of the GaAs peak at ~1.5 eV and left of the GaAs peak at 1.44 eV. However, the asymmetry to the left of the peak is dissimilar. There are additional peaks at 2.2 ML at 1.39 and 1.42 eV. The AFM for both these samples showed a bimodal distribution with both having populations centred around 0.5 to 1.5nm and 8 to 9nm. The additional peaks at 1.39 and 1.42 eV are likely attributed to the increased population of 1 to 2 nm QDs. The low level of emission would be indicative of a high concentration of non-radiative recombination within these QDs. Alternatively, it is also possibility that the majority of the small QDs do not survive the capping process

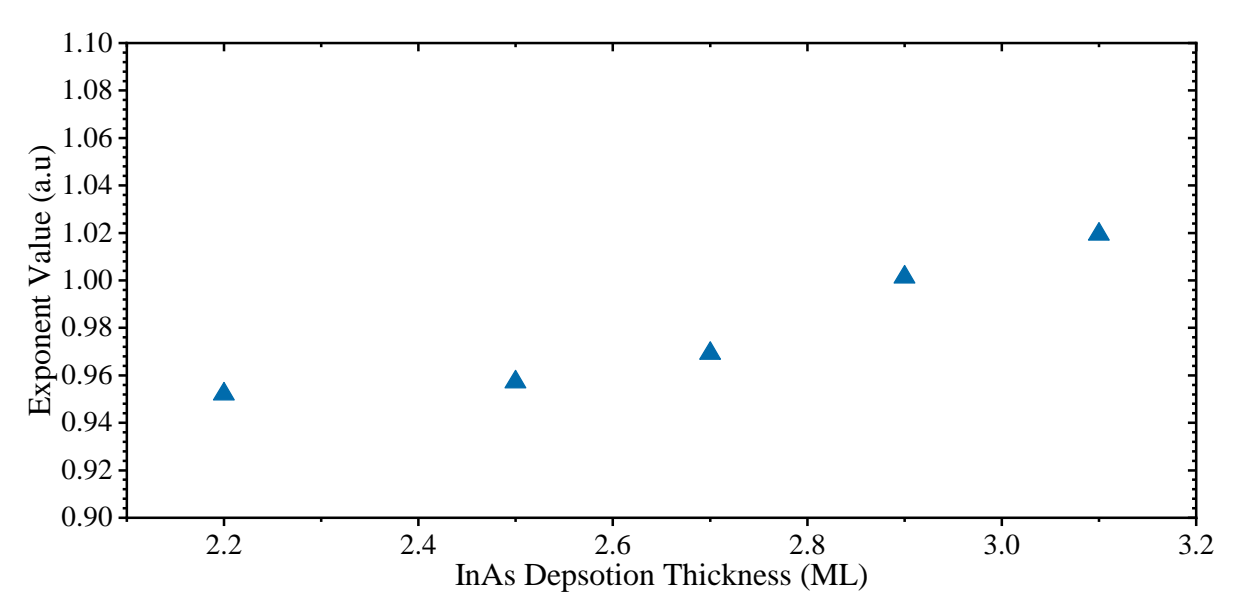


Figure 49 Power dependent exponents for InAs QD samples with InAs deposition layer thicknesses between 2.2 - 3.1 ML measured at 20 K.

and are destroyed. Observing the raw PD of 3.1 ML of InAs deposition there is no contribution to PL from the small population of 1 to 2 nm QDs as seen in 2.2 ML. This is another indicator they may not be surviving the capping process as they are present on the surface of both 2.7 and 3.1 ML samples. There is a broad distribution in the PL emission with overlapping excited states as with 2.2 ML sample. This would align well with the measured surface QD morphologies which had overlapping populations. The results of 2.2 ML and 3.1 ML indicate an upper and lower bound for the operating window in which to achieve tight QD uniformity and narrow PL linewidth. Based on the data the 2.7 ML deposition appears the optimal point to carry forward for this growth study.

Focusing on the position and spacing between the excited states (ES) shown in the PD PL spectra of Figure 48 and plotted in Figure 50A, provides a measure of the quantum confinement within the QDs. The relative spacing between and position of excited states are shown in Figure 50B. There is a gradual reduction in the energy separation between the excited states with increased InAs deposition thickness. This indicates the confinement is decreasing with increased deposition thickness. However, this trend does not align with increased energy of the ground states and corresponding excited states. These show a gradual increase with increased InAs deposition. The ground state positions correspond to the trend observed in the height of the surface QDs. This was a gradual decrease in height with increased InAs deposition thicknesses. Except for the 2.2 ML sample which had a lower QD height than the 2.5 ML sample. This increased ground state (GS) emission energy combined with reducing QD confinement would indicate a changing bandgap within the QDs This arising from intermixing between the Ga in the substrate and In in the QDs during growth. The impact of the intermixing is reduced at lower deposition thicknesses. As seen in the increased quantum confinement, based on higher energy gaps between the excited states at 2.2 ML. It is of note that the separation between PL emissions for the ground state and each subsequent excited state was clearest at 2.7 ML of InAs deposition.

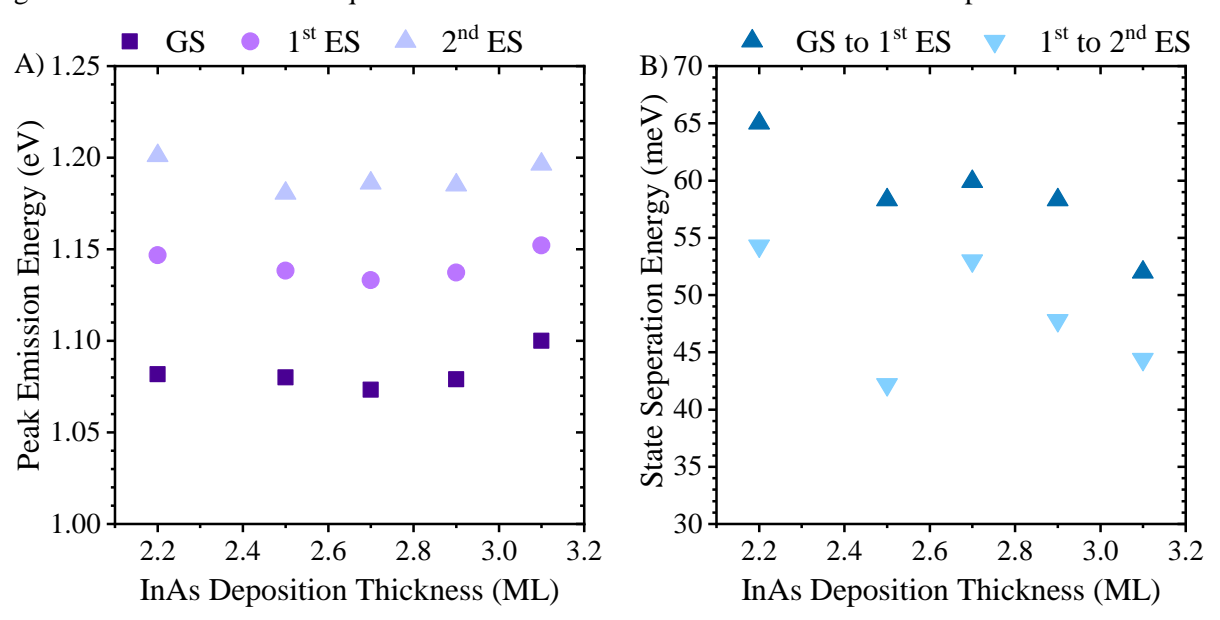


Figure 50 A) Peak emission energies of ground, 1<sup>st</sup> and 2<sup>nd</sup> excited states, B) energy separation between ground state (GS) and subsequent excited state (ES) emission.

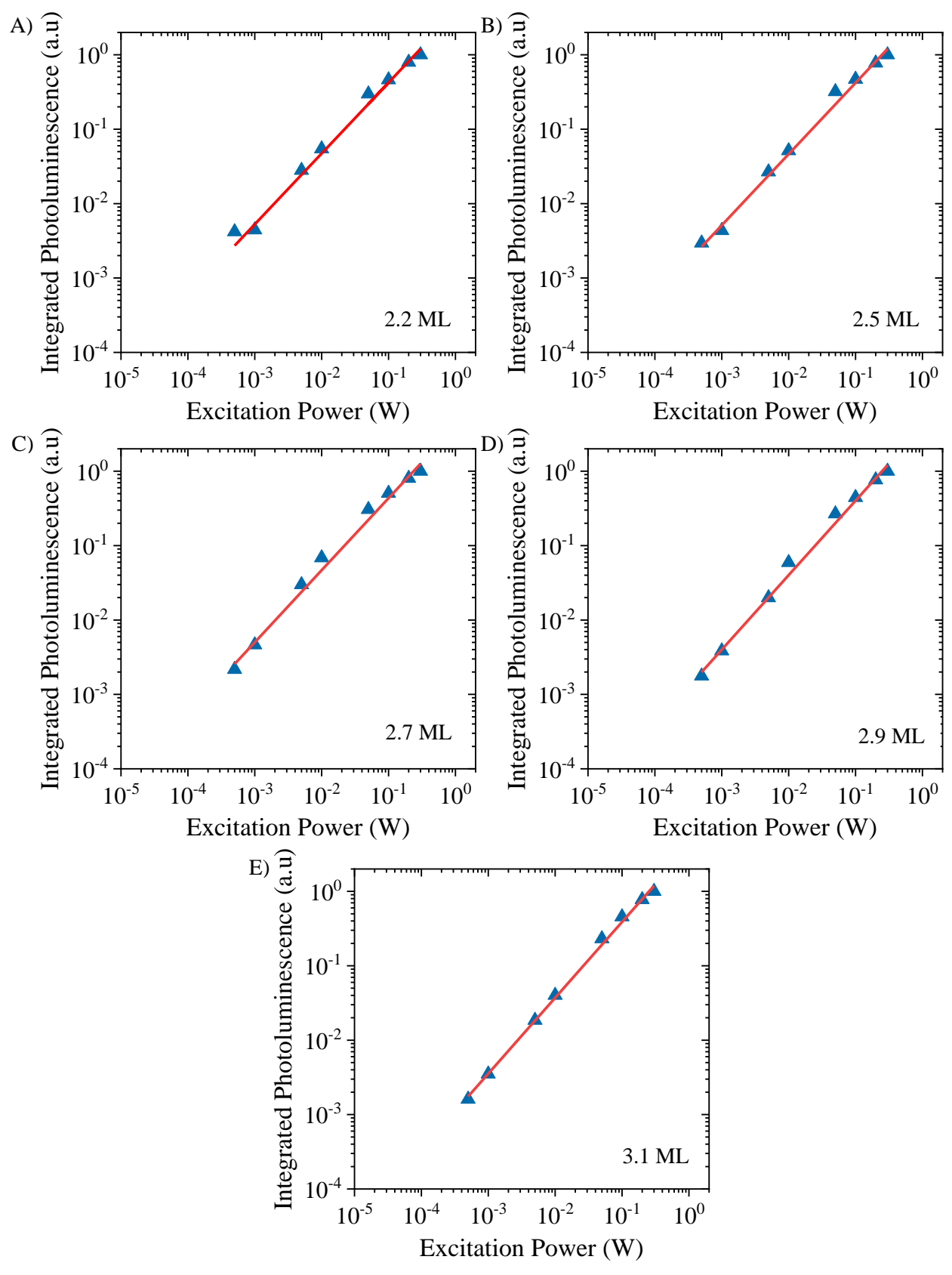


Figure 51 Normalised integrated photoluminescence vs excitation power for InAs QD samples with InAs deposition thicknesses between 2.2 - 3.1 ML. Where, A) 2.2 ML, B) 2.5 ML C) 2.7 ML D) 2.9 ML and E) 3.1 ML.

### 4.2.4 Temperature Dependent PL

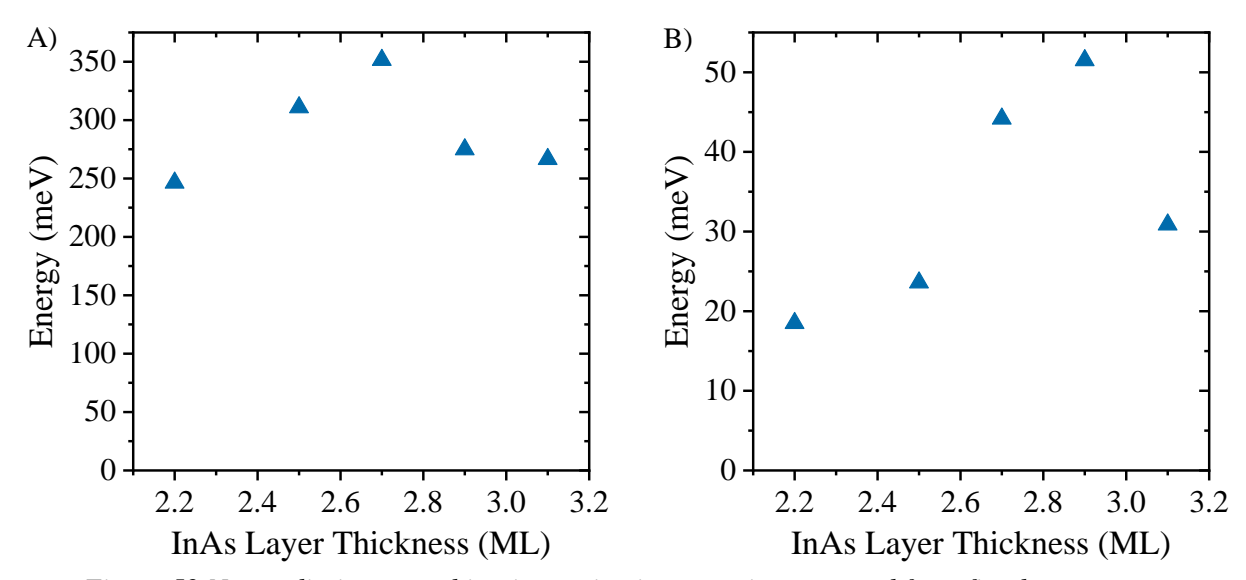


Figure 52 Non radiative recombination activation energies extracted from fitted temperature dependent photoluminescence for InAs QD samples with InAs deposition layer thicknesses between 2.2 - 3.1 ML. A) Ea<sub>1</sub> B) Ea<sub>2</sub>.

Further analysis of the non-radiative recombination defects within the optical QD structures can be achieved by observing the luminescence as a function of temperature. Non radiative recombination pathways which decrease the quantum efficiency are commonly thermally activated processes. The integrated normalised photoluminescence as a function of temperature is shown in Figure 55. With a representative example of the raw temperature dependent PL of the 2.7 ML sample shown in Figure 54. With reducing temperature increased brightness of the luminescence was observed in all samples.

The data has been fitted with a dual of Arrhenius formula shown in equation (12) with 4 fitting parameters. Two energies  $Ea_1$  and  $Ea_2$  which are related to the activation energies of the trap state and two constants of  $C_1$  and  $C_2$  which relate to the corresponding concentration of these defects. The fitting well models the data presented in Figure 55. The dominant trap state is fitted with parameters  $Ea_1$  and  $C_1$  and produced values between 246 to 351 meV peaking at the centre value of 2.7 ML of InAs deposition. These energies far exceed the thermal energy available at room temperature. However, would align well with carrier escape into the wetting layer or smaller QD populations previously observed in the AFM on the GaAs cap. The asymmetry observed in the GaAs substrate peak at 1.42 eV at 297 K in Figure 41 and Figure 54 at 20 K, both indicate the presence of energy states in close proximity. These would align well to ultra-thin InAs QWs formed from the remnants of the wetting layer or from small 1 to 2 nm InAs QDs. The  $C_1$  fitting provided an indication of relative concentration of the detected non-radiative recombination pathways in each sample. There is an initial rise in the value of  $C_1$  going from 2.2 ML to 2.5 ML followed by a plateau. The deposition of 2.7 ML gives an outlying spike to this trend with a  $C_1$  value 2 orders of magnitude higher. Counter intuitively this does not correlate to a reduction in photoluminescence. This is likely the result of a limitation of the fitting due

to the assumption of only 2 discrete energy levels associated with the non-radiative recombination process. It is much more likely we have a distribution of energy levels, and the fits are approximating statistical indications of medium values of these distributions. Higher energies with higher relative concentrations would strongly indicate the distribution of non-radiative recombination pathways are more concentrated at higher energies. More higher energy process may be preferable to lower but more readily active lower energy related defects and processes. The values of Ea<sub>1</sub> fall back to 250 to 260 meV range with increasing InAs deposition thicknesses.

The dominant process at 20 K is fitted with the coefficient Ea<sub>2</sub> and C<sub>2</sub>. Here we see a trend of steadily increasing activation energies from 18.5 to 51.5 meV with increasing InAs deposition thickness from 2.2 ML to 2.9 ML above 2.9 ML a drop is observed from 51.5 to 30.9 meV similarly mirroring the maxima behaviour observed in the Ea<sub>1</sub> energies. The energies here are much closer to the mean thermal energy at room temperature and correspond with known values for phonon assisted recombination [88], [89]. The value extracted here are also likely an indication of medium activation energy from a broader distribution of non-radiative recombination pathways corresponding to different defects within the material.

The concentrations  $C_2$  are much more tightly grouped for  $Ea_2$  varying across 1.5 orders of magnitude. A general trend of increasing concentration is observed with increasing InAs layer thickness. These values however remain 4 to 6 orders of magnitude lower than  $C_1$ . This give us the indication that the vast majority of the trap states are not active at room temperature. It also supports the argument that there is near complete suppression of  $Ea_1$  trap states at temperatures below~100 K. Below which it is observed in all samples that  $Ea_2$  states dominate the luminescence, which would otherwise be overshadowed by the  $Ea_1$  process.

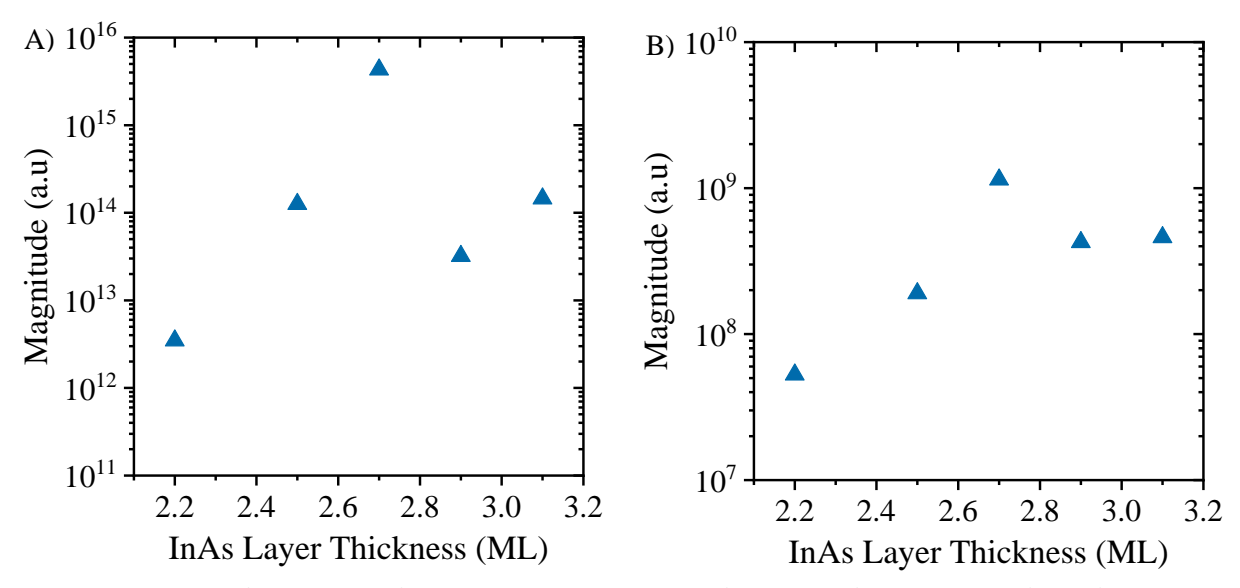


Figure 53 Non radiative recombination constants extracted from fitted temperature dependent PL for InAs QD samples with InAs deposition layer thicknesses between 2.2 - 3.1 ML. A)  $C_1$  B)  $C_2$ 

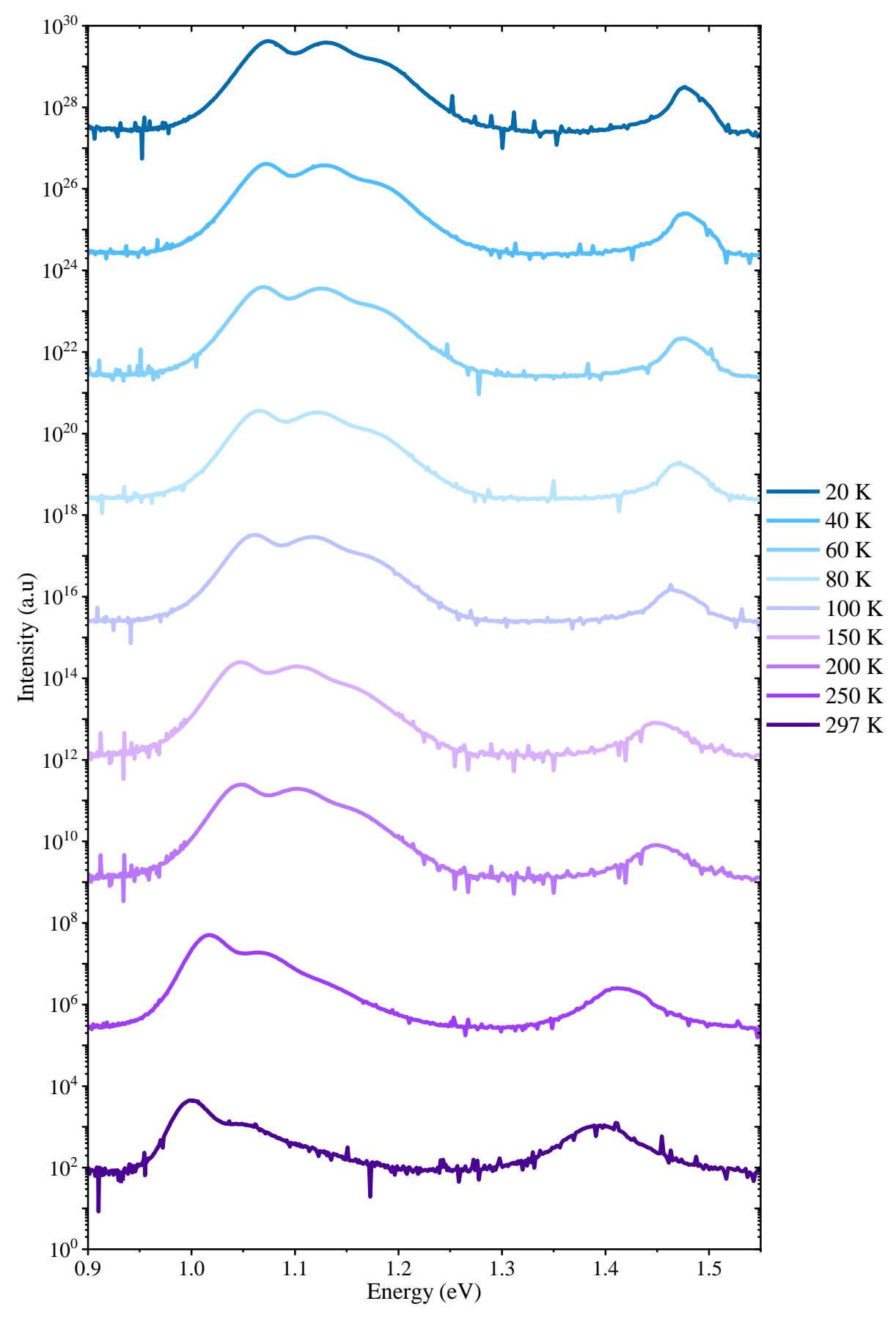


Figure 54 Temperature dependent PL of QD with 2.7 ML of InAs deposition at temperatures between 20 K to 297 K.

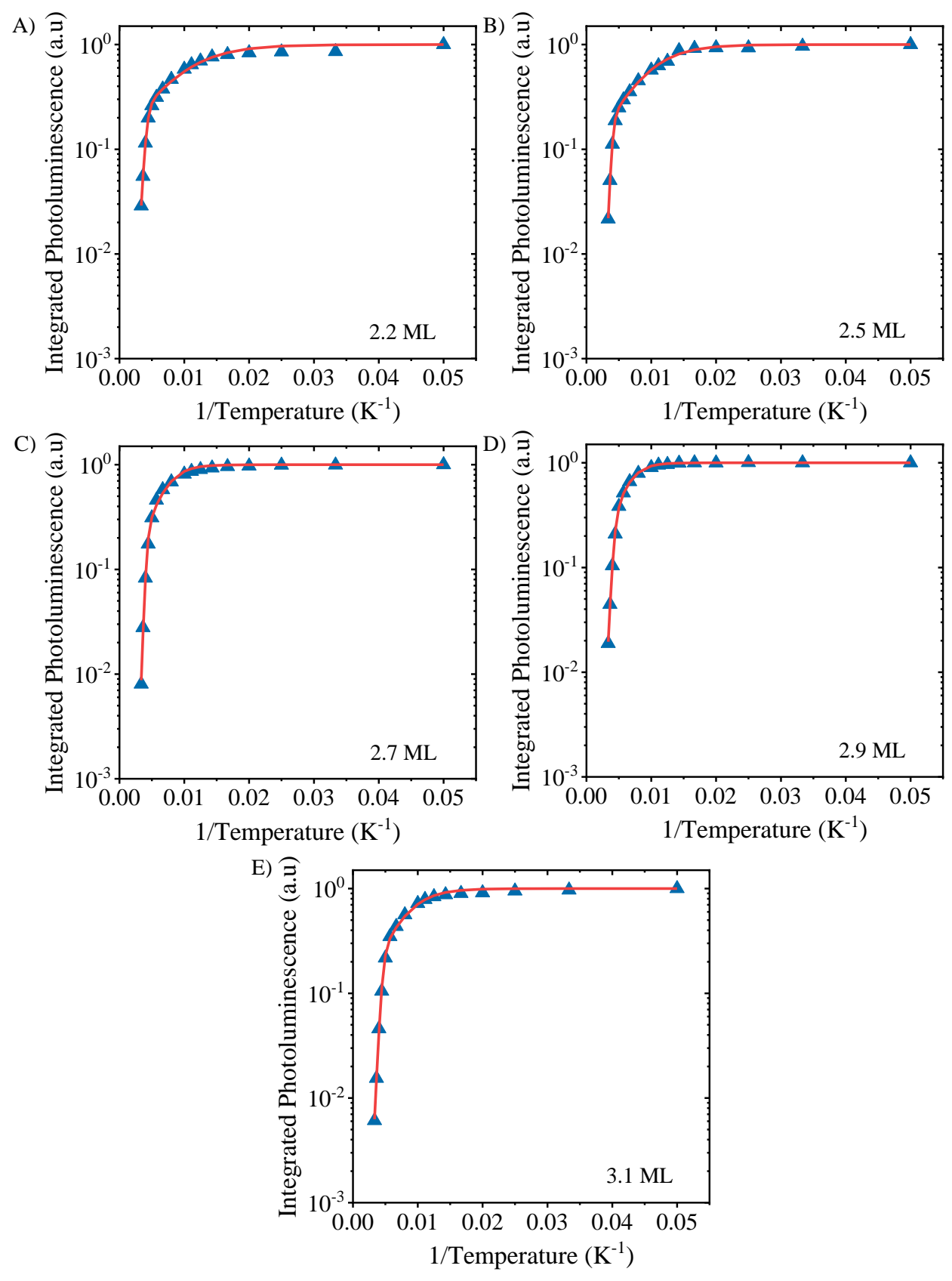


Figure 55 Normalised integrated photoluminescence vs temperature for InAs QD samples with InAs deposition layer thicknesses between 2.2 - 3.1 ML. Where, A) 2.2 ML, B) 2.5 ML C) 2.7 ML D) 2.9 ML and E) 3.1 ML. Data is shown by blue triangle with the red line showing the fitting.

## **4.3 Growth Temperature**

Continuing to set out the underlying parameter space within which this study was conducted the second optimisation presented is the QD growth temperature. This is a key growth parameter in self-assembled InAs QD growth. Many critical parameters are affected by growth temperature including the surface mobility of In and As species as well as desorption rate and interlayer diffusion. QD Growth followed the experimental procedure for the sample architecture outlined in section 4.1 with QD growth temperature and capping temperature varied between 450 to 510 °C across 3 samples. This included the sample bought forward from the QD thickness series as outlined in section 4.2. This was STL 95 with 2.7 ML of InAs deposition. Samples were then subsequently analysed using PL and AFM to determine the growth temperature to carry forward within this study. The samples of the series are shown in Table 3, they were grown as part of the wider QD series, hence the jumps in the sample ID.

Sample ID	Growth Temperature (°C)
STL95	510
STL99	480
STL9A	450

Table 3 Sample IDs of growth temperature optimisation samples.

### 4.3.1 PL

Having selected a fixed InAs deposition of 2.7 ML the next parameter for optimisation was the substrate temperature during QD growth and capping. Photoluminescence spectra of 3 samples grown at temperature between 450-510 °C are shown in Figure 56 with peak positions shown in Figure 57. Decreasing the growth temperature from 510 to 480 °C redshifted the peak emission by 29.2 meV at 20 K. Further decreasing the growth temperature resulted in a blue shift of 142.2 meV at 20 K and a dramatic decrease in the brightness of the luminescence from the QDs. This combined with a lack of PL emission at 297 K from the QDs grown at 450 °C indicate this growth temperature is on the lower temperature limit for QD formation. Both the sample grown at 480 and 510 show strong luminescence at bother 297 K and 20 K. The lowest emission energy is seen in the at 480 °C sample which is interesting and country to expectation. This effect can't be explained alone by changes to indium mobility on the surface and the induced morphological changes observed in the later presented AFM measurements. There is a secondary mechanism underpinning no linear shift across the series. Likely this is caused by indium and gallium intermixing at higher growth and capping temperatures causing an increase in the bandgap of the QDs [90].

At the upper two growth temperatures evidence of excited states with a partial filled 1<sup>st</sup> excited state at 297 K and full 1<sup>st</sup> with partial 2<sup>nd</sup> excited state at 20 K present for the 480 and 510 °C samples. This has

been confirmed with power dependent photoluminescence discussed later. There is a broad shoulder to the 297 K PL at 1.13 eV which is likely from a partially filled 2<sup>nd</sup> excited state due to concurrent state filling. The excited states observed at 20 K are most clearly differentiated in the sample grown at 480 °C. This would be indicative of a narrower distribution in QD size and composition.

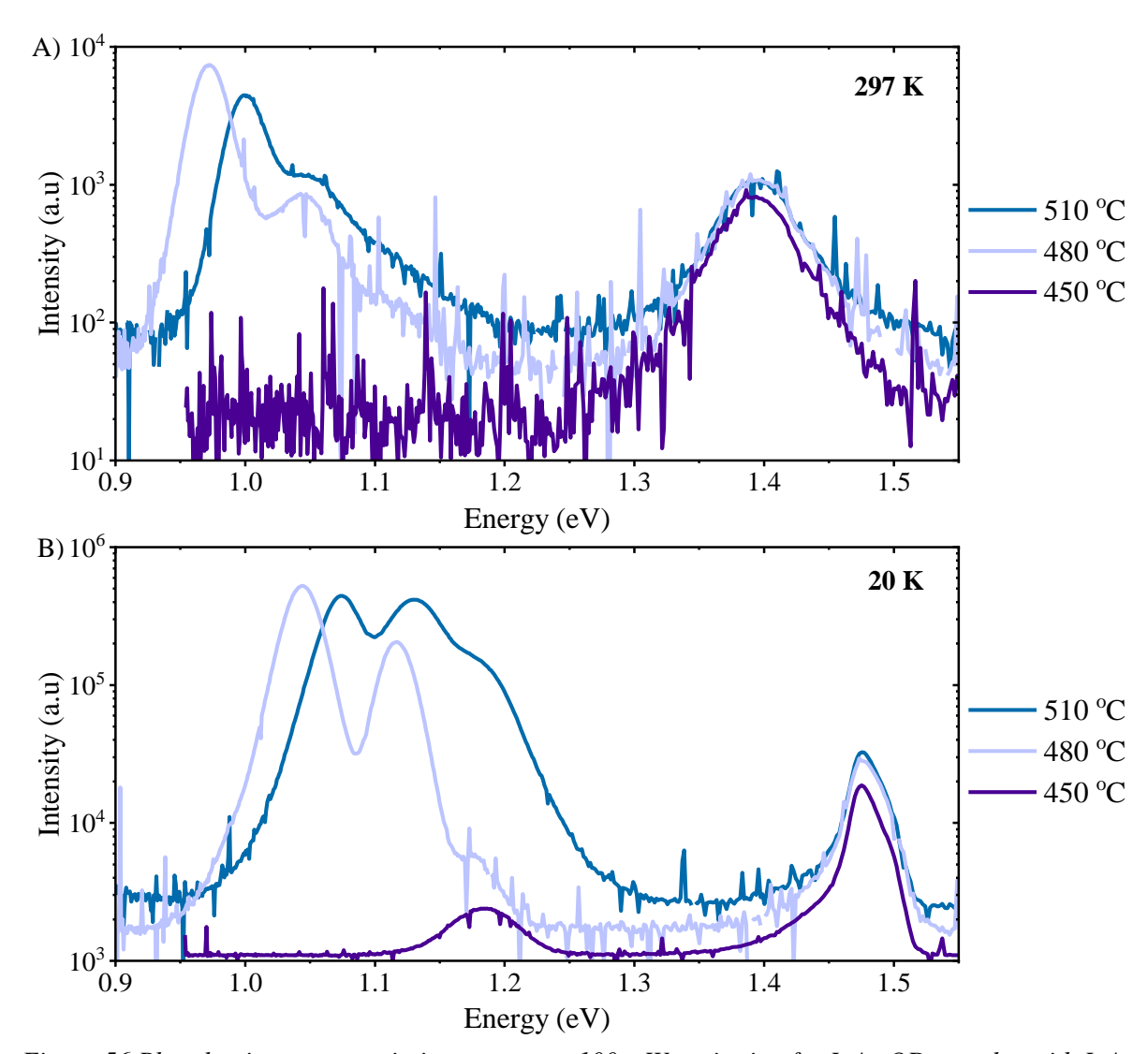


Figure 56 Photoluminescence emission spectra at 100 mW excitation for InAs QD samples with InAs growth temperatures between 450 to 510 °C, measured at temperatures of A) 297 K and B) 20 K.

There is also some asymmetry in the GaAs substrate observed at 20 K in Figure 56B. This value of 1.44 eV at 20 K aligns well with an ultrathin InAs quantum well. This would be formed from the crystallisation of the residual indium wetting layer. The suppression of luminescence from this layer at higher temperatures would indicate a high concentration of non-radiative recombination centres within this layer. This was also previously observed in the thickness series. This would also correlate with the total reduced luminance from this sample shown Figure 58. Increasing the growth temperature dramatically improved the total luminance. There was a 4 order of magnitude increase from 450 to 480 °C with a further order of magnitude increase from 480 to 510 °C. However, the highest peak intensity was observed in the sample grown at 480 °C in Figure 56A

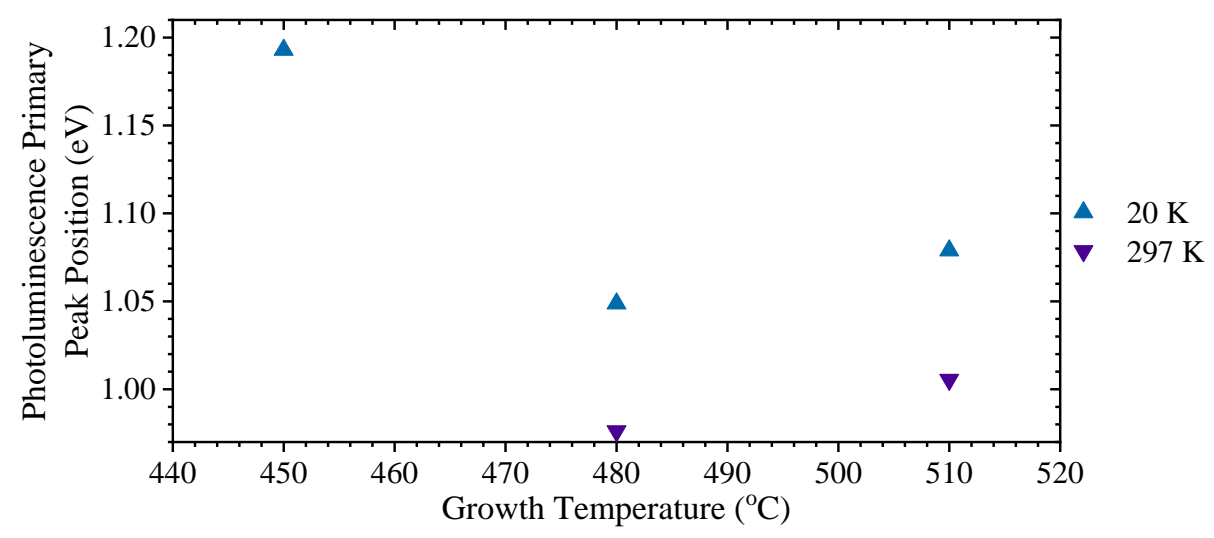


Figure 57 Primary peak position of photoluminescence emission spectra at 100 mW excitation for InAs QD samples with InAs growth temperatures between 450 to 510 °C.

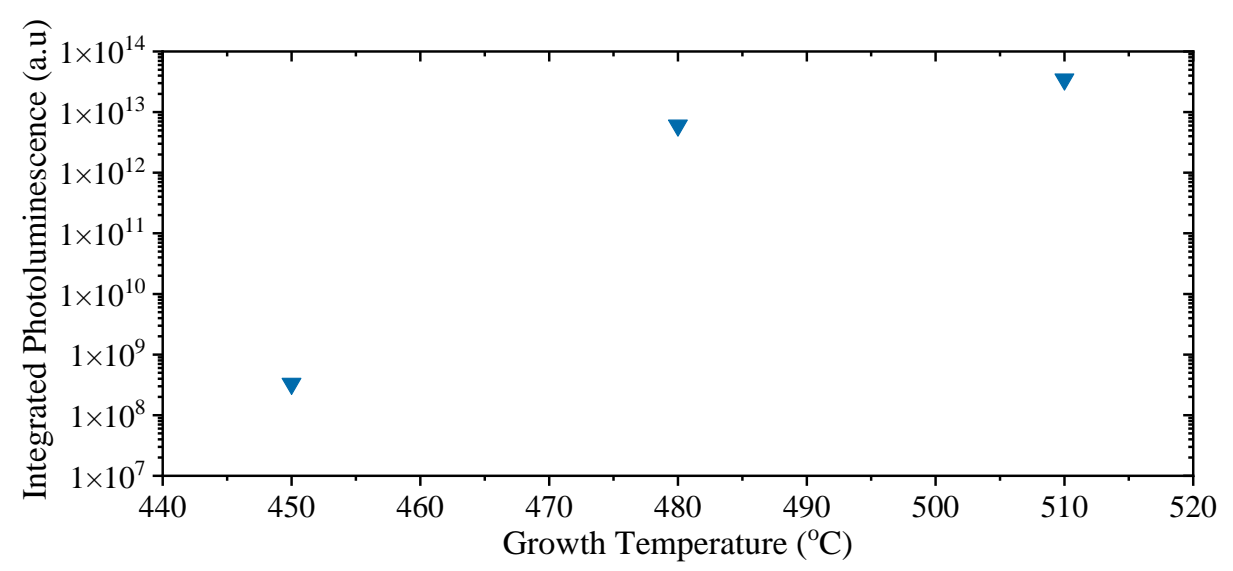


Figure 58 Integrated Photoluminescence spectra at 20 K of for InAs QD samples with growth temperatures between 450 to 510 °C.

#### 4.3.2 AFM

Bimodal populations of QDs are observed at all 3 growth temperatures tested in the AFM of the surface QDs, this is shown in Figure 59. Decreasing the surface temperature linearly reduces the height of the QD distributions. This is in line with the expectations as the mobility of indium on the surface is exponentially temperature dependent with an Arrhenius relation. The reduced the mobility at lower growth temperatures limits the coalescence of QDs on the surface by reducing the distance they can travel within a fixed timeframe. This is observed with an increased number of smaller QDs at the lower growth temperatures of 480 and 450 °C in Figure 63.

The height of the largest populations for the grown samples varied linearly between 8.3 to 2.6 nm. There is some uncertainty in the sample grown at 480 and 450 °C as to the contribution from each population

to observed PL emission due to the strong overlap between the populations observed both in height and aspect ratios as shown in Figure 61 and Figure 62 respectively. It is likely for the 450 °C sample the spectra is dominated by the broader population centred around 2.6 nm with an SD of 1.97 as the second population would give a quantum confinement giving emission at a similar wavelength to the GaAs and wetting layer peaks. Although distinguishing between the two is not possible without further measurements. The small variance in population is observed at a growth temperature of 450 °C which has a SD of 0.085. However due to other issues discussed regarding the 450 °C the comprises required to achieve this aren't warranted. The reduction of SD at 480 °C is still a marked improvement compared to 510 °C with a drop from 1.44 to 0.35 and much tighter grouping of the dual QD populations giving a sharper ground state peak in the PL.

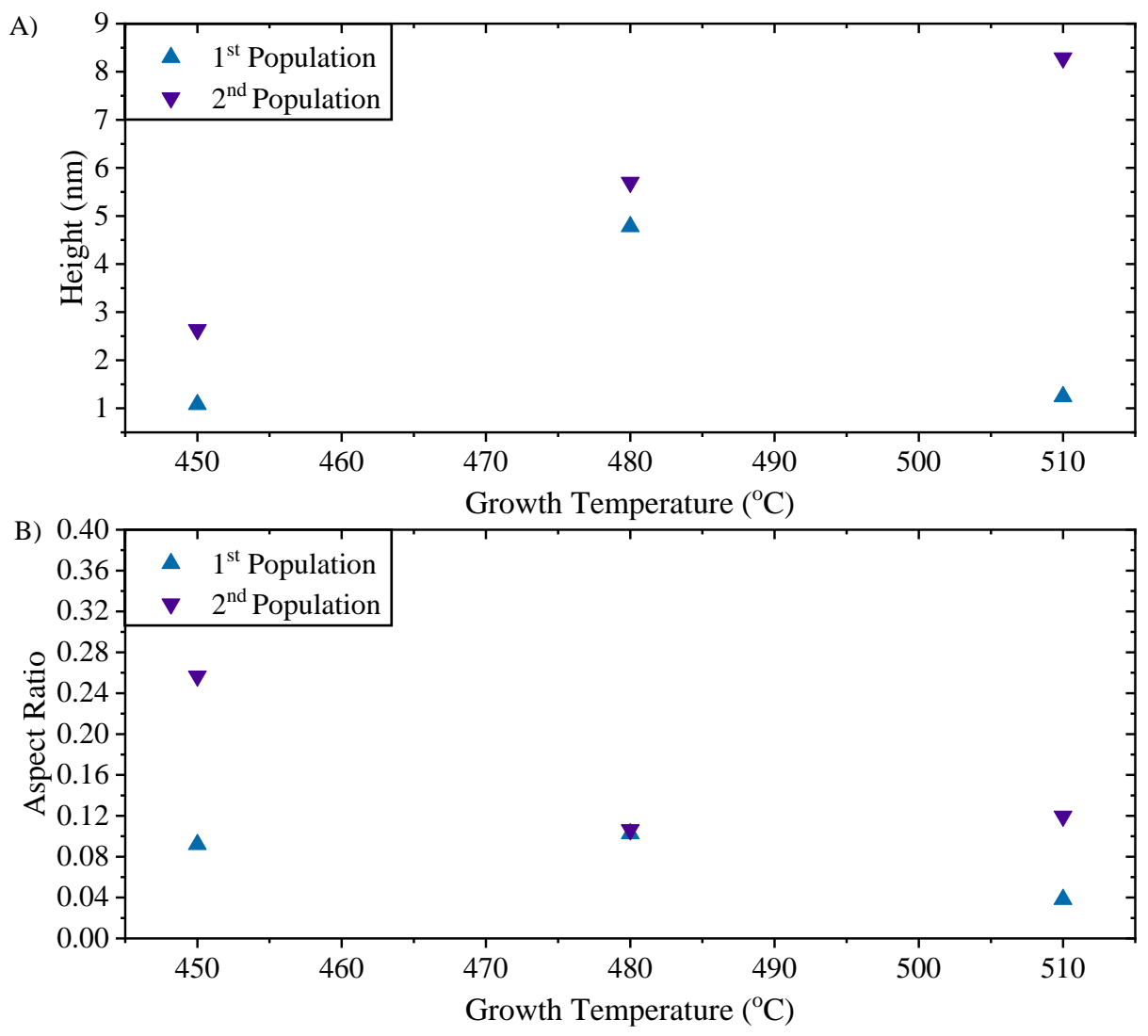


Figure 59 QD populations of height and aspect ratio for InAs QD samples with InAs growth temperatures between 450 to 510 °C.

The relation between height and aspect ratio remains consistent to the previous series with larger QDs possessing larger aspect ratios at 480 °C and 510 °C, this is shown in Figure 62. However, at 450 °C the larger population of QDs centred at 2.6 nm deviate from this trend. The QDs are much taller for the

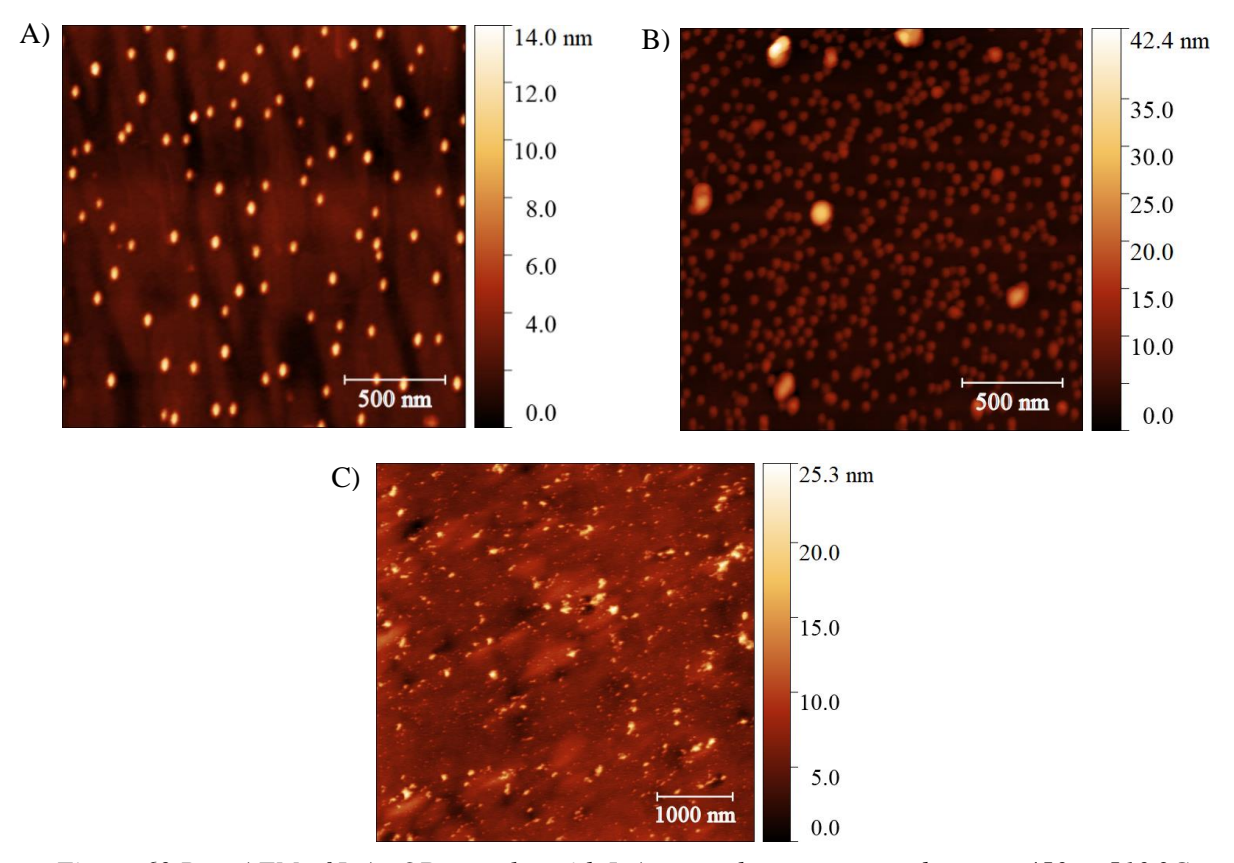


Figure 60 Raw AFM of InAs QD samples with InAs growth temperatures between 450 to 510 °C, where A) 510 °C, B) 480 °C and C) 450 °C. Note the 450 °C image is of a comparatively larger area.

width than any other QDs measured within this study at 450 °C as shown in the increased range of aspect ratios observed. This is likely due to the diminished heights stabilising the hemispherical geometry as the interplay between bulk and surface energy shifts in favour of reduced surface area. Of note is the small proportion of QDs at 1 nm is not an artefact of the histogram but the cut off from the particle size analysis. However the justification for a dual population is also supported by the aspect ratio fitting shown in Figure 61C. The aspect ratios at 480 °C and 510 °C are similar although there is an inverted distribution where tighter grouping of QD heights produced a larger aspect ratio dispersion at 480 °C compared with 510 °C. The aspect ratio distribution continues to worsen for reduced QD growth temperatures indicating an increasing kinetic limit to QD coalescence. This is expected with reducing indium surface mobility at decreasing substrate temperatures. The QD density shown in Figure 63 is also indicative of this trend. The reduced coalescence and size of the QDs at lower growth temperatures results in higher densities of smaller QDs. The plateau of QD density between 450 and 480 °C can be attributed to the presence of 1-3 disproportionately large QDs per µm<sup>2</sup>. Their presence indicates some of the InAs has become trapped and unable to diffuse as would be the case at higher temperatures. It is likely much of the InAs has been sourced from the wetting layer, which at higher temperature diffuses across the surface as a uniform material source. However, in some instances have instead been coalesced into a singular InAs agglomerates in the samples grown at 450 and 480 °C. It can be assumed that under these growth temperatures and experimental conditions the In desorption from the surface is negligibly impacting this behaviour.

The observed trends within the AFM of Figure 59 do not correspond to those seen in the PL in Figure 57. The linearly decreasing QD height and thus increasing quantum confinement would be expected to cause a continual blue shift across the series. This not being the case, it would support the previous assertion that surface mobility is not the only contributing factor and likely this effect is caused by higher levels of intermixing of indium and gallium at 510 °C. This alteration of the bandgap through alloying during the capping or QD growth is resulting in the observed blue shift at higher temperatures. The capping layer being 50 nm in depth and grown at the same growth temperature as the underlying QDs. While intermixing cannot be ruled out entirely for 480 °C and 450 °C, the results indicate the PL peak emission of these samples is more strongly dependent on the QD morphology as a function of surface indium mobility.

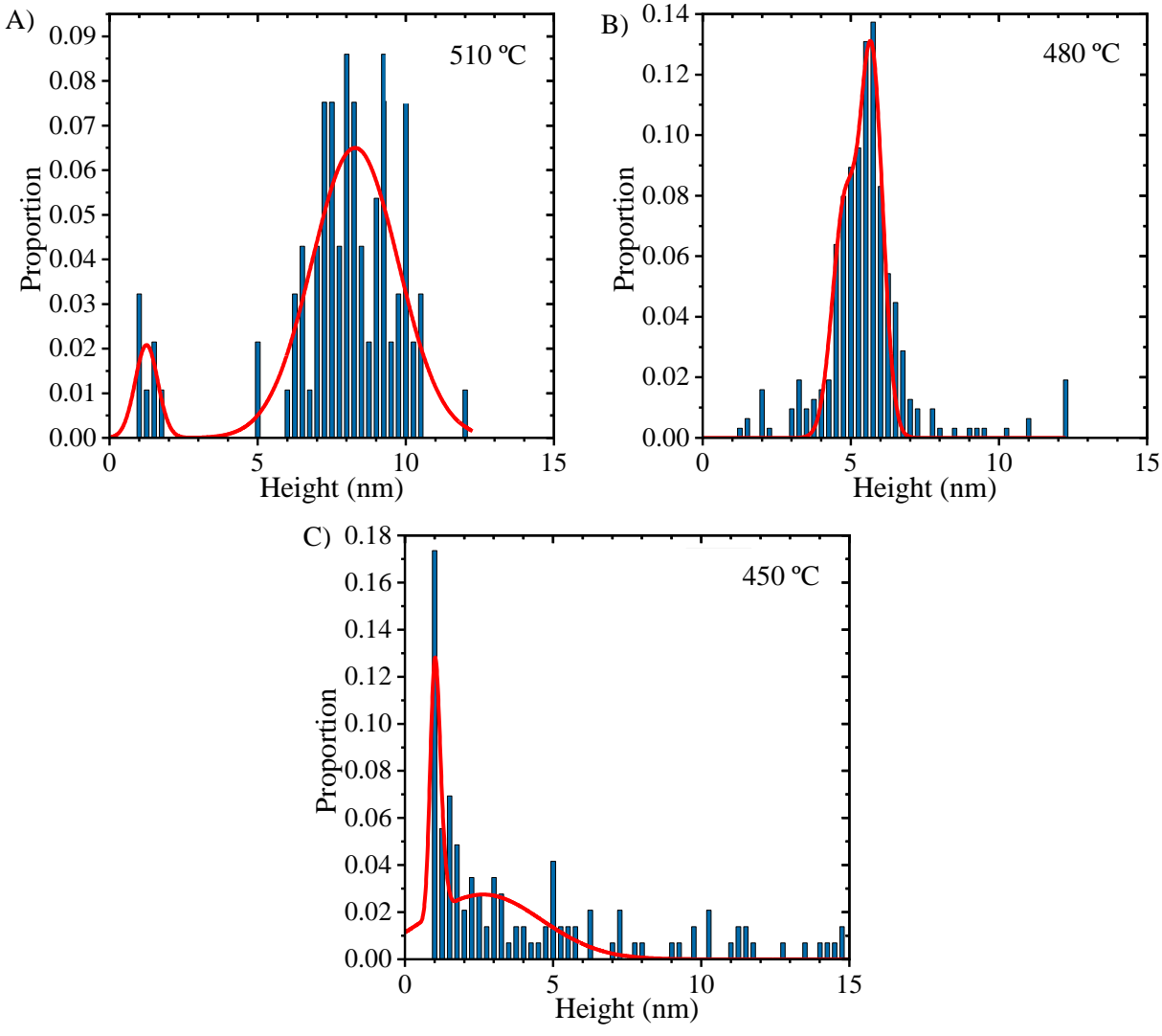


Figure 61 QD Height distributions for InAs QD samples with InAs growth temperatures between 450 to 510 °C, where A) 510 °C, B) 480 °C and C) 450 °C. Experimental data is indicated by blue bars with gaussian fits shown by the red line.

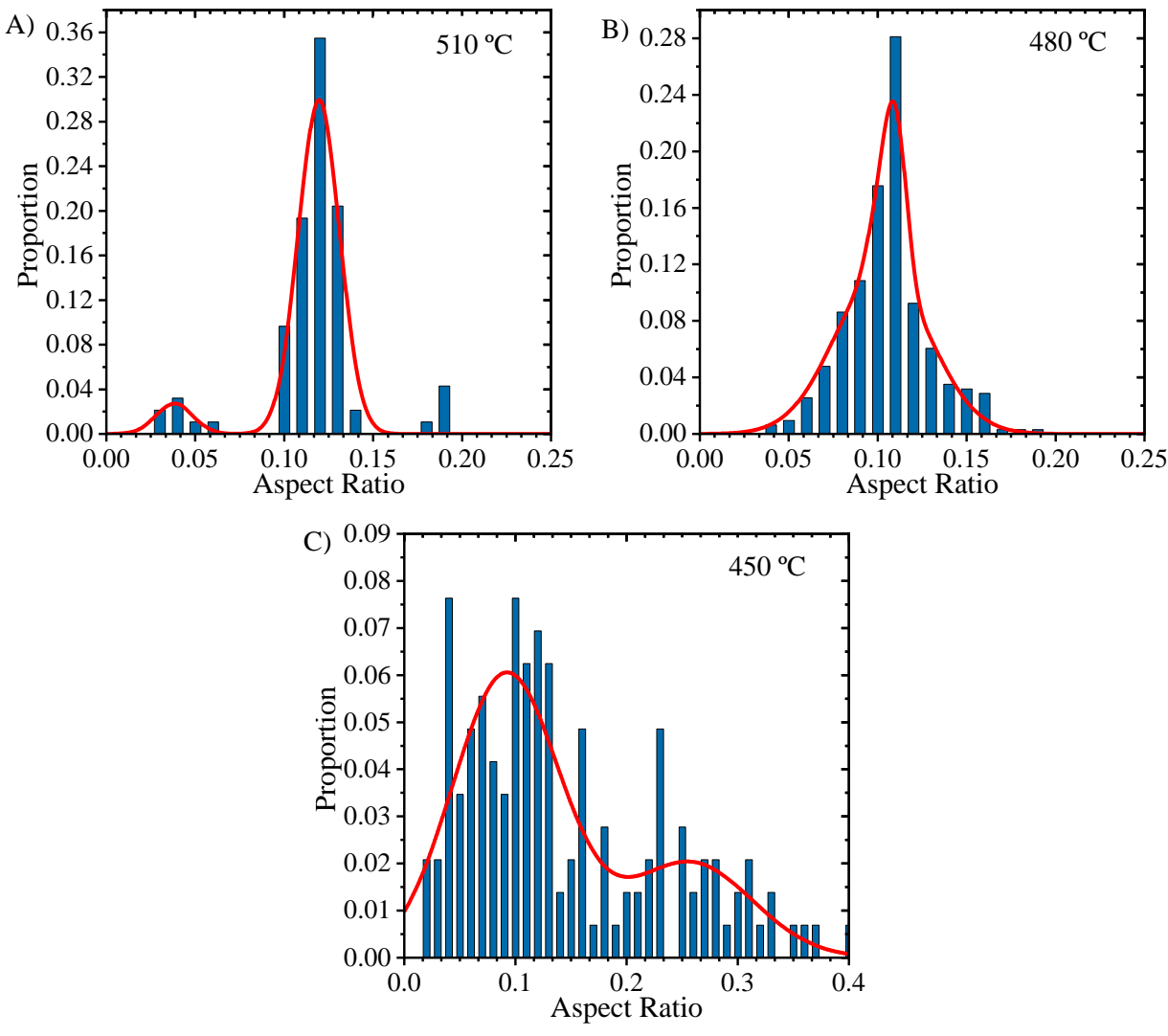


Figure 62 QD aspect ratio distributions for/ InAs QD samples with InAs growth temperatures between 450 to 510 °C, where A) 510 °C, B) 480 °C and C) 450 °C. Experimental data is indicated by blue bars with gaussian fits shown by the red line.

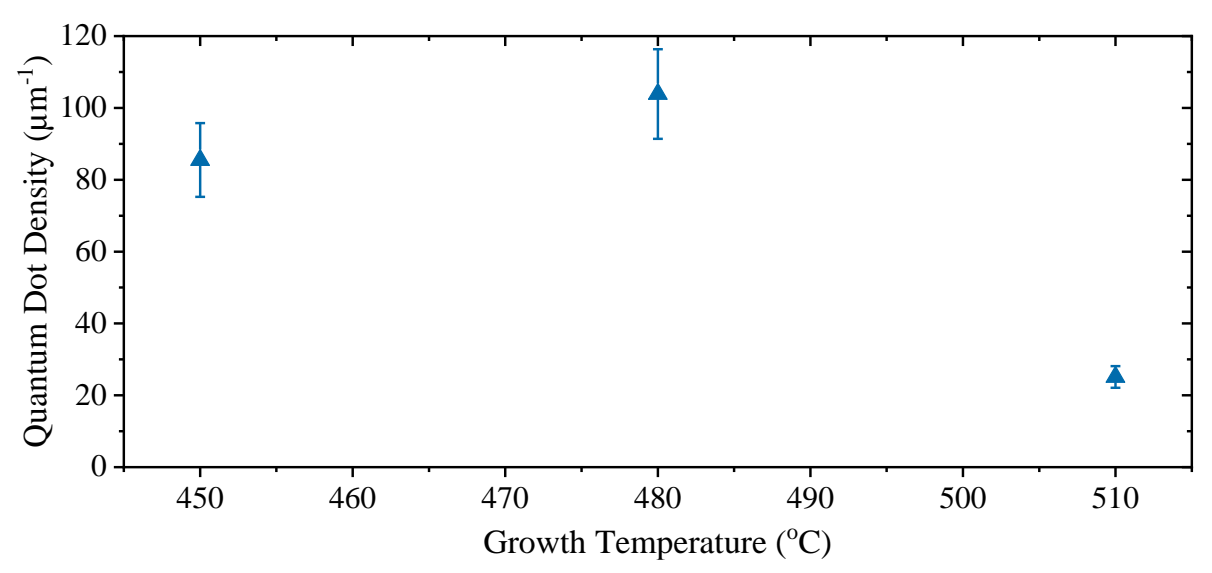


Figure 63 QD densities for InAs QD grown between 450 to 510 °C.

## 4.3.2 Power Dependent PL

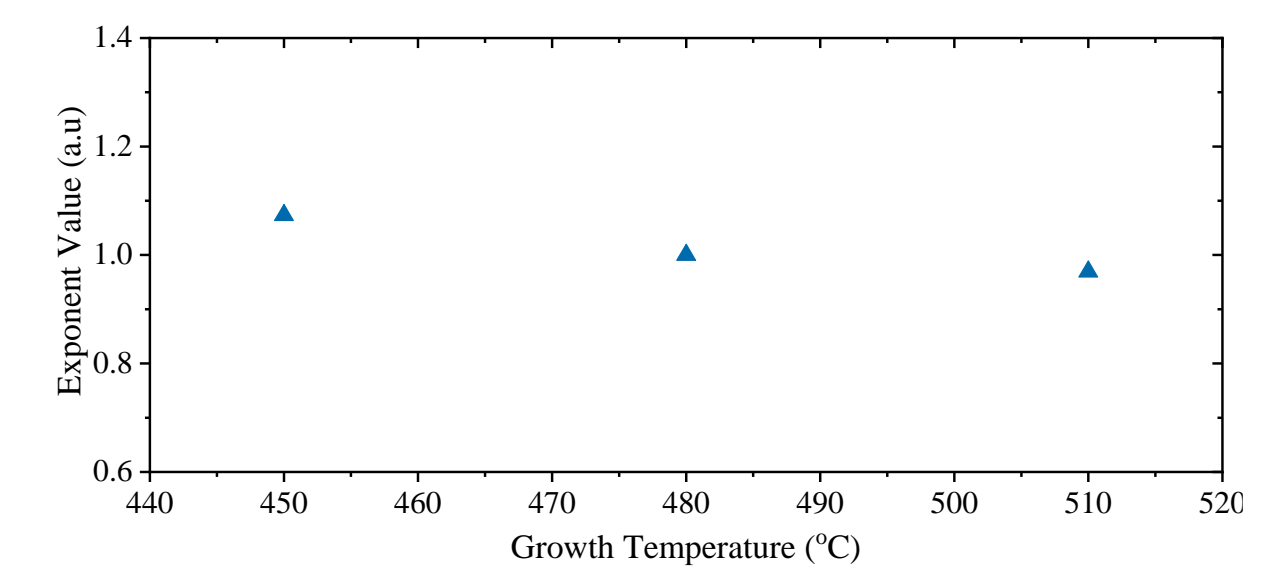


Figure 64 Power dependent exponents for InAs QD samples with InAs growth temperatures between 450 to 510 °C measured at 20 K.

Power dependent PL exponents at 20 K, as shown in Figure 64, demonstrated the recombination behaviour of carriers was radiatively dependent with exponent values close to 1. The measurements were taken by integrating the entire measured spectra. The exponent coefficients have been extracted from the integrated Pl shown in Figure 66 when fitted with equation (11). There is a slight rise in the value of the exponents for the sample grown at 450 °C which would indicate the loss of carried to non-radiative recombination pathways. However, for samples grown at 480 and 510 °C carried losses at 20 K were negligible. This can be inferred from the power dependent PL as the increase in carrier generation at higher powers can lead to saturation of non-radiative recombination pathways.

There is a slight deviation from the linear trend at higher powers, seen in Figure 66B and C at the highest excitation power tested. This is the result of sample heating within the cryo-shroud causing the activation of additional non-radiative recombination pathways. This can be more clearly seen in the redshift of the substrate peak in Figure 65. This is a representative sample from this series grown at 480 °C. The only features present at the lowest excitation are the QD ground state at 1.051 eV and GaAs substrate and capping layer peak at 1.478 eV. The 1st excited state begins to appear at 5 mW of excitation at 1.117 eV as the ground state is saturated. Increasing the optical excitation above 100 mW and both the ground and 1st excited state with the emergence of a 2nd excited state at 1.180 eV begin to fill. However, at this point the 1st excited state has not yet reached saturation or equivalence luminescence with relevance to the ground state. There is therefore concurrent state filling occurring between 100 to 200 mW. By 200 mW the 1st excited state has saturated. The spacing between the 3 peaks is equal and characteristic of excited states. This can be observed in separation of peaks positions shown in Figure 65B. It can also be seen that sample heating occurs between 100 to 200 mW of excitations power in this sample as the ground states and 1st excited state begin to shift. The final feature of note in Figure 65A

is the asymmetry seen in the GaAs peak which presents a clear shoulder at 1.485 eV. This is likely the expected contribution from the crystallised wetting layer. It is expected that this region is of lower crystal quality and a potential centre of non-radiative recombination centres as previously discussed.

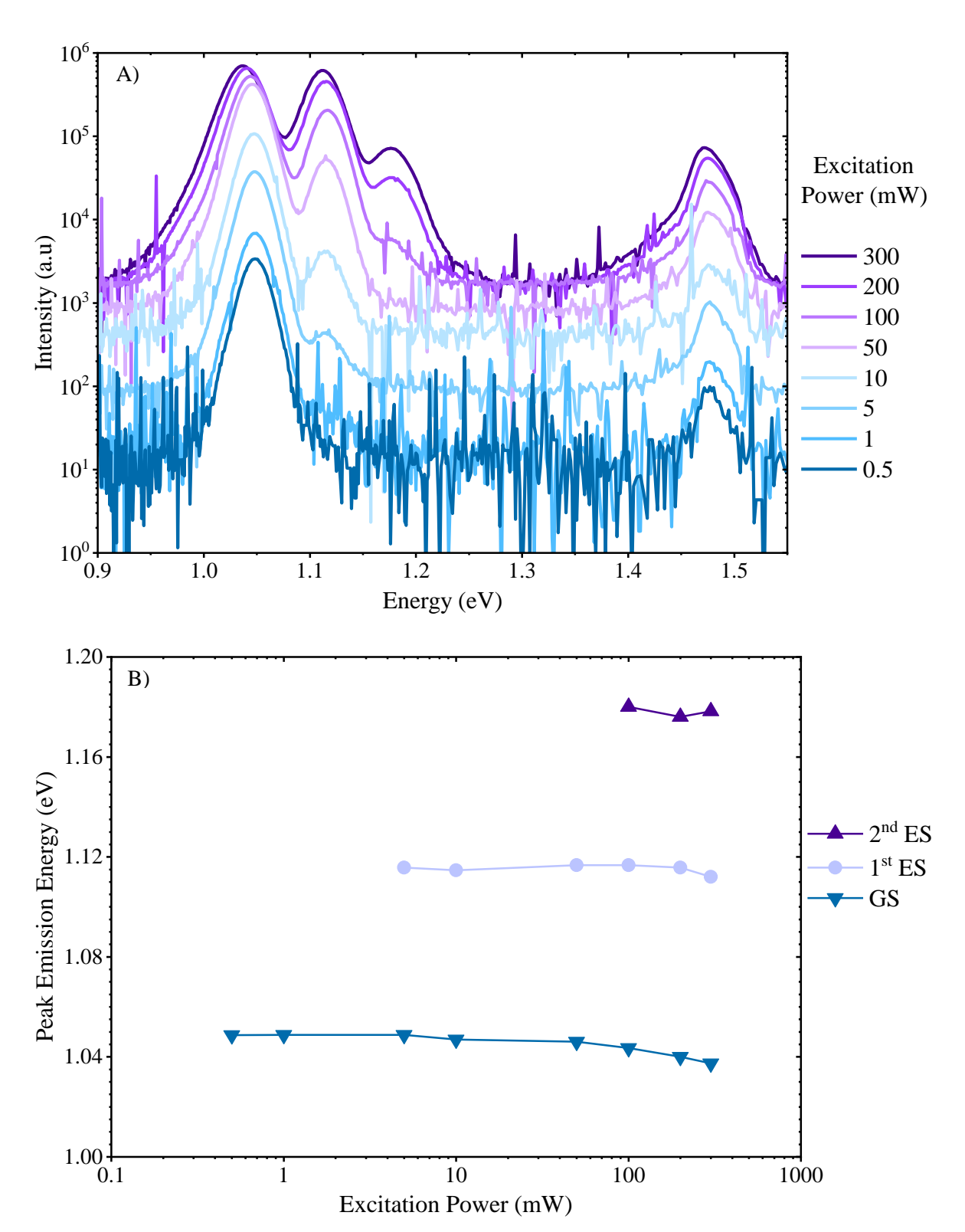


Figure 65 A) Representative power dependent PL at 20 K of sample grown at 480 °C. B) Corresponding peak positions from QD emission.

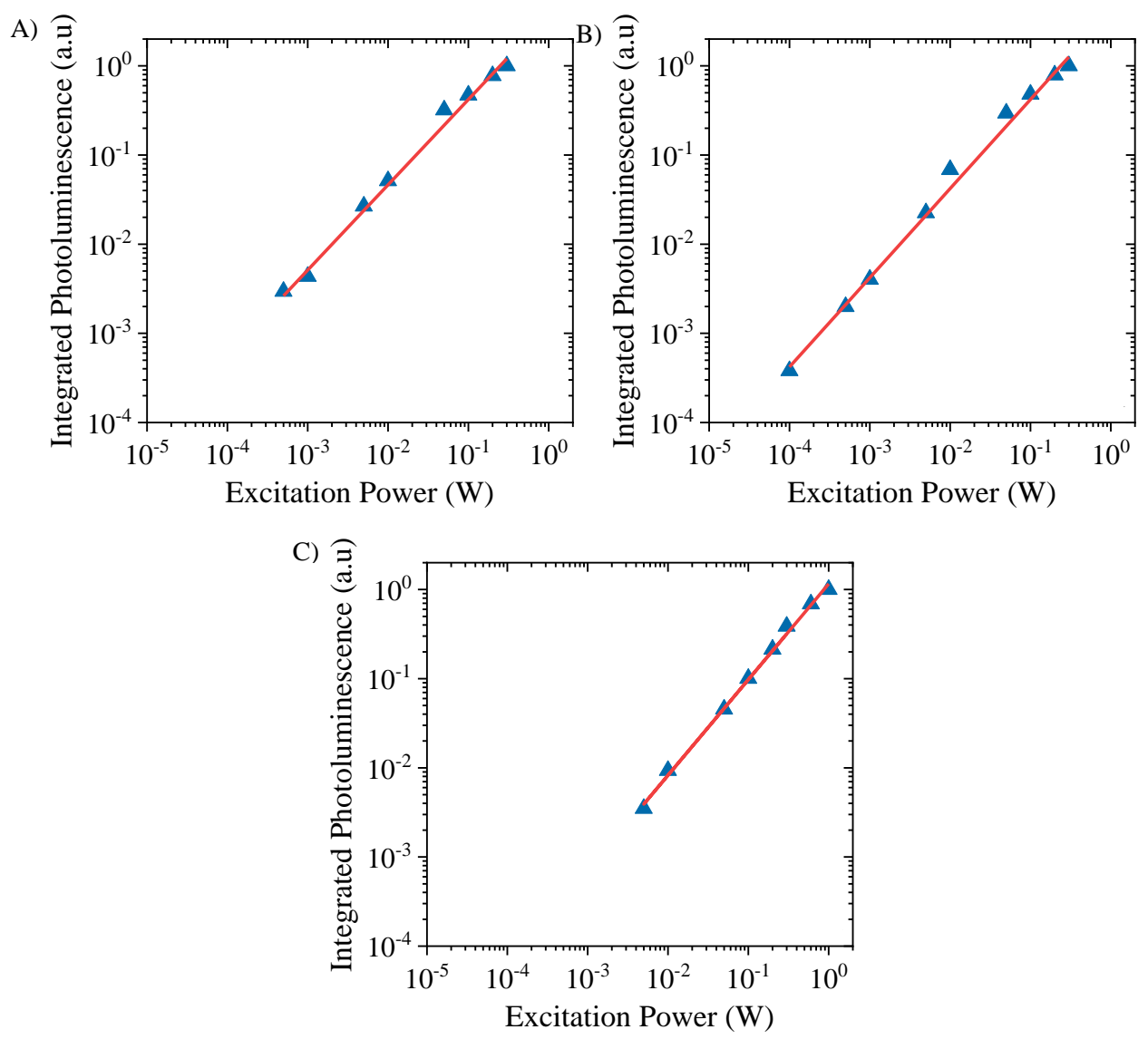


Figure 66 Normalised integrated photoluminescence vs excitation power for InAs QD samples with growth temperatures between 450 to 510 °C. Where, A) 510 °C, B) 480 °C and C) 450 °C.

## 4.3.3 Temperature Dependent PL

The fitting to the integrated TD PL for the temperature sub series using equation (12) is shown in Figure 67. The values of the 4 fitting coefficients  $Ea_1$ ,  $Ea_2$ ,  $C_1$  and  $C_2$  are shown in Figure 68 and Figure 69 respectively. The fitting achieved well approximates the experimental data, however of note in Figure 67C is that the full roll over at higher temperatures hasn't been observed. This is an experimental limitation in which measurable signal at higher temperatures can't be achieved without using optical powers that will cause sample heating at the lower temperature measurements. This will predominantly affect the confidence in the fitting for  $Ea_1$  and  $C_1$  for the sample grown at 450 °C.

The extracted value of Ea<sub>1</sub> for 480 and 510 °C, shown in Figure 68, can be approximated to the energy difference between the ground state at 1.05-1.1eV and GaAs as well as the potential InAs wetting layer

at ~1.4 eV. This would indicate carrier escape into the GaAs capping layer or InAs wetting layer is the dominant non radiative recombination mechanism at temperatures above 125 K This however does not hold true for the sample grown at 450 °C which has a value significantly lower, at 159 meV. This would be more closely approximate to the difference between the emission of the two QD populations observed in Figure 56A. The primary ground state emission is attributed to the larger QD population while the broad shoulder observed is attributed to the 1 nm population observed in the AFM of Figure 61C. Assuming this observation is correct it would indicate the non-radiative recombination centres are strongly concentrated in the smaller population of QDs within this sample. Lower growth temperature QDs have previously been shown to be of poorer material quality and from the AFM we are beginning to approach the temperature limit for effective QD coalescence and formation. This is based on previous

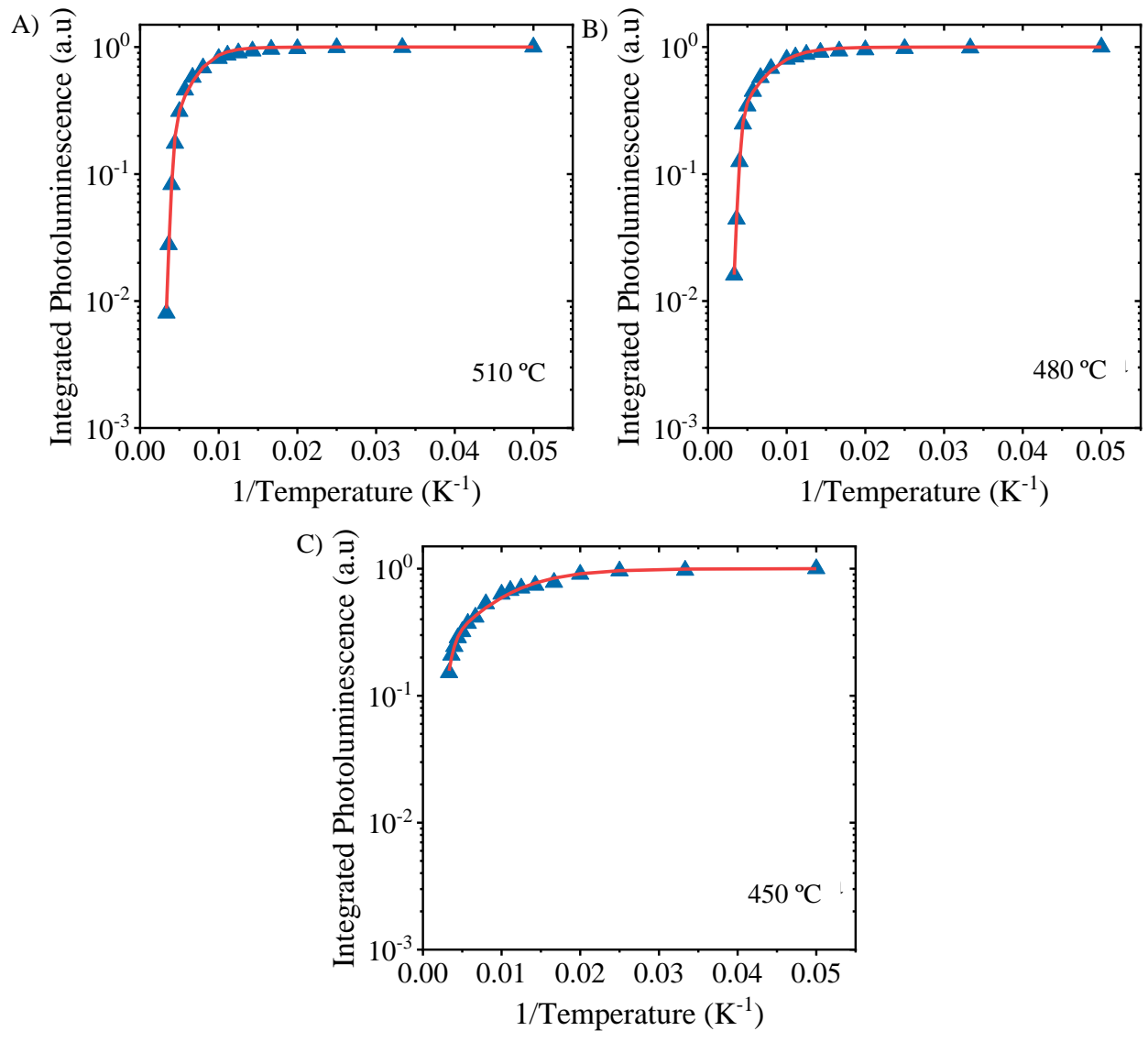


Figure 67 Normalised integrated photoluminescence vs temperature for InAs QD samples with InAs growth temperatures between 450 – 510 °C. Where, A) 510 °C, B) 480 °C and C) 450 °C. Experimental data is indicated by blue triangle with the fits shown by the red line.

deepening on the desired application work in which without the aid of a Bi surfactant QDs were unable to form at 370 °C [29]. The lower value of C<sub>2</sub> appears contradictory to expectations, however it can be inferred from this and the known limits of TD PL being that you can only measure nonradiative recombination centres which can be thermally quenched. That the lower value of C<sub>2</sub> combined with the diminished PL intensity comparative to the samples grown at 480 and 510 °C indicates that one or a combination of the following two processes occurred. The carriers are recombining within the capping layer or crystalised InAs wetting layer which is suffering from reduced material quality due to the lower growth temperature. Alternatively, there are a large concentration of nonradiative recombination centres within the primary QD population which is also indicative or poor material quality. Both would explain the observed behaviour within this sample.

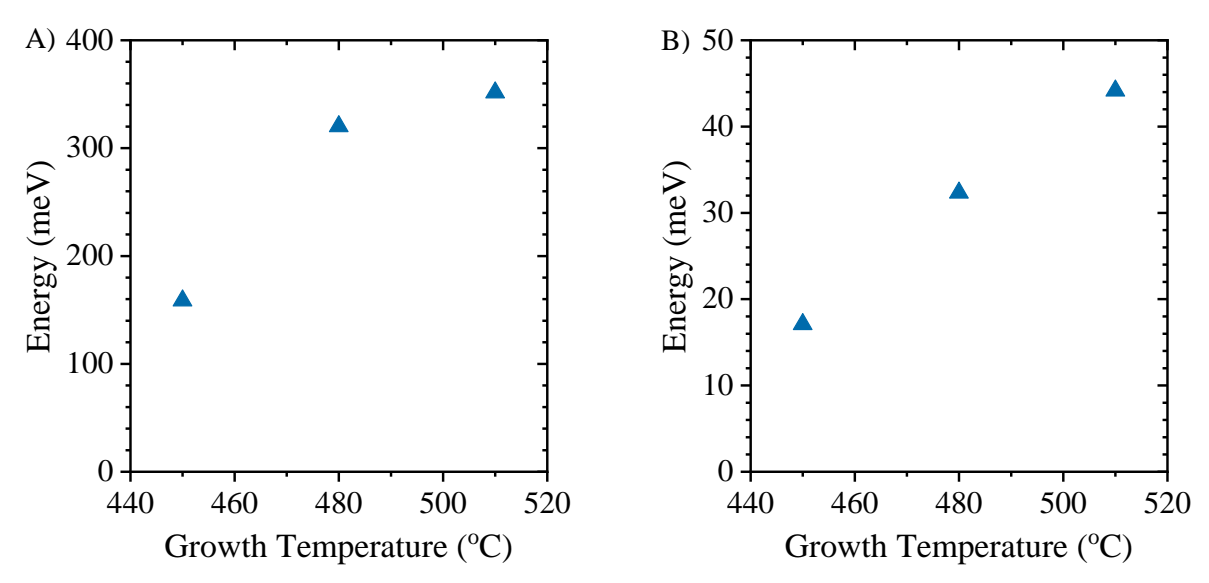


Figure 68 Non radiative recombination activation energies extracted from fitted temperature dependent photoluminescence for InAs QD samples with growth temperatures between 450 to 510 °C.

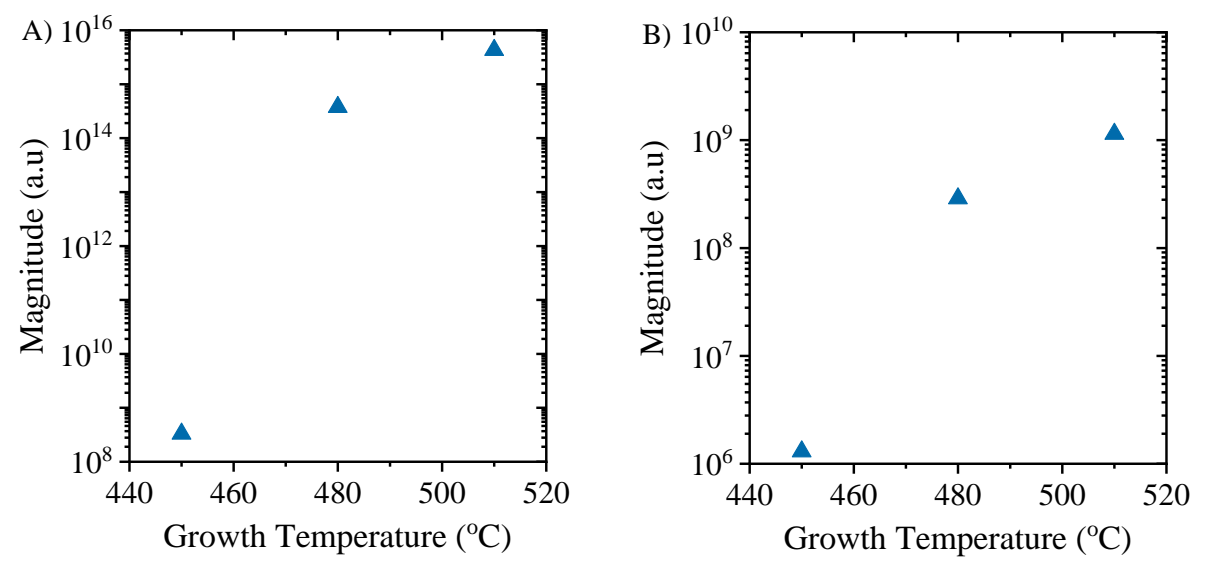


Figure 69 Non radiative recombination constants extracted from fitted temperature dependent photoluminescence for InAs QD samples with growth temperatures between 450 to 510 °C.

The values of Ea<sub>2</sub> shown in Figure 68B fall within the range that is indicative to phonon energies, 30 to 40 meV, for the samples grown at 480 to 510 °C. This phonon dependent mechanism dominates the non-radiative recombination at lower temperatures in these two samples. Commenting on the sample grown at 450 °C is difficult due to the partially completed fitting. However, bearing this caveat in mind, the lower value of Ea<sub>2</sub> would indicate trap assisted recombination (Shockley Read Hall) (SRH). Is it also likely the possess underpinning the Ea<sub>2</sub> energy are phonon and trap state dependent, and the decreases seen are indicative of increasing concentration lower energy trap states. The results presenting within this section strong suggest that the optimum growth temperature is 480 °C. Clear of the lower formation limit of self-assembled QDS and with either no or significantly reduced impact from Ga and In intermixing. Further its PL emission energy was the closest thus far to the target O and C band.

#### 4.4 Bi Flux Series

This section focused on the impact of a concurrent supply of Bi flux with InAs deposition to ascertain the impact of varying levels of Bi surfactants on InAs QD formation. The key experimental conditions of growth temperature and InAs deposition thickness have been taken from the previous 2 optimisation sections. These are 480 °C and 2.7 ML of InAs deposition selected for the emission wavelength and high optical quality as measured by PL. Bi fluxes between 0 to 3.5 nA were supplied concurrently during InAs deposition which the sample ID and Bi flux supplied shown in Table 4. Sample were grown chronologically in hexadecimal order according to the last 2 digs of the sample ID. The sample architecture is shown in Figure 70 with the Bi surfactant shown by the purple layers. This does not indicate the Bi remains within the sample post QD formation. These values of flux are taken from measurements by the movable ion gauge outlined in section3.1.4.1. Presented within this section is a study of 5 samples using photoluminescence, power and temperature dependent in addition to atomic force microscopy (AFM) to ascertain the impact of various levels of Bi surfactant during InAs QD growth.

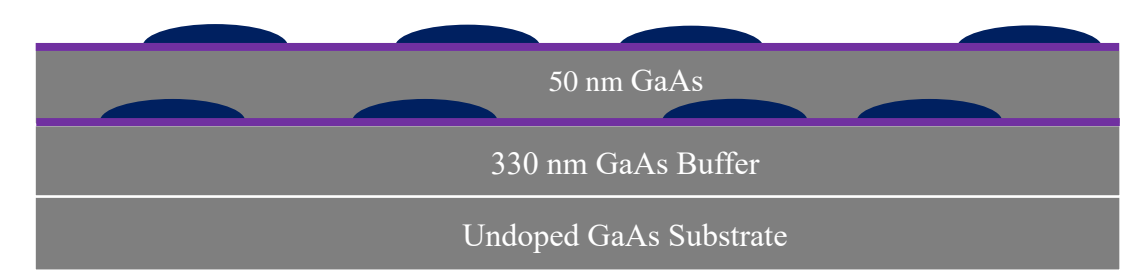


Figure 70 QD cross sectional sample structure with InAs QD shown in blue and bismuth layers shown in purple.

A concurrent Bi and InAs deposition was selected as a result of the chosen growth temperature. It is not expected that Bi will be able to incorporate or remain stable on the substrate surface for an extended time period at 480 °C. This is based on the bulk growth of InAsBi and GaAsBi which are conducted at growth temperatures below 400 °C. Therefore, to give the best chance of observing the impact of a Bi

flux on QD formation a co-deposition method was selected. This ensures the Bi will exist on the surface under a state of equilibrium between desorption and supplied atomic flux. The study therefore assesses how varying Bi surface coverages and metallic layer thicknesses impact the QD formation process.

Sample ID	Bi Flux (nA)
STL99	0
STL9D	1.2
STL9C	2
STL9E	2.6
STL9F	3.5

Table 4 Sample ID for Bi flux QD series.

### 4.4.1 PL

The addition of Bi flux during the QD growth resulted in a blue shift of the PL emission of up to 72 meV for the range of tested Bi fluxes between 1.2 to 3.5 nA. The trend of blue shift is shown in Figure 71, is not a linear trend across the entire series. There appears to be an outlier at 1.2 nA of Bi flux in which we see a marked blue shift of 72 meV. Beyond this between 2 to 3.5 nA we see a more linear trend in the blue shift is seen with incremental jumps of 20, 38 and 42 meV for 2, 2.5 and 3.5 nA of Bi flux respectively. It is observed in Figure 72S that at 2 nA of Bi there is a maxima in the PL brightness before observing a gradual decrease in the intensity of the QD ground state peaks with higher Bi fluxes. The outlier at 1.2 nA has the lowest ground state intensity of the series at 297 K. Reduced temperature measurements at 20 K show peak intensity of the ground states decreases linearly with the blue shift and increasing Bi fluxes, excluding 1.2 nA. However, it is noted the luminescence observed at lower temperatures is more tightly grouped that at 297 K.

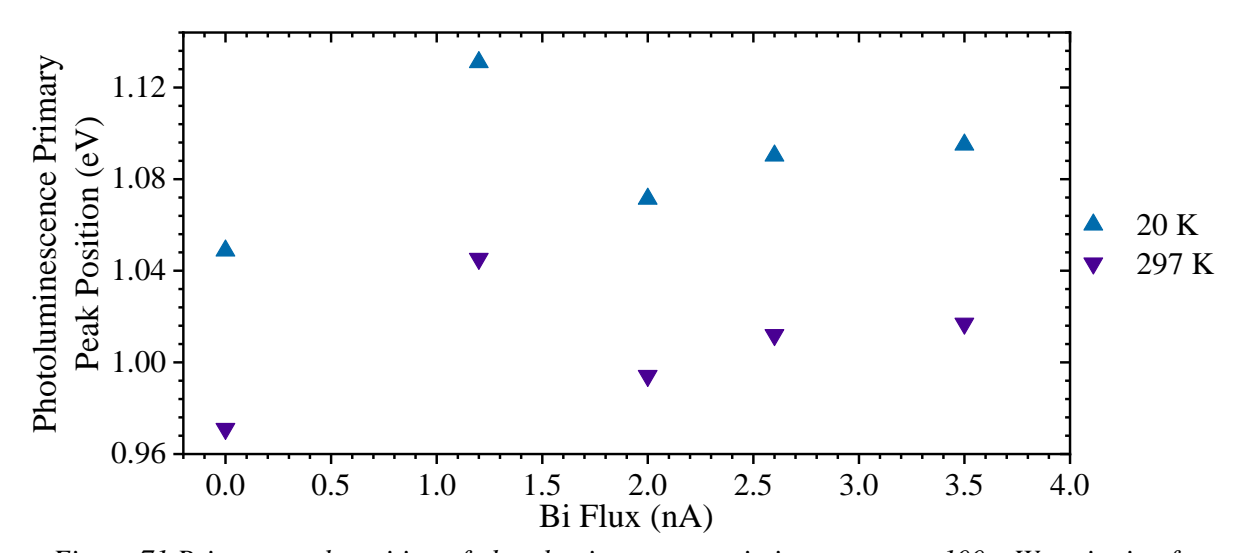


Figure 71 Primary peak position of photoluminescence emission spectra at 100 mW excitation for InAs QD samples with Bi flux during QD Growth of between 0 to 3.5 nA.

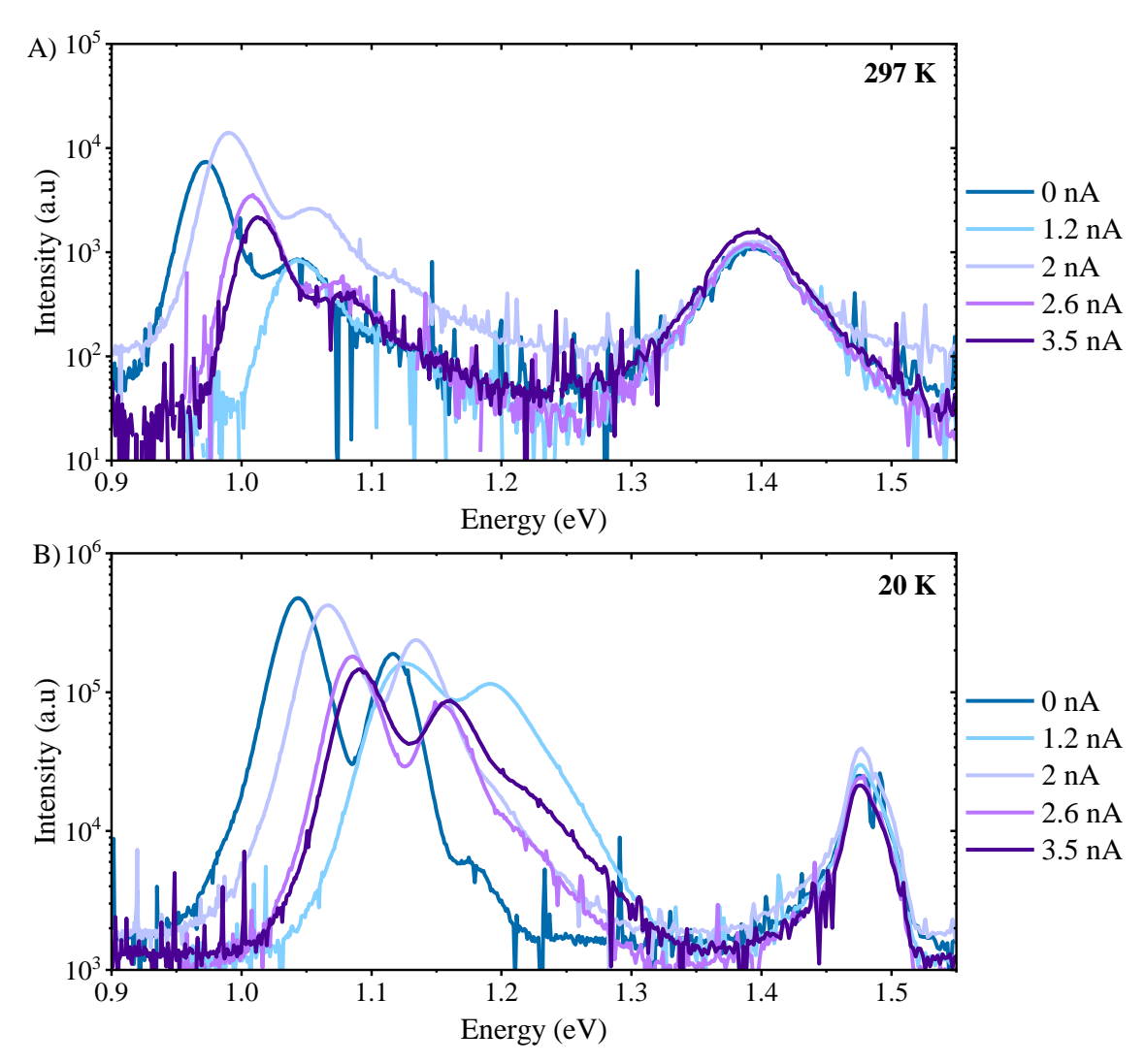


Figure 72 Photoluminescence emission spectra at 100 mW excitation for InAs QD samples with Bi flux during QD Growth of between 0 - 3.5 nA, measured at temperatures of A) 297 K and B) 20 K.

There is an asymmetry present to the left of the substrate peak at 1.44 eV in Figure 72B. This would correspond to a contribution from an ultra-thin InAs QW as has previously been observed in this study. There are indications of excited states in all samples within the series, with the ground state fully saturated at 20 K, this will be confirmed in the later presented PD PL measurements. There is extended shoulder observed between 1.1 to 1.2 eV in all samples this is likely another partially filled excited state. The trend in integrated luminescence across this series is shown in Figure 73. Generally, a lower total luminescence is observed with the addition of any amount of Bi flux during QD growth. The exception is the sample grown with 2 nA which does not appear to be impacted by reduced quantum efficiency. The remainder of the series appears to be equally impacted by the presence of Bi during QD formation independent of the supplied flux. It is worth noting at the growth temperature used of 480 °C no Bi incorporation into the QDs is expected and this is further inferred from the PL. There is no observed redshift with increasing Bi flux to any of the emission peaks as would be expected if Bi was incorporating and altering the bandgap. The surfaces of these sample also remained free for any adverse

surface defects commonly seen with Bi growth. The supplied quantity of Bi in all samples would result in metallic droplets unless it is able to incorporate or desorb from the growth surface. This would indicate that the Bi is functioning as a surfactant on the growth surface and desorbing.

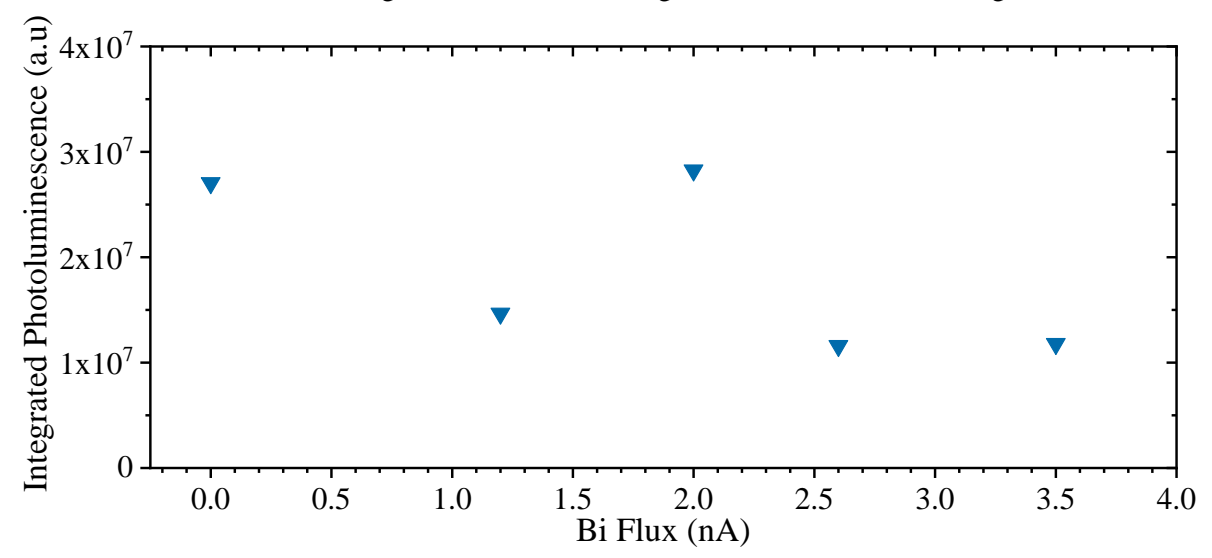


Figure 73 Integrated Photoluminescence spectra at 20k of for InAs QD samples with Bi fluxes of 0-3.5 nA

#### 4.4.2 AFM

The trends previously observed in the PL emission from this series are not mirrored in the AFM results. This would indicate that QD morphology and changes to the quantum confinement are not the complete picture in explaining the relation between Bi flux and bandgap of the QDs. Initially the application of a Bi flux increased the height of the larger population from 5.7 to 10.0 nm. It is also observed that the population distribution transitioned from bimodal to trimodal for the 1.2 nA sample. Two populations of taller QDs are observed with a majority population and then slight reduced height minority population visible as a broadening shoulder to the left of the peak in Figure 79B. There is a further small population of uncoalesced 1 to 2 nm QDs. The 1.2 nA sample possesses the tallest QDs measured across the series. Increasing the Bi flux to 2 nA appears to reverse this trend with a decrease in mean heights for all QD populations. However, there is the loss of the partially formed QD population at 1 to 2 nm under 2 nA of Bi Flux. This would indicate more complete QD coalescence is being observed under these conditions. The population grouping is very close to that achieved at 480 °C with 0 nA of Bi flux. However, the QD populations are taller with higher aspect ratios in the Bi surfactant assisted sample. The increase in QD heights observed was 2.6 nm for the larger QD population with a 0.065 increase in aspect ratio. Increased Bi supple to 2.6 nA during QD formation increased the height at the expense of an increased range of population distributions. There are 2 broad populations instead of the narrow shoulders seen previously, with an increase in SD of 0.4 and 0.45 for the 4.65 and 8.45 nm populations respectively. When pushed to the furthest extreme tested, with a supply of 3.5 nA of Bi flux, a return to the narrower distribution of QDs heights is observed as also seen at 0 and 2 nA. However, a significant reduction in the average height of these distributions is observed with a reduction of 4.44 and 4.39 nm

for the 2.85 and 3.85 nm QD populations respectively. In addition, the re-emergence of the partially formed 1 to 2 nm QDs is also observed on the uncapped QDs. This indicates at this level of Bi surface coverage QD formation is drastically impeded. The QDs measured in this sample are the smallest observed in this investigation. This really highlights the control over morphology that can be achieved through careful application of a Bi surfactant with control over the QD height between 3.8 to 10.0 nm with high QD uniformity. It is expected at these growth temperatures that the Bi will desorb from the surface during the QD growth. Therefore the thickness of the Bi wetting layer will remain stable under a supply and desorption equilibrium. Any remaining Bi on the surface post QD growth will desorb in the subsequent annealing stages or growth of the capping layer.

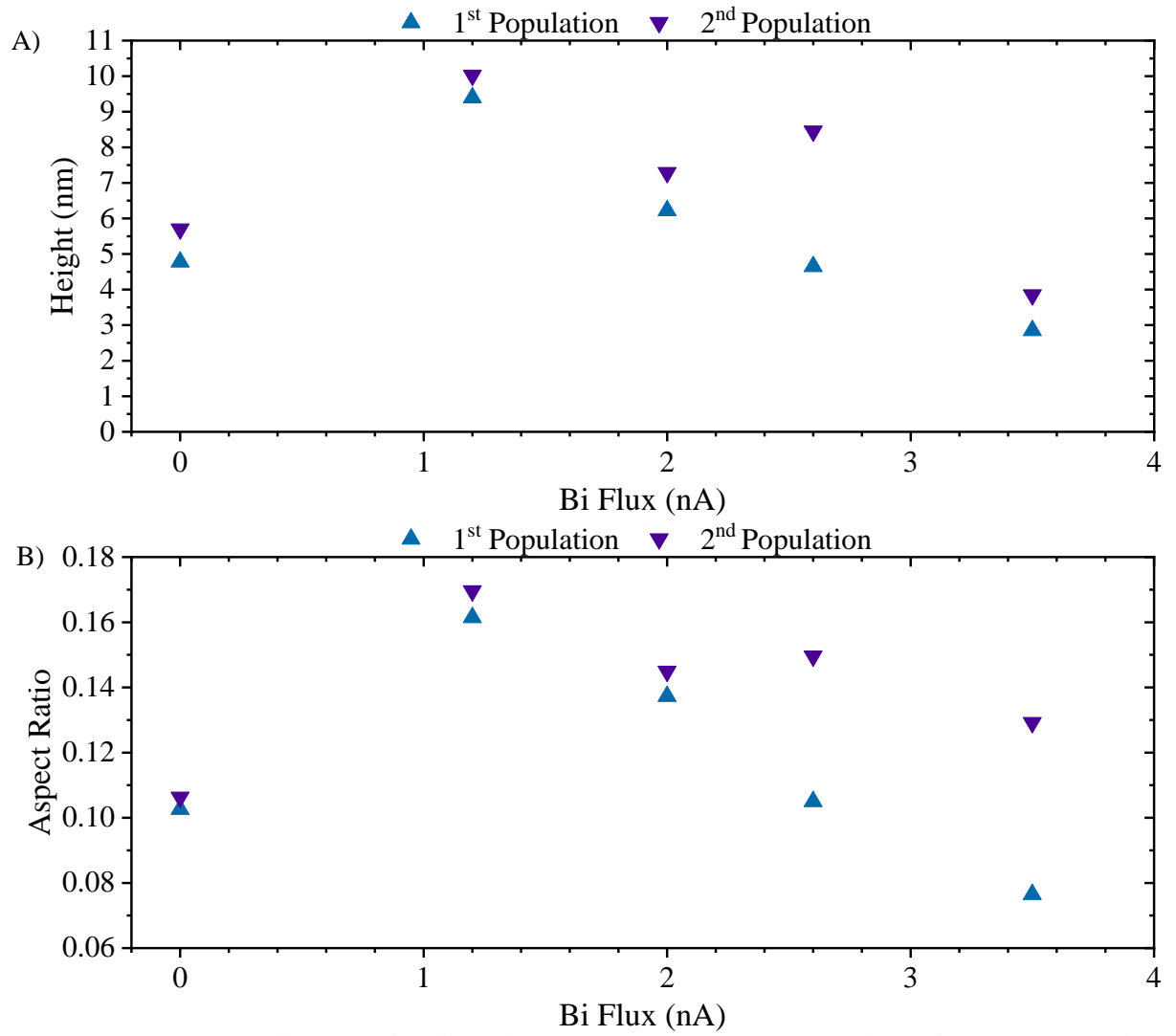


Figure 74 QD populations of height and aspect ratio for InAs QD samples with InAs QD samples with Bi flux during QD Growth of between 0 to 3.5 nA,

Within the 3 samples which contain narrower population groupings of QDs; 0, 2 and 3.5 nA, it is observed that the aspect ratio distribution is similar between the 3. The aspect ratio of these 3 increases with increased QD height in line with previous observations of the thickness and temperature series. The 2 remaining samples of this series 1.2 and 2.6 nA both displayed more separated height distributions, and this can also be observed in the aspect ratio distribution as seen in Figure 80B and D.

The transition between the wider and narrower population distributions is tied to the limitation of QD formation with increasing Bi fluxes. The transition in morphology between 1.2 to 2 nA can be described as the loss of the 10 nm population and rise of the shoulder at 8 nm to create the distribution seen at 2 nA. From 2 to 2.6 nA this transition is best described as a splitting and divergence of the 2 populations. Producing a wider distribution at 4.5 and 8.5 nm. This could be indicative of a critical Bi flux at which In/Ga intermixing is more prevalent as indicated by the PL shift for 2 larger population of QDs. Finally, from 2.6 to 3.5 nA it is again the increase and splitting of the 4 nm peak into 2 close populations with the loss of the entire 8 nm population. This illustrates a clear picture of Bi surfactant limiting the QD coalescence.

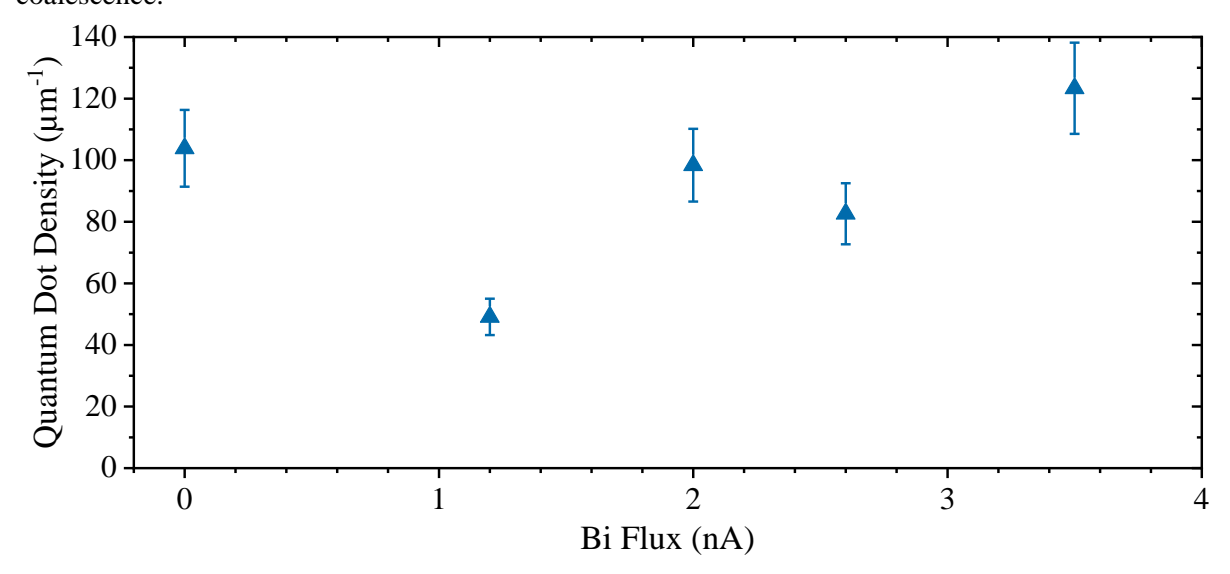


Figure 75 QD density for InAs QD samples with InAs QD samples with Bi flux during QD growth of between 0 to 3.5 nA,

The QD densities shown in Figure 75 show a reversal in trend at the 1.2 nA of Bi sample, closely mirroring the behaviour of the QD heights. This may be an anomalous result with a lower than expected QD density or an indication of 2 stage behaviour of Bi surfactant on QD formation. To determine this further growths at finer increments between 0 to 2 nA of Bi are required. The point of surfactant effect onset cannot be determined from the data beyond it placement between 0 to 1.2nA. Furthers growths at finer increments below 1.2 nA would be required to return a more accurate value. However, it can be seen that the initial interaction and application of 1.2nA of Bi flux to the surface aids in the QD formation and coalescence to produced lower densities of taller QDs. Further supply can increase the QD heights while reducing the density as expected. Supple beyond this continues to limit the QD coalescence although competing processes do not make the relationship simples to describe,

From the overall estimates of QD volumes across the series shown in Figure 78 there does not appear to be any difference in In desorption rate from the surface and the volume remains consistent across the sample series. However, the trend in height is not matched by the shift the PL emission. This is shown in Figure 77 were there is a contradiction in which decreasing QD height is not always resulting in higher energy emission. The increased quantum confinement should blue shift the emission this is

observed between 3.8 to 6 nm. However, for QDs taller than 8 nm the opposite trend is observed. This would indicate the bandgap is increasing with decreasing QD confinement this is strong indication of intermixing between In and Ga in the taller QDs. It is highly unlikely Bi is intermixing at the 480 °C growth temperature. The observed redshift at 5.7 nm can be accounted for with a reduction of the QD confinement energy as heights reduce. This is then overshadowed by change in bandgap due intermixing with Ga for the taller QDs.

The morphological changes observed due to the Bi surfactant during QD formation aren't the only mechanism that bears consideration. There is also the possibility residual Bi present on the surface during the QD capping. The interplay of Bi during the capping process has not been investigated and is

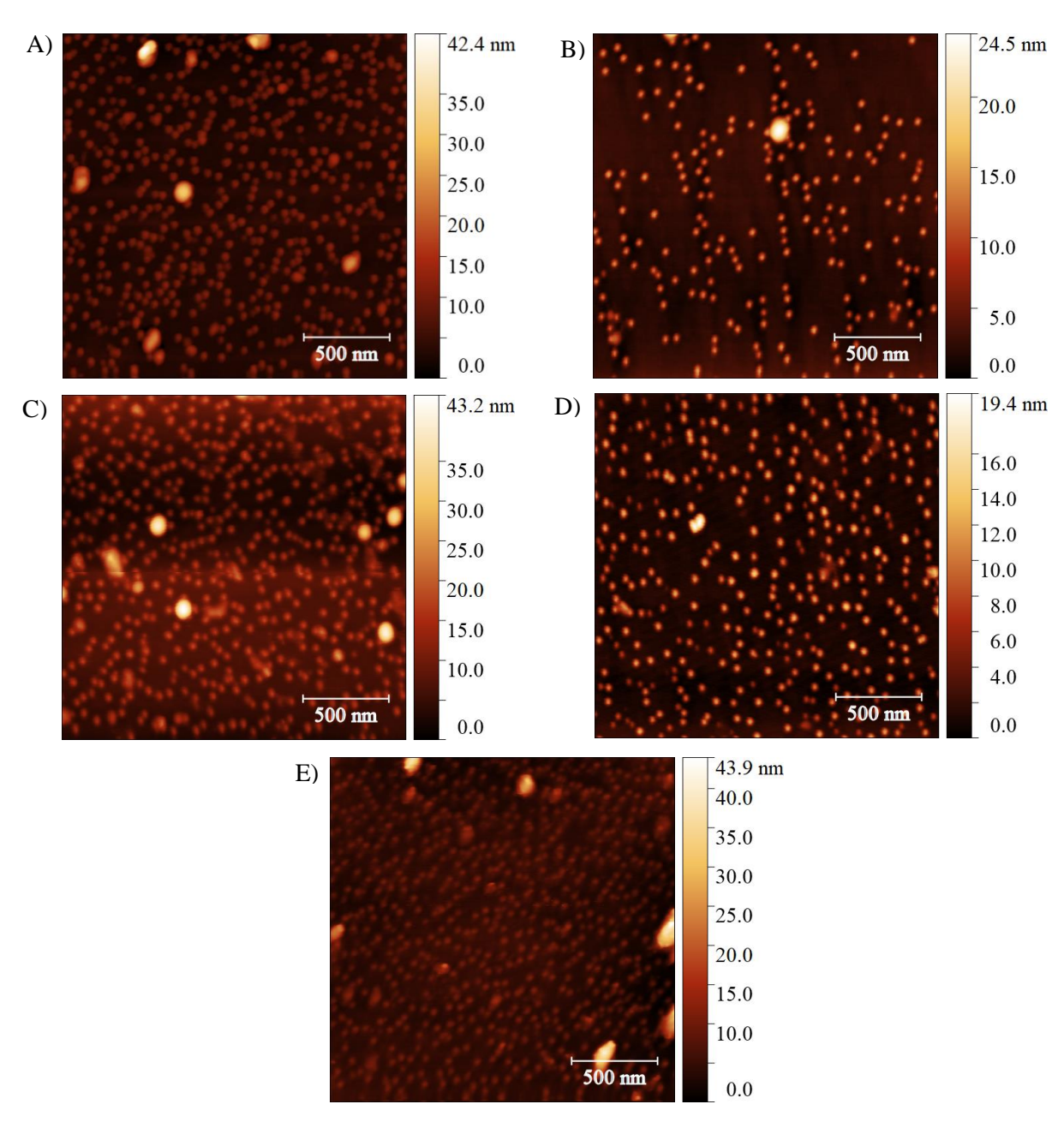


Figure 76 AFM Images of InAs QD samples with a Bi flux during QD growth between 0 to 3.5 nA. Where, A) 0 nA, B) 1.2 nA C) 2 nA D) 2.6 nA and E) 3.5 nA.

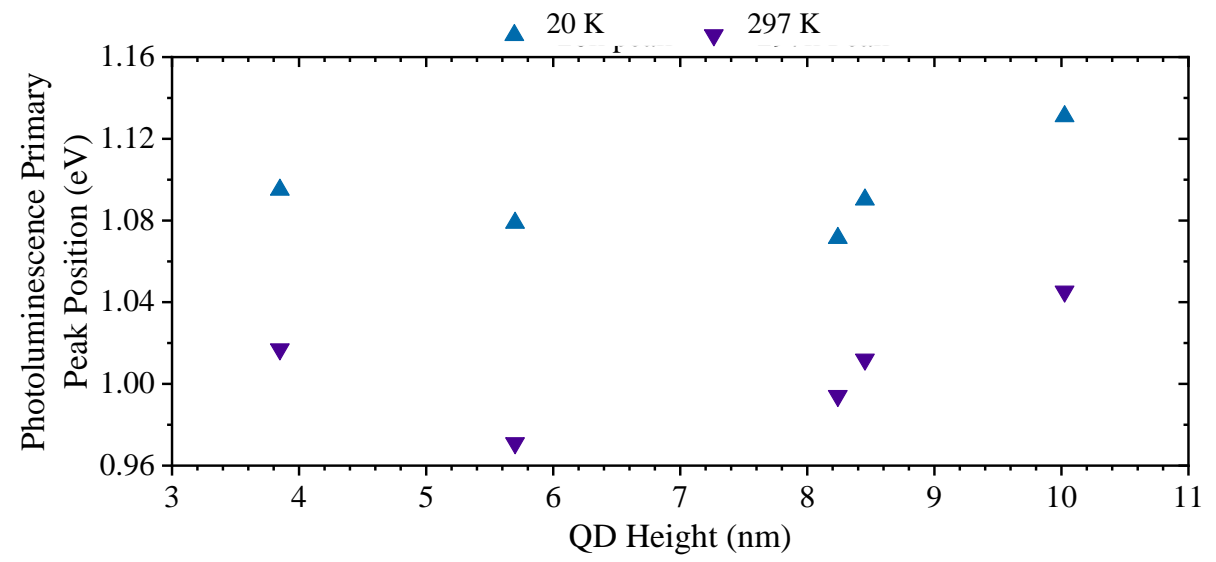


Figure 77 QD height vs PL peak energy for Bi flux QD series with fluxes between 0 to 3.5 nA.

beyond the analysis reported here. It is unlikely however this effect would be beyond marginal at the growth temperature used. However, the RHEED reconstruction on the surface prior to capping remained a C 1x1 with satellite spots, showing QD formation but providing no indication as to the remaining surface Bi. Irrespective of the presence of Bi the capping process is known to alter the buried QD morphology and is another factor not directly measured within this study [91], [92]. This bears relevance as the morphology measurement are taken from the surface QDs. However, the comparative luminescence measurements are of the buried QD layer. In order to assess either of these cases it would require cross sectional TEM and EDX of the buried QDs and additional sample with a post QD formation Bi deposition to isolate the two effects. All assertions presented within the study assume that the capping process is consistent across the range to a degree that any difference is marginalised in comparison to the observed trend of interest. To conclude the interaction with the Bi during QD

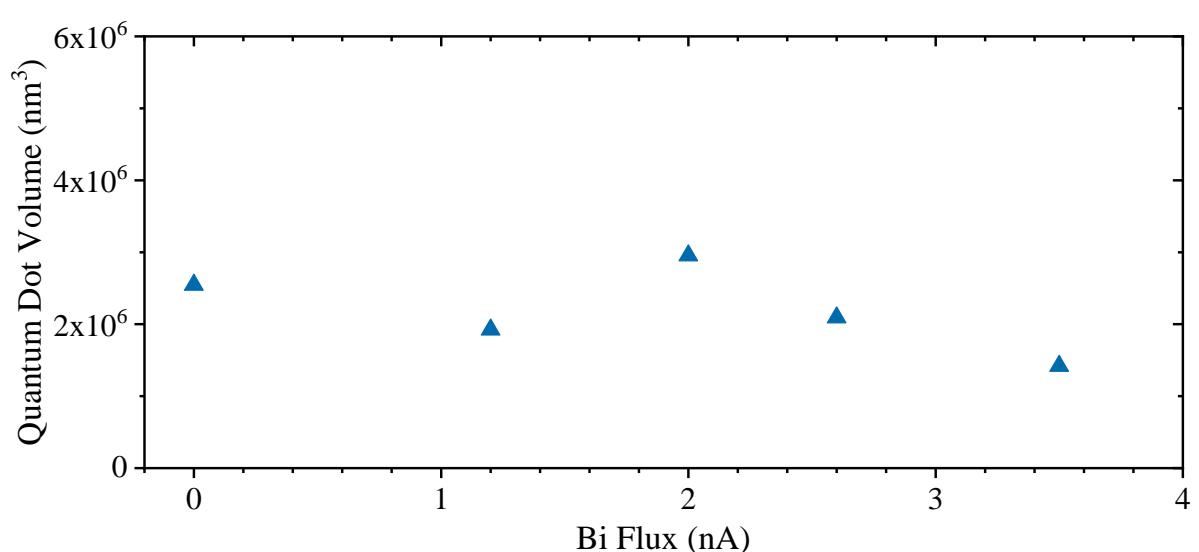


Figure 78 QD volume density for InAs QD samples with InAs QD samples with Bi flux during QD growth of between 0 to 3.5 nA,

formation under the tested growth conditions in non-trivial to describe as the complete experimental variations of QD growth formation and capping.

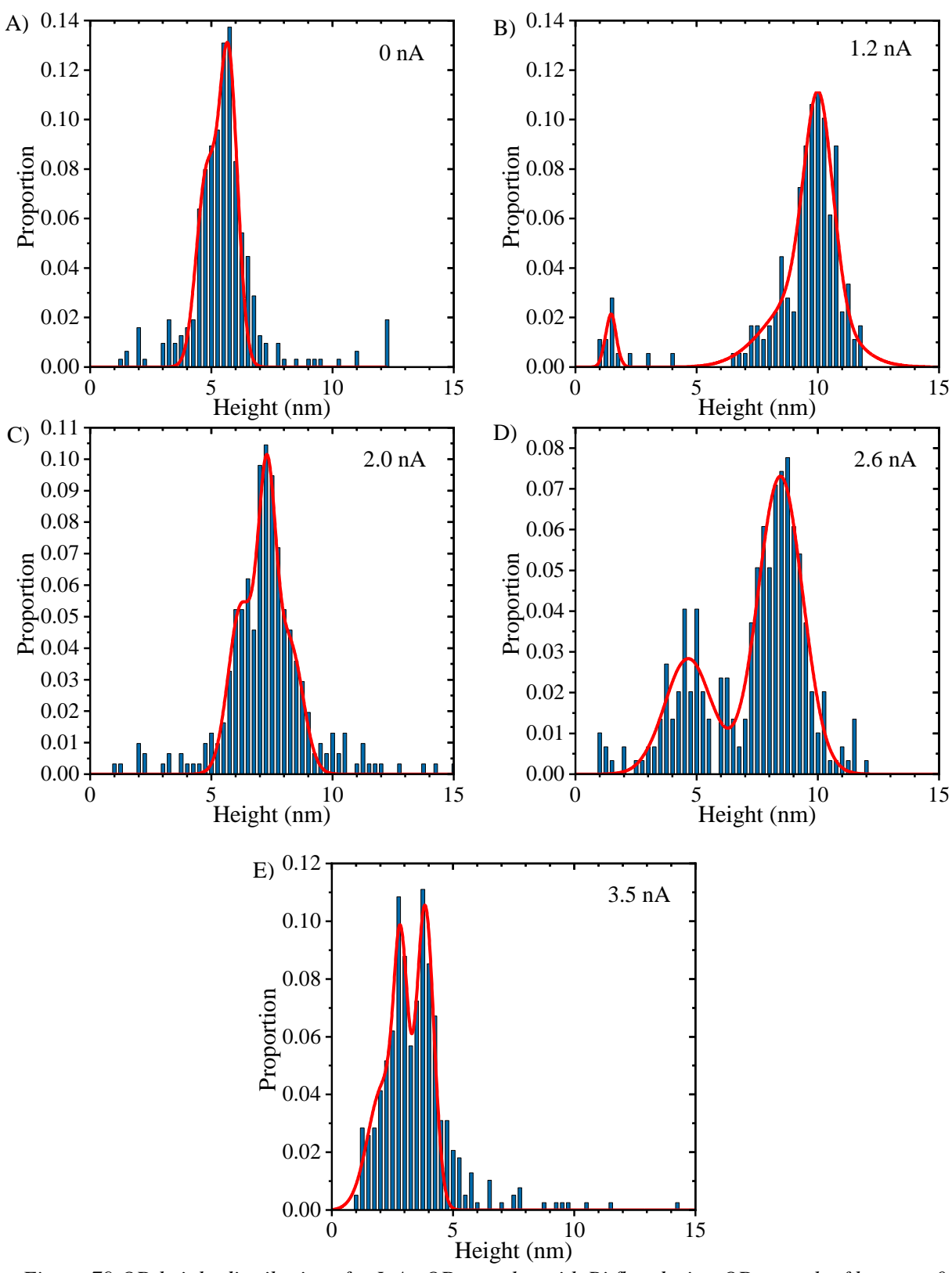


Figure 79 QD height distributions for InAs QD samples with Bi flux during QD growth of between 0 to 3.5 nA. Where, A) 0 nA, B) 1.2 nA C) 2 nA D) 2.6 nA and E) 3.5 nA. Experimental data is indicated by blue bars with gaussian fits shown by the red line.

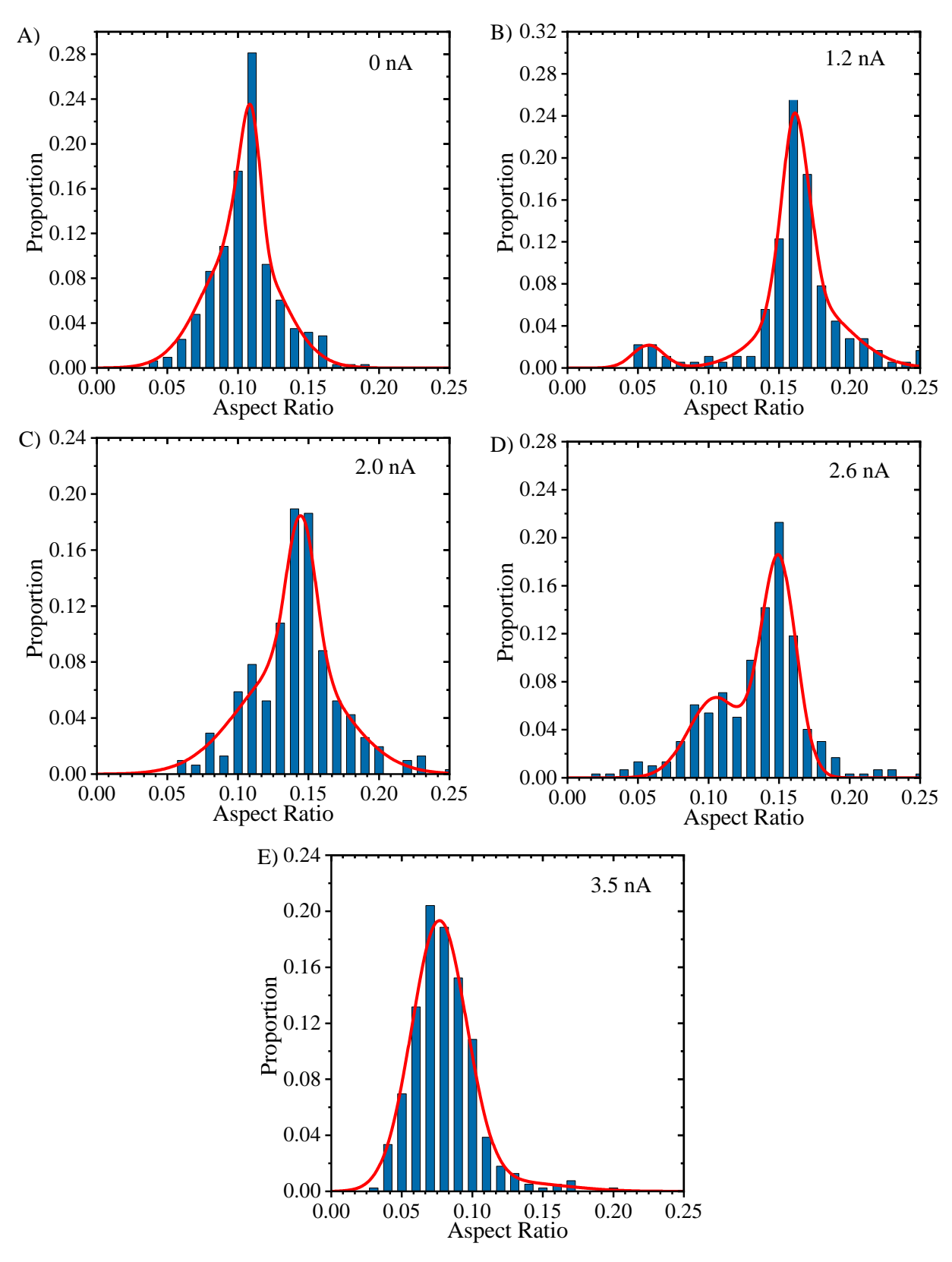


Figure 80 QD aspect ratio distributions for InAs QD samples with Bi flux during QD growth of between 0 to 3.5 nA, Where A) 0 nA, B) 1.2 nA C) 2 nA D) 2.6 nA and E) 3.5 nA. Experimental data is indicated by blue bars with gaussian fits shown by the red line.

The results observed within this section are particularly interesting when compared against a similar study of Bi alteration conducted by N. Bailey. In his work the alteration of QD morphology with increasing Bi flux gave a more simplified relation with linear increase in QD height observed [29]. This aligns well with reported improvements in height and aspect ratio with the application of a Bi surfactant [35], [48]. This study agrees with these finding initially, an enhancement to QD height along with dramatic blue shift was observed at lower Bi fluxes. However, when the Bi supply is extended beyond 1.2 nA the results presented deviate from the previously reported trend in the literature. One key difference in accounting for the this is the increased growth temperatures of some of these studies. The increased rate of Bi desorption from the surface at 510 °C with a 30 °C degree increase from 480 °C between this study would account for a 160% increase in the relative Bi desorption rate. This based on the exponential increase in flux from a standard Bi effusion cell with the same temperature increase. It is clear in these studies that Bi incorporation did not occur [29], [93]. This then defines the surface quantity of Bi is a function of the supplied Bi flux and the effective Bi sicking coefficient. Estimating the effective sticking coefficient by accounting for the increased rate of Bi desorption at 510 °C, estimated as a 160 % increase. This would equivalated the Bi on the surface in the study by N. Bailey et al to fall within the equivalent range of 0 to 1 nA of the scale presented with this growth study at 480 °C.

The increased heights observed can be partially attributed to the increased indium mobility combined with the surfactant effect at 510 °C. Aspect ratios and populations distributions remained similar between both studies. This infers a temperature insensitivity to the Bi surfactant effect over the 30 °C range, which has also been reported in other studies [93]. It would also strongly support that the surfactant thickness under equilibrium is the key parameter for controlling QD morphology by Bi surfactant. However in studies conducted at similar QD growth temperatures of 470 °C and comparable structures, the Bi flux levels reported are very low ~ 1.0 × 10–8 Torr [48]. In another study with a growth temperature range between 475 to 500 °C and Bi flux of 1.09 nA (Beam equivalent pressure of ~8.8 × 10<sup>-9</sup> torr). There was good agreement with observations of increased height and aspect ratio for the 1.2 nA Bi flux sample. contents[36]. Reviewing the literature, I can find no case where the Bi flux matches the range investigated within this study. The 1.2 nA sample fits with available data, however this accounts for why a similar trends for the higher flux sample within the QD literature haven't been previously reported. It is also a key finding that as previously seen there are drawbacks to oversupply of Bi for use as a surfactant However these can be turned to an advantage depending on the desired application and QD design criteria.

#### 4.4.3 Power Dependent PL

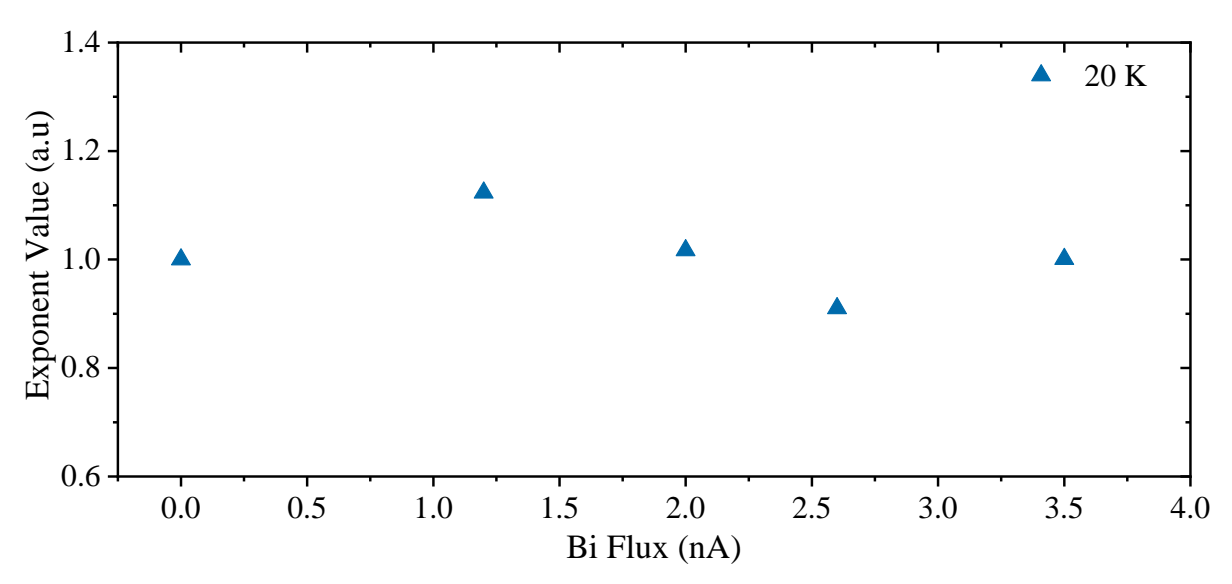


Figure 81 Power dependent exponents for InAs QD samples with InAs QD samples with Bi flux during QD growth of between 0 to 3.5 nA, measured at 20 K.

Assessing the optical characteristics of the Bi flux series, the power dependent PL exponents at 20 K are shown in Figure 81. Indicating that across this entire series the luminescence remains radiatively limited with all values close to 1. The integrated PL spectra vs the excitations powers are shown in Figure 83 and have been fitted with equation (11). The power range tested is similar across the entire series. The samples overall luminescence across the series as shown in Figure 73 is comparatively excellent and as such sustained a measurable signal across approximately 4 orders of magnitude. This give high confidence in the fitting and is another indication of high material optical quality. The addition of Bi had a constant effect in this regard, and no trends are observed in minimum power to achieve a measurable signal. There are no indications in this series that any sample heated during the 20 K PL measurements, although this may just be due to a better contact between the samples and copper mounting plate.

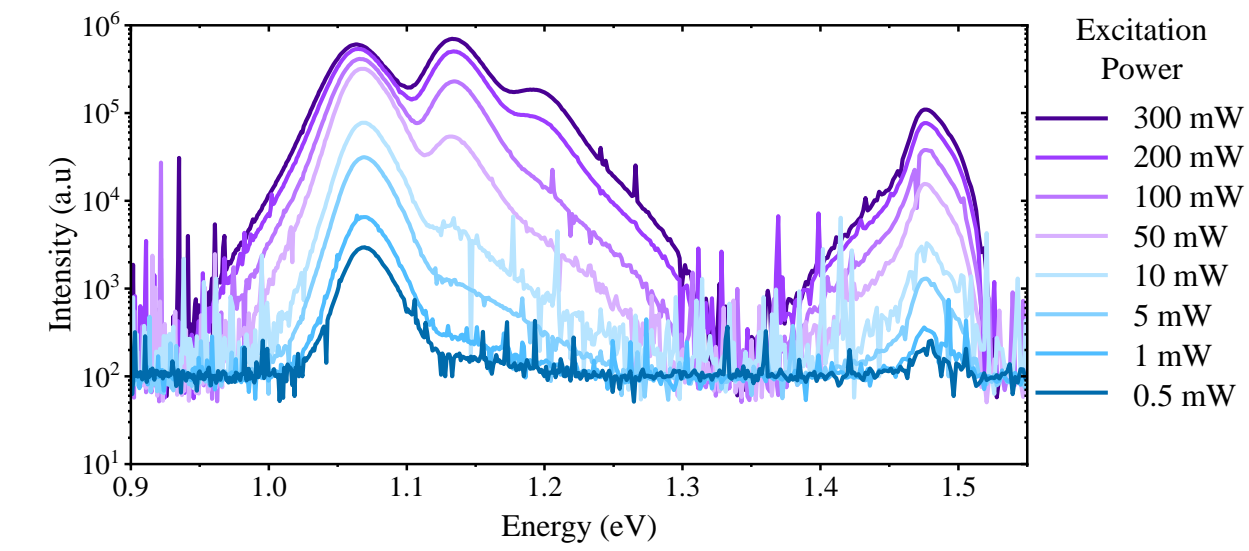


Figure 82 PD PL of sample grown with 2 nA Bi flux.

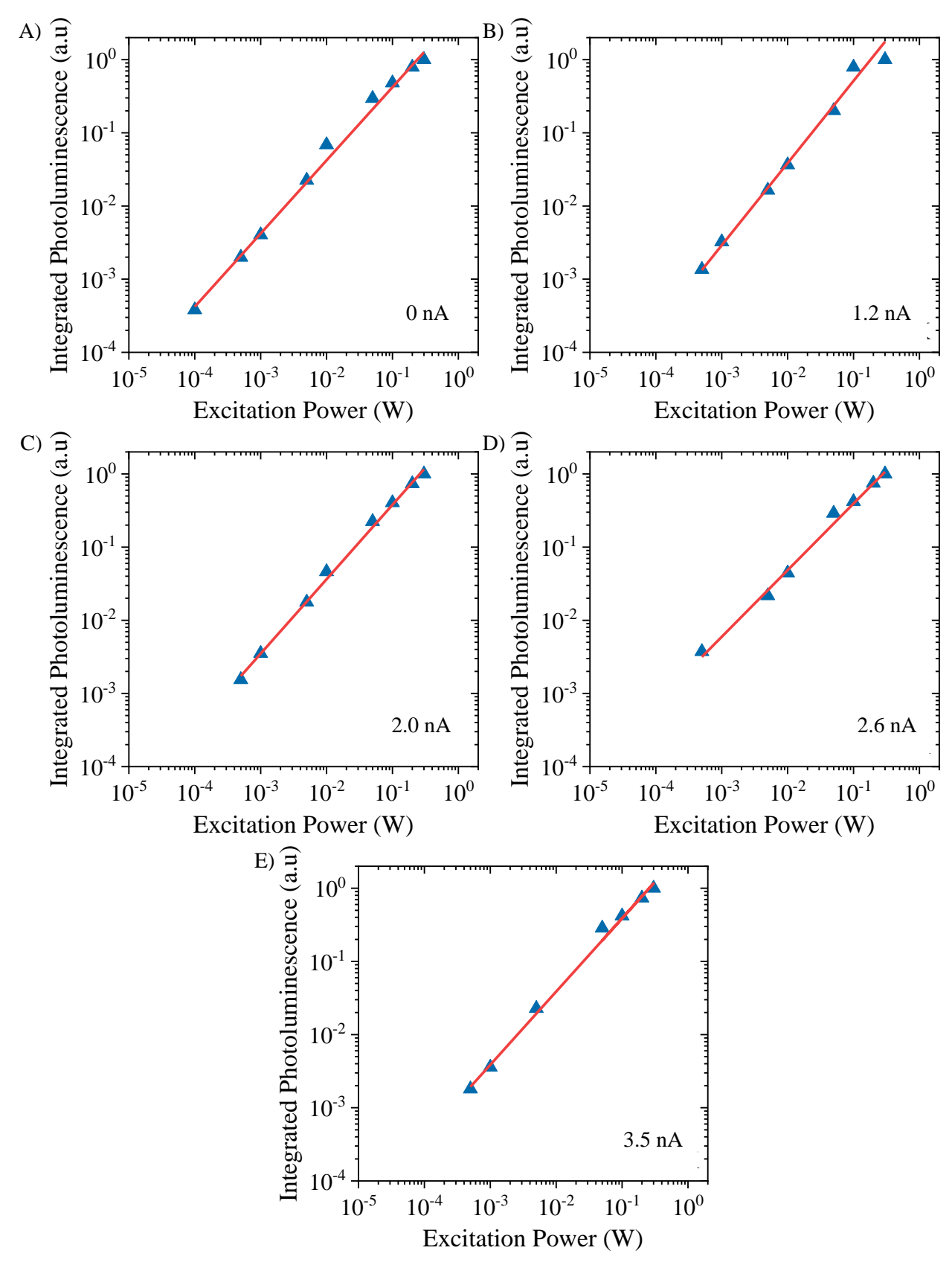


Figure 83 Normalised integrated photoluminescence vs excitation power for InAs QD samples with Bi flux during QD growth of between 0 to 3.5 nA. Where, A) 0 nA, B) 1.2 nA C) 2 nA D) 2.6 nA and E) 3 5 nA

The spectra shown in Figure 82 from the PD PL of the 2 nA sample demonstrate the state filling we've previously observed in the QD's with this series. Contrasting this to the PL of the 480 °C 0 nA Bi sample shown in Figure 65A and the state filling appears similar although the emission from each state is wider in the Bi surfactant assisted sample. Both of these samples have similar QD densities which aligns with the similar levels of state filling observed in the PL. There is a large difference in the emission around the substrate with 2 distinct shoulders both above and below the substrate emission. Previously this was attributed to an ultra-thin InAs QW formed from the wetting layer and this contribution still remains as the higher energy shoulder to the substrate peak as previously seen. However, the lower energy shoulder was attributed to a small population of 1 to 2 nm QDs as also seen in the PL of the thinnest sample grown with 2.2 ML of InAs shown in Figure 41B. There is no indication of Bi incorporation into any of these layers. The impact remains isolated to effect of the surfactant layer on morphology and control of the interdiffusion of Ga and In. The rate of the interdiffusion across the series changes with the Bi flux appearing initially enhanced at 1.2 nA before reducing with increased Bi flux.

## 4.4.4 Temperature Dependent PL

Temperature dependent PL measurements are shown in Figure 84. The change in PL emission with temperature seems consist across the series with a single exception. The sample grown at 1.2 nA of Bi flux showed a more pronounced increase in the emission at lower temperatures with approximately a further half order of magnitude increase observed. The data has been fitted with the dual Arrhenius equation given in equation (12).

The values extracted for Ea<sub>1</sub>, Ea<sub>2</sub>, C<sub>1</sub> and C<sub>2</sub> are plotted in Figure 85 and Figure 86. The energy Ea<sub>1</sub> would be indicative of carrier escape into the GaAs capping layer or InAs wetting layer. For the first 3 samples within the series the energies well align to the energy difference. However, for the samples grown at 2.6 and 3.5 nA of Bi flux the energies drop without a commensurate blue shift in the PL. This indicates a new mechanism for carrier escape is starting to overshadow escape into the capping layer or wetting layer. This would likely be caused by the increase in the population of smaller QDs within these two samples as seen in Figure 79D and E. The energies of these QDs lies ~50 meV below the GaAs cap as measured from emission can at high optical powers. As shown In Figure 82, This would suggest there is a large quantity on non-radiative defects present within these small QDs and the energy difference could well account for the trend in Figure 85A. Alternatively it may also be considered that with the coincidence of the emerging smaller QD populations with higher Bi fluxes that a 2 stage carrier escape mechanism is become more prevalent. This would align with the observed outlier at 2 nA, in which the measured QDs under AFM showed a larger separation than in 2.6 and 3.5 nA with much lower 1 to 2 nm QD population than the 1 to 2 nA sample. The closest approximation for the dispersion

of 1 to 2nm QD is 0 nA and here a slight increase in Ea<sub>1</sub> is observed, which corresponds to an increase in measured QD height higher quantum confinement and expected blue shift in PL emission.

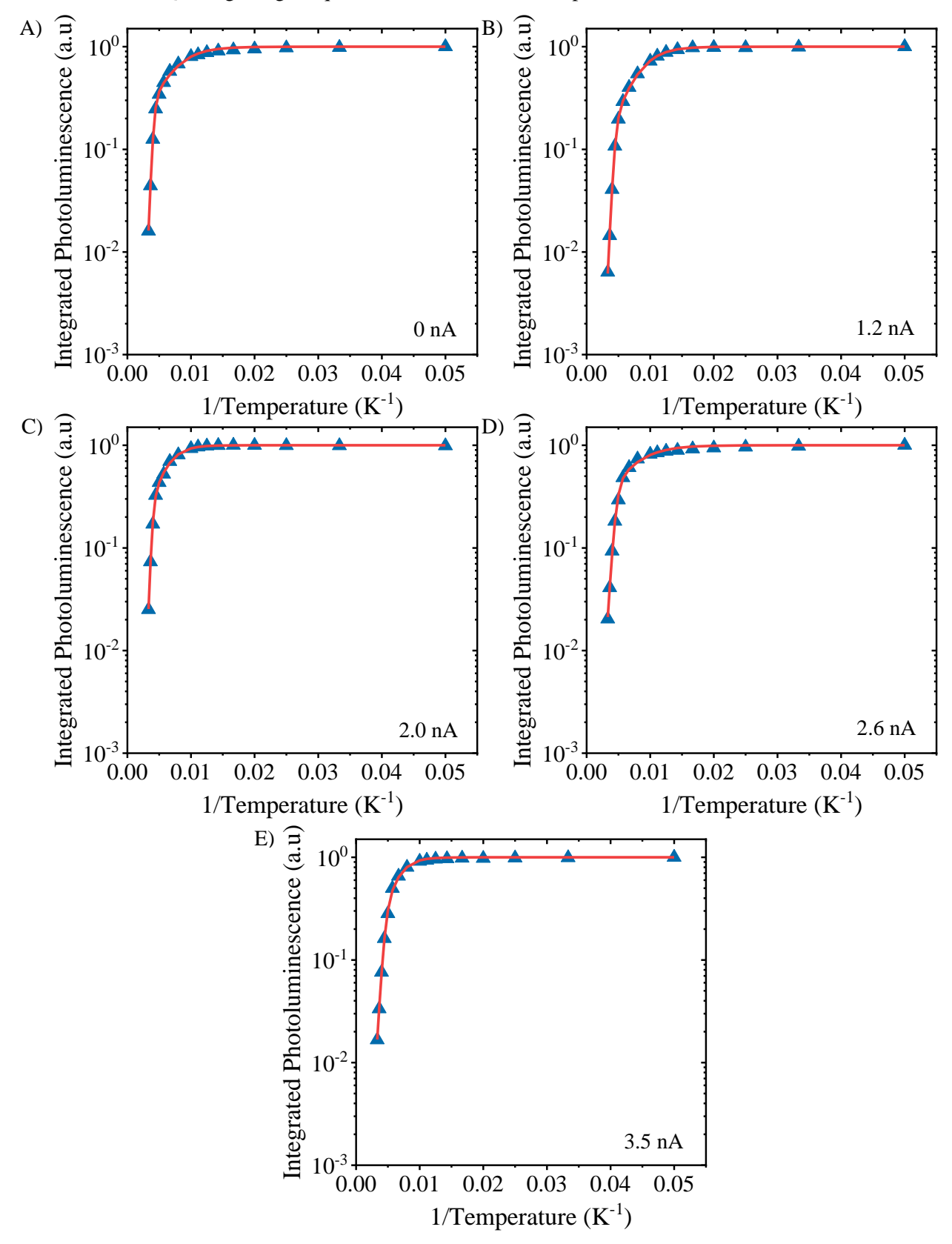


Figure 84 Normalised integrated photoluminescence vs inverse temperature for InAs QD samples with Bi flux during QD growth of between 0 to 3.5 nA. Where, A) 0 nA, B) 1.2 nA C) 2 nA D) 2.6 nA and E) 3.5 nA.

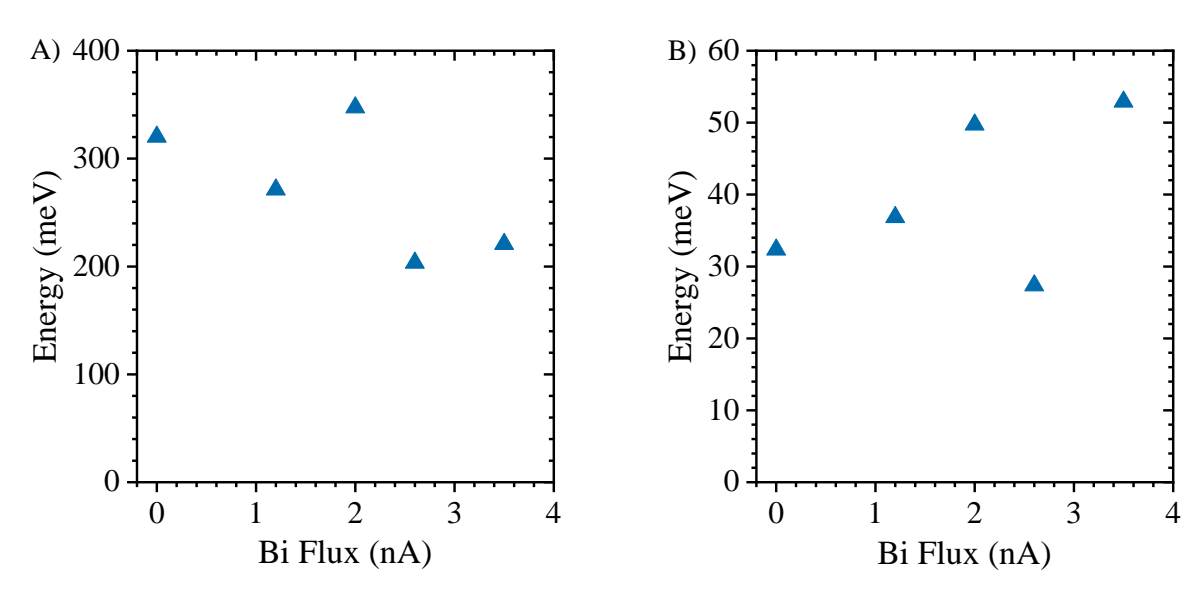


Figure 85 Non radiative recombination activation energies extracted from fitted temperature dependent photoluminescence for InAs QD samples with Bi fluxes of 0-3.5 nA

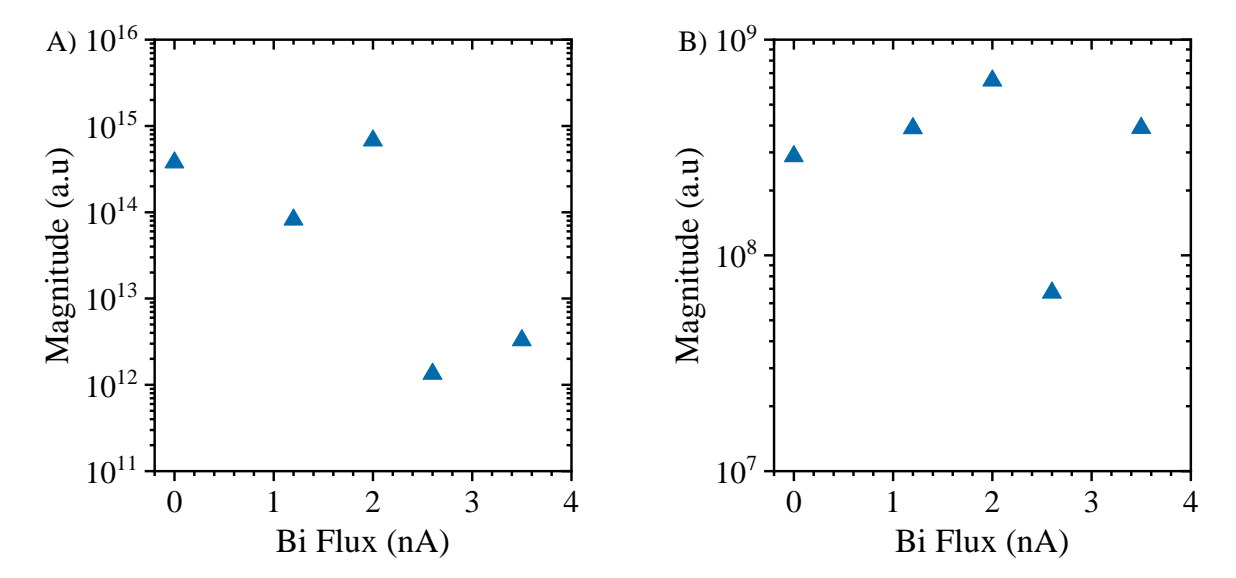


Figure 86 Non radiative recombination constants extracted from fitted temperature dependent photoluminescence for InAs QD samples with Bi fluxes of 0 to 3.5 nA

The energies extracted for Ea<sub>2</sub> are indicative of those associated with phonon assisted non radiative recombination. It can be observed there is a general linear increase in the energies extracted with increasing Bi flux. The deviation from this trend at 2.6 nA is also reflected in a lower-than-expected value for Ea<sub>1</sub>, C<sub>1</sub> and C<sub>2</sub>. This would be a fitting artifact where the Ea<sub>1</sub> process is remaining dominant down to lower temperature than in the other samples and is skewing the energies extracted. The phonon processes that dominate the Ea<sub>2</sub> energies are further complicated by the relative strains that will be observed for bimodal distributions of the QD population as well as the potential existence of single and multiple phonon assisted recombination pathways at play. In addition to the likely presence of trap assisted recombination (SRH) also present. Accounting for all these processes within the fitting is not fundamentally possible as it would necessitate to many degrees of freedom to allow for confidence in

the values extracted. This is a fundamental limit of the accuracy of the TD PL study when probing the defect mechanisms.

## 4.5 QD Study Conclusions

This study has demonstrated the growth of InAs QDs on 001 GaAs substrates both with and without a Bi surfactant. This has been conducted under conditions optimised for high optical quality and lower energy emission. This identified for the experimental conditions given in the growth methods that 2.7 ML of InAs at 480 °C was optimal for these criteria. It was found that a small application of 1.2 nA of Bi flux increased QD heights and aspect ratio. This came at the cost of increased In/Ga intermixing which negatively impacted the optical quality at 297 K but was recovered at 20 K. Further supply of Bi flux between 2 to 3.5 nA was found to impede surface In mobility and QD coalescence. In all samples it was observed that the emission energy increased. This in contradiction to the reduced quantum confinement that would be expected based on the trends seen in QD height. The rate of Ga and In interdiffusion across the series changes with the Bi flux appearing initially enhanced at 1.2 nA before reducing with increased Bi flux. Roughly reaching parity with the 0 nA control at 2.6 nA of Bi flux. The interdiffusion was most prevalent in the taller QDs of the series. While the cross over indicates there is a critical Bi surface coverage thickness at both In and Ga mobility is suppressed. This study therefore shows the limitations of Bi oversupply but gives a promising indication of the ability to alter QD morphology at Bi fluxes between 0 to 2 nA. The lowest energy emission achieved within this study was for the sample grown at 480 °C 2.7 ML of InAs and without a Bi surfactant. This emitted at 1.049 eV and 0.971 eV for PL measurements at 20 and 297 K respectively. Further studies would be well justified to continue within this parameter space as would additional investigations to corroborate the finding of this chapter with cross section TEM and EDX of the buried QDs. It may also be interesting to conduct post growth annealing of the QD structures to see how the morphology continues to evolve.

# 5. Growth of Studies of Epitaxial Al<sub>x</sub>Ga<sub>1-x</sub>As<sub>y</sub>Bi<sub>1-y</sub> on 001 GaAs

High sensitivity avalanche photodiodes (APDs) are the backbone of fibre telecommunications networks as well as having huge potential in applications such as LIDAR [94], [95]. This specialised class of diode operates at high reverse bias and speed amplifying weak optical signals using a process known as impact ionisation. However, existing APDs suffer from excess noise which limits their sensitivity and speed. There are two underpinning mechanisms behind this, firstly the stochastic nature of the impact ionisation process causes excess noise which is exacerbated by increased gain limiting the sensitivity [96]. Secondly due to multiple transits within the high field avalanche region most APDS have a higher gain bandwidth product (GBP) [97]. This diminishes the device performance with increase operating frequency. Both of these processes are dependent on  $\alpha$  and  $\beta$ , the electron and hole ionisation rates respectively. Optimal performance is achieved when only a single carrier species initiates the avalanche multiplication process [96]. Hence drastically different values of  $\alpha$  and  $\beta$  are desirable. These values are dependent on the band and crystal structure of the material used for the avalanche region of the APD as a function of the applied electric field.

Commonly competing APDs based on materials such as silicon possess low noise and reasonable multiplication. However, Si's indirect bandgap necessitates thick absorbing layers which limit its speed, further its detection is also limited to wavelengths below 1  $\mu$ m due to the intrinsic bandgap [98]. To achieve the high gain and operating speed necessitated for the LIDAR and fibre telecommunications a direct bandgap material with drastically different  $\alpha$  and  $\beta$  coefficients is desirable. Significant efforts have been spent in developing novel III-V materials. To meet this requirement investigations into ternary and quaternary systems of AlGaAs and InGaAsP have been conducted. These showed that alloying commonly causes changes significant changes in both  $\alpha$  and  $\beta$  [99], [100]. This can produce a III-V alloy with an enhanced value of the ionisation ratio k, shown in equation (14) . However, it has yet to provide a mechanism for tuning a singular coefficient independently. Controlling a singular ionisation coefficient has proven difficult to achieve with attempts utilising band structure engineering techniques such as heterojunctions or QDs [101]–[105]. However, the increased complexity of these processes has not yielded a reliable procedure which significantly enhanced the ratio of the ionisation coefficients k. Minor success has been reported by Ren et al with a small enhancement of  $\alpha$  resulting from conduction band edge discontinuity without alteration of  $\beta$  [102].

$$k = \frac{\alpha}{\beta} \tag{14}$$

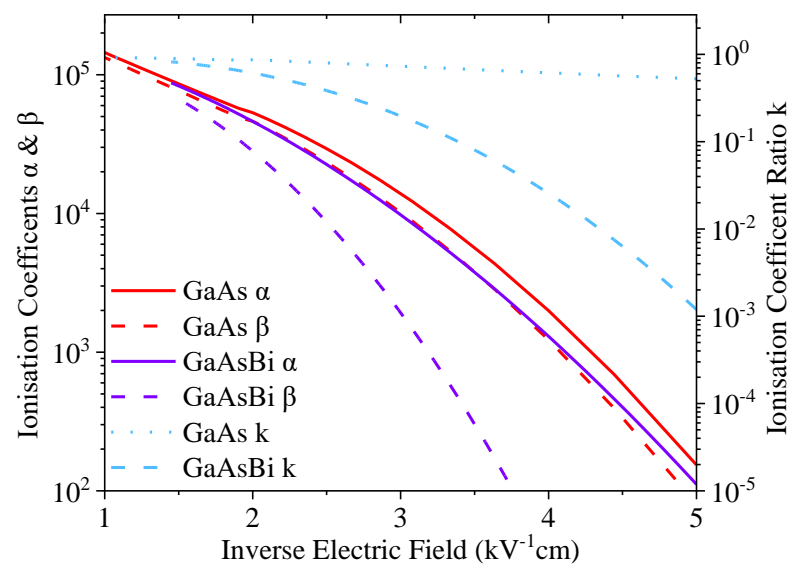


Figure 87 Comparative graph of  $\alpha$ ,  $\beta$  and k of GaAs & GaAs<sub>0.96</sub>Bi<sub>0.04</sub>[106].

Alloying with Bi into GaAs has however demonstrated remarkable results in providing a novel mechanism to tune and engineer the impact ionisation process. Bi alloyed into GaAs, at contents between 0.7 - 4 at %, has shown that the ionisation ratio can be improved by an order of magnitude, as shown in Figure 87 [106]. Bi when incorporated reduces the band gap of GaAs by up 88 meV per at% Bi for contents up to 5 at% [107]. However most crucially for ADP engineering it predominately affects the valence band structure, resulting in an increase in the valence band spin-orbit splitting energy  $(\Delta so)[108]$ . This alteration increases the energy barrier for holes to scatter from the heavy hole and light hole bands into the split off band, thus increasing the energy threshold for hole ionisation[109]. This is illustrated in Figure 88. where the energy level of carriers between a single impact ionisation event is shown. It is of note that carriers generated from impact ionisation can themselves go onto impact ionise. The limitation of the results shown in the study of GaAsBi by Yuchen. Liu et al, lie in the intrinsic value of k for starting alloy GaAs, which is close to unity. Initiating Bi alloying into a more suitably tuned III-V system may be able to improve the k values further. The ternary III-V Al<sub>0.8</sub>Ga<sub>0.2</sub>As possesses a much more desirable intrinsic ionisation ratio of 0.2 compared to 0.95 at 1.5 kV<sup>-1</sup>. The addition of Bi into this ternary to produce the quaternary Al<sub>x</sub>Ga<sub>1-x</sub>As<sub>y</sub>Bi<sub>1-y</sub> could yield a material that matches or exceed Si level noise performance without the draw backs of an indirect bandgap.

It is with this aim that I present a study of growth of the quaternary alloy AlGaAsBi as a potential APD material. To date there is no report within the literature of any growth of this quaternary alloy. There has been a singular study conducted by N. Bailey et al which gave indications that Bi incorporation remained insensitive to Al content between 30-80 at% Al [110]. However, analysis was limited to XRD and RBS with no optically active material produced. Further there was no exploration of parameter space to establish how key growth factors would impact the alloy. This effectively gave a small snapshot into AlGaAsBi and was based on the assumption that AlGaAsBi would behave similarly to AlGaAs

when altering the group III contents. In effect that the impact would be limited to subtle difference in growth temperature with no further considerations. Therefore, a significant amount of work remains to confirm the viability and properties of this alloy for optical applications and to fully understand operating flexibility available in parameter space for epitaxial growth on GaAs.

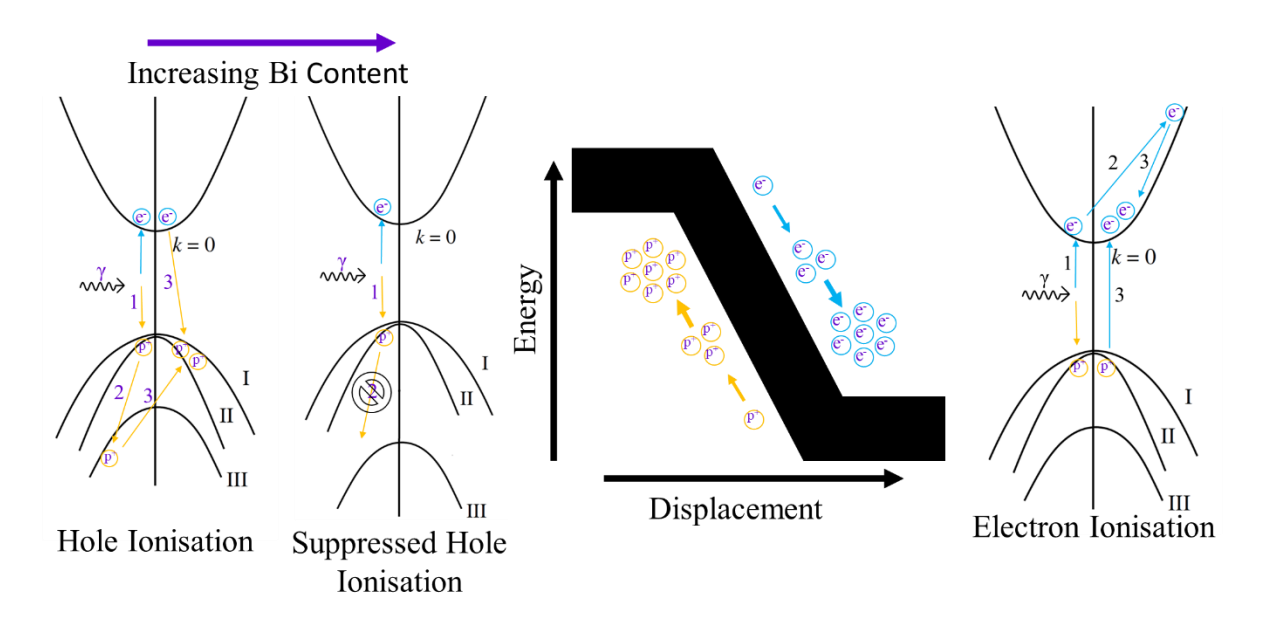


Figure 88 Diagram of the impact ionisation process and effect of Bi incorporation on band structure.

## **5.1. Growth Methodology**

All samples within this series were grown on an Omicron MBE STM system described in section 3.1.1. Standard calibration techniques outlined in the MBE experimental section were used for determinations of substrate temperatures, cell fluxes and the Ga:As unity value at the selected growth rate. Sample growth occurred over the span of 3 weeks with temperatures calibrations conducted prior to and post the series completion. Additional calibrations of growth rates and fluxes were conducted at the start of each week with drift subsequently accounted for in effusion cell temperatures as required. The sample architecture used is shown in Figure 89 and is dictated by the analysis techniques utilised within this study. Capping thickness is a balance between sufficient barrier thickness to confine carries and prevent

20 nm GaAs	560 °C
20 nm Al <sub>0.3</sub> Ga <sub>0.7</sub> As	590 °C
100 nm AlGaAsBi	280-340 °C
300 nm Al <sub>0.3</sub> Ga <sub>0.7</sub> As	590 °C
UD GaAs Substrate	

Figure 89  $Al_xGa_1$ -y $Bi_1$ -y series sample structure.

oxidation of the AlGaAs allowing for photoluminescence investigation. While maintaining the total

sample thickness below 150-200 nm to allow for Ion beam analysis by TOF ERD and RBS across the entire structure. Due to this the thickness of the AlGaAsBi region is well below the critical thickness for relaxation commonly observed in thickness GaAsBi samples at the intended target Bi contents.

Cleaved 11.8 x 11.4 mm undoped GaAs substrates were out gassed at 380 °C for 20 minutes followed by the removal of the native oxide at 620 °C under an As<sub>2</sub> flux for 40 minutes. The Al<sub>0.3</sub>Ga<sub>0.7</sub>As buffer was then grown at 590 °C at a rate of 0.3 MLs<sup>-1</sup> to a thickness of 300 nm. The Ga:As<sub>2</sub> flux ratio during was 1:1.7. An allowance of 5 minutes was given to allow for changes in cell and substrate temperatures following completion of the buffer growth. This included stabilisation of the surface reconstruction, alteration of the Ga and Al cell temperatures, lowering of the III:As<sub>4</sub> flux ratio to 1:1.1 changing the As species from As<sub>2</sub> to As<sub>4</sub> and lowering the substrate to temperature to 320 °C. Ga and Al cell temperature are varied for the Al content series to alter the Al content while maintaining the 0.3 MLs<sup>-1</sup> growth rate. Substrate temperature was varied between 280-340 °C for the temperature series with 320 °C the common centre point sample. While Bi cell temperature was varied to output a Bi flux between 0.8-2.8 nA for the Bi flux series with 1.4 nA used as the common centre point sample. Post the buffer layer a stabilised 2x4 reconstruction as shown in Figure 90a was visible. Only a single azimuth can be seen due to the heater stage geometry. The growth rate was fixed at 0.3 MLs<sup>-1</sup> to for deposition of 100 nm of AlGaAsBi with a concurrent opening of Ga, Al and Bi shutters for growth.

Post AlGaAsBi growth was followed by an allowance of 5 minutes to stabilise the surface, post 5 minutes a 1x1 reconstructions remained as seen in Figure 90b. The 5 minutes was also utilised to enact changes to substrate temperature, fluxes and As species. 20 nm of Al<sub>0.3</sub>Ga<sub>0.7</sub>As was then grown at 590 °C at a rate of 0.3 MLs<sup>-1</sup> with a III:As<sub>2</sub> flux ratio of 1:7. This was immediately followed by 20nm of GaAs capping layer to protect the structure from oxidation. The Al cell shutter was closed, and the substrate temperature adjusted to during the growth of the GaAs layer to 560 °C. From measurements of surface

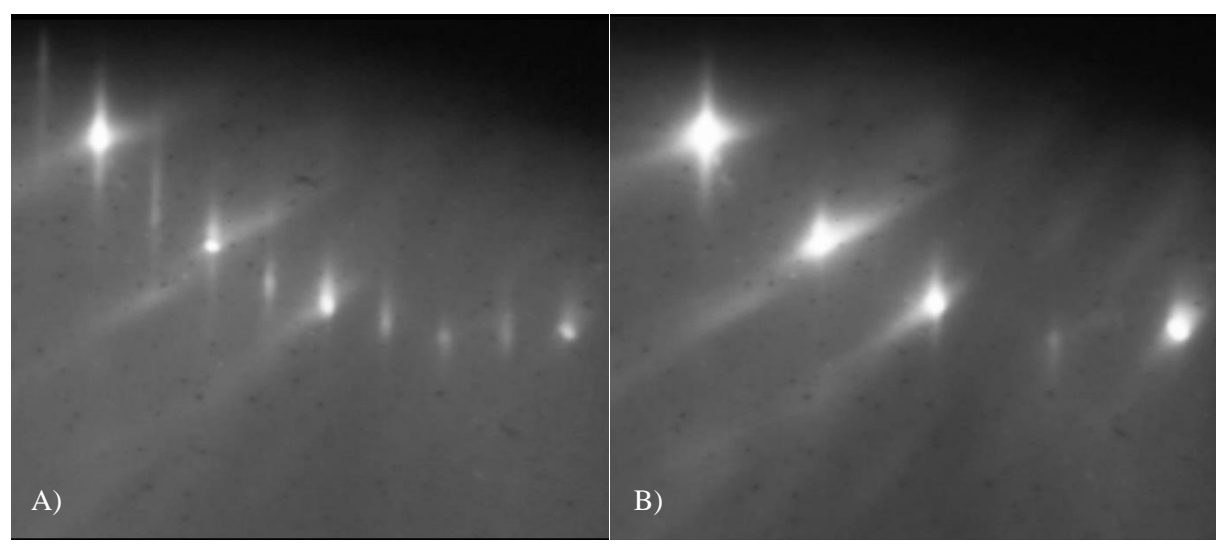


Figure 90 RHEED patterns of the sample surface A) post AlGaAs buffer growth and B) post AlGaAsBi layer growth.

temperature stabilisation, on this system it is expected that 560 °C was stabilised within the first 30 s of the 350 s GaAs layer growth. The growth was conducted at a rate of 0.21 Mls<sup>-1</sup> with a Ga:As<sub>2</sub> flux ratio of 1:1.83. These parameters are well within the optimised window for epitaxial GaAs. Once the GaAs capping layer was completed the heater power was set to standby and allowed to cool under an As flux for 2 minutes prior to unloading.

Prior to commencing of the series two control samples were grown to validate the quantity of the constituent ternary alloys. One was a GaAs/AlGaAs quantum well structure to access the quality of AlGaAs, the structure is show in Figure 91A. The second was an optimised GaAsBi structure grown in an identical sample architecture to the rest of this series. This is features in the Al content series as the 0% Al containing sample. The conditions for these layers are the standard conditions set out previously for the respective material system. Acceptable levels of surface and optical quality were achieved this is demonstrated in the RT PL shown in Figure 91. This was defined by reaching a comparable luminescence intensity with an internal Bi containing standard sample. The wafers were observed to have high quality surface by Nomarski microscopy and good optical quality from the PL The growth parameters calibrated to achieve the growth of the AlGaAs QW control sample were then utilised within the AlGaAsBi study. These two-control samples serve to remove the variable of poor quality AlGaAs and GaAsBi as a consideration in the analysis of the AlGaAsBi quaternary.

This series was directed by PL measurements at 297 K and 004 omega 20 XRD measurements taken at pace with the ongoing growth. The investigations first selected an Al content to use as the centre point for the growth study with subsequent series varying growth temperature and Bi flux. Samples were subsequently analysed by power and temperature dependent photoluminescence at temperatures

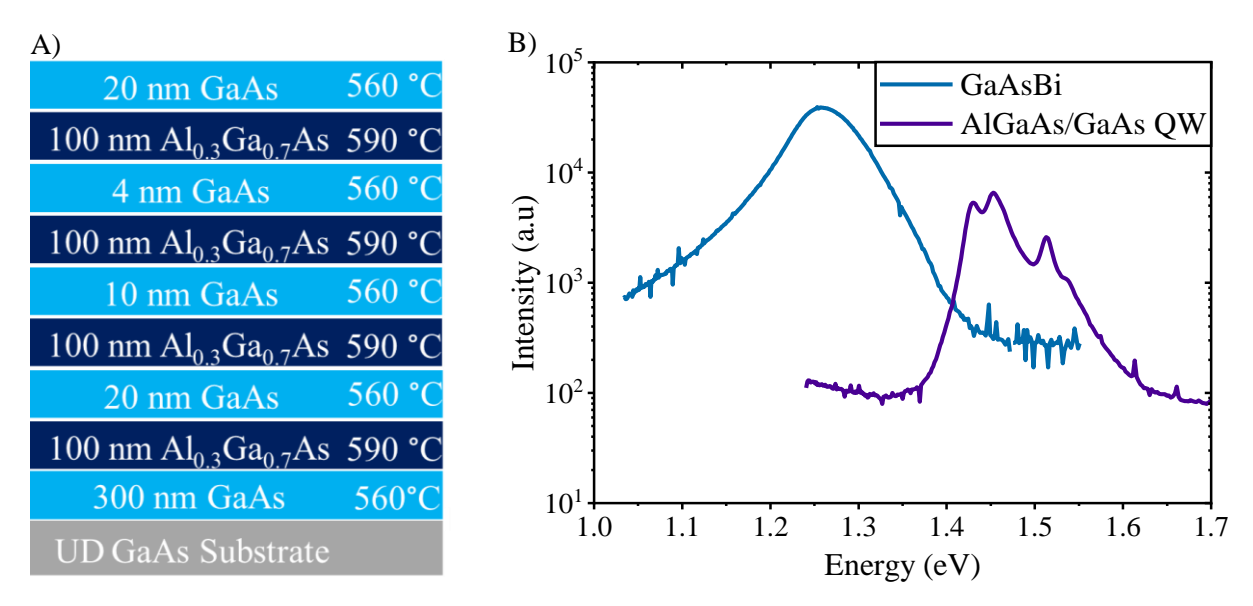


Figure 91 A) AlGaAs/GaAs QW sample structure B) Room temperature PL of control samples for AlGaAsBi growth study featuring a GaAs<sub>0.976</sub>Bi<sub>0.024</sub> and AlGaAs/GaAs QW sample.

between 20-297 K. Further analysis was conducted on sectioned off pieces at the UK national Ion beam centre for ion beam analysis and TEM analysis by Prof Daneil Reyes at the University of Cadiz.

#### **5.1.2 Growth Study Subseries**

Growth studies for the AlGaAsBi system were divided into 3 sub series each focussing on a singular control parameter. The 3-parameter investigated and outlined within this chapter are the Al content by changing the Ga:Al flux ratio. Substrate temperature during AlGaAsBi layer growth and finally changing the group III: Bi flux ratio. All samples in each sub series were measured at pace by PL and XRD. Further in-depth studies by Ion beam, TEM and PD and TD PL analysis were conducted post series completion. The results are discussed collectively within this chapter and grouped by analysis technique.

#### **5.1.2.1** Al Content Series

The initial focus of the first subseries is on the relation between concurrent incorporation of Al and Bi into the GaAs system. This was conducted by incorporating varying quantities of Al into optimised GaAs<sub>0.976</sub>Bi<sub>0.024</sub>. This was done under optimised GaAsBi growth conditions previously described in the growth methods section. Al contents were varied between 0-15 at% on the group III site with a fixed Bi flux and III;As<sub>4</sub> ratio. The Al content values were based on Al and Ga growth rate measurements in preceding test structure samples.

#### **5.1.2.2** Growth Temperature Series

The second subseries focused on the impact of growth temperature with a fixed Al:Ga flux ratio targeting a fixed content of 5 at% Al and Bi flux of 1.4 nA. All growth conditions aside from growth temperature follow the methodology set out in section 5.1. Substrate growth temperature was varied between 280 - 340 °C across 4 samples in 20 °C increments. This series included the centre point sample of 5 at% Al, at a growth temperature of 320 °C.

#### 5.1.2.3 Bi Flux Series

The final subseries focused on altering the III:Bi flux ratio to assess the limits of Bi flux control within growth parameter space. This is centred around the centre point sample of 5 at% Al, Al<sub>0.05</sub>Ga<sub>0.95</sub>As<sub>0.976</sub>Bi<sub>0.024</sub>, grown at 320 °C under a Bi flux of 1.4 nA. The Bi flux was varied between 0.8 – 2.8 nA as measured on the beam flux monitor in the MBE STM reactor. No 0 nA flux sample was investigated due to the known issues of GaAs and AlGaAs when grown at substrate temperatures below 480 °C. The inclusion of Bi negates this by altering the growth dynamics such that it isn't an apple to apples comparison. I also contest that validity of Bi growth is predicated on achieving higher Bi contents, hence our efforts are best focused on focusing on the upper rather than lower limits.

## 5.2 PL 20 & 297 K

#### 5.2.1 Al Content

The photoluminescence shown in Figure 92 for the 0 at% Al containing sample i.e. GaAsBi is typical of what we would expect for a well grown GaAsBi sample of 2.4 at% Bi. The broadness of Pl emission is owing to the large dispersion of localised states at the band edge that is typical of bismide growth [111]. This sample was optimised for optical quality and the growth condition were tuned to reduce the concentration of non-radiative defects within the 100 nm bismide containing layer of interest. The range used for the PL measurements was determined by the layers of interest measurements above 1.55 eV were not taken. This was due to the lack of emission from the Al<sub>0.3</sub>Ga<sub>0.7</sub>As buffer and cladding layers due to no conferment of carrier in these layers, hence further measurements used the range of 0.9-1.55 eV.

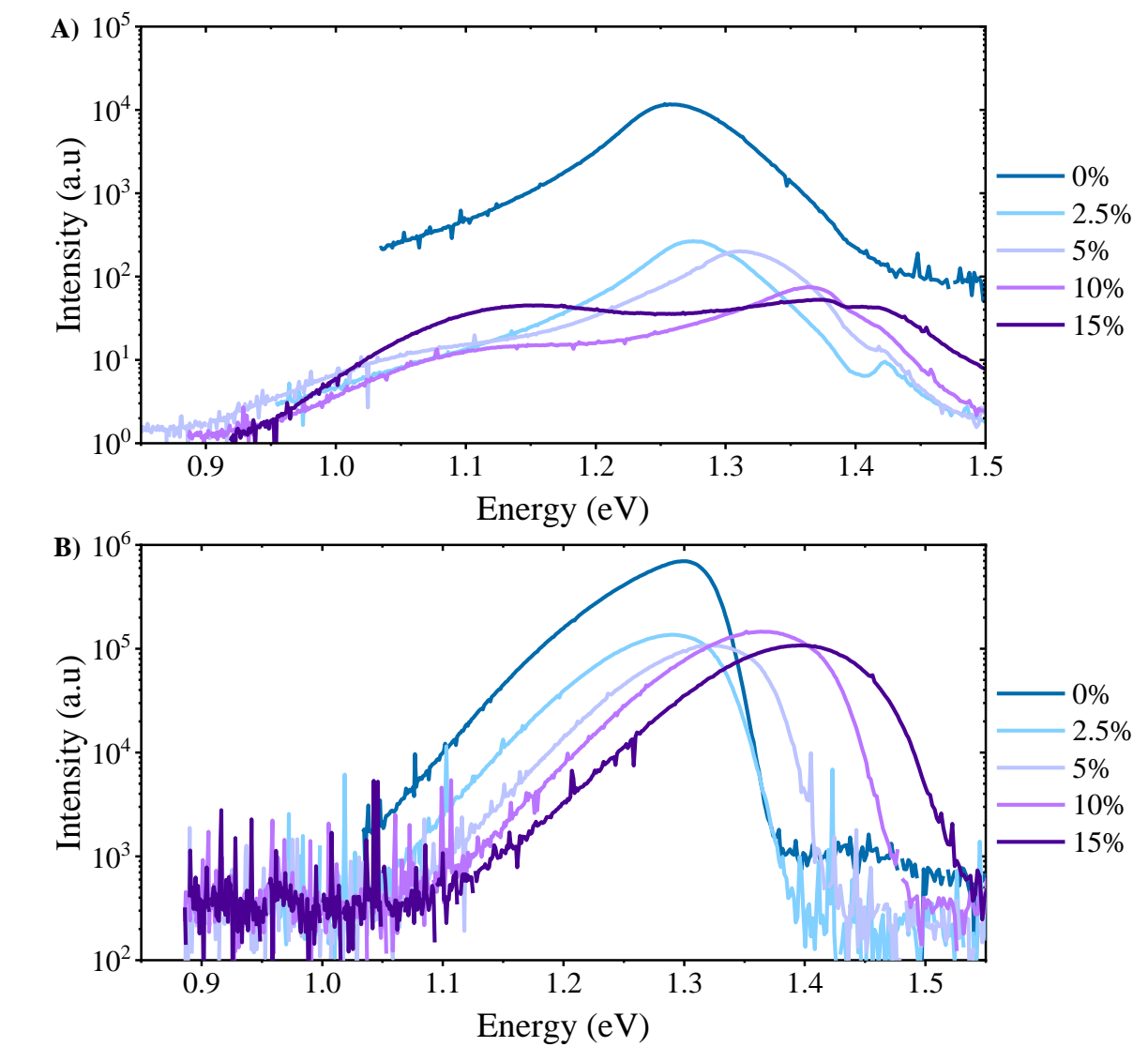


Figure 92 Photoluminescence emission spectra at 100mW excitation for AlGaAsBi samples with Al content between 0-15 at% measured at temperatures of A) 297 K and B) 20 K.

The incorporation of even dilute quantities of Al into the ternary result in a dramatic increase in the concentration of non-radiative recombination centres. This can be observed in reduction of peak luminescence by 2 orders of magnitude when incorporating 2.5 at% Al onto the group III site. Commensurate increases in the Al content do not cause further significant reduction in the PL intensity. Only slight decreases within the same order of magnitude are observed with further increasing aluminium contents. The change in line shape with Al containing samples is most apparent at lower energies between 0.9-1.15 eV. The 0 at% Al sample showed a broad peak from the Bi layer and then falls back to the noise floor

with 200 meV of the peak position. However, in the Al containing layers It can be seen that beyond the initial broad Bi peak there is an additional very broad shoulder between 0.9-1.15 eV. This could indicate the presence of extremely localised areas of high Bi contents within the material. The emission wavelength and broadness of the peak associated with this potential Bi clusters would indicate there is a significant gradient of Bi contents within the cluster regions. Based on the wavelength it would be estimate that these contain between 4-9 at% Bi, potentially higher depending on the Al contents of these regions. This broad emission could also be the results of a substantial quantity of point defects within the crystal structure, both Bi and non Bi related. These Bi clusters and point defects coincide with the dramatic decrease in PL intensity which would strong indicate a causational relationship. High content GaAsBi can have very high levels of non-radiative defects and these Bi cluster and or point defects appear be acting as centres for non-radiative recombination [112].

Localised areas of high Bi content could cause of the point defects as the crystal lattice tries to compensate for increased localised strain. Several defects within GaAsBi have been theorised and observed. Some are induvial defects such as As antistites or Ga vacancies,  $As_{Ga}$  and  $V_{Ga}$  respectively. Other defects are also possible and form in binary pairs or as part of large defect compensation mechanisms. Common defects observed with GaAsBi materials are shown in

	Experimental	Energy (eV)	Defect origin
	energy (eV)		
Majority-	0.23-0.28	0.36	(VGa+BiAs) <sup>2-/3-</sup>
electron trap	0.56-0.61	0.69	VGa2 <sup>-/3-</sup>
ciccii on trup	0.60-0.67	0.78	(VGa+BiAs) -/2-
	0.87-0.88	0.80, 0.84, 0.84, 0.89	BiGa+ <sup>/0,</sup> AsGa+ <sup>/0,</sup> (AsGa+BiAs)
			+/0, (BiGa+BiAs) +/0
Majority-hole	0.50-0.53	0.46, 0.52, 0.52	AsGa2+ $^{/+}$ , (AsGa+BiAs) $^{2+/+}$ ,
trap			(BiGa+BiAs) <sup>2+/+</sup>
	0.27-0.30	0.33	BiGa2+/+
	0.08	0.02-0.08	VAs+nBiAs, VGa+nBiAs

Table 5 [113]. The observed energy range and distance from both the conduction and valence band edges of majority electrons and majority hole traps respectively could align with the observed emission. Antistites of  $Bi_{Ga}$  and the binary defect ( $V_{Ga} + Bi_{As}$ ) both look to be the most suitable fit. This is with reference to the energy gap observed between the broad shoulder at 0.9-1.15 eV and the AlGaAsBi emission between 1.25-1.37 eV depending on Al content at 297 K . This value is ~300 meV. However, the exact local crystallographic environment can alter the energies, so other defects are likely also present. Some binary defects such as ( $Bi_{As} + Bi_{Ga}$ ) can also lead to not only non-radiative recombination centres but also counteract the bandgap reduction from Bi incorporation [114]. This can cause discrepancies between the Bi contents calculated from the PL and other measurements such as XRD or TOF ERD.

The proportion of emission observed in the GaAsBi sample against the total loss of carriers observed in the PL measurements of Al contents at 2.5 at% and above indicates a high proportion of non-radiative recombination centres and hence a high number of defects. Attributing with full certainty to a singular or group of defects is not possible with the measurements available. Indeed, it is entire feasible that the observed behaviour could be a summation of contributions from all previously described defects and clusters. The Bi clusters and point defects may be the highly localised centres where the point and binary lattice defects are highly concentrated. The carriers are evidently reaching the states associated with point defects or Bi clusters due to the observed luminance between 0.9 -1.15 eV at 297 K in Figure 92A. Assessing the first possibility, the absence of this secondary peak in measurements at 20 K could indicate that the defects observed are extremely localised. This is based on the reduced carrier mobility at 20 K restricting the timeframe and distance that a carrier can travel within the bulk. Less carriers are therefore reaching the Bi clusters and point defect traps at 20 K. This would support the proposition that a high proportion of the defects are not evenly distributed throughout the lattice but concentrated in highly localised regions. Hence at 20 K the vast majority of carrier recombine radiatively in the bulk Bi layer and the gap between Al and non-Al contain Bi regions narrows significantly from 2 to a single order of magnitude.

	Experimental	Energy (eV)	Defect origin
	energy (eV)		
Majority-	0.23-0.28	0.36	$(V_{Ga}+Bi_{As})^{2-/3-}$
electron trap	0.56-0.61	0.69	$V_{Ga}^{2-/3-}$
ciccion trap	0.60-0.67	0.78	$(V_{Ga}+Bi_{As})^{-/2-}$
	0.87-0.88	0.80, 0.84, 0.84, 0.89	$Bi_{Ga}^{+/0}$ , $A_{sGa}^{+/0}$ , $(As_{Ga}+Bi_{As})^{+/0}$ ,
			$(Bi_{Ga} + Bi_{As})^{+/0}$
Majority-hole	0.50-0.53	0.46, 0.52, 0.52	$As_{Ga}^{2+/+}$ , $(As_{Ga}+Bi_{As})$ $^{2+/+}$ ,
trap			$(Bi_{Ga} + Bi_{As})^{2+/+}$
	0.27-0.30	0.33	Bi <sub>Ga</sub> <sup>2+/+</sup>
	0.08	0.02-0.08	$V_{As}+nBi_{As},\ V_{Ga}+nBi_{As}$

Table 5 Energies of defects commonly observed with GaAsBi materials. Energy levels of majorityelectron traps are relative values below conduction band minimum and majority-holes traps above valence band minimum.

Alternatively considering the point defects. The observed narrowing of the difference in magnitude can be attributed to suppression of non-radiative recombination pathways by the reduced thermal energy available to the carriers. The remaining gap in the PL intensity can then further be attributed to incomplete thermal quenching of point defects or from lower energy point defects such as  $(V_{As} + nBi_{As})$ ,  $(V_{Ga} + nBi_{As})$  for both cases. This underscores that theses defects remain the limiting factor in optical quality of Al and Bi containing alloys. However, the increased presence of these Bi clusters and point defects in the Al containing alloys would indicate the growth conditions are unoptimized for AlGaAsBi. This would indicate further consideration for concurrent incorporation of both Al and Bi is required beyond typical GaAsBi growth. It is confirmed by demonstration that the AlGaAsBi is optically active at Al contents between 2.5-15 at% Al. The elimination of the defect states would greatly improve the optical quality.

The shift in emission across the series is counterbalanced between the redshift due to Bi incorporation and blue shift from increasing Al contents. This makes determination of content from PL alone impossible. However comparatively assessing the blue shift in the PL with increasing Al contents provides an acceptable approximation to the shift expected with changing Al content in AlGaAs. This applied for Al contents between 0-15%, with an approximate 30 meV shift expect per % Al incorporated. More direct methods of measuring Bi content are reported later, XRD and RBS There are some run to run variations in Bi content which while within normal tolerances of  $\pm 10\%$  add an inherent noise to the exact position. Bi contents were extracted using the valence band anti crossing model for GaAsBi and by assuming Al content blue shift is identical to AlGaAs [67], [115]. In order to

calculate Bi contents, the Al content was assumed to be as intended, the extracted values of Bi content are show in Table 6.

Al Content (assumed)	Bi Content (at %)
0.0	2.29
2.5	2.38
5.0	2.15
10.0	2.17
15.0	2.71

Table 6 Bi contents calculated from RT PL of AlGaAsBi

At 20 K the shift in PL emission energy remains consistent with changing bandgap expected from changing Al content. However, the 0 at% Al sample deviates slightly from the trend with a higher emission energy than the 2.5% AlGaAsBi. This is the result of unequal levels of localised state filling between the GaAsBi vs AlGaAsBi which is discussed in more details in the temperature dependent PL section. This is not observed in the Al containing sample due to the higher levels of non-radiative recombination centres which lead to lower levels of localised state filling for the Al contents measured. The secondary emission observed in the 10 and 15 at% samples at 297 K is also not present at 20K with a single broad emission in all samples. The final point of interest is the difference in Vashni shift between the GaAs peak and the AlGaAsBi peak. The Varshini equations is shown in equation (15), where Eg(0) is the band gap at 0 K and,  $\alpha$  and  $\beta$  are material constants [116]. Note this  $\alpha$  and  $\beta$  are different material constants from those previously discuss in regard to ionisation coefficients. With decreasing temperature, it would be expected that the band gap should decrease and at the contents of alloying applicable here it would be expected that both the GaAs and AlGaAsBi peak should have similar values of α and β. However this isn't seen, the GaAs peak shift by ~80 meV while the AlGaAsBi samples shift between 30-50 meV when cooled from 297 to 20 K. This is likely the result of carrier's recombination shifting from the band edge at high temperatures to localised states just above the valence band at 20 K. This will be further discussed in the temperature dependent PL section.

$$E_g(T) = E_g(0) - \frac{\alpha T^2}{T + \beta}$$

#### **5.2.2** Growth Temperature

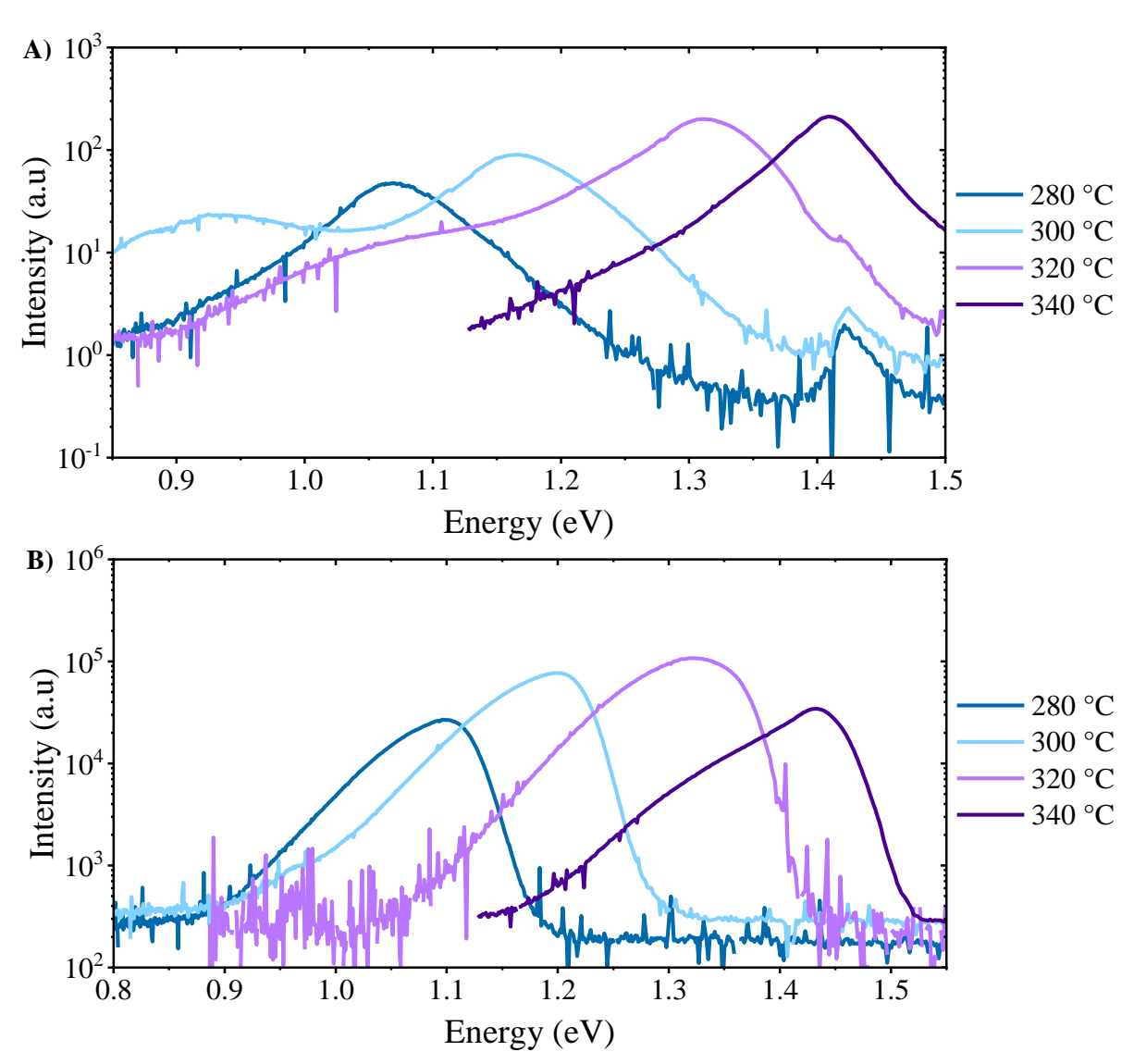


Figure 93 Photoluminescence emission spectra at 100 mW excitation for AlGaAsBi samples grown between 280 -340 °C measured at temperature of A) 297 K and B) 20 K.

The PL showed a redshift in peak emission of between 72-320 meV from the Al<sub>0.05</sub>Ga<sub>0.95</sub>As starting composition for growth temperatures of 340-280 °C respectively. The Bi contents inferred from the valence band anti crossing model for GaAsBi are given in Table 7. This gives a range between 6.21 to 0.8 at% Bi across a substrate temperature delta of 60 °C. From this it can be observed that the Bi incorporation efficiency drops by 87.2% when increasing the substrate temperature from 280 to 340 °C. The excess Bi at higher temperatures is desorbing from the growth surface as there are no indication of metallic droplets on the surface. The photoluminescence spectra seen in Figure 93 at 297 and 20 K show similar line shapes across the series, translated across with changing Bi contents. The substrate peak can also be seen at 297 K in the samples grown at 320 °C and below. The close proximity of the broad Bi emission is likely overshadowing the substrate at 340 °C. There is again an indication of PL emission from Bi clusters and either or in conjunction with point defects at 0.95 eV and 1.05 eV in sample grown

at 300 and 320 °C respectively. This further evidence that the cause of this emission is strongly related to the Bi contents due to the inconsistent nature of the cluster and defect emission as related to the main Bi emission. In the 2 centre samples of the series the shift in energy of the emission is broadly in line with the Bi content suggesting these two samples share similar defects sitting above the valence band edge. Either in clusters or as single point defects within the lattice as previously discussed and shown in

	Experimental	Energy (eV)	Defect origin
	energy (eV)		
Majority-	0.23-0.28	0.36	(VGa+BiAs) <sup>2-/3-</sup>
electron trap	0.56-0.61	0.69	VGa2 <sup>-/3-</sup>
ciccion trap	0.60-0.67	0.78	(VGa+BiAs) <sup>-/2-</sup>
	0.87-0.88	0.80, 0.84, 0.84, 0.89	BiGa+ <sup>/0,</sup> AsGa+ <sup>/0,</sup> (AsGa+BiAs)
			+/0, (BiGa+BiAs) +/0
Majority-hole	0.50-0.53	0.46, 0.52, 0.52	AsGa2+/+, (AsGa+BiAs) <sup>2+/+</sup> ,
trap			(BiGa+BiAs) <sup>2+/+</sup>
	0.27-0.30	0.33	BiGa2+ <sup>/+</sup>
	0.08	0.02-0.08	VAs+nBiAs, VGa+nBiAs

Table 5. Interestingly at either end of the series this defect emission is not observed. This may be attributed to increased incorporation efficiency at 280 C impeding the segregation of Bi within the sample. This would reduce the driving force for Bi cluster formation and Bi related defect compensation mechanisms within the lattice. Which would indicate the cluster formation is during the AlGaAsBi layer growth and not due to segregation during overgrowth of subsequent layers. However, there is not a corresponding increase in the PL emission which indicates there are still a higher number of defects present. Hence the clusters may not the only issue with AlGaAsBi growth.

Examining the other extreme at growth temperature of 340 °C the formation of cluster is likely limited due to lack of available Bi due to increase Bi desorption at higher temperatures. However again the PL intensity is significantly decreased from the GaAsBi control sample. It is therefore likely that a significant proportion of the lattice defects are related to the interplay of Al and Bi within the zinc blend structure. The defects are likely formed to compensate for reduced Al-Bi bond length. The sensitivity to changing Bi content seen in this series and changing Al content seen in the previous subseries are similar in terms of loss of PL intensity across the contents measured. From this it can be interfered that the atomic compensation mechanism for co incorporating Al and Bi can be expanded to accommodate a wide range of contents. For clarification rather than each Al- Bi bond having a corresponding defect in isolation I'd argue it is much more likely that the induced compensation defect can be shared. This would account for the sudden drop in PL with a small quantity and then the much lower sensitivity to larger changes in both Al and Bi contents. To confirm this simulation of possible defect compensation

mechanisms and atomic structure within AlGaAsBi would need to be conducted. However, to this date no such investigation has been undertaken. Without ascertaining the structure of the defects and their formation mechanism. Any attempt to alleviate their formation in growth would be conducted blind rendering it prohibitively difficult.

Growth Temperature (°C)	Bi Content (at%)
280	6.21
300	4.44
320	2.15
340	0.8

Table 7 Bi content extract from 297 K PL.

Lowing the measurement temperature to 20 K the emission intensity increases by approximately 3 orders of magnitude uniformly across the series. The highest intensity of the PL its observed at the centre of the series at 300 and 320 °C. This indicates there is falling optical quality at either end of the series. The fixed Al content indicates the cause of this change must be associated with either the Bi content or growth temperature. At lower growth temperatures and higher Bi contents, the increase in non-radiative recombination centres aligns with expectation of epitaxial growth. The previous argument withstanding in regard to Al- Bi related compensation mechanisms, this does not exclude those also seen in GaAsBi. The hotter you grow Bi containing material the better the optical quality, assuming all other growth conditions allow. The reverse is also true with lower growth temperature comes a higher quantity of defects. This is what is likely being seen at 280 °C. However, at 340 °C an increase in luminescence would be expected. At 297 K this is observed with increasing Pl intensity with increase growth temperature. However, at low temperature measurements this sample deviates from the expected trend. Potentially this could be caused by a loss in the carrier confinement due to the increased bandgap with carriers more readily escaping into the upper GaAs cladding or less likely to fall into and recombine in the AlGaAsBi region.

## **5.2.3 Bi Flux**

Photoluminescence measurements taken at 297 K and 20 K, of samples grown with Bi fluxes between  $0.8-2.8\,\mathrm{nA}$  are shown in Figure 94. With decreasing levels of Bi flux the maximum intensity increases with concurrent blue shift in emission. The Bi contents extracted from the PL are show in Table 8. The Bi content window is narrower than observed in the temperature subseries with a range of 3.18 at% between 1.41 to 4.59 at% compared with 5.41 at% between 0.8 and 6.21 at% for the temperature subseries. The range of PL peak intensities also increased with an approximate 1 order of magnitude decrease observed from 1.41 to 4.59 at%. This indicates a more significant detriment to optical quality with increasing Bi content when utilising flux control. When this range is limited to 0.8- 2.2 nA of Bi

flux and a content up to 3.21 at% Bi the drop in PL intensity is within the same order and roughly equal to the centre point 5 at% Al sample. This would indicate the limit of flux control under these experimental conditions lies between 2.2 nA and 2.8 nA. It is again observed that in sample grown with 1.4 ,2.2 and 2.8 nA of Bi flux the PL measurements contain a shoulder at between 0.95 to 1.05 eV. Decreasing in energy with increased flux and Bi content. The variation in Bi content between these 3 samples matches the approximate 2 at% Bi difference seen in the temperature series with all sample falling within the same range of 2.15-4.59 at%. This would indicate the formation of defects is sensitive the composition of the alloy and less on the two control parameters used to vary the Bi content. The shoulder peak observed at 297 K corresponds with the GaAs substrate at 1.42 eV. It is overshadowed by the broad Bi peak at 0.8 nA due to the proximity of the AlGaAsBi and GaAs at lower Bi contents.

Bi Flux (nA)	Bi Content
0.8	1.41
1.4	2.15
2.2	3.21
2.8	4.59

Table 8 Bi content extract from 297 K PL.

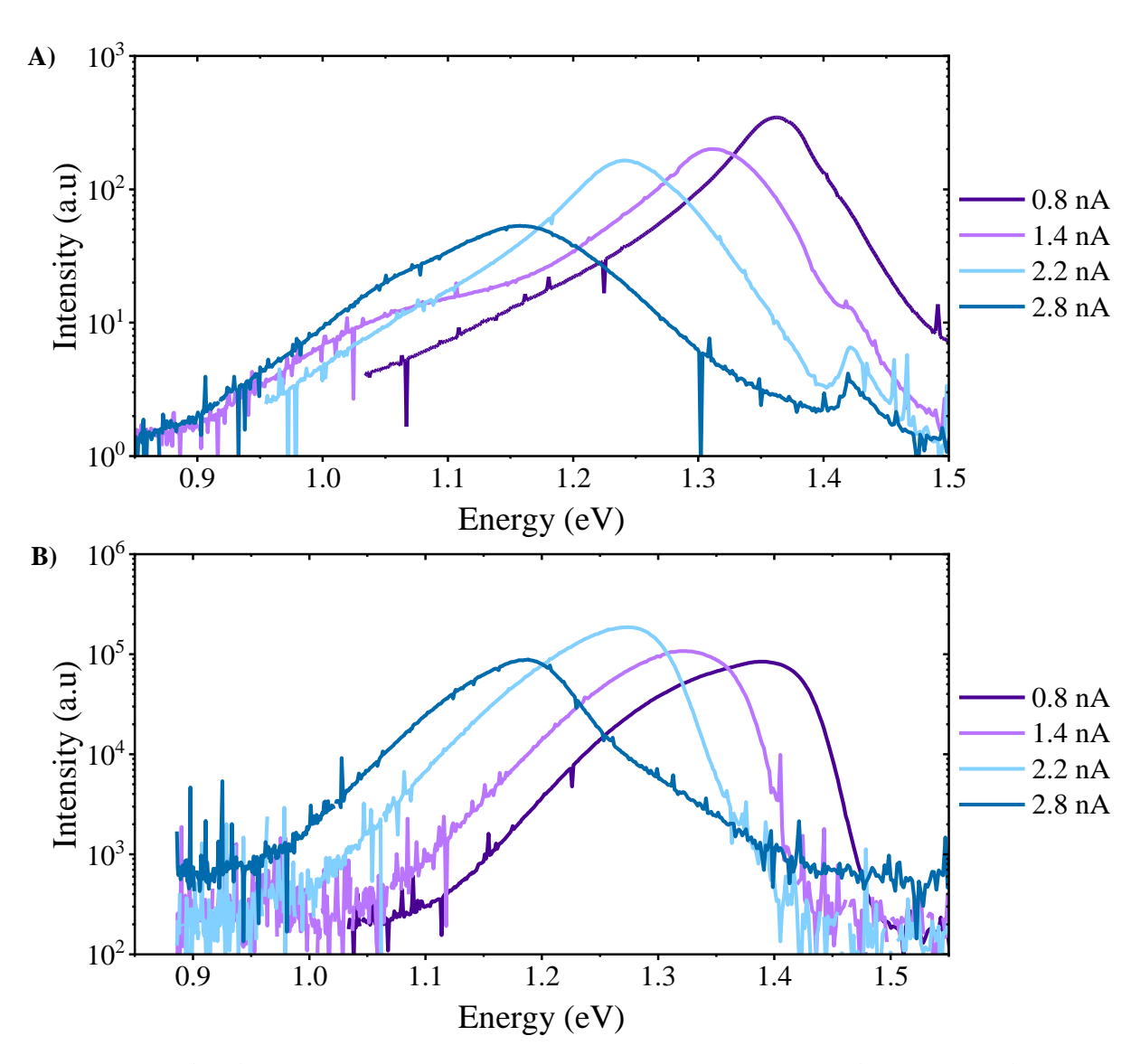


Figure 94 Photoluminescence emission spectra at 100 mW excitation for AlGaAsBi samples grown with Bi fluxes between 0.8 - 2.8 nA measured at temperature of A) 297 K and B) 20 K.

Measurement taken at 20K improve the grouping of PL intensities across the series with values all falling within the same order of magnitude, similar to what has been previously observed. This infers that there are higher concentrations of thermally activated non radiative recombination centres in the higher Bi content samples. The higher 2.8 nA Bi flux sample has unique shape to the emission in comparison with the rest of the series. Instead of the sharp cutoff at higher energies with broad tail from localise states there appears to be a shoulder sitting above AlGaAsBi the band edge at 1.3 eV. This could be due to some diffusion of Bi at the interface into the A<sub>10.3</sub>Ga<sub>0.7</sub>As cladding layer. It is again observed that there is an inconsistent Varshni shift observed between the GaAs and AlGaAsBi layers. This is again attributed to the change in emission from band edge dominated at 297 K to localised state dominated at 20 K as previously seen and discussed. The detriment in the PL brightness to the 2.8 nA

Bi sample compared with the higher Bi content sample seen in the temp series. Would suggest that when engineering for higher Bi contents alteration of the III:Bi flux ratio is a more narrowed control parameter for variation of Bi content and may best be reserved for fine tuning.

#### **5.3 XRD**

#### 5.3.1 Al Content

Three peaks are present in each of 004 omega2θ XRD scans of the AlGaAsBi layers shown in Figure 95. This corresponds to 3 expected compositions and lattice spacing present within the sample structure shown in Figure 89. The tallest peak is the substrate and is taken as our centre point at 0 arcseconds with all spectra aligned accordingly. The closest peak centred at -150 - -130 arcseconds corresponds to the Al<sub>0.3</sub>Ga<sub>0.7</sub>As buffer and upper cladding layers with the broadest peak centred between -850 - -650 arcseconds the result of the AlGaAsBi layer. The additional smaller peaks present are interference fringes and are related to the thicknesses and interface quality of the measured layers. The raw data was fitted with model using lattice constants of 6.28 and 6.23 A for GaBi [66] and AlBi [68] respectively. Lattice constant of 5.653 and 5.662 for GaAs and AlAs respectively were also used. This enable the extraction of composition from the extracted lattice constant of each layer along with the layer thickness and extraction of strain in each layer from the fitting.

It is observed that the variation of Bi content ranges between 2.31 to 2.5 at% Bi with the exception of 15 at% al which had a slightly higher content of 2.86 at% Bi. The variation seen in the Bi contents accounts for the disparity between the expected and observed level of blue shift with increasing Al contents in the PL. However, while the Bi content can be confidently confirmed from the fitting of the omega20 XRD scan due to a shift of 300 arcseconds per at% Bi. Determination of the Al from this same peak is overshadowed as Al contributes 5 arcseconds per at% Al. The additional Bi measured at 15 at% Al while within typical growth spec of  $\pm$  0.5 at% cannot be accounted for in the growth conditions or error in calibration. It is possible additional Bi was supplied due to short term instability of the effusion cell. However, the Ga and As source materials depleted before being able to test this by growing a repeat sample. It is also noted that the surfaces remain free of any defect or droplets that would be expected if the Bi cell where to undergo a spitting event. The variations in the broadness of the Bi peaks would indicate slight variation in the layer thickness, although this doesn't correlate to any other variables in the experiment. The loss of the fringes would indicate the quality of the interfaces between the Bi containing layer have deteriorated with the addition of Al. The extracted compositions for the AlGaAsBi layer are shown in Table 9. The values are in very close agreement with those inferred from

the PL measurements. This would indicate the Al contents are also reasonably close to intended as the bandgap shift due to Al content aligns with the expected Bi content induced shift.

Al Content	Bi Content
0.00	2.50
2.54	2.31
5.71	2.40
10.10	2.49
12.40	2.86

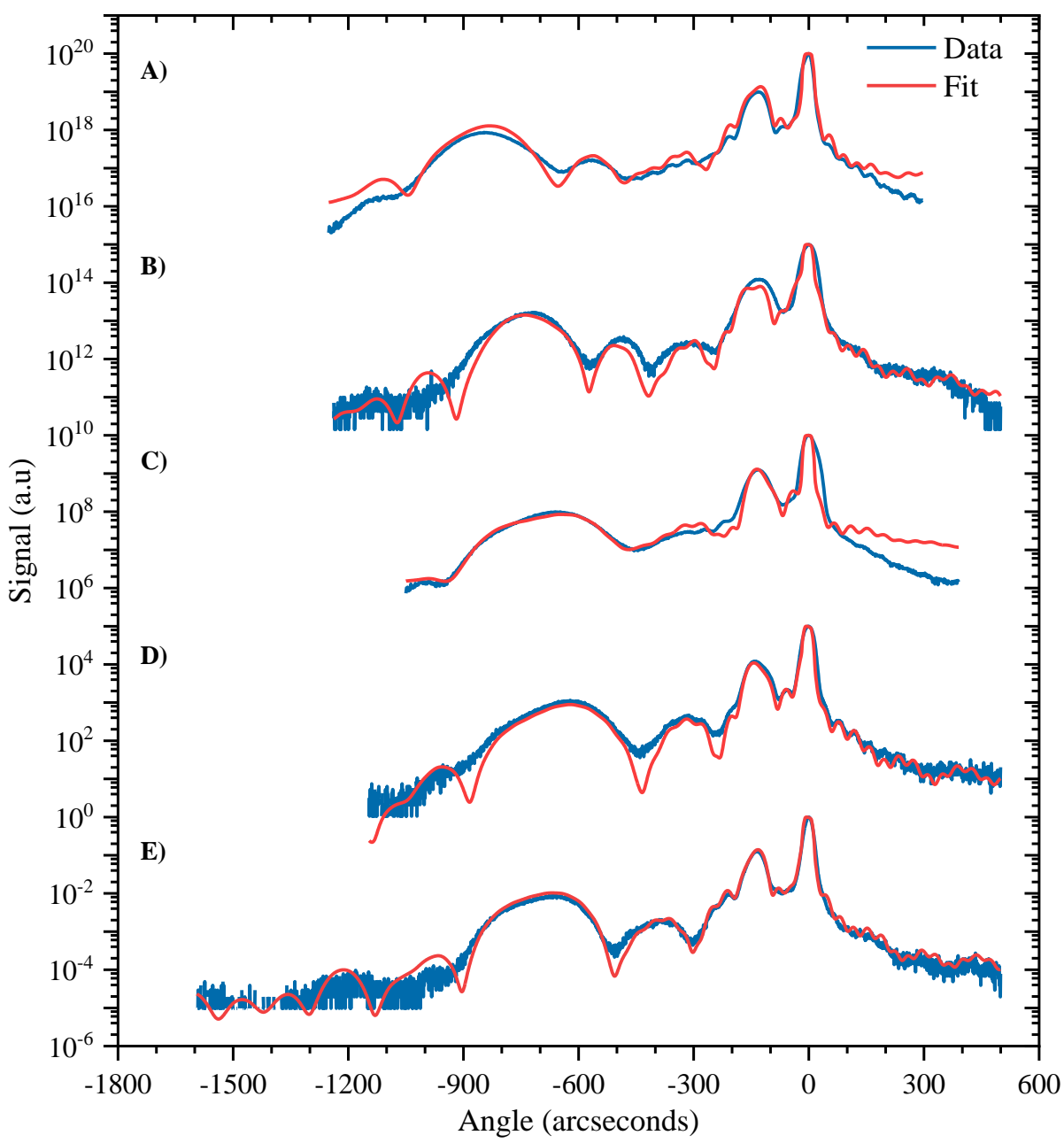


Figure 95 X Ray Diffraction for Al content series with fitted XRD data generated from layer models. Where, A) 15 at%, B) 10 at%, C) 5 at%, D) 2.5 at% and E) 0 at%.

## **5.3.2** Growth Temperature

The stacked 004 omega $2\theta$  XRD scans of the AlGaAsBi samples grown between 280-340 °C are shown in Figure 96. This confirms the changing Bi content previously asserted from the 297 K and 20 K PL measurements. The Bi and Al contents extracted from each layer are shown in Table 10. The fitting indicates there is no observed alteration of the Al contents with changing growth temperature. This is

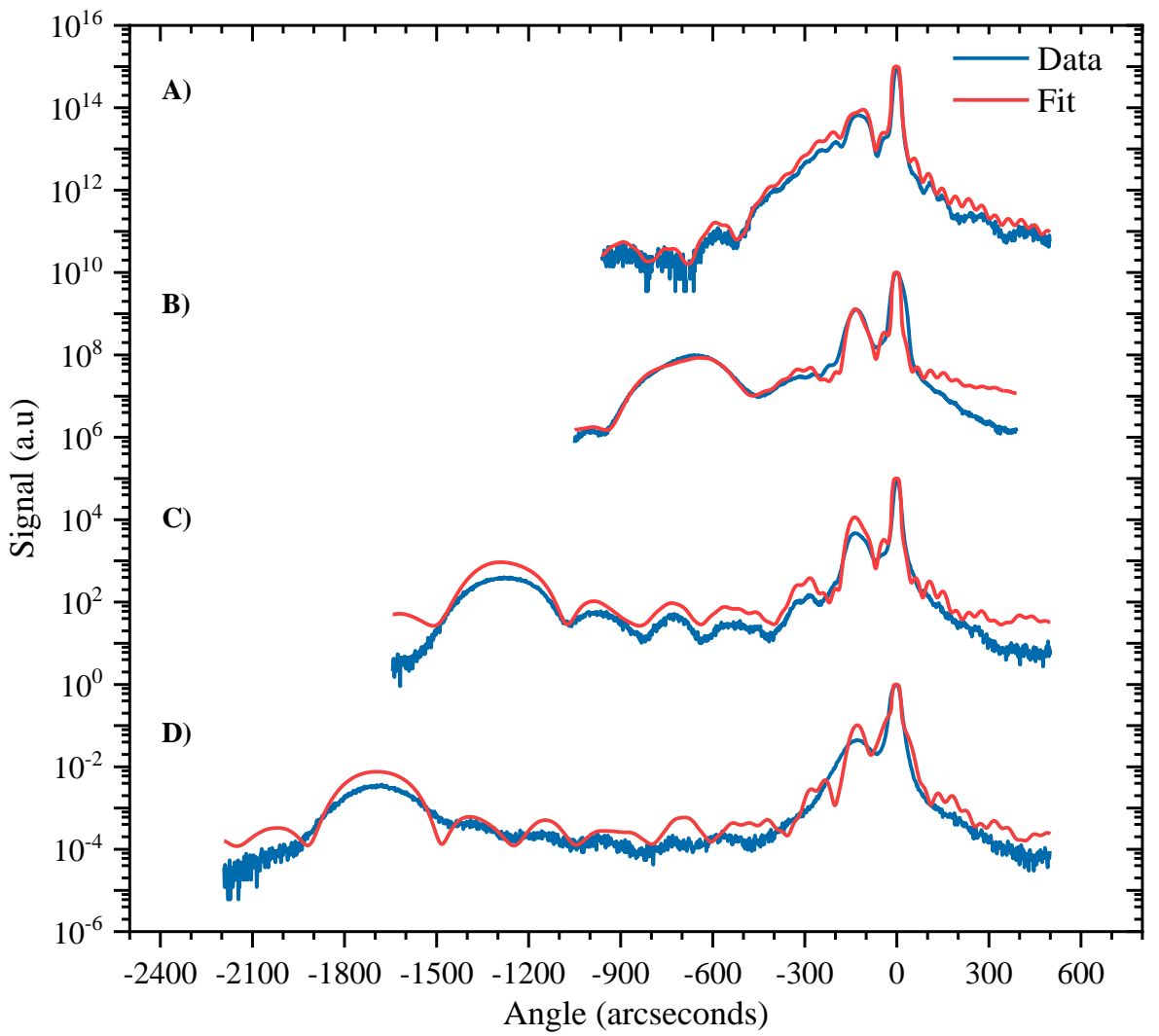


Figure 96 X ray diffraction for Al content series with fitted XRD data generated from layer models. Where, A) 340 °C, B) 320 °C, C) 300 °C and D) 280 °C.

given with the previously discussed caveats in determination of Al content from XRD. Bi contents extracted from the XRD fitting closely match up with he values determined from PL. The epitaxial matching of the 3-layer structure remains unchanged with the centred GaAs peak used to align in all scans. To the left of this peak approximately -130 to -150 arcseconds is the  $Al_{0.3}Ga_{0.7}As$  buffer and cladding layers. There was no change within these layers across the series. The AlGaAsBi layer moves further left with increasing Bi content and corresponding compressive strain. The Bi contents range from 6 to 0.92 at% Bi for sample grown at 280 - 340 °C respectively with the XRD peak shifting from

approximately -1680 - -450 arcseconds. The interference fringes are present on all sample grown from 300 °C and above. The loss of the fringes at 280 °C would indicate a significant roughening of the interface between AlGaAs and AlGaAsBi layers. This may be caused interdiffusion of Bi during overgrowth of the AlGaAs and GaAs layer at temperatures significant above 280 °C. The situation is also likely made more prevalent by the increased Bi content at the lower temperature. Similar effects have been observed in previous studies of GaAsBi/GaAs heterostructures and quantum well structures [116], [117].

Growth Temperature (°C)	Al Content	Bi Content
280	5.40	6.00
300	5.68	4.52
320	5.74	2.41
340	5.70	0.92

Table 10 Al and Bi contents extract from XRD Fitting of sample grown between 280-340 °C.

#### **5.3.3** Bi Flux

XRD 004 omega20 scans confirm the alteration of Bi contents as a function of incident Bi flux. The range of Bi contents is narrower than within the temperature series with values extracted from 1.67 to 4.58 at%. The full list of contents extracted from the fitting is given in in Table 11. This can also be observed in the raw scan shown in Figure 97. The peak range is considerably narrow ranging from than the temperature ranges from -1350 to -500 arcseconds compared to -1630 to -450 arcseconds. It can be seen that same 3 peaks attributed to the GaAs substrate, Al<sub>0.3</sub>Ga<sub>0.7</sub>As and AlGaAsBi layers previously described are again present. There is no observed shift in the upper AlGaAs cladding or lower buffer region indicating there has been no drift over the sample series growth. The higher Al content sample grown under a 2.8 nA flux has no visible sign of interference fringes indicating poor interface quality. This may be caused interdiffusion of Bi during overgrowth of the AlGaAs and GaAs layer at temperature significant above a critical Bi content as it was also observed in the 6.0 at% Bi sample grown at 280 °C. The XRD value of Bi content are in close agreement with the PL values indicating the impact of Bi on the AlGaAs band gap at 5 at% Al is very similar to GaAs. The broadness of the Bi peak

remains consistent across the series at approximately 300 arcseconds in width at half height. This is indicates a consistent AlGaAsBi layer thickness across the series.

Bi Flux (nA)	Al Content (at%)	Bi Content (at%)
0.8	5.69	1.67
1.4	5.74	2.41
2.2	5.70	3.19
2.8	5.75	4.58

Table 11 XRD fitting values from Bi flux series.

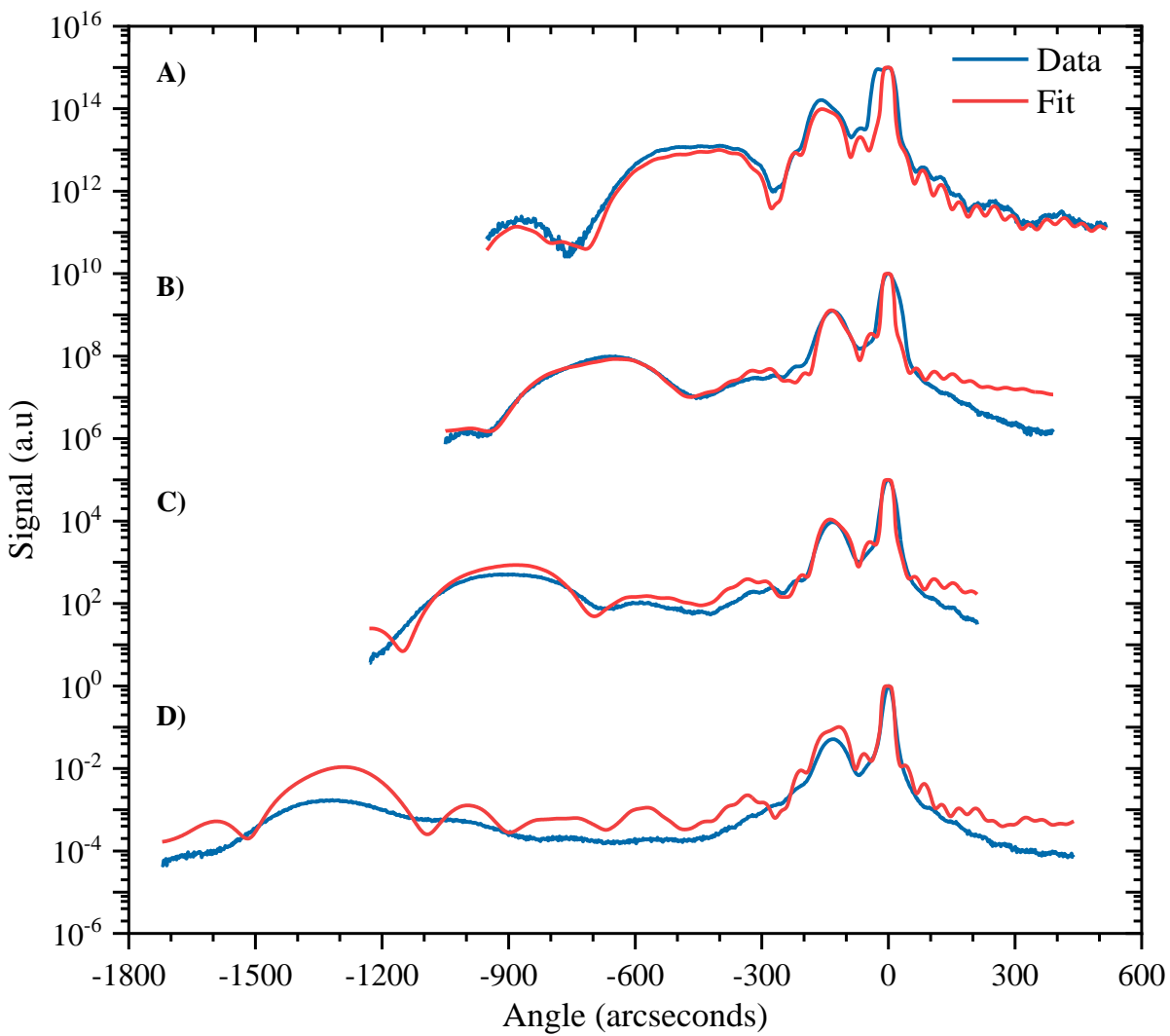


Figure 97 X Ray Diffraction for Al content series with fitted XRD data generated from layer models. Where, A) 0.8 nA, B) 1.4 nA, C) 2.2 nA and D) 2.8 nA.

# 5.4 Nomarski Microscopy

#### 5.4.1 Al Content

Further indications of the material quality seen with varying Al content can be inferred from observations of the sample surfaces under Nomarski microscopy. This highlights differences in refractive indices which in III-V epitaxial layers are commonly centred around defects. Representative

images of the surfaces of the samples are shown in Figure 98. Across the entire series there are smooth surfaces with no sign of relaxation or roughening. Relaxation would appear as a crosshatching pattern and would not be expected in samples which are comparatively thin. The vast majority of surfaces are featureless without any indication of metallic droplet formation. This indicates all sample are grown under reasonably optimised conditions with high surface quality. There are signs of some surface contamination in the 10 at% Al sample however this has occurred post growth and is more damming of cleaning procedures post PL and XRD analysis. In this sample there is also a few examples of coffee

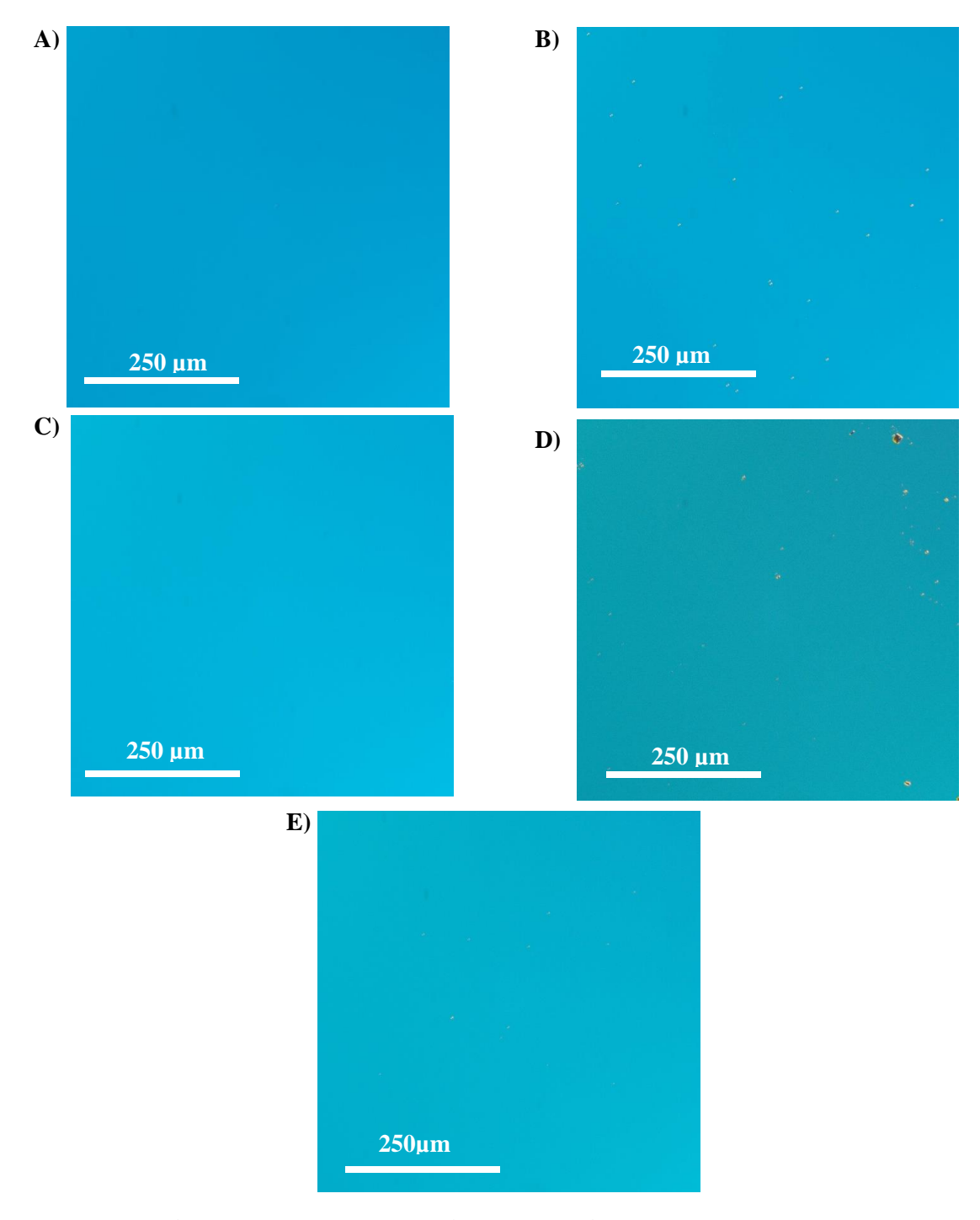


Figure 98 Nomarski images of as grown sample surfaces. Where, A) 0 at%, B) 2.5 at%, C) 5 at%, D) 10 at% and E) 15 at%.

bean defects from a small metallic droplet in the centre left of the image. These however cover a very minute proportion of the surface and are not cause for concern. Similarly in the 2.5 at% Al sample a number of metallic droplets can be observed on the surface however the density is too low to cause any negative impact on the material quality. These droplets are likely Bi droplets indicating our operating growth regime is quite close to either a temperature, Bi flux or III:As<sub>4</sub> flux limit.

#### **5.4.2** Growth Temperature

The sample surface appeared smooth and clear across all samples grown between 280-340 °C as shown in Figure 99. These images are representative of the entire sample surface. There are a few metallic droplets present on the surface of sample grown at 280 and 300 °C. However, the densities are borderline non-existent and no impact on optical quality would be expected. Indeed none is observed. The increased incorporation efficiency and high Bi content seen at lower temperatures does not appear to have impacted the surface roughness of the samples at 280 and 300 °C. The high quality of the sample

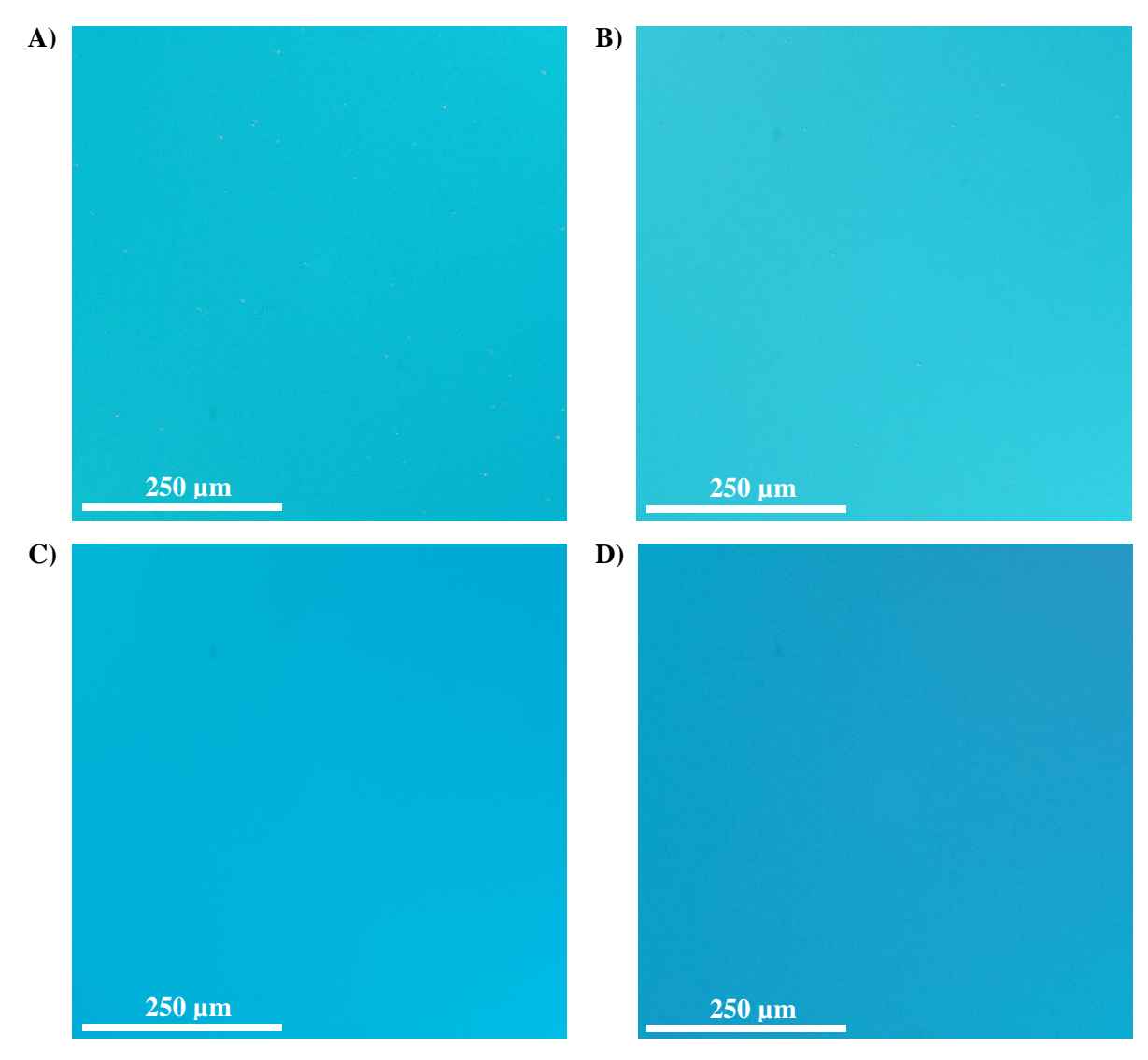


Figure 99 Nomarski images of as grown sample surfaces. Where, A) 280 °C, B) 300 °C, C) 320 °C and D) 340 °C.

surface would indicate there is further room for increased Bi incorporation. This would be achieved by further decreasing the growth temperature to the Bi flux limit. Alternatively, through increasing the Bi flux and maintaining the growth temperature, this is explored further in the Bi flux sub series. Above 320 °C there is no change to surface quality with increasing temperature, this is due to the pristine surface quality achieved at 320 °C.

#### **5.4.3 Bi Flux**

The surface quality as seen in Nomarski begins to degrade when the Bi flux exceeds 2.2 nA during AlGaAsBi layer growth. The raw Nomarski microscopy images are shown in Figure 100. Samples grown at Bi fluxes of 1.4 nA and below have pristine surfaces clear of any defects. The slight alteration of colour between samples is due to slight differences in the polarisation filter position and is not related to the material quality. The sample grown under 2.2 nA of Bi flux has a low surface density of coffee beam defects due to metallic droplet formation of the surface. These droplets are almost certainly excess

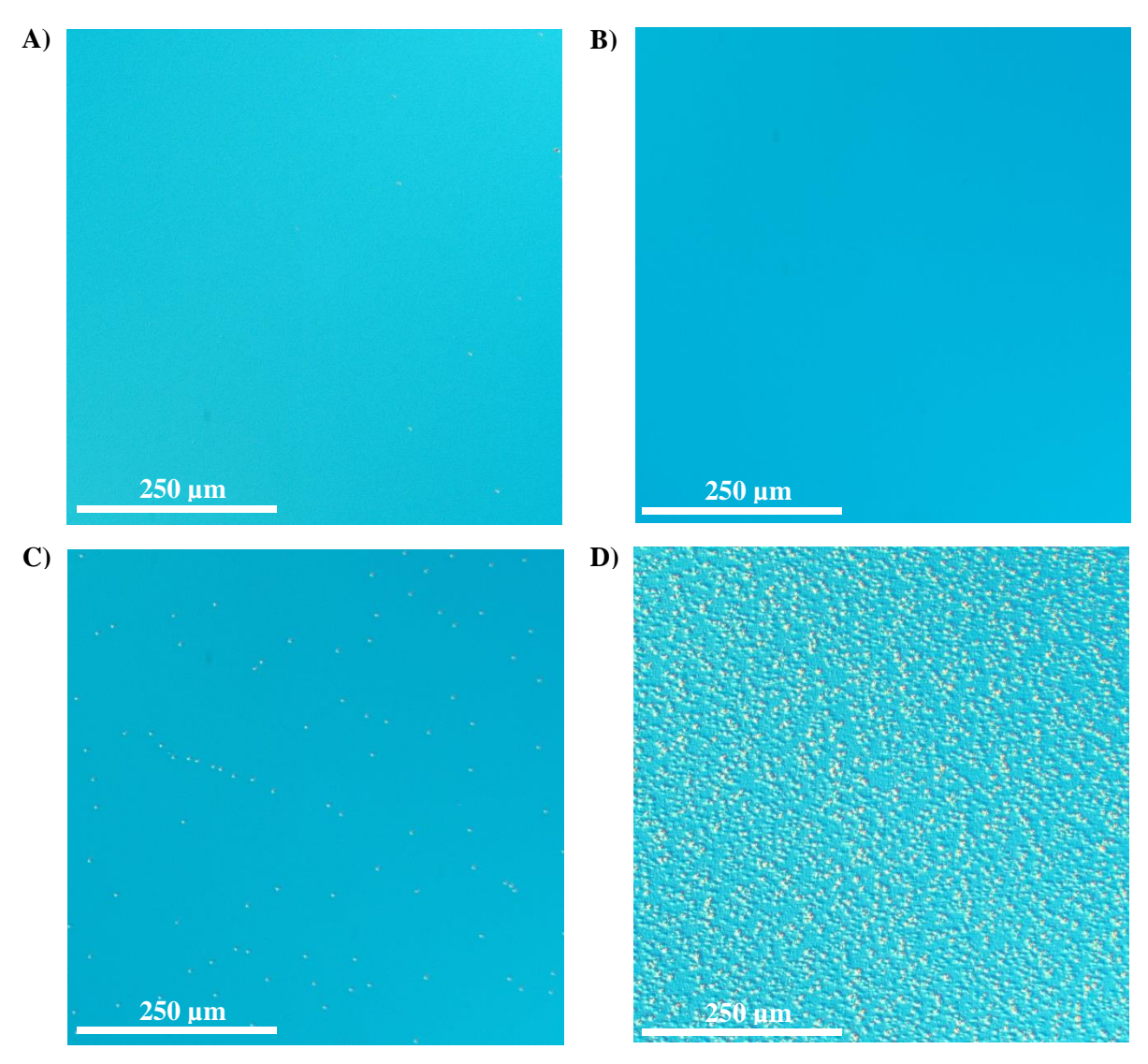


Figure 100 Nomarski images of as grown sample surfaces. Where, A) 0.8 nA, B) 1.4 nA, C) 2.2 nA and D) 2.8 nA.

Bi that has been unable to incorporate or desorb from the surface during growth. Further increased Bi flux to the surface greatly increases the density of the metallic droplets. High level of surface roughening can be observed due to increase proximity of droplets to each other. The increase with increased Bi flux strongly supports the case that these are majority Bi in their composition. Droplets with compositions of Ga-Bi have been reported and it is also possible that the droplets may contain some Al content depending on the interdiffusions between the droplets and underlying layer [62]. Due to the size of the droplets, which are two small to analyse with the EDX system available, confirming their composition is not possible. However, the surface quality and underlying layers in the sample grown at 2.8 nA is severely degraded due to the droplets. This is reflected with a corresponding drop in PL intensity and optical quality.

# 5.5 Power Dependent PL

#### 5.5.1 Al Content Series

The exponents extracted from the power dependent fitting indicate at 20 K the recombination is radiatively limited with all exponents close to 1. This informs us that the majority of the non-radiative recombination centres have been supressed. This is consistent across the series with the exponent value within run-to-run variance of  $\pm 0.05$ , as seen in Figure 101. Measurements at 297 K do show a small decrease in exponents from 1.55 to 1.4 with increasing Al contents. This indicates a shift toward more radiatively limited PL emission at higher Al contents. This is in contrast to what has been observed in the raw PL where the higher Al contents have reduced PL intensity. Accounting for this may indicate that there is a higher continually active population of non-radiative recombination centres at higher Al contents.

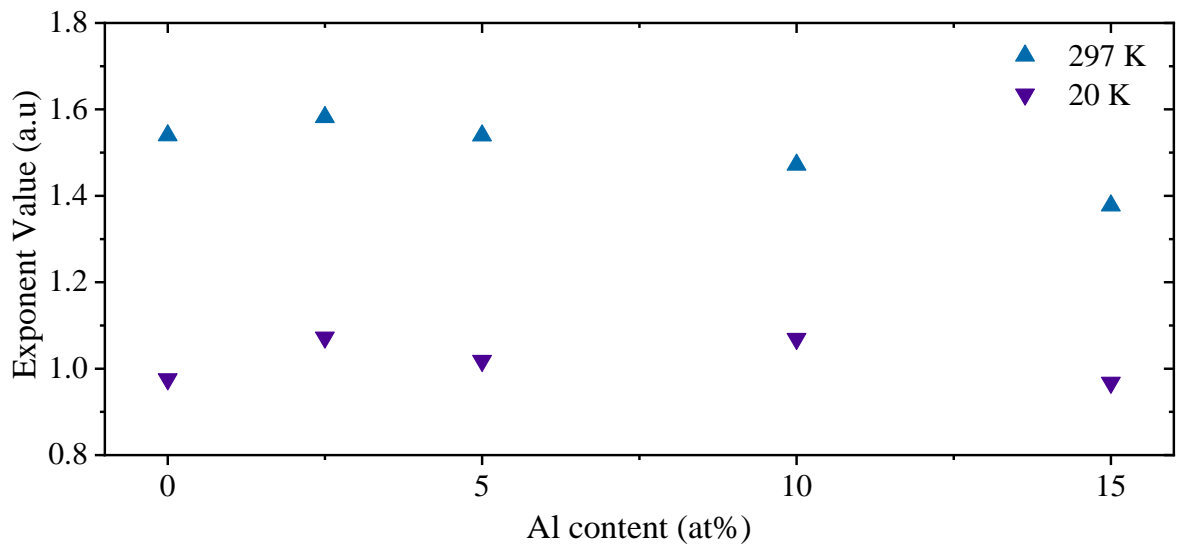


Figure 101 Exponent values extracted from lines of best fit for normalised integrated Photoluminescence vs excitation power at temperature of 20 K & 297 K for changing aluminium contents between 0 to 15 at%..

The raw data shown in Figure 103 displays signs of sample heating in the measurements taken at 20 K. This can be observed as the trend deviates from the linear fitting at higher optical excitations, typical above 100 mW. It is visible in all samples except the 0% control. This could infer a significantly higher quantum efficiency which would correspond to the increased PL intensity observed in Figure 92. Alternatively, it could also be the results of a better thermal contact to the mounting plate during measurements. In general, the fitting of the integrated PL using equation (11) at both 297 K and 20 K closely approximates the raw data.

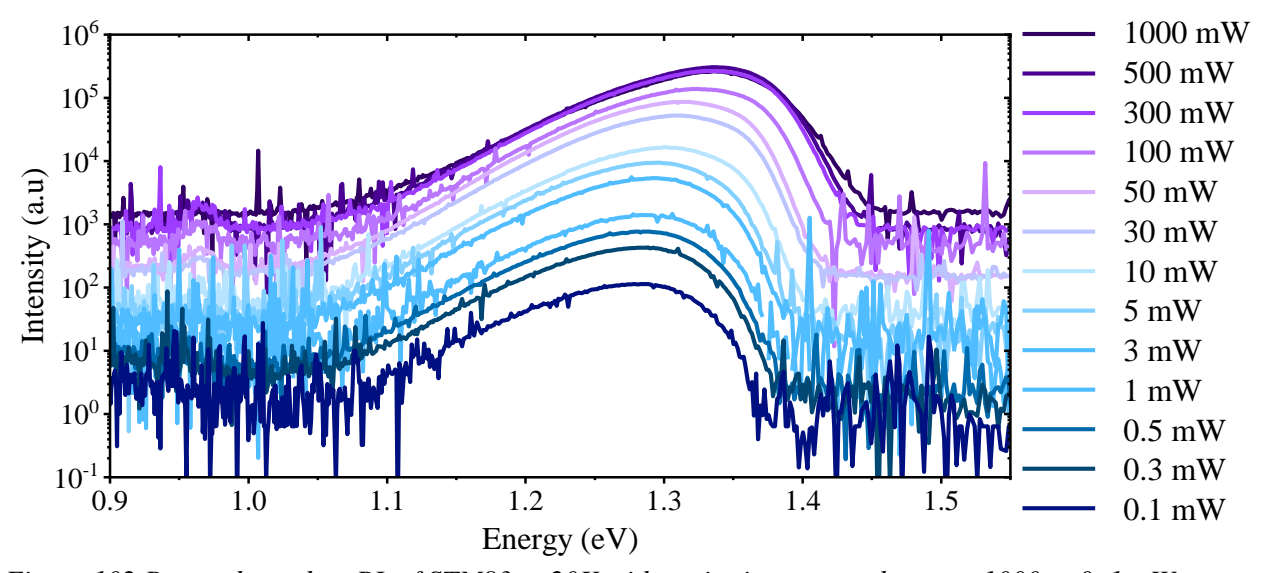


Figure 102 Power dependent PL of STM83 at 20K with excitation powers between 1000 to 0. 1 mW.

Observing the raw power dependent PL results of a representative sample from this series, in this case STM 83 the 5 at% AL centre point, provides an insight into the bandgap and recombination processes within the alloy. This is shown in Figure 102 with optical excitation powers spanning 4 orders of magnitude between 1 W to 100µW by a 532 nm green continuous laser. There are some indications of recombination at 0.96 to 0.97 eV outside of the bulk emission, these are attributed to high content Bi clusters or point defects within the sample. The energy at which peak PL intensity is observed blue shifts with increasing optical excitation. Initially emitting at 1.285 eV with 100µW of excitation the emission steadily shifts to 1.346 eV at 0.3 W. The state filling appears exponential in relation to the excitation power, this is observed as a linear blue shift in Figure 102 which is however plotted on a logarithmic scale on the y axis and the optical excitations power are also logarithmic. The blue shift does not appear as a translation of the PL peak as the point at which emissions reaches the noise floor remains consistent at ~1.05 eV for all excitations. The shift in emission is coming from an increased broadness of the peak which extends to higher emission energies at higher optical excitations. This is due to increased state filling within the localised states which dominate the emission at 20 K. This effect can be separated from sample heating by contrasting the point at which the shift is no longer observed and the deviation from linear behaviour in the fitting of the integrated PL. This occurs at 0.3 W and between 0.1 - 0.3W as shown in Figure 103C, for peak stretching and sample heating respectively.

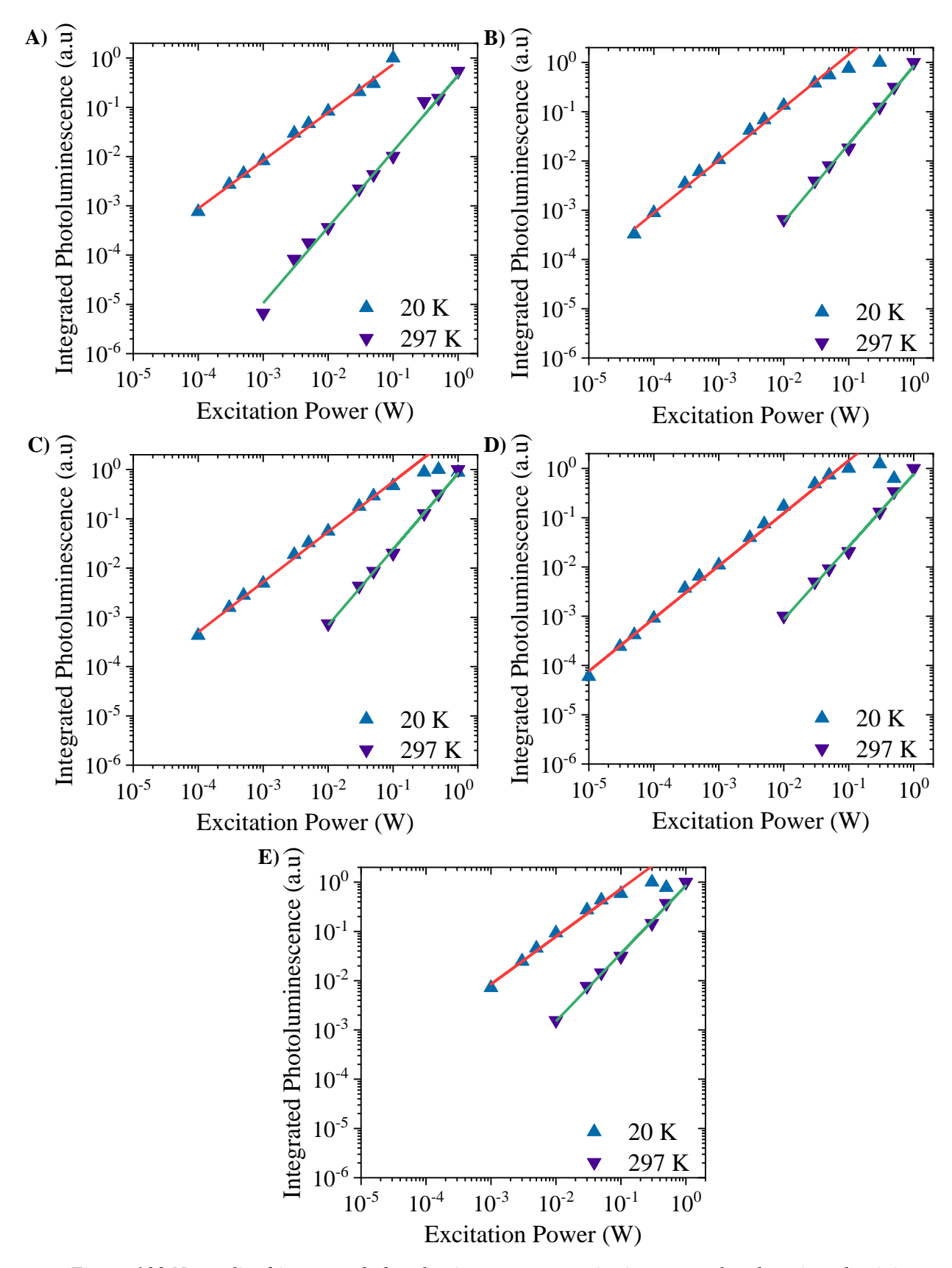


Figure 103 Normalised integrated photoluminescence vs excitation power for changing aluminium contents between 0-15 at%. Where, A) 0 at%, B) 2.5 at%, C) 5 at%, D) 10 at% and E) 15 at%.

It can therefore be demonstrated that the peak stretching due to deeper state filling and corresponding blue shift is not due to sample heating. This indicates that increasing the carrier generation with increased optical excitation is activating higher energy renomination pathways within the sample. Filling the available localised states with emission therefore occurring closer to the band edge with higher quantise of carriers injected. This behaviour corresponds with similar observation of the saturation of localised states in GaAsBi with the localised states occupying sites just above the valence band edge [61], [111]. It is logical to expect the effects to be similar due to the alloy contents under investigation within this study. The increasing carrier density is saturating the excited states sitting further above the valence band, leading to the carrier's recombination at states closer to the valence band edge. This confirms the presence of localised states within our material and exponential distribution of states with decreasing density further from the valence band edge. It also indicates the localised state distribution is not significantly impacted by the incorporation of Al into GaAs<sub>x-1</sub>Bi<sub>x</sub>.

## **5.5.2** Growth Temperature

The power dependent exponents extracted from fitting the integrated PL at excitation powers between 1 W to 100µW are shown in Figure 104 for the samples grown at temperatures between 280 to 340 °C. The integrated PL is shown in Figure 105, and was fitted with equation (11) in the linear regions. Measurements were conducted at 20 K and 297 K with some sample heating observed at excitation powers exceeding 100 mW for low temperature measurements. The exponents extracted for samples grown above 320 °C are very similar with lower temperature measurements giving a value close to 1 indicating the recombination is radiatively limited. Fitting at 297 K produced an exponent of 1.54 for both samples indicating recombination is partially limited by non-radiative defects within the material. Lowering the growth temperature to 300 °C and a sharp rise in the value of the low temperature exponent

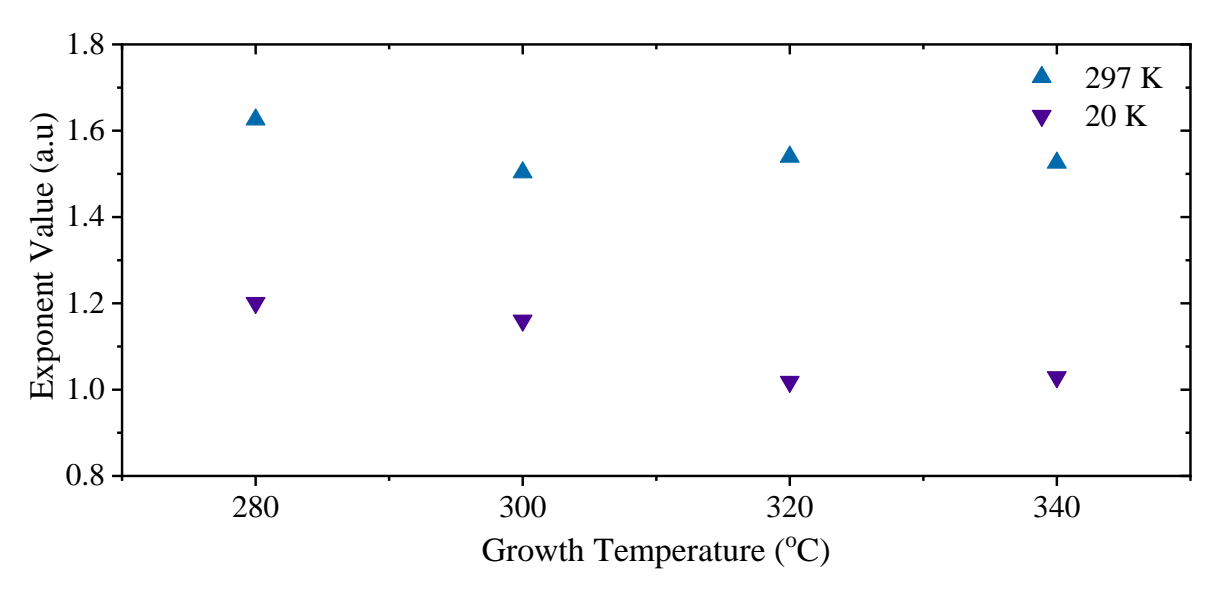


Figure 104 Exponent values extracted from lines of best fit for normalised integrated Photoluminescence vs excitation power at temperature of 20 K & 297 K for varying growth temperatures between 280 to 340 °C.

is observed from 1 to 1.18. This indicates the non-radiative defects remain limiting at 20 K. This would indicate the material quality is decreasing with the reduced growth temperature. This is likely the product of both the lower growth temperature and the increased quantity of Bi content due to the higher incorporation efficiency. Quantifying the individual contribution of temperature from Bi flux is not possible due to the interdependency between the two factors. The high temperature exponent remained unaffected, which could indicate the limiting factor in quantum efficiency is recombination through the Bi clusters or point defects on the lattice. These have been demonstrated to be active at temperature above 150 K for the 5 at % Al sample and remain present in all sample within this series. Lowering the growth temperature, a further 20 °C to 280 °C and both high and low temperature exponents increase in value. The low temperature sees an incremental increase to 1.21 and I would assert that the previously described effects for 300 °C also apply here. The rise in high temperature exponent is likely also the result of the increased defects associated with both lower growth temperature and higher Bi contents. It may also be the case that the reduced energy difference between the defect emission and Bi layer contributes to the more defect limited recombination observed. Figure 93 showed the separation between the bulk emission at 1.068 eV and cluster emission at 0.92 eV is 148 meV for the 280 °C sample. This is substantially lower than in all other sample of the series which all have separations in excess of 200 meV. This could lead to an increased quantity of the free carriers generated recombining non radiatively in the defect region. The narrowing of the gap between the defect region and bulk layer is likely the product of the increased Bi incorporation efficiency. This concurrently with the reduced temperature should reduce the driving force for Bi segregation within the alloy. Which will reduce the Bi contents in the clusters and the quantity of defects this results in. This could indicate a potential method to eliminate cluster formation. However, it would not alleviate the detriments in the PL from isolated point defects within the lattice or from atomic compensation complexes related to the Al-Bi bonding. Both of which would become more prevalent at higher Al and Bi contents. It may be though that these would be less detrimental to optical properties when not localised together within Bi clusters. Hence removing the driving force for Bi segregation by decreasing the growth temperature should still yield some improvements. However, this is unlikely to yield a linear improvement in optical quality. Further narrowing the energy barrier between the defect region and Bi layer may be possible however the reduced energy would likely be a detriment to the optical quality until the elimination of the defect region. The exact cross over where quality would see an increase is indeterminant from the data within this study. It could also be that temperature is only part of the solution, and reducing the total Bi flux could produce a similar result with similar improvements to defect densities. The optimal route would likely be a trade-off between lower growth temperatures and a reduced Bi flux to yield improvements to defect densities.

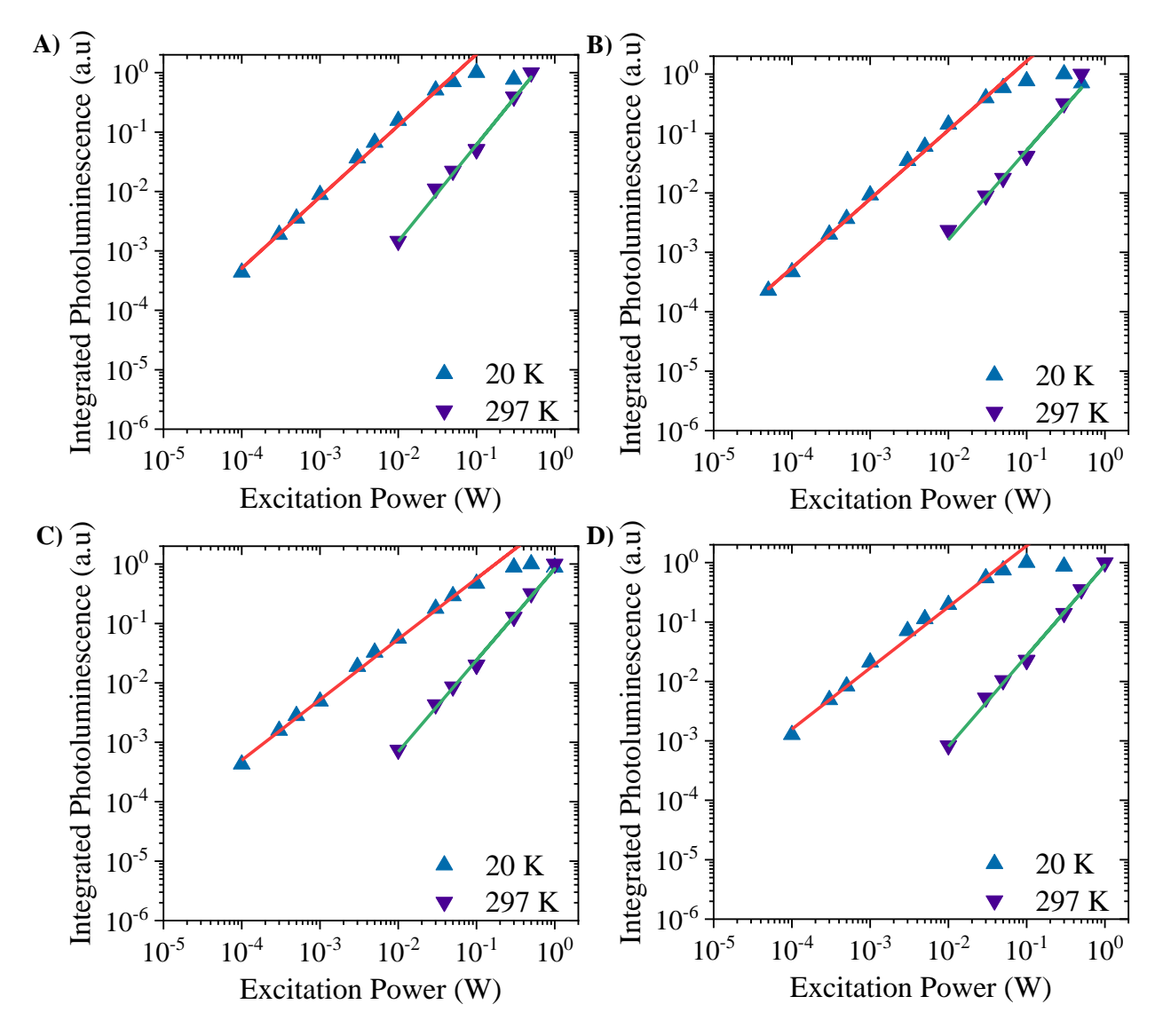


Figure 105 Normalised integrated photoluminescence vs excitation power for growth temperatures between 280 to 340 °C. Where, A) 280 °C, B) 300 °C, C) 320 °C and D) 340 °C.

# 5.5.3 Bi Flux

The power dependent exponents extracted for sample grown with Bi fluxes between 0.8-2.8 nA are shown in Figure 106. These values are extracted from the integrated luminance against optical excitation powers at 20 K and 297 K, this date is shown in Figure 109 and fitted with equation (11) to extract the power exponent. The fitting achieved to the data was very good with some indications of sample heating at higher optical powers above 100 mW. These points were disregarded for the fitting as it deviated from the linear trend due to a disproportionate quantity of traps states becoming active with the increased temperature. Measurements at 297 K showed no overall trend in the exponent with all values between 1.5-1.55, within standard run to run variance. Measurements at 20 K however showed a gradual increase with higher Bi fluxes starting from 0.98 and linearly increasing to 1.12. This is indicative of an increase in the quantity of non-radiative recombination centre from high densities of defects within the material. The 297 K PL and 004 XRD both previously showed the increased Bi flux

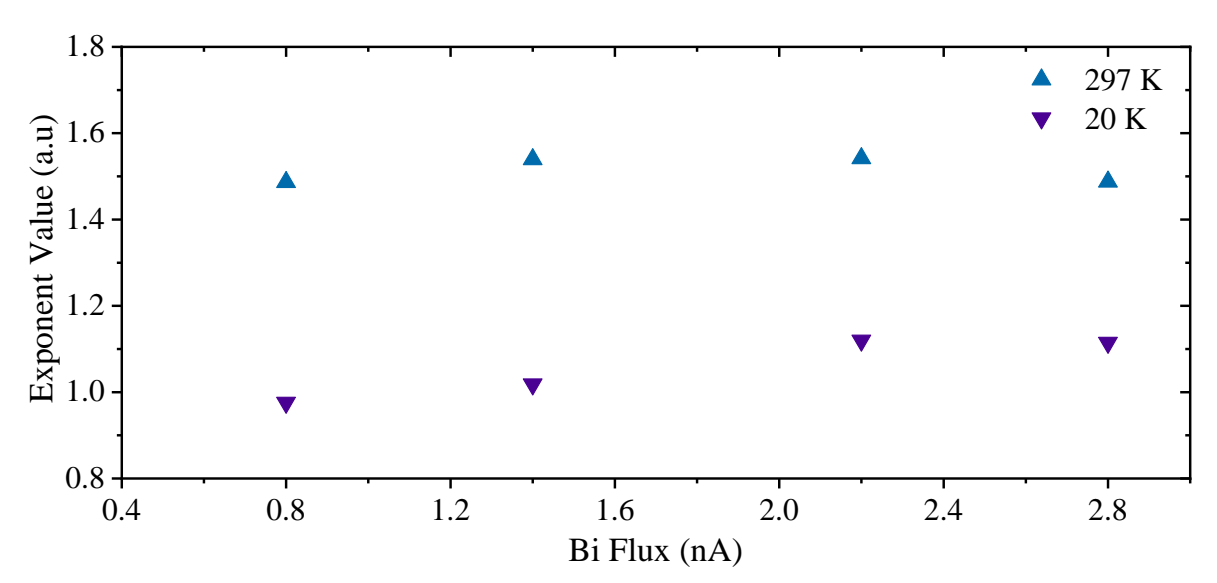


Figure 106 Exponent values extracted from normalised integrated photoluminescence vs excitation power at temperatures of 20 K & 297 K for Bi fluxes between 0.8 to 2.8 nA.

resulted in higher Bi contents within the material. It would be expected the number of defects would rise proportionally to the Bi content as this is what disrupts the standard GaAs lattice. The Al-Bi compensation mechanism previously proposed and attributed with the significant drop in PL is still prevalent within this sample. However, it is more likely the previously reported defects listed in

	Experimental	Energy (eV)	Defect origin
	energy (eV)		
Majority- electron trap	0.23-0.28	0.36	(VGa+BiAs) <sup>2-/3-</sup>
	0.56-0.61	0.69	VGa2 <sup>-/3-</sup>
	0.60-0.67	0.78	(VGa+BiAs) -/2-
	0.87-0.88	0.80, 0.84, 0.84, 0.89	BiGa+ <sup>/0,</sup> AsGa+ <sup>/0,</sup> (AsGa+BiAs)
			+/0, (BiGa+BiAs) +/0
Majority-hole	0.50-0.53	0.46, 0.52, 0.52	AsGa2+/+, (AsGa+BiAs) 2+/+,
trap			(BiGa+BiAs) <sup>2+/+</sup>
	0.27-0.30	0.33	BiGa2+ <sup>/+</sup>
	0.08	0.02-0.08	VAs+nBiAs, VGa+nBiAs

Table 5 are causing the effects observed in the power dependent PL. Dependent on the changing Bi contents and related primarily to the Ga-Bi interaction. It must also be considered that at 2.2 nA and in higher abundance at 2.8 nA there are Bi droplets present on the surface. These will have further disrupted the growth dynamics locally in areas in close proximity to the droplet. Highly likely this will also cause significant defects within the local crystal structure. This can be more clearly seen in the SEM image of the sample surface of the 2.8 nA sample, shown in Figure 107. It can be clearly seen where the damage caused due by metallic droplet migration across the growth surface has left tails or distorted crystal structure at the macroscale. The composition within these regions is highly likely to differ from the intended due to interdiffusion between the bulk and metallic droplets. It is also worth noting that the droplet sizes range significantly from large ones seen under Nomarski to much smaller droplet which have no visible disturbance of the lattice around them. Determining the composition is not possible with the EDX installed on the SEM due to volume of detection being significantly large than the droplets.

The integrated PL shown in Figure 108 displays a maximum point peaking in luminescence at 2.2 nA. This indicates that the increased Bi content is minorly improving the optical quality. Above this and where the surface coverage of Bi droplets is extensive there is a reduction in the PL. However, the value at 2.8 nA is similar to the 0.8 and 1.2 nA sample so the defects resulting from the droplets are of a similar order to the lower Bi content samples. The increased Bi content is likely reducing the number of  $V_{Ga}$  defects and instead forming  $V_{Ga}$ -Bi<sub>As</sub><sup>2-/3-</sup> a binary defect complex which has a lower reduced

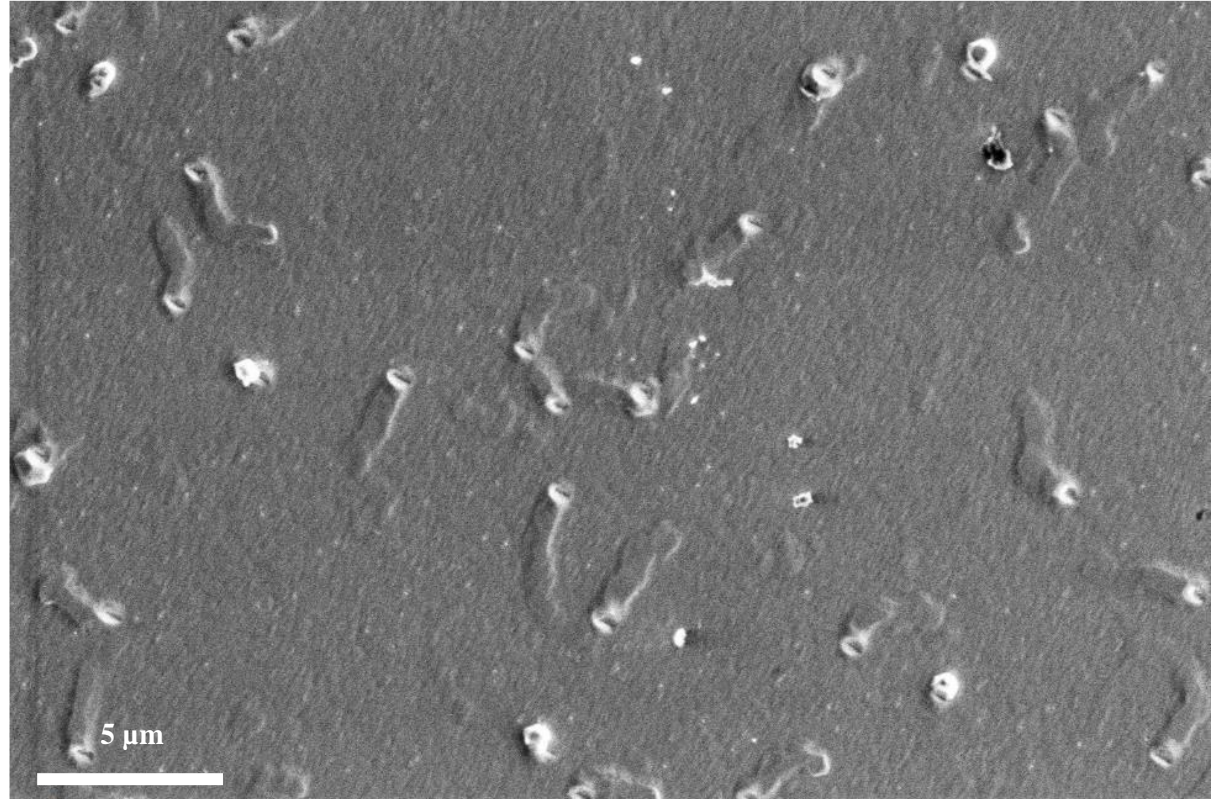


Figure 108 Int Pl Integrated Photolyminescence spectra at 20k of varying Bi flyres between 0.8 to Figure 107 SEM image of metallic droplets present on surface of sample grown under 2.8 nA of Bi flux.

carrier trapping rate[113]. It's interesting this wasn't observed in the temperature series with increased Bi contents however it may be the lower growth temperature initialised more trap states than the higher Bi content could compensate for. The difference in behaviour of the higher content samples depending on their growth conditions give some insight into the trade-off between adjusting the Bi content through Bi flux or substrate growth temperature. There could conceivably be circumstances where one would be more favourable however the growth temperature appears to have a wider operational window

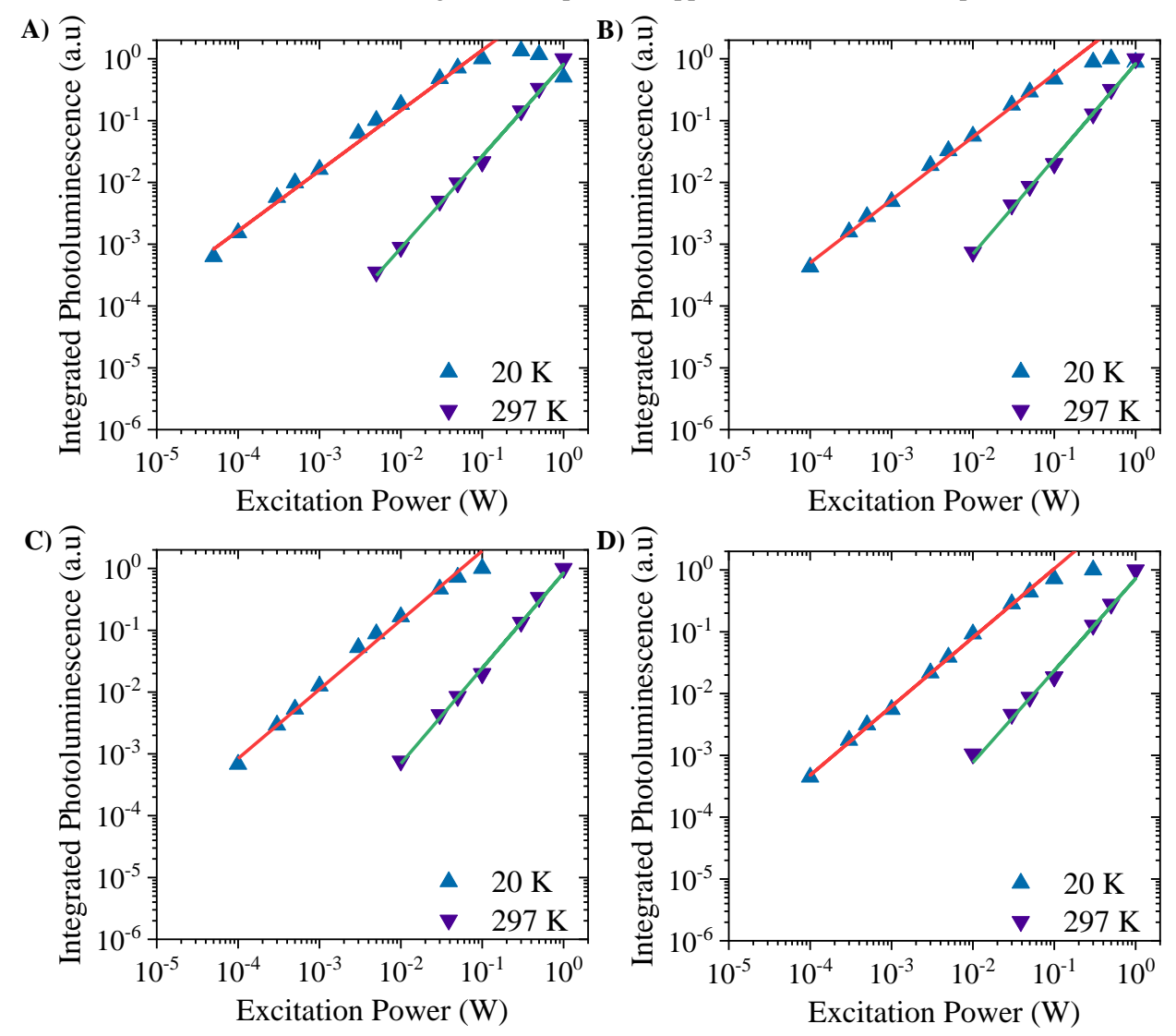


Figure 109 Normalised integrated photoluminescence vs excitation power for changing Bi fluxes between 0.8 - 2.8 nA. Where, A) 0.8 nA, B) 1.4 nA, C) 2.2 nA and D) 2.8 nA.

compared to the Bi flux. This follows to the conclusion that alteration of the Bi flux is best for fine tuning the Bi content under the tested growth conditions. Particularly when small levels of metallic droplets are present a slight lowering of the Bi flux can resolve this issue. The flux at which droplets appear is a function of both the incorporation efficiency and desorption rate of Bi from the surface. Hence it is expected that the Bi flux control could be extended by reducing the growth temperature.

## **5.6 TD PL**

#### 5.6.1 AL Content

The integrated luminescence at 20 K shown in Figure 110 demonstrated the presence of Al at contents between 2.5 -15 at% in GaAs<sub>0.976</sub>Bi<sub>0.024</sub> results in a dramatic loss in PL intensity. The decrease is roughly an order of magnitude at 20 K and is present in all Al containing samples. However, it is independent of the Al:Ga ratio within the tested range. This was attributed to Bi clusters and point defects acting as centres of non-radiative recombination in the previous section 5.5.1, which while restricted at 20 K remained active. The contribution from this region of the PL constitutes a small portion of the overall PL spectra. The temperature dependent PL results presented in this section and associated fitting therefore does not reflect contribution from the Bi clusters/point defects as it is overshadowed by the bulk recombination proportion of the PL spectra. This results in the TD providing information which is limited to the properties of bulk Bi containing layer. The data has been fitted with the dual Arrhenius

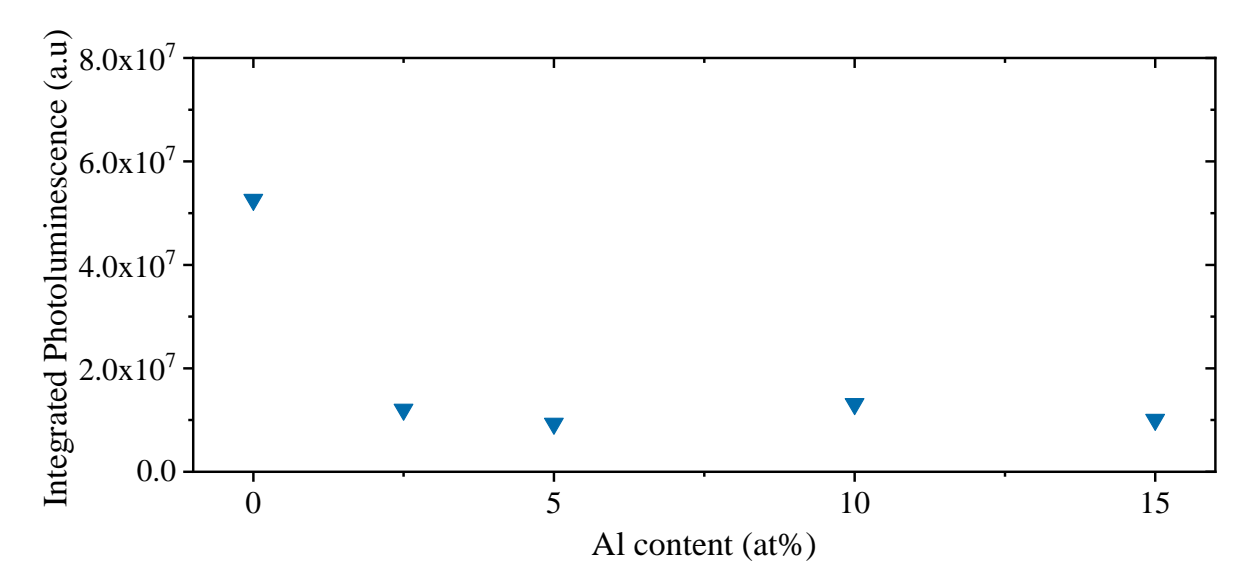


Figure 110 Integrated Photoluminescence spectra at 20k of varying Al contents between 0 to 15%.

equation given in equation (12). This gives 4 fitting parameters with two energies  $Ea_1$  and  $Ea_2$  which are related to the activation energies of the trap state and two constants of  $C_1$  and  $C_2$  which relate to the corresponding concentration of these defects. However, the concentrations are only relative within a singular sample. The values of these fitting coefficients are shown in Figure 111 for  $Ea_1$  and  $Ea_2$  and Figure 112 show the ratio of  $C_1:C_2$ .

Both activation energies broadly increase with increasing Al content having initially dropped with the incorporation of 2.5 at% Al into GaAsBi. The activation energies Ea<sub>1</sub> and Ea<sub>2</sub> of the 15 at% Al sample line up closely with the values of the 0% GaAsBi sample. Values of Ea<sub>1</sub> range between 23.5 to 13.7 meV with the lowest value at 2.5 at%. The trend is similar for Ea<sub>2</sub> with ranges between 106 to 66.9 meV with the lowest value at 5 at% Al content. It is of note that both the 2.5 and 5 at% Al sample are very closely matched in the Ea<sub>1</sub> and Ea<sub>2</sub> energies. is The values for Ea<sub>1</sub> and Ea<sub>2</sub> are shown in Figure 111a and b respectively. The value range of Ea<sub>1</sub> would indicate this process is a phonon dependent non radiative

recombination mechanism. The Values of Ea<sub>2</sub> however more closely align with the difference between the PL emission peaks. In this case it is the difference between the dominant peak at room temperature

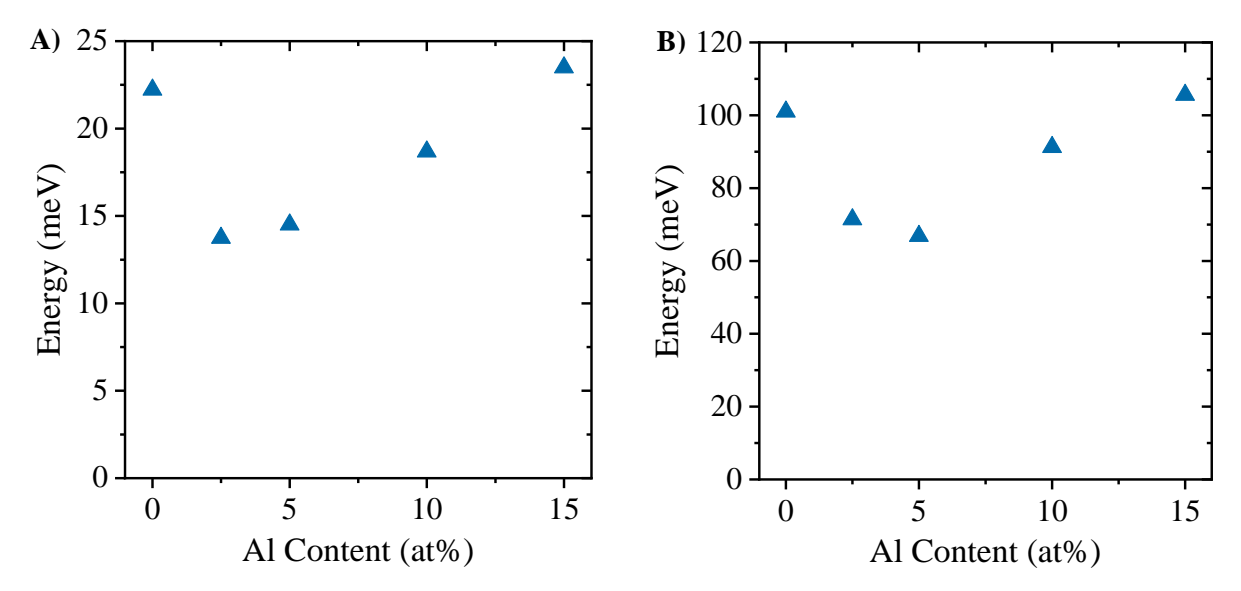


Figure 111 Non radiative recombination activation energies extracted from fitted temperature dependent photoluminescence for aluminium contents between 0-15 at%. A) Ea<sub>1</sub> B) Ea<sub>2</sub>.

and the dominant peak that appears with decreasing temperature, becoming dominant by 175-150 K. Therefore, Ea<sub>1</sub> is a measure of the transition from band edge to localised state emission. The ratio of magnitude for the fitting show a steady ratio for all Al containing samples. However, for the control GaAsBi sample the ratio increases indicating a shift to a higher proportion of phonon related defects. This also corresponds to a higher PL intensity which may signify that a large proportion of the defects induced by the co presence of Al and Bi are related to the energy separation of the localised states from the VB edge.

Examining this more closely the TD PL data for STM83 is presented in Figure 113, this is a representative sample of this series with all samples displaying similar behaviour. This is with the caveat of the 0 at % Al sample which does not have the peak between 0.95 and 1.15 eV but is otherwise alike. The transition of line shape with decreasing temperature offers a valuable insight into the recombination mechanism underpinning this alloy. Measures taken at 297 K consist of the main PL peak at 1.313 eV from the bulk Bi containing layer and a shoulder between 0.95 to 1.15 eV from the Bi clusters and or point defects. Decreasing the temperature from 297 K to 150 K alters the PL line shape significantly. There is the appearance of a new dominant peak at lower energy in the case of 5 at% Al at 1.292 eV. The previous dominant peak has blue shifted to 1.364 eV with the value closely matching that predicted

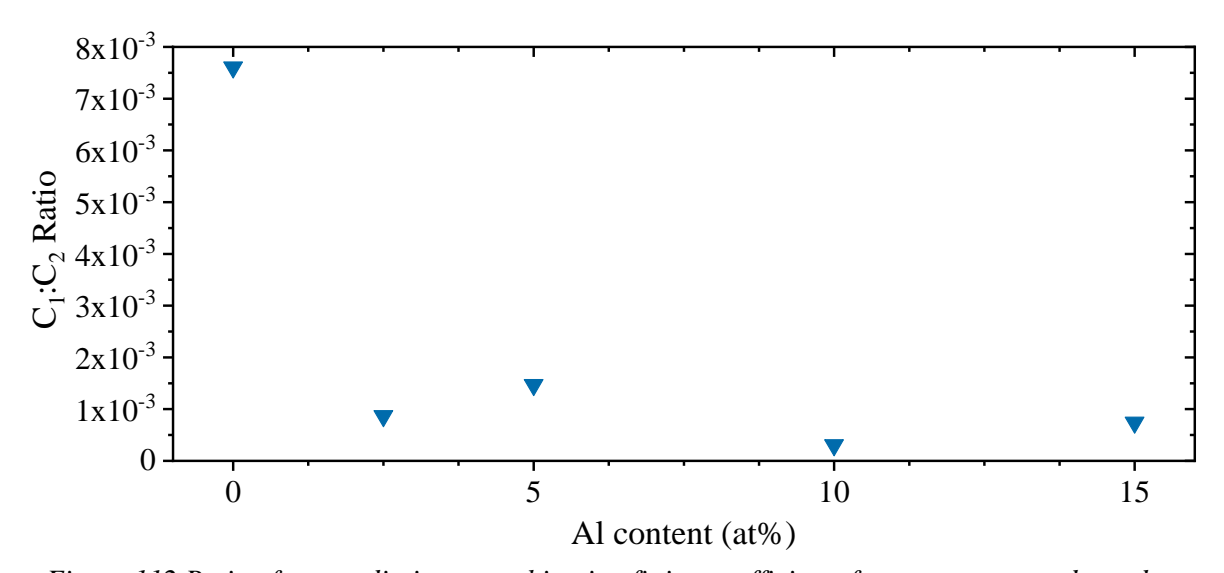


Figure 112 Ratio of non-radiative recombination fitting coefficients from temperature dependent photoluminescence for aluminium contents between 0 to 15 at%.

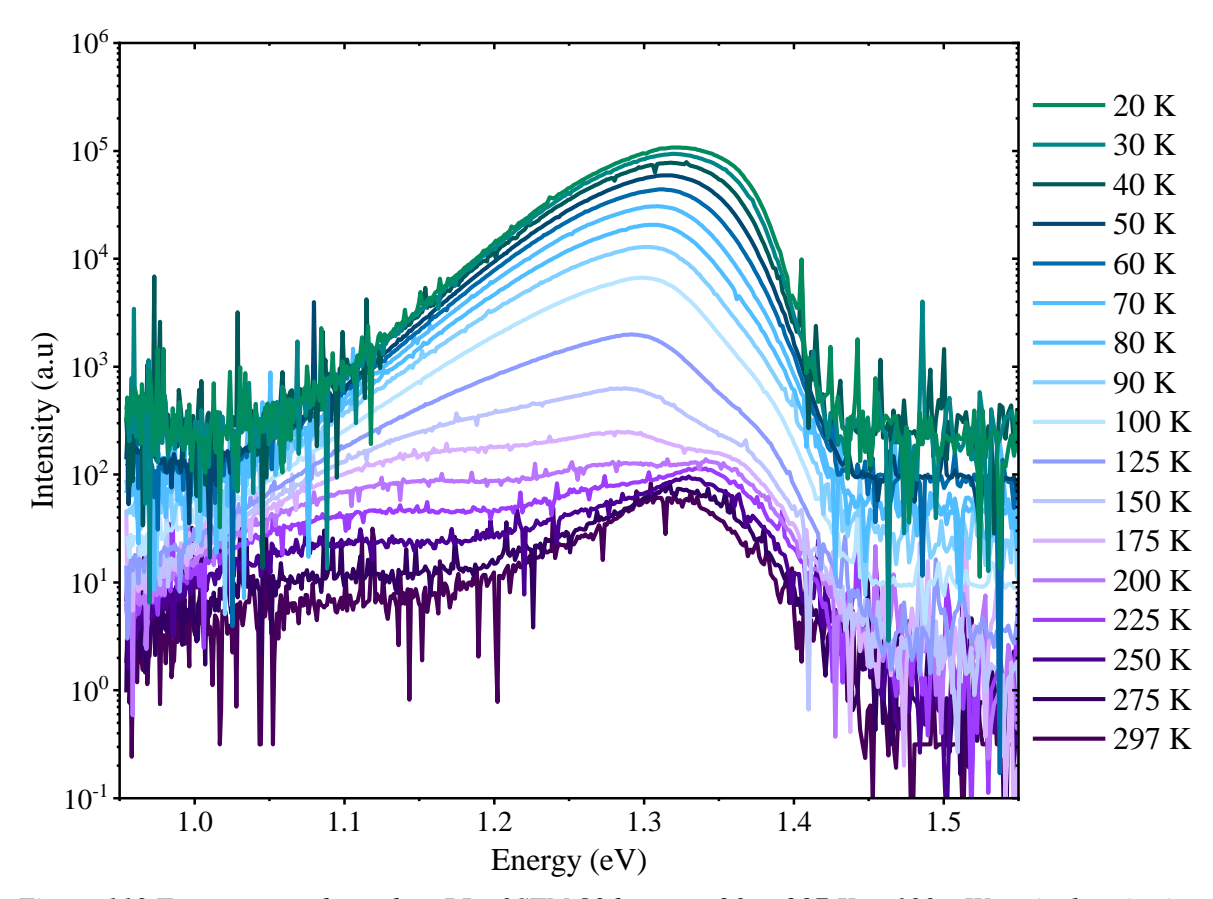


Figure 113 Temperature dependent PL of STM 83 between 20 to 297 K at 100 mW optical excitation.

by the Varshni shift of GaAs [118]. Finaly emission from the Bi clusters and or point defects peak between 0.95 to 1.15 eV has started to form part of a shoulder to the new dominant peak however its contribution to the overall PL is steadily decreasing. Lowering the measurement temperature further to 20 K and only a singular broad peak remains centred at 1.322 eV there is some slight blue shift however the value is significantly lower than would be expected by Vashni. The peak possesses a long tail trailing off to lower energies however there is no sign of contribution from the Bi cluster and or point defect states. Moving towards higher energies there is a much sharper drop to the Bi layer peak giving a sharp asymmetry there is no indication of a shoulder from the previously dominant emission at 297 K. This suggests the recombination mechanism has changed with decreasing measurement temperature. This is further enforced by the apparent redshift of the PL emission with decreasing measurement temperature which without a mechanism change would contradict traditional semiconductor theory [118].

The line shape at 20 K as previously described in section 5.2.4 corresponds to recombination dominated by localised Bi states sitting above the valence band edge. Increasing the carrier mobility by raising the measurement temperature allows for recombination to occur at states closer and up to the valence band edge. This is indicated from the shoulder observed down to 90 - 100 K. This is the remaining contribution from the peak which dominated at 297 K and followed the expected Varshini shift of standard valence band (VB) to conduction band (CB) recombination. Hence measurements taken

between 90-297 K provide insight into the ratio between localised state – CB and VB - CB recombination with the balance more in favour of VB – CB at higher temperatures. The increased presence of carriers able to reach the VB edge also coincided with the emergence of the Bi cluster/point defects emission. This has been previously stated as a centre of non-radiative recombination. Carriers which are able to make it from the localised states to the VB are therefore also capable of migrating into the Bi clusters/point defects. The approximate energy gap between the centre of localised state emission and centre of VB edge emission at 5 at% Al is 72 meV at 150K. This matches up closely with the extracted Ea<sub>2</sub> energy. This is not isolated to this sample and this trend is consistent across the series.

This behaviour can be described kinetically by carrier mobility. When mobility is more limited carriers are more readily trapped within localised states and thus recombine close to their initial excitation. Increasing the kinetic energy of the system allows the carrier to migrate for longer within the bulk before recombining. This increases their chance of encountering a localised Bi cluster or point defect, becoming trapped. Thus, the chance of non-radiatively recombining is greatly increased reducing the PL luminescence with increase sample temperature.

The presence of the Bi clusters and point defects within the lattice would indicate the Al causes an increase in Bi segregation compared with Ga. Disaffirming the assumption that Al could be substituted for Ga in GaAsBi without further consideration. The XRD measurements in section 5.3.1 confirm the crystal structure remains zinc blende with no additional phases. However, Al would prefer to make a significantly shorter bond with Bi than Ga-Bi. The bond length could be causing severe stress and instability in the zincblende structure making it very energetically unfavourable for a Bi to be bound to any Al without severely distorting the lattice structure. This would conceivably enhance Bi diffusion through an Al containing lattice as it would be more energetically favourable for bonds to break than in a solely Ga based zincblende structure. This could also lead to the formation of atomic compensation mechanisms in case where Al and Bi do bind creating vacancies or antistites. There has been no theoretical study into the defect formations within an AlGaAsBi crystal. It must also be interjected however that this effect would also be expected to alter the incorporation efficiency of Bi into the alloy under traditional incorporation. Higher Al contents would lead to lower incorporation efficiency of Bi which is not observed within this series. However, it could be this effect merely narrows the III:As flux window, and in the case of this study we've successfully threaded the eye of a needle without being impacted by the constricting of parameter space.

### **5.6.2** Growth Temperature

The integrated PL at 20 K at 100 mW excitation is shown in Figure 114, at either end of the temperature range tested the total luminescence decreases. For the sample grown at 340 °C the peak intensity is the highest across the series however the peak itself is narrower that the sample grown at lower temperatures. This is due to the lower Bi incorporation with increase growth temperature leading to lower Bi contents reducing the number of localised states. Toward the other extreme the PL intensity is again decreased relative to samples grown at 300 and 320 °C. This can be attributed to the increased Bi content of the sample due to the lower growth temp at 280 °C. This sample as previously discussed had a decreased energy gap between the valence band edge and defect region. The increased proximity to the energy states of primary luminance potentially makes carrier escape into the defects states easier. This would also be the case for individual point defects such as Bi<sub>Ga</sub><sup>2+/+</sup> which would fall closer to the valence band edge with the increased Bi content. As would also be the case for any primary electron trap state which sit relative to the conduction band edge. This is because the Bi incorporation will shift the VB significantly more than the CB so any defect with reference to the CB will appear closer at higher Bi contents. The two centre samples grown at 300 and 320 °C have comparable intensities with a minor decrease at the lower temperature, indicating a small increase in in the density of defects.

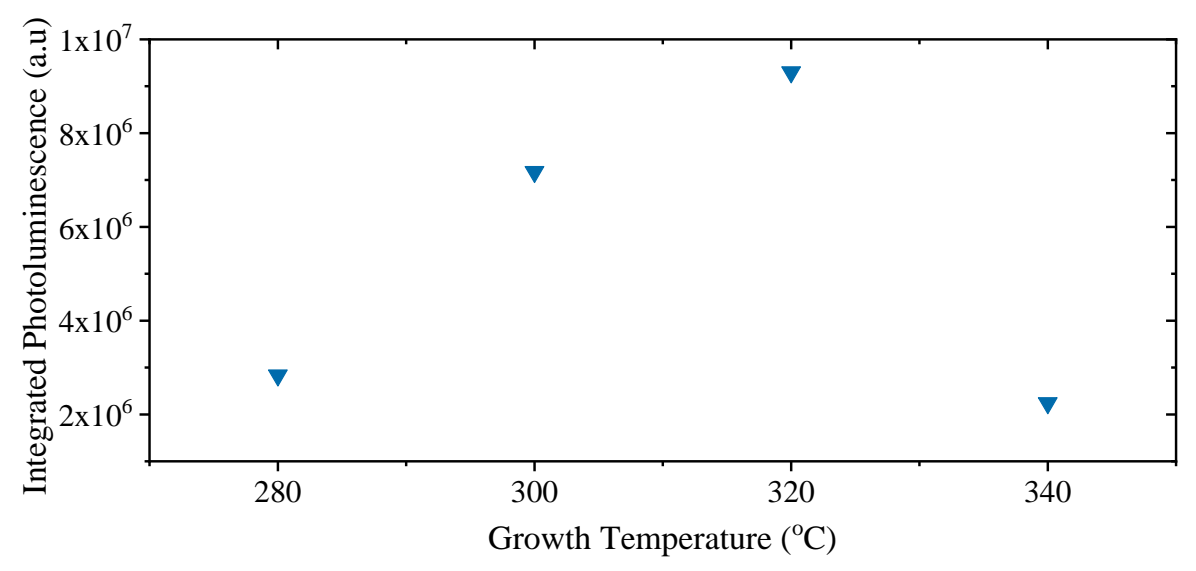


Figure 114 Integrated photoluminescence spectra at 20 K of varying growth temperatures between 280 to 340 °C.

The integrated PL taken at temperatures between 20-297 K is shown in Figure 117, with the energies extracted by fitting with equation (12) shown in Figure 115. The energy Ea<sub>2</sub> rises as the growth temperature is decreased. The energy is again attributed to the difference between the emission from the band edge and emission from localised states. Just as was previously observed in the Al content subseries. Emission from the band edge is seen at 297 K with localised Bi states beginning to contribute to the PL emission at temperatures below 150 K. This can be seen in Figure 116 where a shoulder to the emission from the band edge appears at 150 K at 1.04-1.06 eV. The reduction in the Ea<sub>2</sub> energy with

decreasing Bi contents seen at higher growth temperatures aligns with expectations. The reduced Bi contents will limit the depth of localised states to closer to the valence band edge. This would bring the emission from the states closer to the emission from the band edge which in fitting would be observed as a lower energy difference, as seen here. The energies associated with Ea<sub>1</sub> remain in the range typical

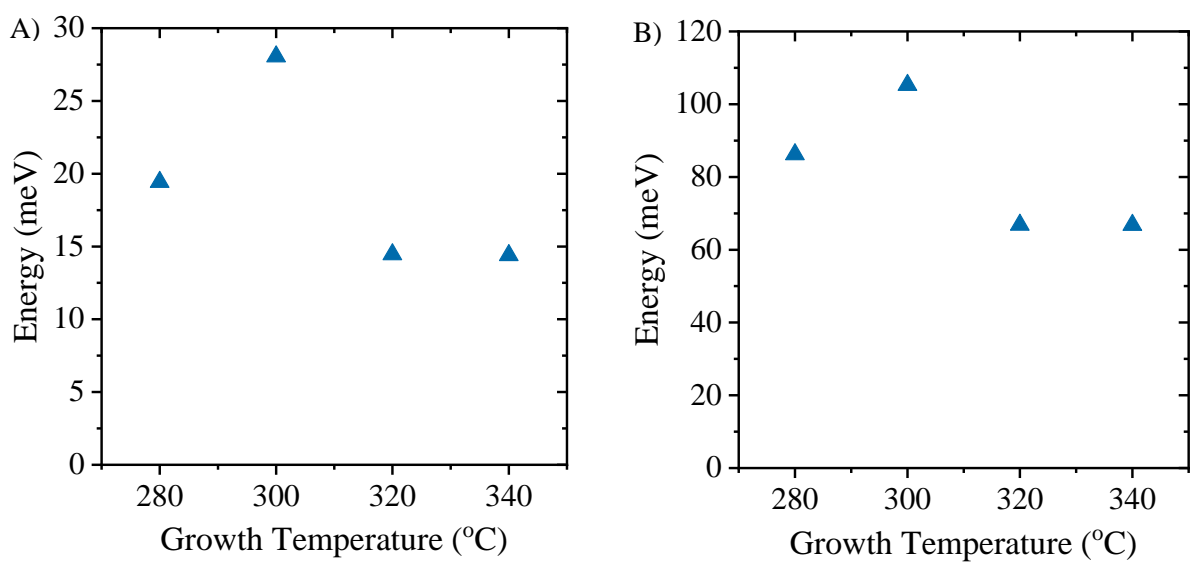


Figure 115 Non radiative recombination activation energies extracted from fitted temperature dependent photoluminescence for varying growth temperatures between 280 to 340 °C.

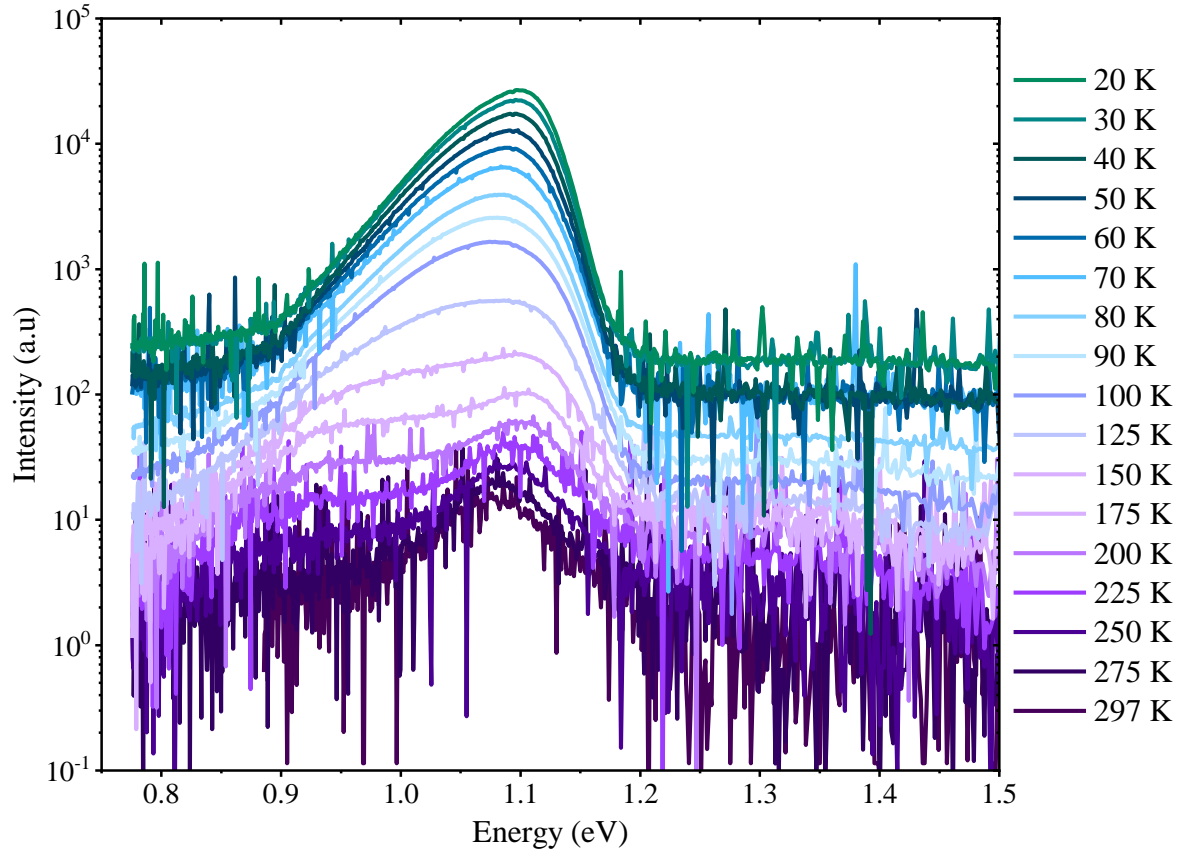


Figure 116 Temperature dependent PL of STM88 a sample grown at 280 °C and measured between 20 to 297 K at 100 mW optical excitation.

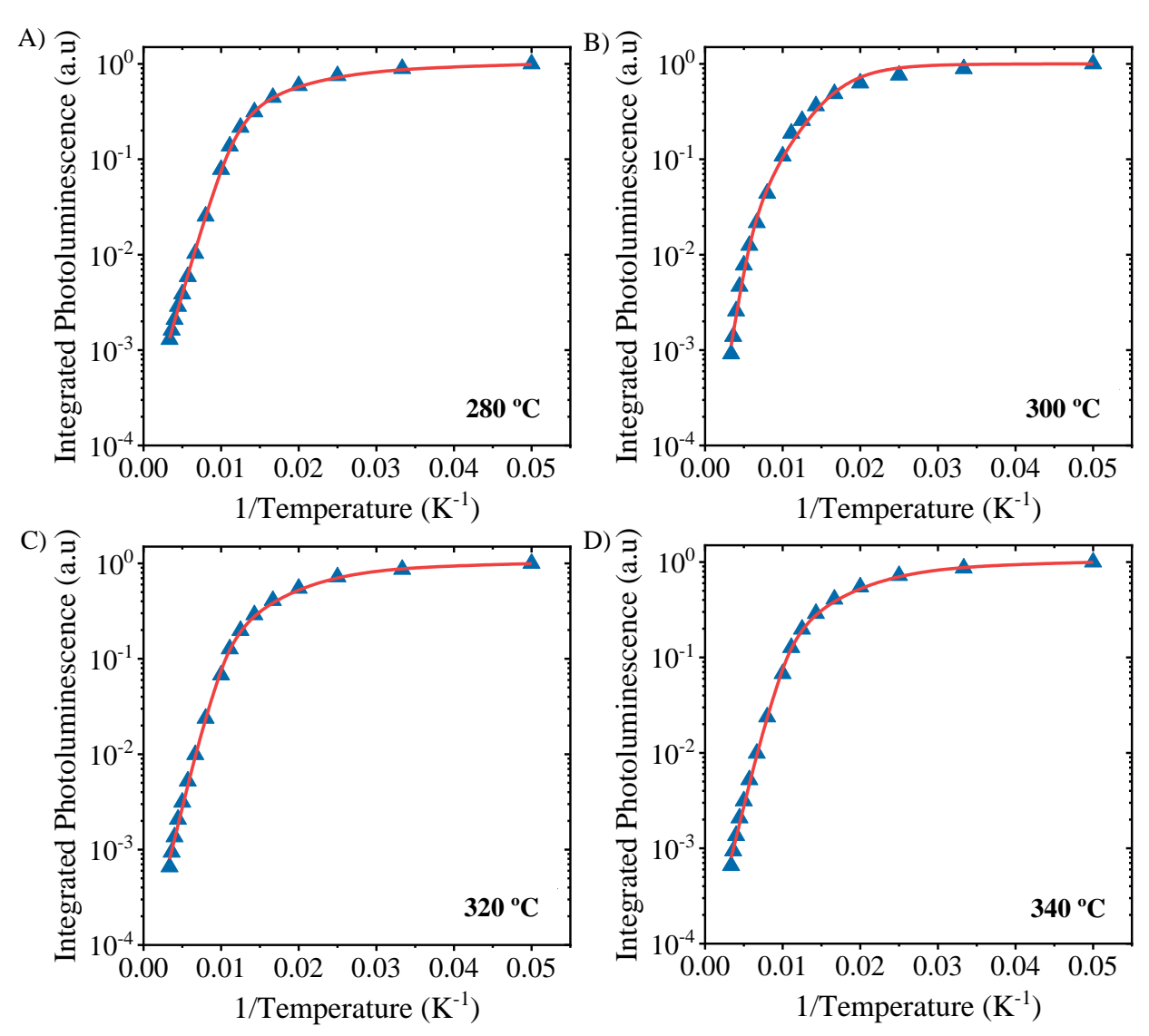


Figure 117 Normalised photoluminescence vs sample temperature at constant excitation for growth temperatures between 280 to 340 °C. Where, A) 280 °C, B) 300 °C, C) 320 °C and D) 340 °C.

of phonon interactions. The point defects previously asserted to be present within the material in section 5.2.1 and

	Experimental	Energy (eV)	Defect origin
	energy (eV)		
Majority- electron trap	0.23-0.28	0.36	$(VGa+BiAs)^{2-/3-}$
	0.56-0.61	0.69	VGa2 <sup>-/3-</sup>
	0.60-0.67	0.78	(VGa+BiAs) -/2-
	0.87-0.88	0.80, 0.84, 0.84, 0.89	BiGa+ <sup>/0,</sup> AsGa+ <sup>/0,</sup> (AsGa+BiAs)
			+/0, (BiGa+BiAs) +/0
Majority-hole	0.50-0.53	0.46, 0.52, 0.52	AsGa2+/+, (AsGa+BiAs) <sup>2+/+,</sup>
trap			(BiGa+BiAs) <sup>2+/+</sup>
	0.27-0.30	0.33	BiGa2+ <sup>/+</sup>
	0.08	0.02-0.08	VAs+nBiAs, VGa+nBiAs

Table 5. Would be dependent on phonon interactions to function as trap states within the AlGaAsBi layers. However, the range of defects suspected to be present would give a broad disruption of phonon energies. The value extracted from the fitting of Ea<sub>1</sub> is an indication of the median of this broad range, although the exact distribution of energies is unknown. The magnitude of defects from the fitting would seem to suggest an increasing number with lower growth temperatures. However, these values are directly related to the value of integrated luminescence and the observed drop at 280 °C is the result of decreasing luminescence. The values therefore can only be utilised to assess the proportion of defects between the two fitted activation energies within the same material. The ratio of C<sub>1</sub> to C<sub>2</sub> is therefore shown in Figure 118. It can be seen that at the lower growth temperature there is a higher proportion of non-radiative recombination from the phonon dependent process. There appears to be a peak at 300 °C with the highest proportion of defects relative to the localised sates. In all cases the intensity of the PL increased due to the localised state emission. This originates from the confining of the carriers at lower growth temperatures with carriers unable to thermally excite to the band edge. Recombination is therefore limited to the localised states. This also supresses the carrier's ability to reach the defect regions of the material. This combines to give a 2 order of magnitude increase in the PL as the result of thermal quenching of non-radiative recombination pathways. This also accounts for the previous observations that the Al-Bi induced defects are dependent on the energy difference between the VB and

localised states. The carriers are at least for the majority being thermally isolated from the defects at 20 K.

### 5.6.3 Bi Flux

The integrated PL for samples grown with 0.8 - 2.8 nA of Bi flux taken at temperatures between 20-297 K has been analysed at previously conducted for the prior sub series. The thermal quenching

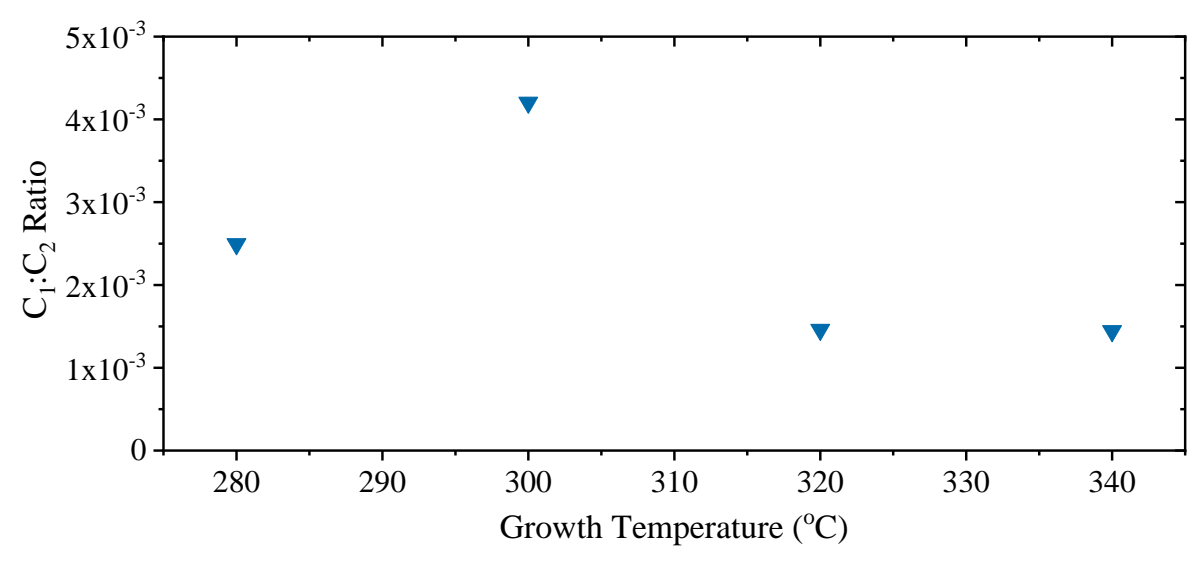


Figure 118 Ratio of non-radiative recombination constants extracted from fitted temperature dependent photoluminescence for varying growth temperatures between 280 to 340 °C.

appeared complete will full roll over observed in all samples. The data was fitted with a dual Arrhenius equation with 2 energies and 2 constants used for fitting. The equation is given in equation (12) with the extracted energies and ratio of constants given in Figure 119 and Figure 120 respectively. In line with previously observed trends the Ea<sub>2</sub> energy rises with increasing Bi contents . The underlying mechanisms remains unchanged from previous subseries with higher Bi contents resulting in localised Bi states that sit further above the valence band edge. The sample grown at 2.8 nA of Bi flux plateaus where it would be expected to keep rising in this trend. This is attributed to the increased defect densities and non-radiative recombination due to metallic droplet formation during growth. The energies associated with Ea<sub>1</sub> still align with phonon interactions. This would be expected as the defect mechanism identified with the material rely on phonon interactions for non-radiative recombination within, the trap states. The increases in these energies with higher Bi flux and Bi contents closely matches the trend in Ea<sub>2</sub>. This would indicate the proportion of defects are changing in higher flux samples as the shift in Ea<sub>1</sub> is representative of a broader distribution of defect energies. Non radiative recombination mechanisms with lower activation energies are reducing in concentration which should be beneficial for optical quality, even if only apparent at low temperatures. While pathways centred around different defects with higher activation energies are comparatively increasing. One potential example of an interchange in defects could be the transition from isolated  $V_{\text{Ga}}\,$  reducing in density and

being replaced with binary compensation complex  $V_{\text{Ga}}$ -Bi<sub>As</sub><sup>2-/3</sup>. This indicated peak at 2.2 nA shown in Figure 120 appears counter intuitive. The higher ratio would indicate a higher proportion of low temperature defects. However, when compared with the control sample it can be inferred that higher optical quality material has a higher proportion of lower temperature defects. It seems however that the quantity due to the Al-Bi compensation mechanism still remains significantly higher than in the control GaAsBi sample. This would shift the distribution of phonon energy levels to higher energies which would be reflected by a rise in the value of Ea<sub>1</sub>.

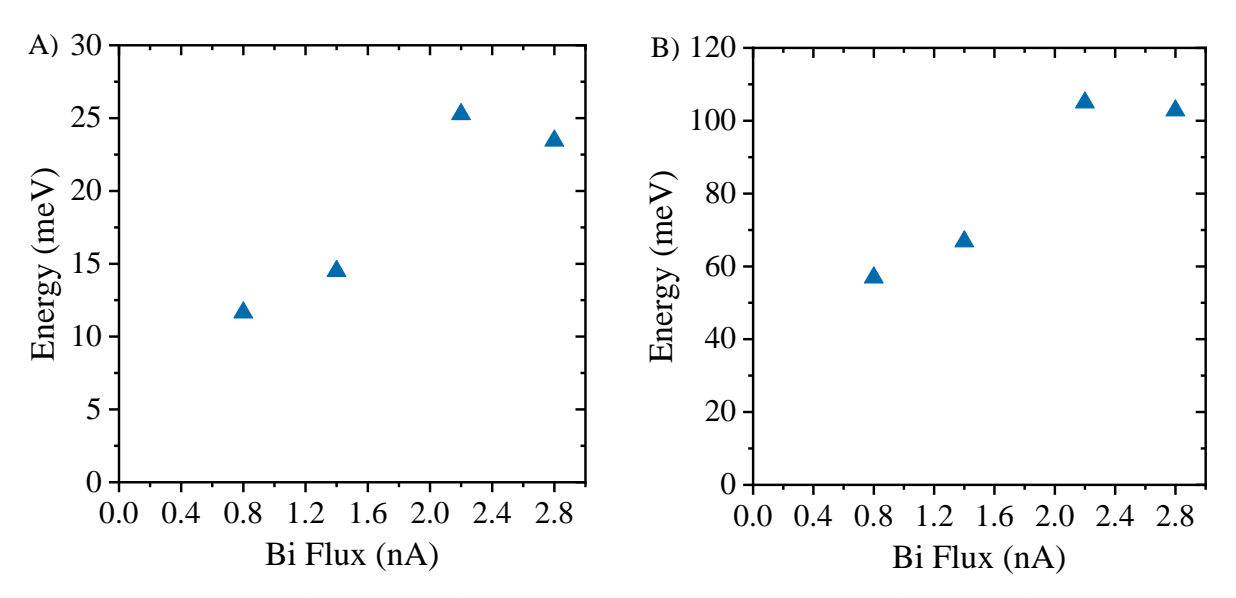


Figure 119 Non radiative recombination activation energies extracted from fitted temperature dependent photoluminescence for Bi fluxes between 0.8- 2.8 nA. A), Ea<sub>1</sub> and B) Ea<sub>2</sub>.

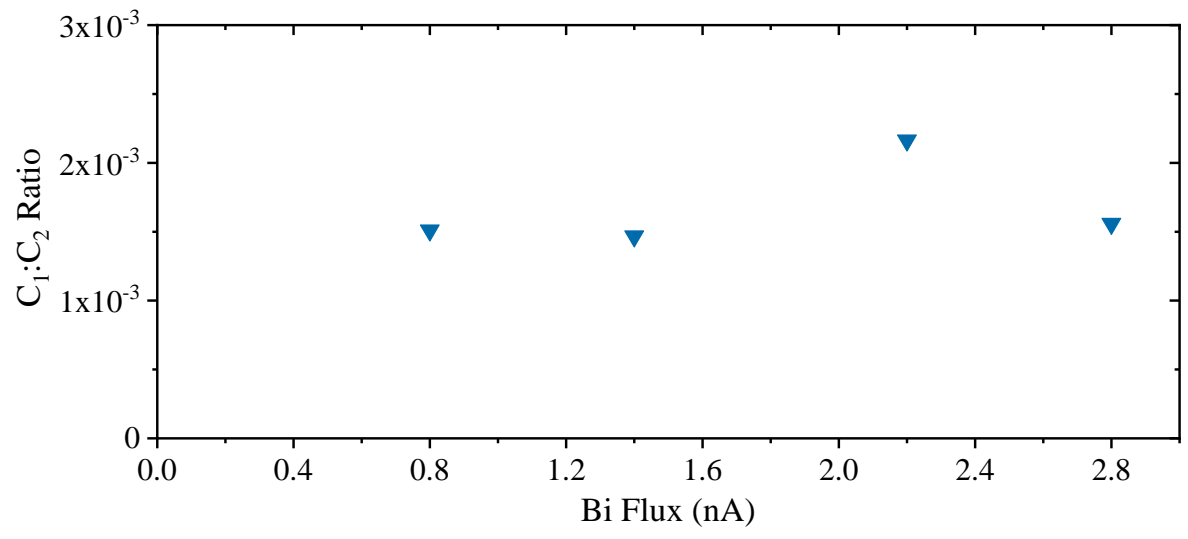


Figure 120 Ratio of constants C1:C2 for Bi fluxes between 0.8 to 2.8 nA. A), Ea<sub>1</sub> and B) Ea<sub>2</sub>.

The total number of defects within the material cannot be quantifiable determined from TD PL alone. Additional analysis of comparable device structures by deep level transient spectroscopy (DLTS) would allow for this however this would require additional growths. However, the 20 K luminescence of the sample grown at 2.2 nA is the brightest AlGaAsBi sample in the entire series at 20 K, as shown in Figure 94 and Figure 108. This would indicate that the number of defects is either holding steady and transitioning to defects with high energy barriers. Alternatively, or concurrently, it may also be indicating a reduction in the total number of defects. The change observed has had no impact on the TD progression with the raw PL data for the sample grown at 2.2 nA of Bi flux shown in Figure 121. The same transitions in PL line shape with temperature as previously described in other sample of this series is observed. The Ea<sub>2</sub> energy again is attributed to the difference between the main PL emission at 297 K and the emission attributed to localised states that becomes dominant at temperatures below 150 K. PL intensity increases by approximately 4 orders of magnitude and is the closest in intensity to the 0% Al GaAsBi control sample which peaks at 10<sup>6</sup>. This high increase in intensity with temperature is again evidence of the high number of defects from either localised areas of high Bi content and associated defects in isolation or in conjunction with isolated point defects within the lattice. The Bi flux would appear to aid in the thermal quenching of some of these defects by either reducing the quantity or transitioning to alternate defect formations with a higher energy barrier to non-radiative recombination.

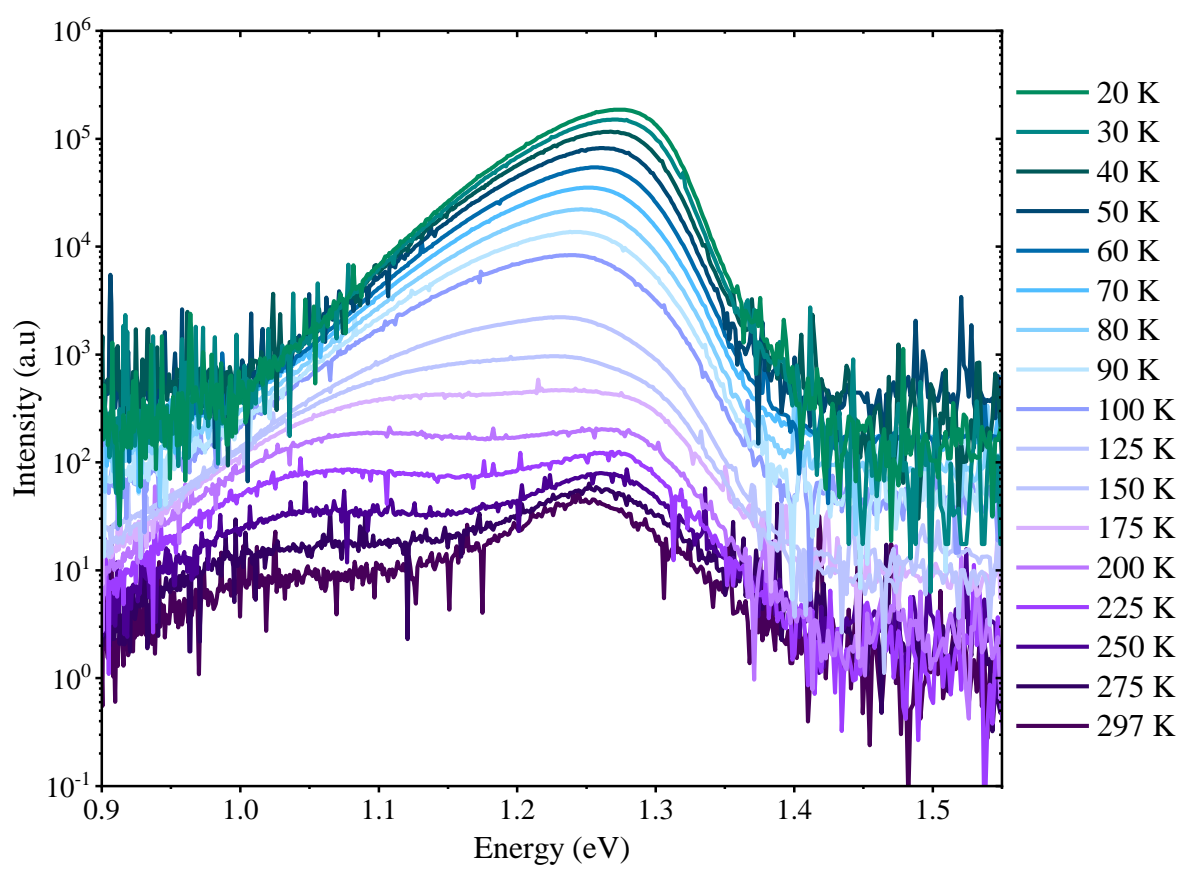


Figure 121 TD photoluminescence of STM 89 a sample grown with 2.2 nA of Bi flux at temperatures between 20 to 297 K.

Country to what was indicated in the temperature series for growth of AlGaAsBi higher Bi fluxes can

improve the optical quality. This does not however provide an insight into a mechanism for removing the formation of these defects from the crystal only in alleviating their presence.

# **5.7 Ion Beam Analysis**

#### 5.7.1 Al Content

The sample structure within this series was considered too allowed for analysis at the UK National Ion Beam Centre using TOF ERD and RBS. This analysis provided quantifiable compositional information for both Al and Bi contents within the material. With lighter elements more accurately quantified with TOF ERD while RBS is more sensitive to Bi contents. Representative examples of the RBS spectra and TOF ERD histogram for the 5 at% centre point sample are shown in Figure 122A and B respectively. TOF ERD is fitted using Potku analysis software which generates a separate energy spectrum for fitting each element within the histogram. This provided the atomic masses and depths at which each particle

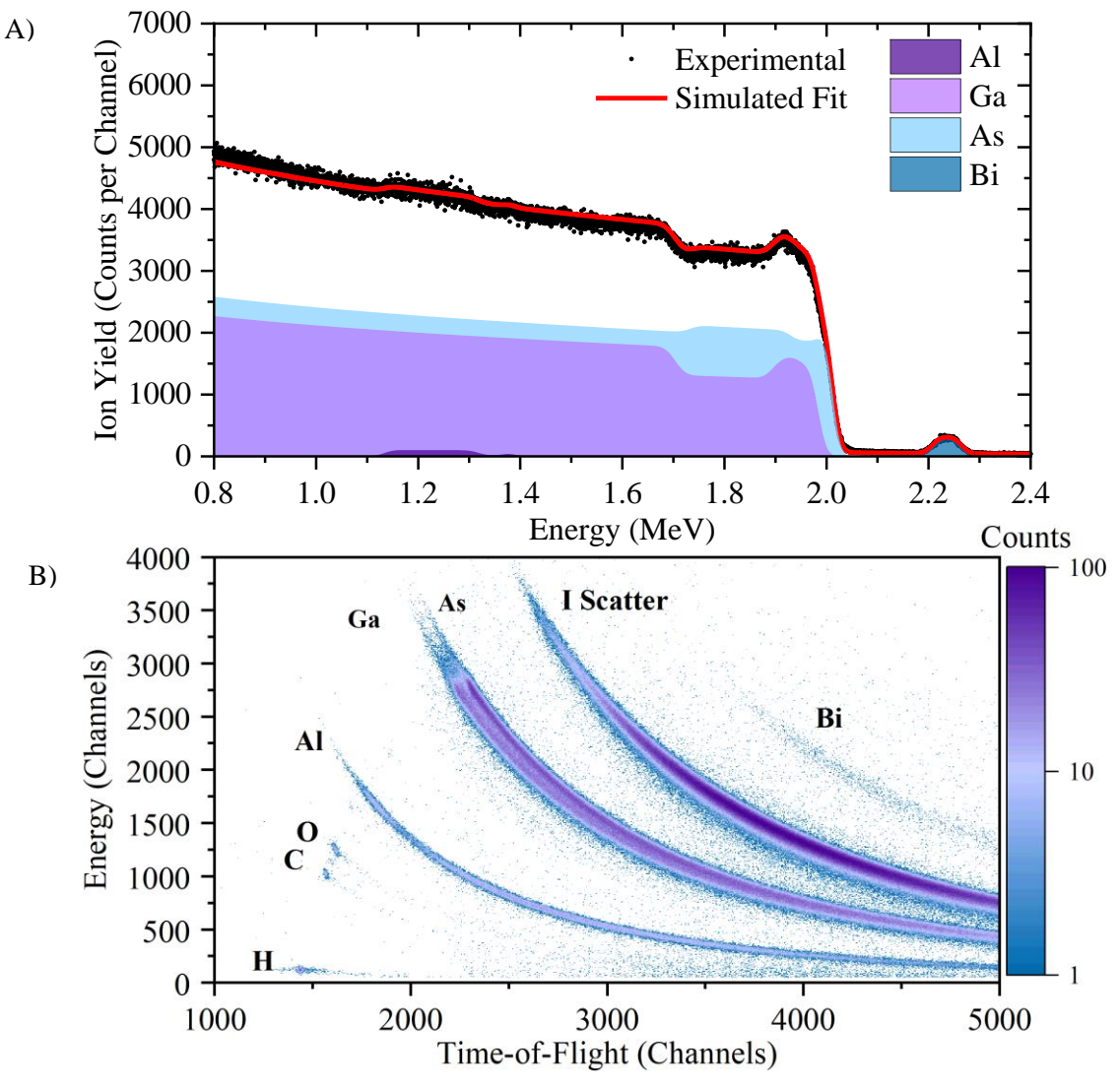


Figure 122 A) Ion beam analysis of STM83 5 at% AlGaAsBi raw RBS spectra with simulated fit B)
Ion beam analysis of STM83 5 at% AlGaAsBi sample TOF ERD Histogram

originated for each element present. Comparative count rates between all the elements present produces a depth profile and compositional information for the sample. Multiple scattering events are accounted for with Monte Carlo elastic recoil detection (MCERD) simulations. All simulations are iterative in fitting to the data. The final depth profile for STM83 the 5 at% Al sample is shown in Figure 124. The extracted contents for Al and Bi from RBS and TOF ERD for the entire series are shown in Figure 123.

The contents of Bi as measured for the AlGaAsBi layer between 0-15 at% Al are shown in Figure 123A. There is some variance in the values measured by the 4 techniques used within this study. However, all values are in general agreement with a maximum observed range  $\pm$  0.4 at% from the average. PL denoted by the upward blue triangles, generally gives the lowest values of Bi content. This is in line with expectation, as the only Bi content the PL measurement accounts for is Bi occupying the intended lattice site. It has been stated that there are significant quantities of defects and been proposed that the vast majority are centred around atomic Bi compensation complexes. While some do emit and can be seen in the PL, there is likely a significant quantity to which PL remains insensitive. TOF ERD denoted by the purple squares is sensitive to all Bi contained within the sample irrespective of the atomic environment in which the atom occupies. Hence the values of Bi content are higher. Although this is not without limits, The atomic weight of Bi exceeds that of the incident I ion beam which dramatically increases the uncertainty with extracting the Bi content from TOF ERD. This gives a substantially reduced signal as seen in Figure 122 and the increased mass will also increase the scattering further reducing signal intensity while complicating the fitting to the raw data. XRD and RBS are the more suitable method for assessing the Bi content. XRD will be sensitive to any Bi that affects the 004 lattice spacing. Defects such as V<sub>Ga</sub> and Bi<sub>Ga</sub> will alter the spacing by different quantities to Bi<sub>As</sub>. The XRD fitting did not account for defect lattice sites in the model. However, the overall fraction of defects within the material is still expected to be a very small in comparison, hence the fitting will not be

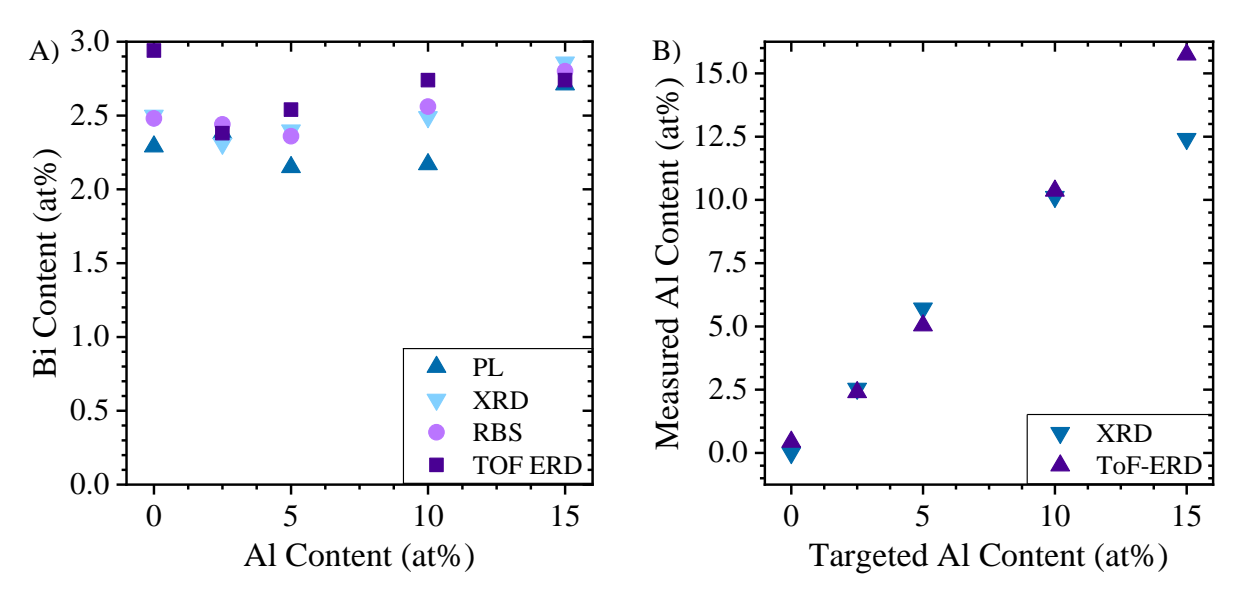


Figure 123 Comparison of A) Bi contents as measured from PL XRD RBS and TOF ERD and B) Al contents as measured from XRD and TOF ERD.

invalidated by their presence. This can be seen as the RBS closely agree with the XRD fitting. The RBS is the most accurate technique to quantify the Bi content due to the mass sensitivity of RBS measurement. The contribution to the RBS spectra from the Bi is distinctly separated from the main body of the spectrum as seen in Figure 122 A at ~2.2 - 2.28 MeV. This however makes it less suitable for determining the Al contents due to the reduced size and atomic mass of Al in comparison. The overall trend seen in this Bi content with changing Al content can be best described as an apparently insensitive relationship. The Bi incorporation appears unaffected by the changing Al contents. There is a slight increase at 15 at% however this would fall within run-to-run variance, as indeed do all Bi contents within the Al content sub series.

Ion beam analysis of the Al content with the AlGaAsBi layer was confined to TOF ERD. The XRD and TOF ERD are in close agreement for AlGaAsBi samples with Al contents between 0-15.3 at% Al as shown in Figure 123B. There is again a discrepancy at 15 at% however the inherent uncertainties of concurrent Al and Bi fitting for XRD previously described account for the error. The TOF ERD value is a more accurate and reliable measure of the Al content as it is an independent measurement and fitting for each element. The difference between targeted and measured values is inconsequential with a maximum variance of  $\pm 0.74$  at% Al at 15 at% Al. This confirms the growth rate calibrations and Ga:Al flux ratios were accurate for the MBE growth of this series. It also justifies the Bi contents extracted from the PL measurements with the vac anti band crossing model.

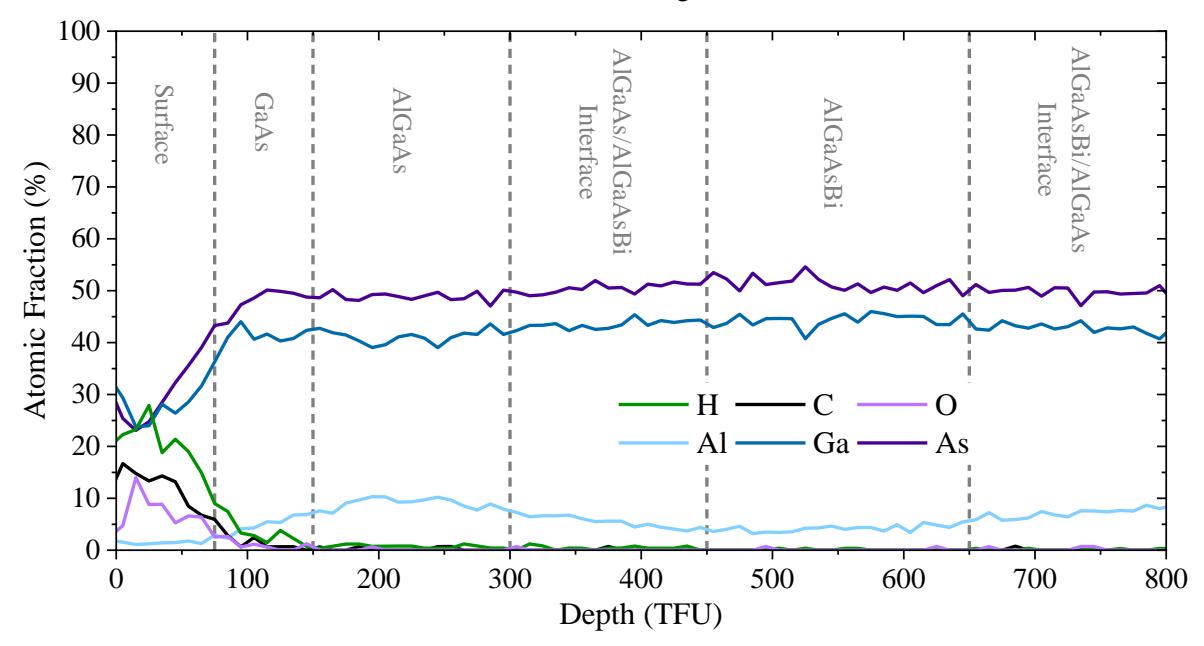


Figure 124 Depth profile of 5 at% AlGaAsBi extracted from TOF ERD by Potku fitting.

Both RBS and TOF ERD show significant interface regions either side of the bismide containing layer. This can be seen in the rising Al contents within these regions on the Potku profile shown in Figure 124. There is no Bi profile due to the uncertainties previously describe in extracting Bi contents from TOF ERD. The interface region between the substrate and AlGaAsBi layer remains at constant thickness of 20 nm in all samples present. This could indicate there is some roughness at the end of the

AlGaAs buffer layer. Which when averaged out over the beam size for the ion beam analysis is producing this wide interface instead of the abrupt change in Al content as intended in the growth.

Cross sectional TEM of the STM83 sample confirms this is indeed the case and the wider interfaces analysis are the product of layer roughness. This can be seen in TEM shown in Figure 125. The cause of the roughness at the interface between the AlGaAsBi and AlGaAs is worth consideration. It can be seen that the GaAs surface post oxide room is reasonably smooth with a few minor areas of damage. The AlGaAs buffer should have alleviated this before the Bi layer was grown. The snapshot provided by the TEM is post layer growth. However, when looking at the top interface between the AlGaAsBi and AlGaAs upper cladding the interface is much smoother. The RHEED previously shown in Figure 90a would also indicate the buffer layer was of reasonable smoothness based on the quality of the RHEED pattern. There is multiple possible explanations for the observed roughness. The buffer growth could be poorly optimised and the induced roughness a consequence. This however doesn't fit with the observed smoothness at the top interface between the upper cladding and the Bi layer. It would be far more reasonable that the surface roughness remained smooth during growth as opposed to the 100nm layer smoothening the inherent roughness post AlGaAs buffer growth. Therefore, the interface likely deteriorated post layer deposition, most likely during the overgrowth of the Bi and capping layers. This

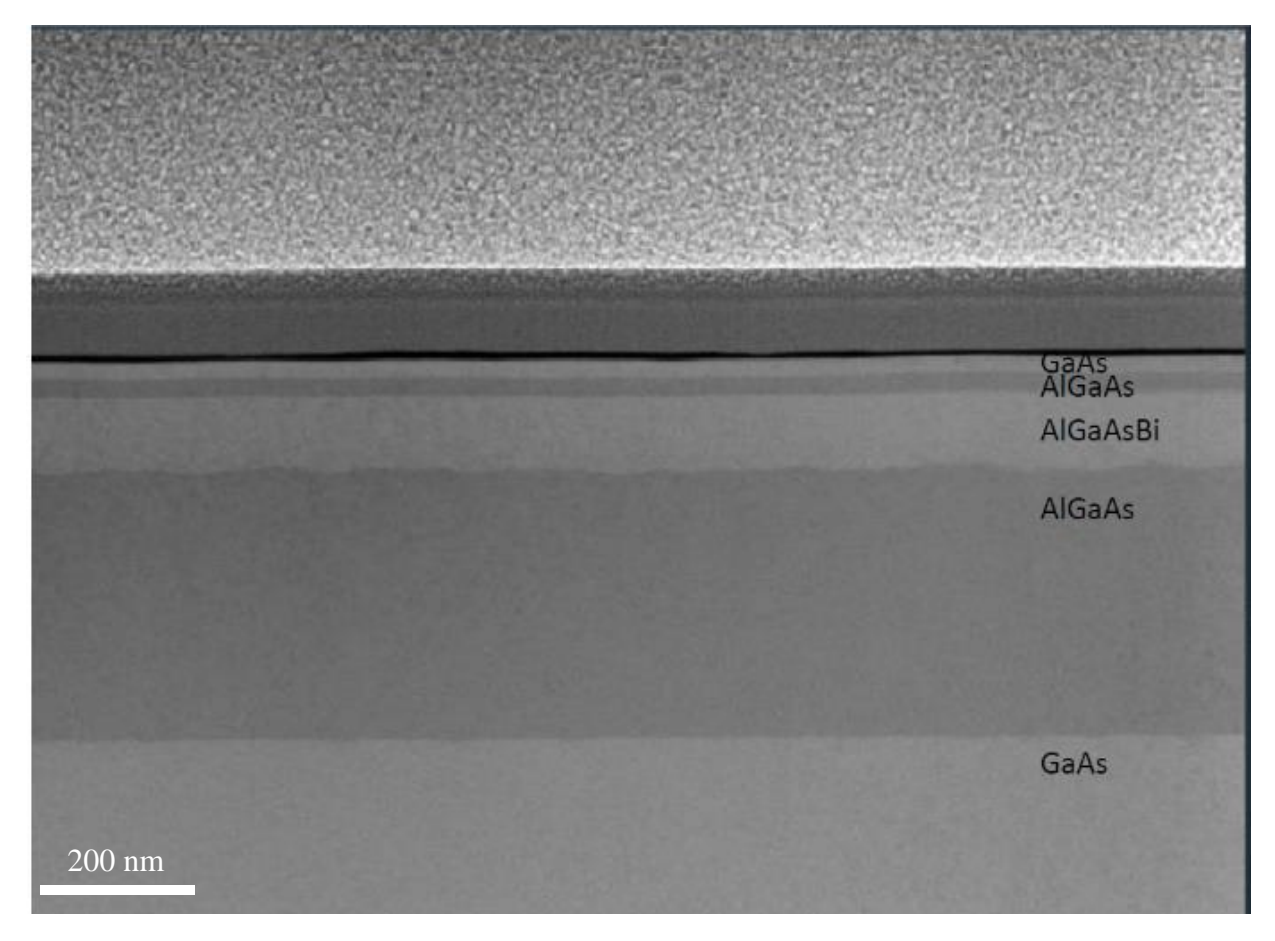


Figure 125 Cross section of STM83 as imaged by high-angle annular dark-field scanning transmission electron microscopy.

would also account for why the interface with the AlGaAs capping layer at the surface is relatively smooth. The graded decline in Al content seen in the TOF ERD could indicated there is some Al interdiffusion between the AlGaAs buffer layer into the Bi layer. This is also noted in the upper interface between cladding layer and GaAs capping layer. Further supported by the detection of 0.44 at % Al in the 0% Al sample which was grown with the Al shutter closed. However, the interface regions above and below are both equal in Al content hence this would not account for roughness observed in one and not the other. It could be that as the Bi surface coverage gradually increased during early layer growth the AlGaAs continued to grow in exposed areas of the surface. While the AlGaAsBi formed underneath the coverage of the Bi wetting layer. This formation could give rise to the interface seen and account for the graded drop in Al content during the layer growth. It would also explain why the growth of AlGaAs atop AlGaAsBi produces a far high-quality interface. It may therefore be a logical step to deposit a Bi layer prior to starting growth of bismide containing materials on AlGaAs.

There are indications of a lack of unity in the III:As ratio within the material with a deficiency of group III elements detected by TOF ERD. This is counter intuitive to III-V epitaxial growth, with growth rates within this study all being group III limited with an excess of As provided. This deficit oscillates around 1-2 at% less Ga and Al than expected and is independent of the Al content. This may be accounted for with defects such  $V_{Ga}$ ,  $Bi_{Ga}$  and  $As_{Ga}$ . However, the level of these defects as indicated by the PL does not align as the brightest 0 at% Al GaAsBi PL sample still retains this slight discrepancy from a unity III:As composition. It's noted that this issue seems particularly prevalent in the GaAs and AlGaAs capping layer where high levels of dechannelling are also observed in the RBS. The RBS results can be used to measure the quantity of atoms sitting interstitially within the lattice by comparing the random and aligned spectra. However, this has seemingly been invalidated by the high dechannelling in the GaAs and AlGaAs capping layer. The results are shown in Figure 126, as can be seen the value for the 0 at% Al sample would indicate 85% of atoms are sitting on interstitial sites. Such values would result

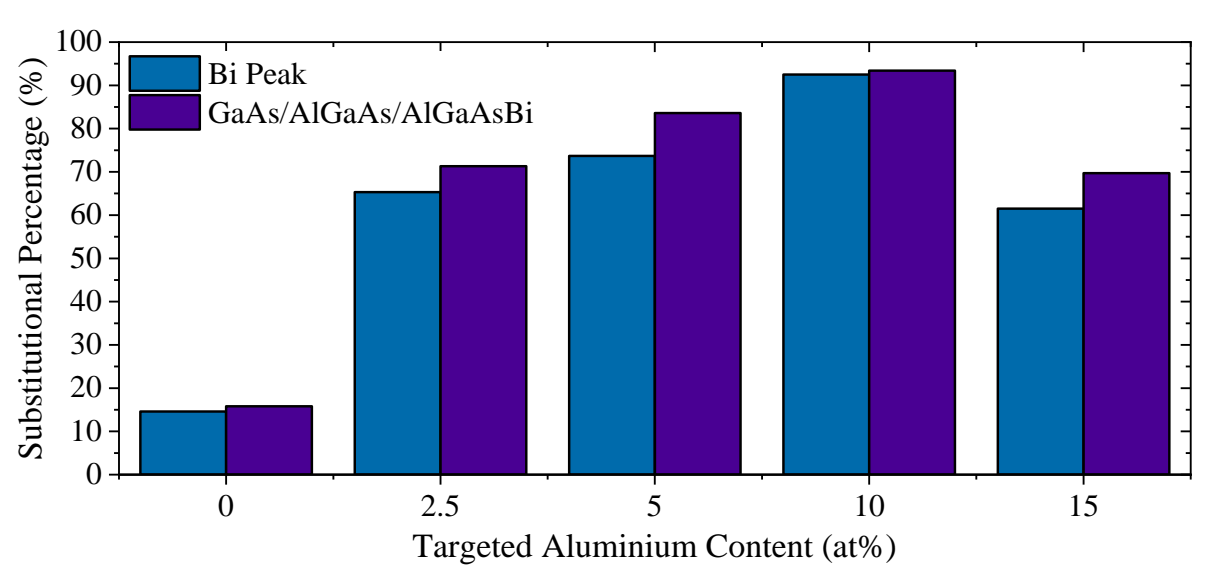


Figure 126 Substitutional contents for Bi and Al, Ga, As as measured by RBS.

in totally unstable crystalline structures and is also in contradiction to the high optical quality shown previously. Part of the RBS issues can be attributed to the interface quality and strain at the interfaces between the layers. The improvement with increased Al content would indicate the reduced compositional difference between AlGaAsBi and AlGaAs cladding at the interface is reading as a higher substitutional proportion. The deviation from this trend at 15 at% Al is likely the result of the slightly higher Bi content as reported for this sample in prior analysis. However, the dechannelling observed in the capping layers and interface would strongly indicate that there is a significant quantity of defects located in these regions. This could be the physical region where the Bi clusters and point defects limiting the optical performance are physically located. I strongly advocate for future work to focus on improving this region of the structure. It could yield a far higher optical quality of AlGaAsBi alloy and realise the material for next generation APDs.

### **5.7.2** Growth Temperature

TOF ERD and RBS analysis were conducted on the samples within the temperature sub series, the results of are shown in Figure 127A and B for Bi and Al respectively. Comparing the Bi contents across the 4 techniques utilised within this study it can be seen that the variance between them increases with higher Bi contents. This even at approximately 6 at% Bi still falls with a range of  $\pm 0.4$  at% with the TOF ERD having the higher variance. This corresponds to the lower level of confidence in TOF ERD for quantifying the Bi content compared with the other 3 techniques. Irrespective it can be stated that the analysis are all in reasonable agreement. There is a minor difference in the Al contents extracted by TOF ERD which are all between 0.4-0.7 at % lower than as determined by the XRD fitting. In both cases the Al content remains stable across the series within 5.6 and  $4.8 \pm 0.2$  at% for XRD and TOF ERD respectively. This difference between the two could easily be accounted for with the reduced sensitivity in XRD fitting to Al composition in the AlGaAsBi. This confirms that Al content remains stable across the temperature series while Bi content reduces with increased growth temperature. This was previously shown in the XRD and PL sections of this sub series. However, the confidence is further enhanced by verification afforded with Ion beam analysis techniques. It can be extrapolated from a linear fit to the data in Figure 127A that the temperature incorporation limit for Bi into AlGaAsBi falls at an approximate value of  $355 \pm 5$  °C. This is under the growth conditions tested with the fixed As flux ratio and 1.4 nA of provided Bi flux. This values is slightly lower than would be expected, as the upper temperature limit for Bi incorporation into GaAs is usually quoted as falling between 380-390 °C [119], [120]. However, this is likely more due to growth conditions used within this study as the 320 °C starting point is also lower than typical GaAsBi growth with comparable Bi contents. It would be expected that the temperature limit could be increased with higher fluxes of Bi supplied to the layer during growth. The trend shown for Bi contents indicates that the growth is operating under a temperature limited growth regime where the Bi incorporation efficiency can still be further improved by reducing the growth temperature. This is not indefinite, and a point will be reached where 100% incorporation efficiency is achieved. The regime will then switch to Bi flux limited one. It cannot be estimated however from the data available at which temperature this would occur or the upper limit that could be achieved with 1.4 nA of Bi flux.

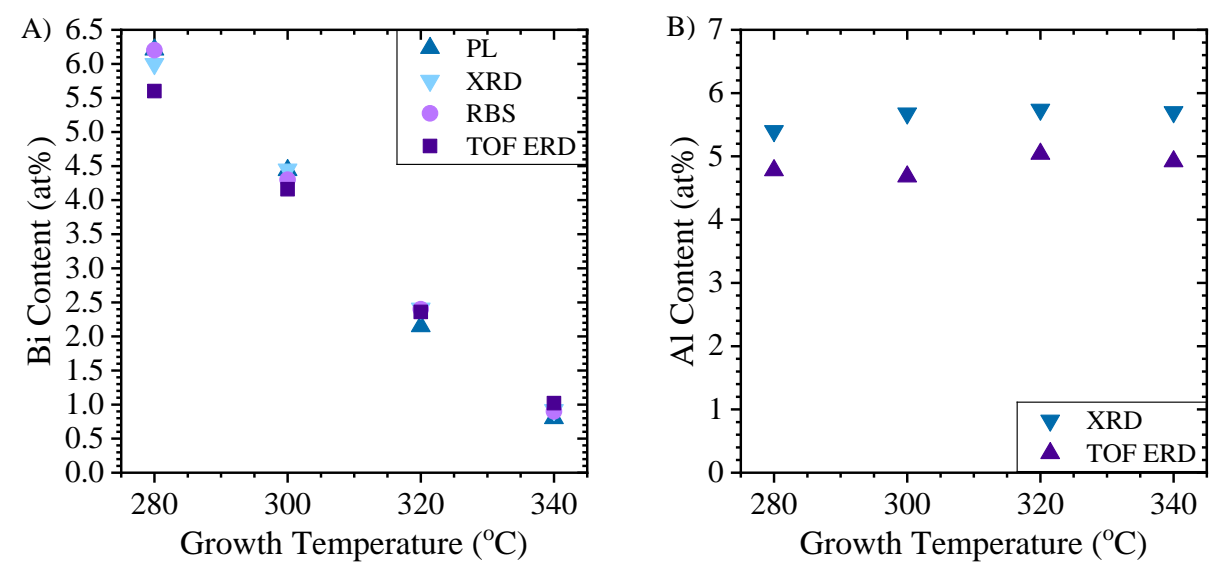


Figure 127 Comparison of A) Bi contents as measured from PL XRD RBS and TOF ERD and B) Al contents as measured from XRD and TOF ERD.

The raw TOF ERD histogram and RBS spectra are shown in Figure 129. The Bi contents are extracted from the RBS spectra. The increased Bi content with lower growth temperatures can be clearly observed in the raw RBS data by comparing the height of the Bi peak at approximately 2.22 MeV. The peak approaches 1000 counts per channel at 6 at% for the sample grown at 280 °C and falls linearly with increasing growth temperature down to approximately 200 counts with 0.9 at% Bi at 340 °C. This can also be observed in the TOF ERD histograms even with the reduced confidence in the quantified content. The Bi contribution in the TOF ERD can be seen in energy channels between 1500-2500 and

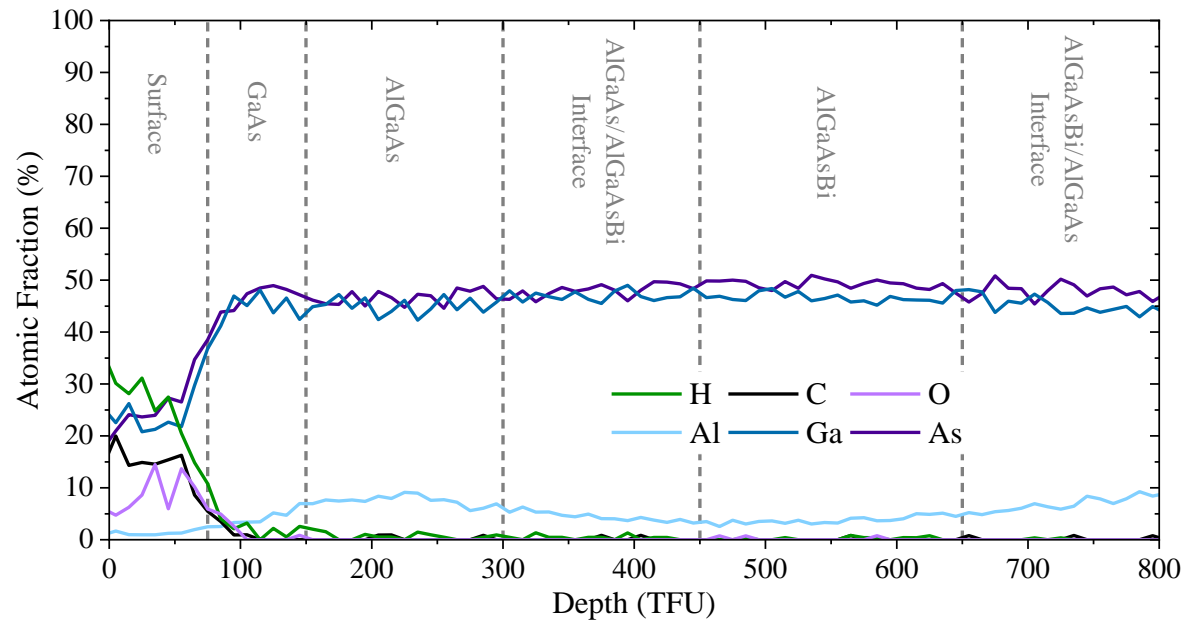


Figure 128 STM 88 280 °C Potku Profile extracted from Tof ERD fitting.

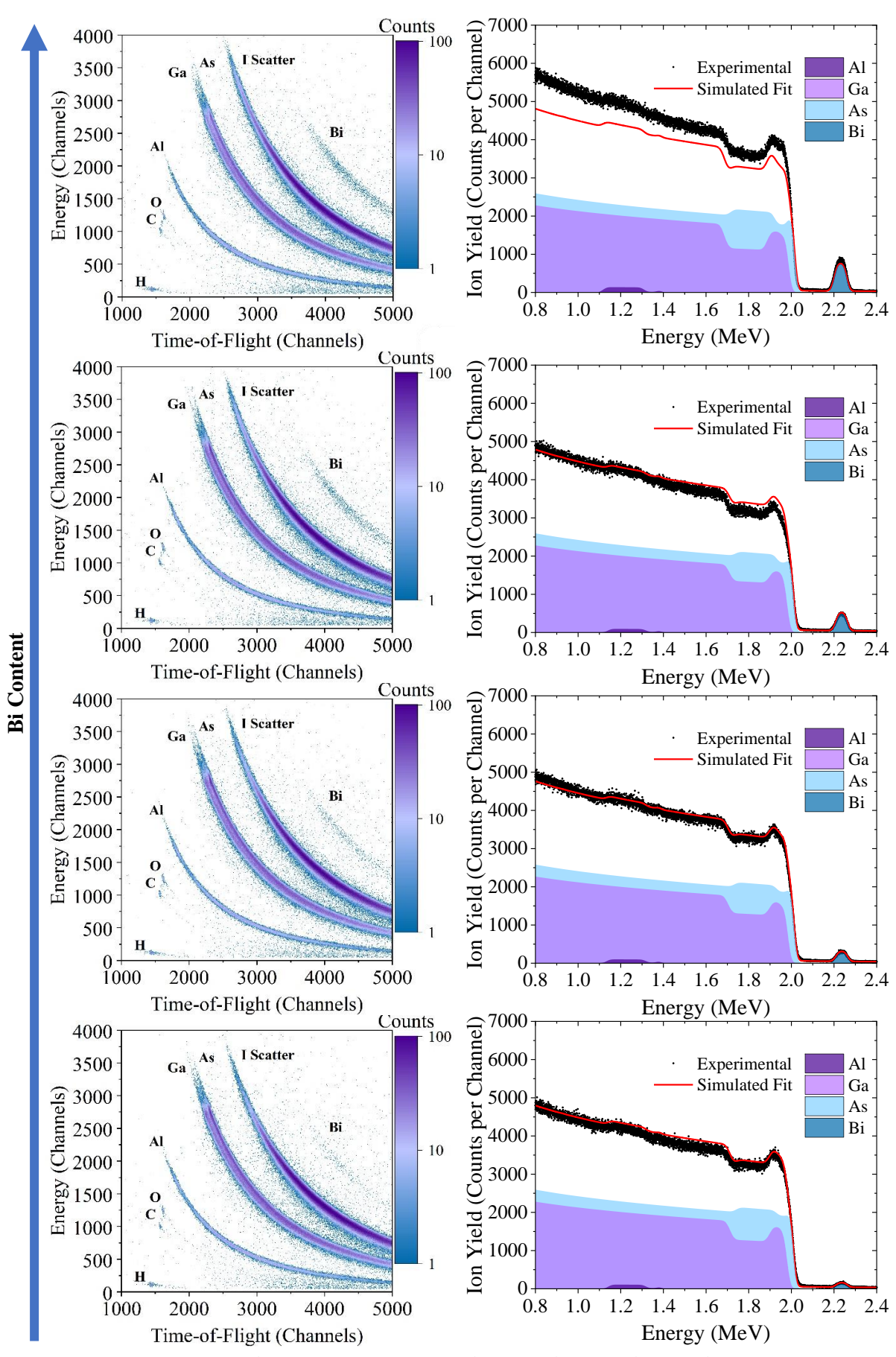


Figure 129 TOF ERD and RBS of Temperature Sub series shown with ascending temperature.

ToF channels between 3700-5000. The density of the counts within this region can be seen to visibly decrease with increased sample growth temperature. There are again also some contaminants present on the surface. The contributions from O, C and H are caused by water and CO<sub>2</sub> adhesion to the surface once samples are removed from a vacuum environment. The GaAs capping layer functions as a barrier to prevent these from degrading the layers for optical analysis, the AlGaAs cladding and AlGaAsBi layer. The Potku depth profile of Al ,Ga As and contaminants shown in Figure 128 confirms the GaAs capping layer functioned as intended. This means atmospheric sources of contamination can be ruled out as the cause of defects observed within the AlGaAsBi layer that have plagued the optical quality of this alloy.

The Al contents can be seen to reduce as intended in the AlGaAsBi layer however there are again interfaces present above and below the Bi containing region. The thickness of the interface regions was unaffected by the temperature. However, it is strongly suspected that the surface roughness observed in STEM of the centre point would still be present within the presented sample grown at 280 °C and other of this sub series. This may be interpreted as an interface region by the TOF ERD which averages the contents over large region. This would also account for why the interface region is interpreted as thicker at the buffer interface with 20nm compared to 10-7nm for the upper cladding interface. This is reflected in the high observed roughness previously seen at the interface between Bi layer to buffer layer with a marked improved at the interface between the Bi layer and upper cladding AlGaAs. It is also of note that the in the measurements of samples grown both above and below 320 °C the ratio of group III:V elements detected is equal. Unlike in the sample grown at 320 °C where a Ga deficiency was detected. Following from this I would suspect that this is more likely an artifact of the measurement or fitting for the 320 °C analysis. The number of defects as indicated in the optical measurements is within the same order of magnitude across this series. Hence the high number of vacant Ga sites indicated only at 320 °C by the TOF ERD results do not align with what is observed in other measurements.

The number of atoms sitting substantially on designated atomic sites has been assessed by comparing the random and aligned RBS spectra. This is not sensitive to antistites defects however would highlight interstitials and discontinuities within the lattice. These both would disrupt the channelling vectors through the crystal structure. The results of this analysis are shown in Figure 130. There is no obvious trend across the series with results ranging from 20-75% of Bi atoms and 30-85 % of the group III species sitting substitutionally within the lattice. This is most certainly a measurement artifact from the RBS. The practical difficulty in finding a channelling direction is further exacerbated by interlayer strain. There were significant issues with high ion dechannelling and the AlGaAs-AlGaAsBi upper cladding interface is likely a considerable cause of these issues. In addition, the change in strain at this interface further increases the challenge. However, there is no trend relating the samples were this high dechannelling was observed. It is unrelated to Bi or Al content nor any correspondence to the sample growth order. There is no cross-section TEM on sample beside the 320 °C within this series. However,

on the few samples from other subseries that have been imaged there is comparable surface roughness observed. Hence the roughness is believed to be consistent across the series. The experimental setup could account for the difficulties as due to the size of sample they were mounted with carbon tape. This means that the sample are not sitting perfectly flat compared to the stage and calibration samples used to align the ion beam and detectors. Hence the difficulty in finding the channelling vector through the lattice could be randomly distributed based on the flatness achieved for each wafer by carbon tape mounting. This being said, the compositions determined from the RBS and TOF ERD measurements were unaffected by the increased the measurement difficulty for the operator.

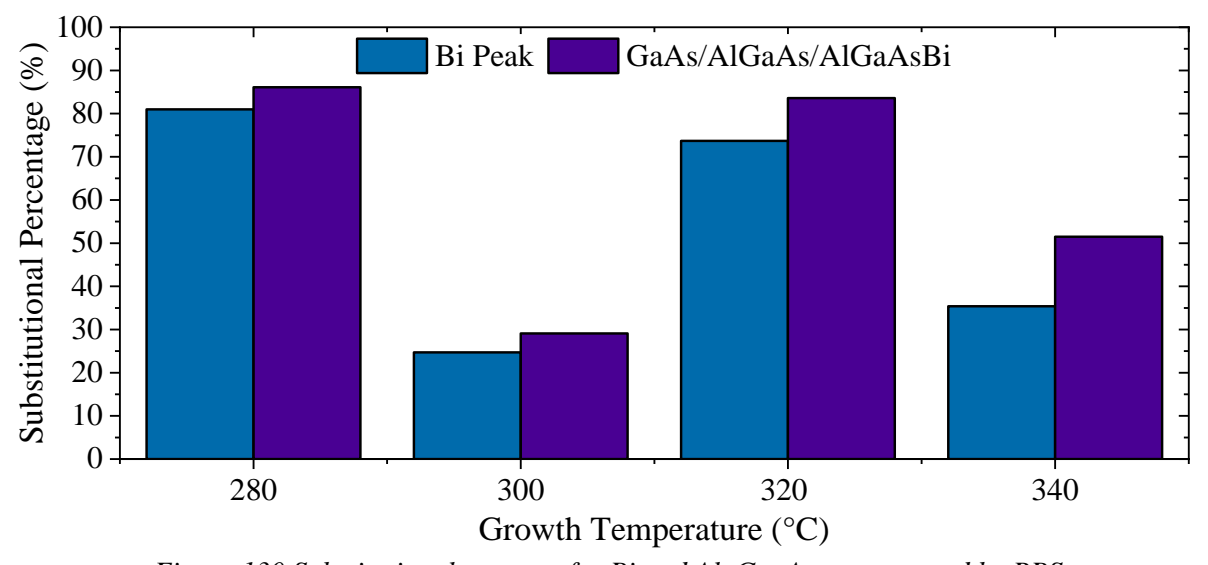


Figure 130 Substitutional contents for Bi and Al, Ga, As as measured by RBS.

# **5.7.3** Bi Flux

The ion beam analysis conducted on the Bi flux subseries is outlined within this section with samples analysed by TOF ERD and RBS. The Bi and Al contents of the AlGaAsBi layer were quantified and the contents as average out over the beam area are shown in Figure 131A and B. The measured Al contents vary more as measured by TOF ERD than the XRD fitting indicated. The values while slightly less stable still remain within  $5.4 \pm 0.8$  at%. This is still within standard run to run variance for compositional difference in MBE growth on this reactor and there is no relation to the observed difference in composition and series growth order. Bi contents as measured by the 4 techniques employed within this study are all closely grouped for samples grown between 0.8- 2.2 nA of Bi flux. The variance is at most  $\pm 0.25$  at%. However, for the sample grown at 2.8 nA the Bi composition returned from the ion beam analysis diverges from the extracted values from PL and XRD. The disparity is approximately 1.4 at%. The results previously presented for PL and XRD of this sample have no obvious flaws that could account for this. In addition, the results are replicable when rechecked, in light of this disparity. Hence, I'm more sceptical of the Bi contents as given by the ion beam study. The increase density of surface Bi droplets and lattice distortion this induced as shown in the Nomarski microscopy of Figure 100D and SEM in Figure 107 could account for this disparity. It would be

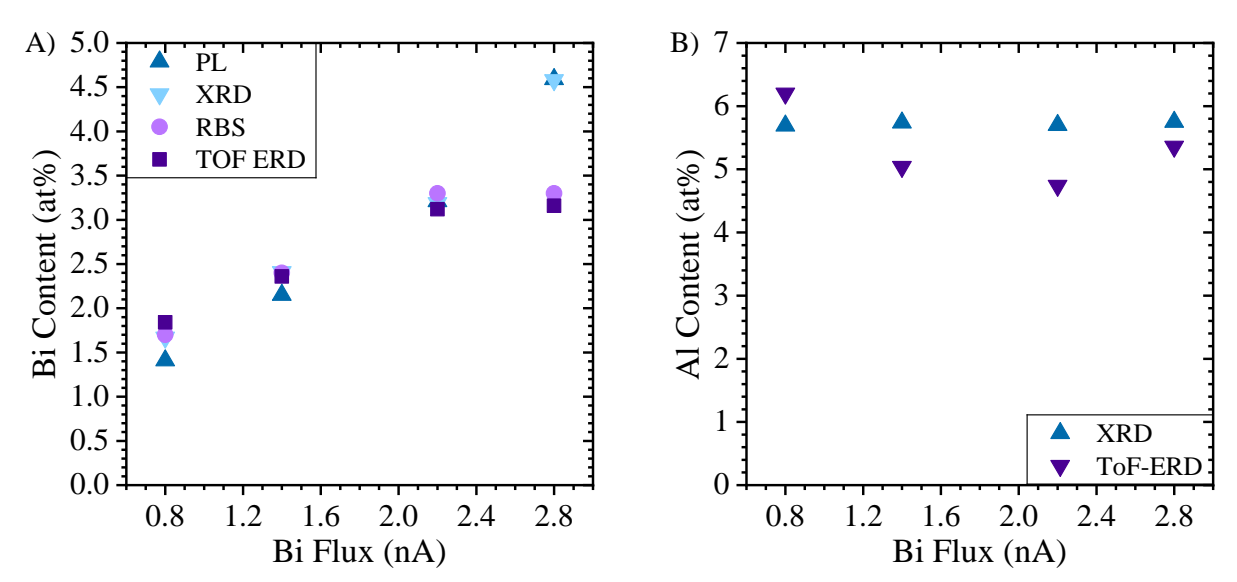


Figure 131 Comparison of A) Bi contents as measured from PL XRD RBS and TOF ERD and B) Al contents as measured from XRD and TOF ERD.

expected that the high level of surface Bi would show on the TOF ERD histograms shown in Figure 132. However, there is no indication of this with the same Bi disruption throughout the structure as seen in all other AlGaAsBi samples analysed. Therefore, it can be assumed the Bi droplet has desorbed during capping layer growth. The observe features in the SEM and Nomarski images are the induced damage from the droplet's migrations and presence on the growth surface. For these reasons I'm treating the ion beam analysis of sample grown at 2.8 nA with some scepticism and relying more readily on the values extracted from the PL and XRD for the Bi content. It is clear from the Bi contents extracted that the growth within the Bi flux subseries is a flux limited regime with Bi content increasing linearly with Bi flux. The upper limit where this regime can be utilised for controlling Bi content sits between the 2.2 and 2.8 nA samples for the growth conditions used in this study. With an approximate range of Bi contents between 1.4 -4.6 at% Bi for fluxes between 0.8 -2.8 nA respectively. The increased concentration of surface Bi droplets seen at higher fluxes could likely be alleviated by increasing the Bi incorporation efficiency. This would likely mean that at lower growth temperature the Bi fluxcontrolled regime would have an increased range of available Bi contents. It is not possible to give both an upper and lower limit on the achievable Bi content within this regime operates for all growth temperatures with the available data. This would require expanding the tested flux window at different growth temperatures in a future series.

The raw RBS spectrum and TOF ERD histograms for the series are shown in Figure 132. The presence of surface contamination from O, C and H due to adhesion of water and CO<sub>2</sub> is again observed. The GaAs cap across all sample has however limited this effect to the upper GaAs region. This is most clearly seen in the potku profile shown in Figure 133. The Bi peak as seen in the RBS at 2.22 MeV can be seen to increase with increased Bi flux corresponding to higher Bi contents. In addition, the contribution from the Al in the buffer and upper AlGaAs cladding can also be seen to be constant across

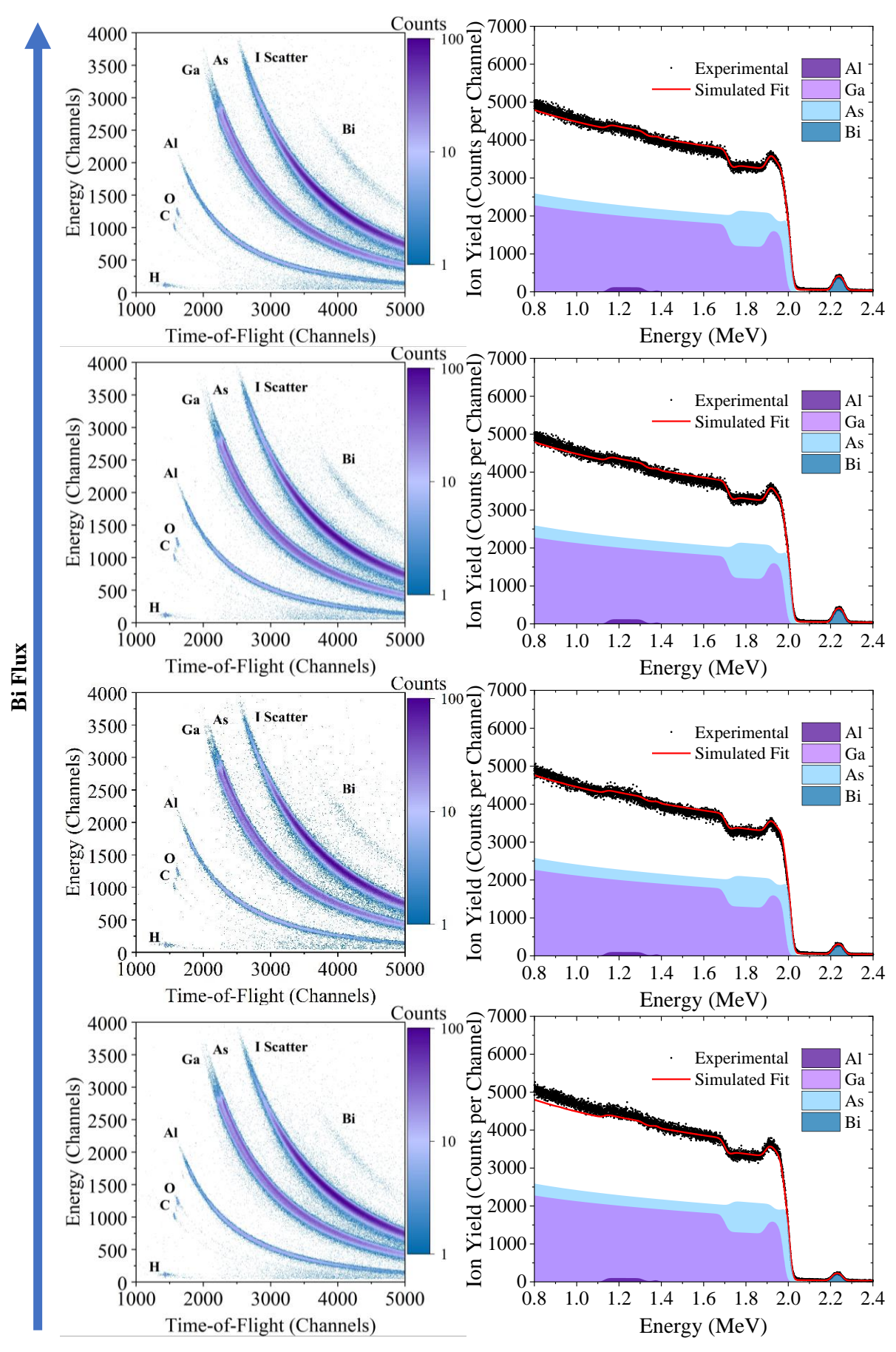


Figure 132 TOF ERD and RBS of growth temperature sub series, shown in ascending order.

the series between 0.9-1.4 MeV. The contributions to the TOF ERD histograms for the Al, Ga and As remains unchanged across the series. The ratios of group III:V elements as detected within the structure is 1:1 except in the centre point sample at 1.4 nA. This is still attributed to a measurement anomaly as previously discussed in section 5.7.1. The higher Bi content can be seen with increased count density in the in energy channels between 1500-2500 and ToF channels between 3700-5000. However, there is no indication of an increased content at the surface confirming the Bi droplet desorption during capping. The Bi sensitivity remains reduced due to the mass of Bi being higher than the incident I ions used for the analysis. The analysis aligns well for samples grown at 0.8,1.4 and 2.2 nA however for determining Bi contents in sample with higher concentrations of Bi droplets and induced crystal damage ion beam analysis may not be best suited.

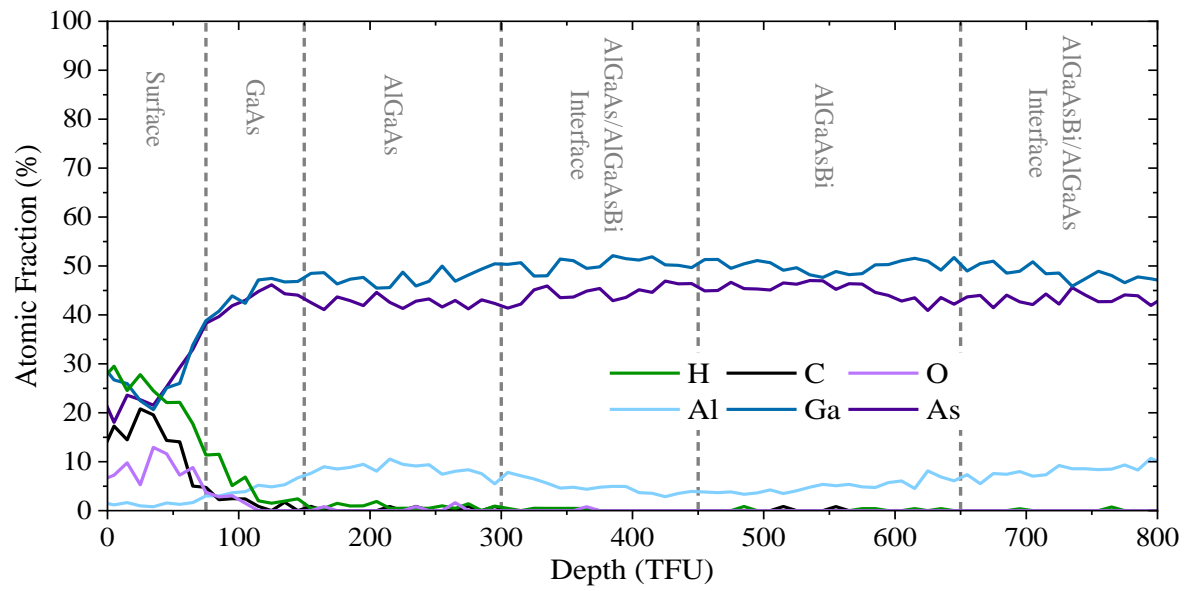


Figure 133 STM 89 Potku Profile of the sample grown under 2.2nA of Bi flux.

The Potku profile for the sample grown with 2.2nA of Bi flux is shown in Figure 133. This is representative of this sample series with interface regions again present both above and below the AlGaAsBi layer. The thickness of the regions remains unaffected by the changing Bi flux and corresponding Bi contents. This would further support the argument that these regions are not true interfaces, but the ion beam interpretations of a rough interface as seen in the cross-sectional TEM of the 5 at% Al centre point sample. The lack of impact in varying the Bi flux eliminates it as a possible control parameter to improve this interface. It may be that a Bi prelayer or more complex annealing stage is required post buffer growth to improve this interface. The upper interface remains slightly rough but is considerably improved. I suspect this is just a function of the roughness from the lower interface that remains due to the thin 100nm layer separating the regions. The cause of the roughness still remains unclear from the analysis available. However, it is indicated that it likely occurs during the Bi layer growth based on the comparative roughness between the upper and lower interface observed in a layer only 100 nm thick.

The fraction of atoms sitting substitutionally within the zinc blend structure was again attempted for this subseries by comparing the random and aligned RBS spectra. The results are shown in Figure 134. There is again no correlation between Bi content, sample growth order or Bi flux that could account for the observed trend. Substitutional percentages range between 30-75% for Bi and 40-85 % for Al, Ga and As. This again is attributed to rapid dechannelling in sample at the upper AlGaAs to AlGaAsBi interface. Removing the roughness at the buffer interface could hopefully eliminate this issue and allow for more accurate substitutional analysis. However, it remains that the values seen here do no align with the defects concentrations as indicated by the optical measurements or the cryptologic modelling for XRD analysis.

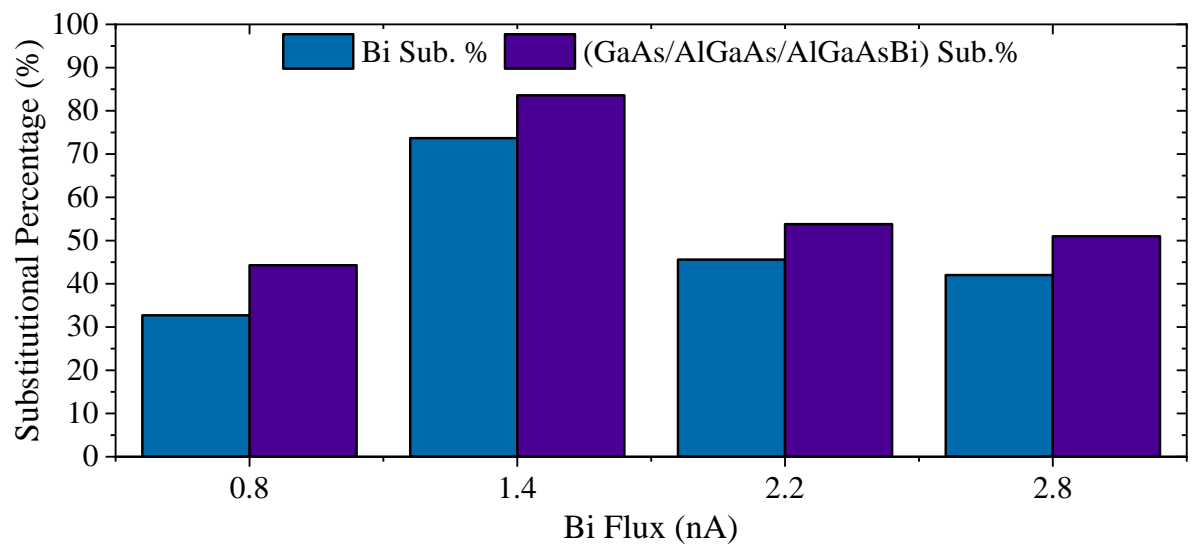


Figure 134 Substitutional contents for Bi and Al, Ga, As as measured by RBS.

## **5.8 Conclusions**

## **5.8.1** Al content Series Conclusions

This series demonstrates optically active AlGaAsBi at contents centred around 2.45 ± 0.35 at% Bi. This has been confirmed with 4 separate measures for Bi content in the 100nm AlGaAsBi layer; PL XRD, TOF ERD and RBS. Aluminium contents for the optically active layer varied from 0-15.74 at% as measured by XRD and TOF ERD. There is evidence of Al diffusion from the AlGaAs layers into the Bi containing layer. However, when Al was concurrently deposited with Bi optical quality at room temperature was reduced by an observed 2 order of magnitude decrease in the PL. However once Al was present the PL reduction was slight with increasing Al contents between 2.5 -15 at%. The situation improved with thermal quenching to 20 K supressing the majority non-radiative defects and narrowing the gap in PL intensity between the Al containing samples and GaAsBi control. This indicates the Al incorporation results in a significant enhancement in the number of defects within the material. These are postulated to be present in both localised regions of higher Bi content, referred to as Bi clusters and as point defects within the lattice structure. These are thought to more preferentially located at the low-

quality interfaces observed in the TEM and indicated in the Ion beam analysis. Despite the remaining issue of increased defect concentrations there is no observed sensitivity to the Al content for the incorporation of Bi into the quaternary alloy AlGaAsBi. The detection of 0.44 at % Al in the 0% sample would indicate extremely high optical quality in the quaternary is possible under the right growth conditions. Controlling the concentration of the defects within the alloy is the main obstacle for the AlGaAsBi system when grown by MBE.

#### **5.8.2** Growth Temperature Series Conclusions

This series has demonstrated that Bi incorporation efficiency remains sensitive to the growth temperature of the layer. Bi contents between 0.9-6.2 at% Bi ,were measured by RBS, for growth temperatures between 280-340 °C at 20 °C increments. The incorporation of Bi remains insensitive to the Al content aligning with previous observations of the GaAsBi system. There continue to be a high number of crystalline defects within the lattice functioning as centres for non-radiative recombination of carries. Hence the optical quality of the alloy is highly sensitive to the concurrent incorporation of Bi and Al. These defects are proposed to be located as both isolated point defects within the lattice as well as in areas of high Bi content creating high density clusters of defects. Higher Bi contents marginally increased the quantity of defects however the relation is sublinear the quantify as indicated by PL remaining within the same order of magnitude across the series. Therefore, the issue is still thought to be cause by the copresence of Al and Bi resulting in the increase of defects in excess of the concentration observed in GaAsBi. The insensitive to both Al content and Bi content suggests the primary defects of concern are part of wider compensation network and not something previously reported within the literature. However further modelling is required to ascertain possible structures to allow for the growth to be altered to target their removal from this alloy. It is proposed that this could be partially alleviated by further lowering the growth temperature to increase the incorporation efficiency of Bi and kinetically limit the formation the defect regions. It may also be that reducing the Bi flux supply at reduced growth temperature would also be beneficial.

The compositional information has been verified by ion beam analysis with indications that there is still issue with rough interfaces between the AlGaAs buffer and Bi containing layer. Although it is not yet clear how this can be resolved. The agreement between all analysis techniques used is very encouraging. The analysis from all techniques indicates an upper temperature limit for Bi incorporation of  $355 \pm 5$  °C, under the experimental conditions tested. The temperature limited regime extends beyond the range tested with further reductions in temperature highly likely to yield higher Bi contents until the transition to Bi flux limited growth regime. The observed behaviour is very similar to that reported for GaAsBi. Based on the evidence present for the sub series it can be concluded that the growth temperature is a highly critical and effective control parameter for engineering the Bi content of the AlGaAsBi alloy.

#### **5.8.3** Bi Flux Sub Series Conclusions

The Bi flux sub series has demonstrated Bi contents can be controlled from 1.4 to 4.6 at% Bi by altering the Bi flux between 0.8 - 2.8 nA under the experimental conditions tested. The upper limit of flux control is between 2.2 - 2.8 nA with severe surface degradation observed due to Bi droplet formation on the surface at 2.8 nA. The high concentration of defects within the material remains the limitation on optical quality of this alloy. Both due to Al-Bi related compensation mechanisms and also previously reported Ga-Bi related defects. All samples within the serries likely retain both isolated point defects within the lattice and defects associated with localised regions of high Bi content. The energy barriers associated with the dominant defects increase by increasing the Bi flux to 2.2 nA. The higher energy barriers should marginally improve the optical quality of the alloy. However, this does not provide a control mechanism for preventing the formation of the Al-Bi related defects at this time. Part of this could be related to the rough interfaces that remain present between the AlGaAs buffer and Bi containing layer which appears to remain a constant across the entire AlGaAsBi series. It is suggested a Bi prelayer or additional annealing step prior to deposition could aid in this regard, though this would require additional sample growths to confirm. It is also strongly suspected that the range of flux controlled Bi growth could be extended further by reducing the growth temperature. This would increase the Bi incorporation efficiency and hence delay the onset of Bi droplet formation on the surface to higher Bi fluxes. The general behaviour of Bi flux variation on the composition and properties of the alloy closely resembles the work on the ternary GaAsBi. It is again noted that aside from the defects limiting optical quality the incorporation of Al into GaAsBi has minimal impact on considerations for growth by MBE.

#### 5.8.4 AlGaAsBi Growth Study Conclusions & Final Thoughts

Summarising the entire AlGaAsBi growth study and material analysis contained within this chapter. In a single sentence, this can be summed up as "yes you can grow AlGaAsBi but the devil is in the defects". Expanding on this there are three main takeaways to move forward with for the work on this quaternary system. If you disregard the optical quality detriment with concurrent incorporation of Bi and Al into GaAs. The Al content sub series confirmed the Bi incorporation is insensitivity to changing Al contents between 0-15 at%. Which translates to the considerations needed are no more complex than for GaAsBi. The sensitivity to key control parameters for Bi content; growth temperature and Bi flux remain indistinguishable between the quaternary AlGaAsBi and ternary GaAsBi systems. Growing sample at 80% Al content and 5-6 % Bi should be easily feasible with the same growth conditions utilised within this study. Higher Bi content may also be achieved that adjusting the substrate temperature and Bi flux as suggested. Facing the reality however of the loss in optical quality, when co incorporating Al and Bi into GaAs. There is clearly a defect compensation mechanism at play that allows the Bi to incorporate in a manner similar to GaAsBi despite the presence of Al. However, the

atomic structure of this compensation mechanism also functions as a severe carrier trap state, which causes the detriment to optical quality. The extent of this is far more so than the defects previously observed in the literature for GaAsBi. It is strongly recommended that as part of future work into realising the potential of this alloy that the possible structural defect compensation mechanisms be modelled to ascertain possible structures. This should hopefully allow for growth to be adapted to prevent their formation if possible. In spite of the continued defect presence within all Al containing samples. For the desired application, which is as the avalanche region in an APD, not an optical detector the low optical quality may be of little consequence. Indeed, in many GaAsBi devices poor optical quality is not always a strong indicator for electrical performance of the material. Depending how these trap states are functioning there could even be a benefit if they are a majority hole trap. Still care should be taken to improve the interface quality between the Bi containing layer. The careful application of a Bi prelayer or heat treatment will I suspect greatly improve the situation. I would further argue therefore that its worth pursuing this alloy for APD devices. A further growth series of PIN or NIP devices with varied Al and Bi contents should be grown and tested to extract the  $\alpha$  and  $\beta$  ionisation coefficients as a final confirmation to the viability of this alloy for APD applications.

# 6. Ex-situ Annealing Studies of Epitaxially Grown Al<sub>x</sub>Ga<sub>1-x</sub>As<sub>y</sub>Bi<sub>1-y</sub> on GaAs 001

#### **6.1 Introduction**

In continuation of the work of the previous chapter exploring potential synthesis routes for the quaternary alloy  $Al_{1-x}Ga_xAs_{1-y}Bi_y$ . Within this section rapid thermal annealing has been applied to assess the impact of post-process annealing on the optical and material quality of  $Al_{1-x}Ga_xAs_{1-y}Bi_y$ . Post-process annealing has been previously demonstrated for the  $GaAs_{1-y}Bi_y$  system as a potential route to reduce the concentration of defects [121]–[124]. The low growth temperature required, sub 380 °C for Bi incorporation into the GaAs and the AlGaAs material systems is considerably lower than the optimised temperatures of 560 °C and 590 °C respectively. This has shown to lead to increased number of defects within the GaAsBi material system, including  $V_{Ga}$  and  $As_{Ga}$ . The surfactant effect of Bi under optimised conditions can significantly mitigate this effect and produces high optical quality material as seen in the  $GaAs_{1-y}Bi_y$  control of the previous chapter. However, the  $Al_{1-x}Ga_xAs_{1-y}Bi_y$  alloy previously presented indicates the surfactant effect is insufficient in the case of concurrent incorporation of Al and Bi.

Thermal annealing of GaAs<sub>1-y</sub>Bi<sub>y</sub> samples in the literature has shown a range of responses and effects on the optical and crystal quality. Studies have shown moderate improvements in PL luminescence with up to an order of magnitude increase [125]. This would indicate the anhelation of some defect complexes and non-radiative centres within the crystal. However, the quality achieved relative to a well grown and optimised GaAsBi layer is not presented. Alteration of the emission wavelength has also been observed although studies are mixed with both redshift and blue shift reported [122], [126]. This would indicate Bi segregation during the annealing process is occurring. However, with redshift also observed Bi is migrating onto the As site from sources within the material likely either clusters, defect complexes or a residual wetting layer. The observed differences can be partially attributed to the range of temperatures used within annealing studies. The annealing temperatures reported between 400 to 800 °C. The annealing durations used typically range between 30-60 s, considerably shorter than the typically capping time for a sample. The other consideration is the strong dependence on the starting Bi composition and growth conditions. Generally, the colder the sample growth temperature and higher the Bi content the greater the improvement observed in annealing and the more likely a blue shift is also observed. Between these two variables the variance of observed outcomes within the literature is understandable. The effect of annealing time and temperature has not been explored within the same study for GaAs<sub>1-y</sub>Bi<sub>y</sub> with studies selecting to focus on a single changing parameter. This make assessing the required time for a given annealing temperature and Bi content more challenging. However, annealing is still a promising route to pursue to reduce the defect concentrations. The effectiveness will be strongly dependent on the types of defect complexes present. However, for As<sub>Ga</sub> significant improvement has been shown with indications that Bi defect complexes can also be improved. This is all dependent on the condition that this can be achieved by further continuation down a thermodynamically favourable mechanism. An unknown factor in the  $Al_{1-x}Ga_xAs_{1-y}Bi_y$  material system due to the unknown structure of defect complexes formed.

The impact of the overgrowth of the AlGaAsBi layer must also be considered for annealing studies. Samples which are capped post Bi layer growth undergo an in situ heat treatment at the capping temperature prior to the annealing study with duration dependent on capping thickness and growth rate. This will already provide significant time for some thermodynamic processes to complete within the material. In the previous work the capping was conducted at 590 °C and 560 °C for the AlGaAs and GaAs layers respectively. This overlaps considerably with the annealing temperatures reported in the literature. Given the thermodynamic dependence of annealing the decision was taken to grow the capping layer for this chapter at the same temperature as the Al<sub>1-x</sub>Ga<sub>x</sub>As<sub>1-y</sub>Bi<sub>y</sub> layer, at 320 °C. This will provide insight into how the capping temperature effected the underlying composition and structure of Al<sub>1-x</sub>Ga<sub>x</sub>As<sub>1-y</sub>Bi<sub>y</sub> layer. In addition to preserving the thermodynamics migration mechanisms for study in the annealing process.

#### 6.2 Growth Methodology

The samples for this series were cleaved from a single  $11.8 \times 11.4$  mm wafer with only the top 2/3rds of the wafer used due to known issues with the temperature uniformity profile of the sample. This eliminated run to run variance for comparison in the annealing study with all annealed samples grown under the same conditions and at the same time. The samples for this series were grown within the timeframe as the previously presented  $Al_{1-x}Ga_xAs_{1-y}Bi_y$  samples. Growth was conducted on an Omicron MBE STM system described in section 3.1.1. Standard calibration techniques outlined in the MBE experimental section were used for determinations of substrate temperatures, cell fluxes and the Ga:As flux unity value at the selected growth rate. The sample architecture used in shown in Figure 135 and is dictated by the analysis techniques utilised within this study. Capping thickness is a balance between sufficient barrier thickness to confine carries and prevent oxidation of the  $Al_xG_{1-x}aAs$  thus allowing for photoluminescence investigation. While maintaining the total sample thickness below 150-200nm to allow for Ion beam analysis by TOF ERD and RBS across the entire structure. Due to this the thickness of the  $Al_{1-x}Ga_xAs_{1-y}Bi_y$  region is well below the critical thickness for relaxation commonly observed in thickness  $Ga_xAs_{1-y}Bi_y$  samples at the targeted Bi contents.

Cleaved 11.8 x 11.4 mm undoped GaAs substrates were out gassed at 380 °C for 20 minutes followed by the removal of the native oxide at 620 °C under an As<sub>2</sub> flux for 40 minutes. The Al<sub>0.3</sub>Ga<sub>0.7</sub>As buffer was then grown at 590 °C at a rate of 0.3 MLs<sup>-1</sup> to a thickness of 300 nm. The Ga:As<sub>2</sub> flux ratio was 1:1.7. An allowance of 5 minutes was given to allow for changes in cell and substrate temperatures following completion of the buffer growth. This included stabilisation of the surface reconstruction,

20 nm GaAs	320 °C
20 nm Al <sub>0.3</sub> Ga <sub>0.7</sub> As	320 °C
100 nm Al <sub>0.05</sub> Ga <sub>0.95</sub> As <sub>0.976</sub> Bi <sub>0.024</sub>	320 °C
300 nm Al <sub>0.3</sub> Ga <sub>0.7</sub> As	590°C
UD GaAs Substrate	

Figure 135  $Al_{1-x}Ga_xAs_{1-y}Bi_y$  annealing sample structure.

alteration of the Ga and Al cell temperatures, lowering of the III:As<sub>4</sub> flux ratio to 1:1.1 and changing of the As species from As<sub>2</sub> to As<sub>4</sub>. The substrate temperature was also lowered to 320 °C. The Ga and Al cell temperatures were set to target 5 at% Al content in the Bi layer while maintaining the  $0.3 \, \text{MLs}^{-1}$ growth rate. Substrate temperature was fixed at 320 °C. This stabilised the 4x4 reconstruction as shown in Figure 136A, only a single azimuth can be seen due to the heater stage geometry. 100 nm of Al<sub>1-x</sub>Ga<sub>x</sub>As<sub>1-y</sub>Bi<sub>y</sub> was then deposited with a concurrent opening of Ga, Al and Bi shutters for the growth.

Post deposition of Al<sub>1-x</sub>Ga<sub>x</sub>As<sub>1-y</sub>Bi<sub>y</sub> was followed by a pause of 5 minutes to stabilise the surface. After 5 minutes a 1x1 reconstructions stabilised as seen in Figure 136B. The 5 minutes was also utilised to enact changes to flux and As species. 20 nm of Al<sub>0.3</sub>Ga<sub>0.7</sub>As was then grown at 320 °C at a rate of 0.3 MLs<sup>-1</sup> with a III:As<sub>2</sub> flux ratio of 1:7. This was immediately followed by 20nm of GaAs capping layer to protect the structure from oxidation. The Al cell shutter was closed, and GaAs growth continued at 320 °C. The growth of the GaAs was conducted at a lower rate of 0.21 Mls<sup>-1</sup> with a Ga:As<sub>2</sub> flux ratio of 1:1.83. Once the GaAs capping layer was completed the heater power was set to standby and allowed to cool under an As flux for 2 minutes prior to unloading.

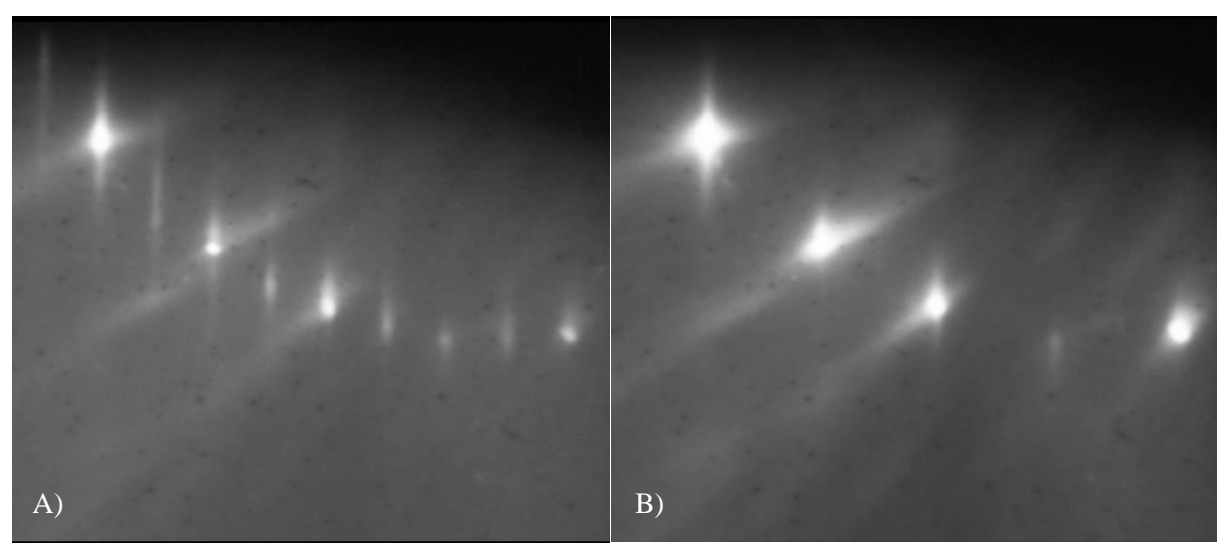


Figure 136 RHEED patterns of the sample surface A) post  $Al_{0.3}Ga_{0.7}As$  buffer growth and B) post  $Al_{1-x}Ga_xAs_{1-y}Bi_y$  layer growth.

The sample was then cleaved into 7 pieces with the bottom third disregarded. This produced 6 samples measuring 3.9 by 3.8 mm. The relative positions of each cleaved section and subsequent annealing temperature is shown in Figure 137. All samples where characterised by XRD and PL prior to annealing to ensure uniformity. Sample were cleaned with a 3 solvent clean , N-butyl acetate, acetone and Isopropyl alcohol prior to annealing. The samples were then subsequently annealed in a rapid thermal annealer at temperatures between 400-650 °C for 30 s. This was conducted under a  $N_2$  atmosphere with a  $N_2$  purge followed by 120s pre ramp to 200 °C. The set annealing temperature was reached in the 45 s with the ramp rate adjusted to keep the timings identical across the series. The heater power was then decreased linearly over 10 s and the sample cooled to RT under the  $N_2$  atmosphere. Post annealing the samples were recharacterised by XRD ,PL PD PL, RBS and ToF ERD analysis to assess the impact of various annealing temperatures. One sample remained unannealed to allow for comparison with the ion beam analysis results.

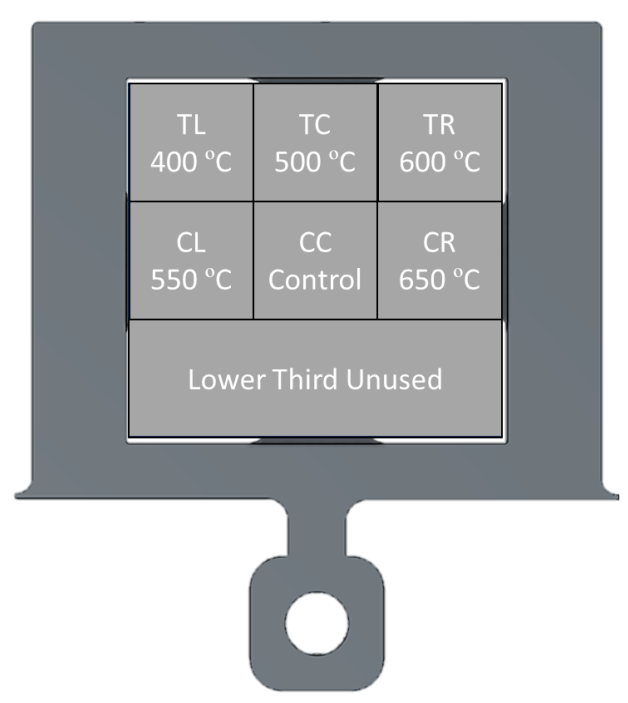


Figure 137 Diagram of STM8F sample in sample holder. Cleaving lines used for sectioning of the wafer for the annealing study with assigned annealing temperatures for each section.

#### 6.1 Unannealed Characterisation XRD and PL

Initial characterisation by 004 omega 2 theta XRD scans for each cleaved section of the sample is shown in Figure 138 with the Bi values extracted from the fitting given in Table 12. The Bi contents ranged by 0.17 at% between 2.61 to 2.79 at% Bi. The highest content was seen in the CR section with the lowest in the diagonally opposite corner at TL. This shows a high wafer uniformity with a slight unavoidable variation due to differences in apparent fluxes across the wafer due to relative proximities to the sources. It is also marginally higher than the 5 at% reference sample grown in the previous chapter of which this was a repeat with the average Bi content increasing from 2.41 to 2.73 This still falls within standard run to run variance especially for samples grown several days apart.

Sample	Bi Content (at%) XRD	Bi Content PL (at%)
Control	2.77	2.76
400 °C 0s	2.61	2.78
500 °C 0s	2.77	2.74
550 ℃ 0s	2.71	2.71
600 °C 0s	2.75	2.67
650 °C 0s	2.79	2.65

Table 12 Bi contents prior to annealing.

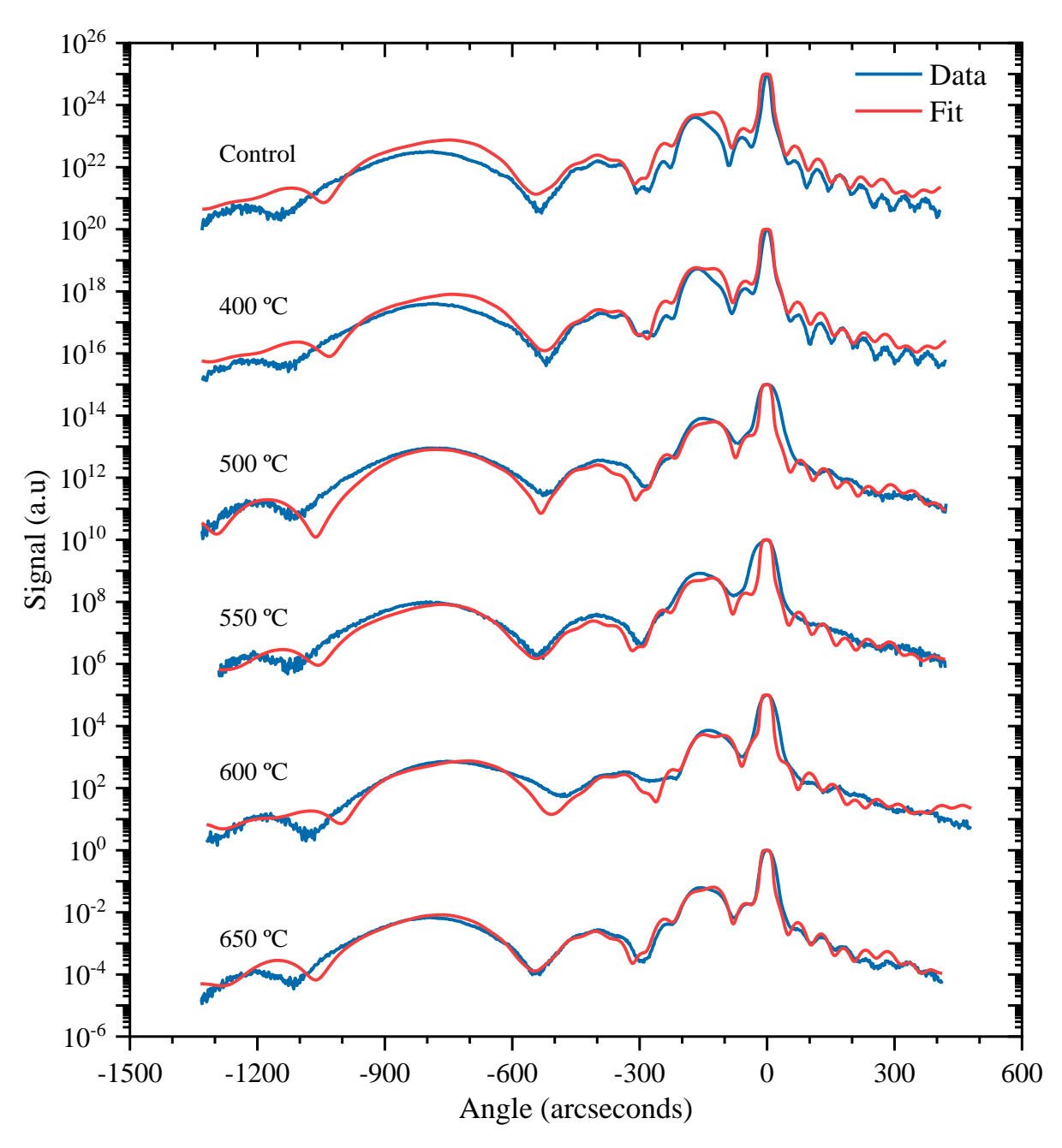


Figure 138 X-ray diffraction for sections of STM8F as grown prior to the conduction of the annealing study. Included are the fits to the XRD data used for extracting Bi contents and layer thicknesses.

There are no other trends apparent in the XRD measurements. The Bi peaks remains consistently broad across the series peaking at  $\sim$  -800 arc seconds with the AlGaAs buffer and upper cladding layers also present at -180 arcseconds.

PL analysis at room temperature showed a similarly tight grouping in both emission wavelength and emission intensity. This can be seen in Figure 139A with the close grouping of the Bi peaks. The Bi variation as extracted from the PL was 0.13 at% across the 6 samples with contents between 2.65 to 2.78 at% Bi. The relative luminesce between the Bi emission and GaAs substrate has decreased with an overall drop in the PL luminescence as compared with the 5 at% AlGaAsBi control from the previous chapter. This highlights the detriment of cold growth on the quality of AlGaAs and GaAs capping layers, with the increased losses attributed to defects within the capping layer. There is also an observed absence of an emission peak between 1-1.1 eV which has been previously associated with Bi clusters and areas of high defect concentrations. However, a significant shoulder at a lower energy to the main

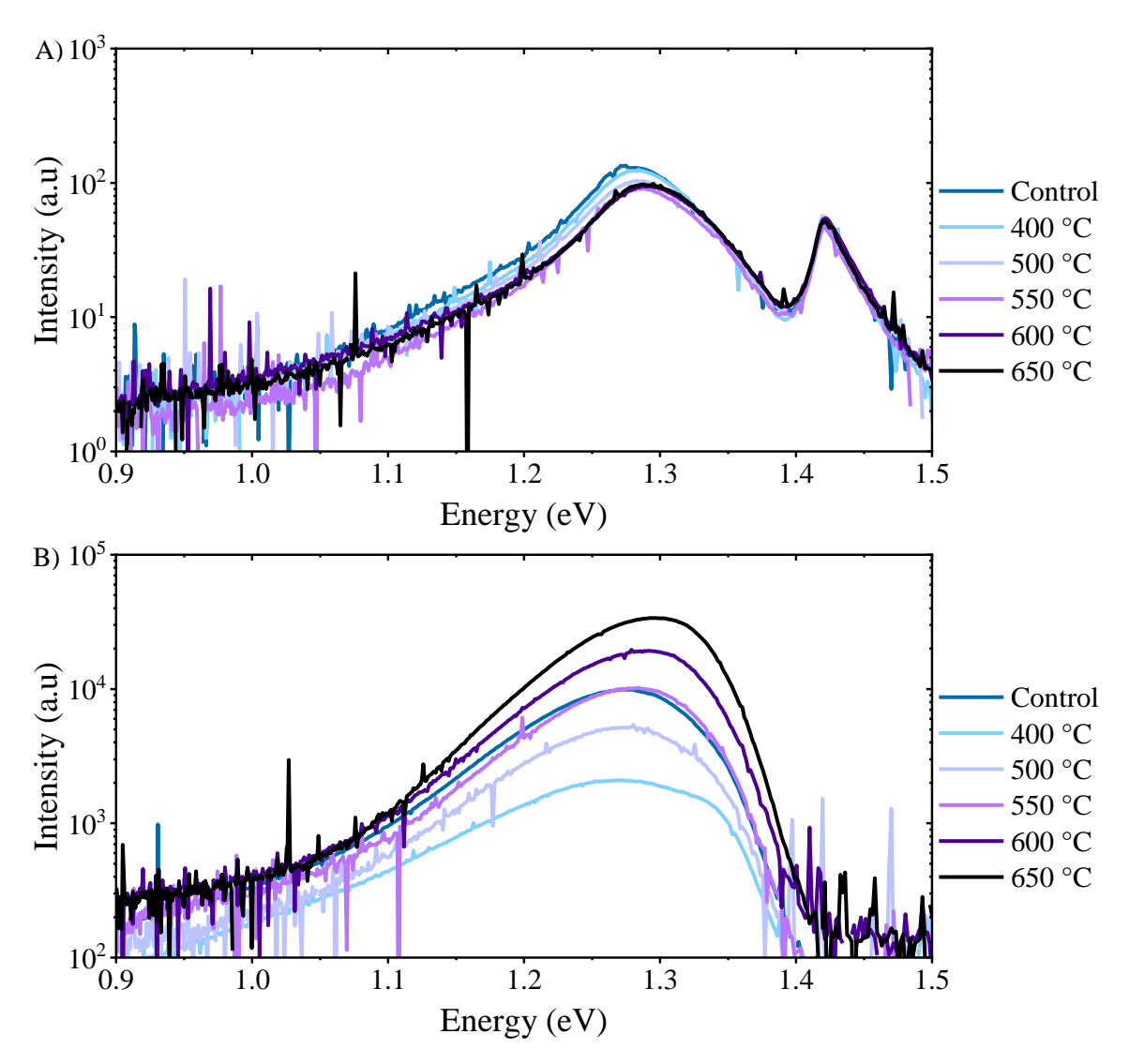


Figure 139 Photoluminescence emission spectra at 300 mW excitation for AlGaAsBi annealing sample sections as grown measured at temperatures of A) 297 K and B) 20 K.

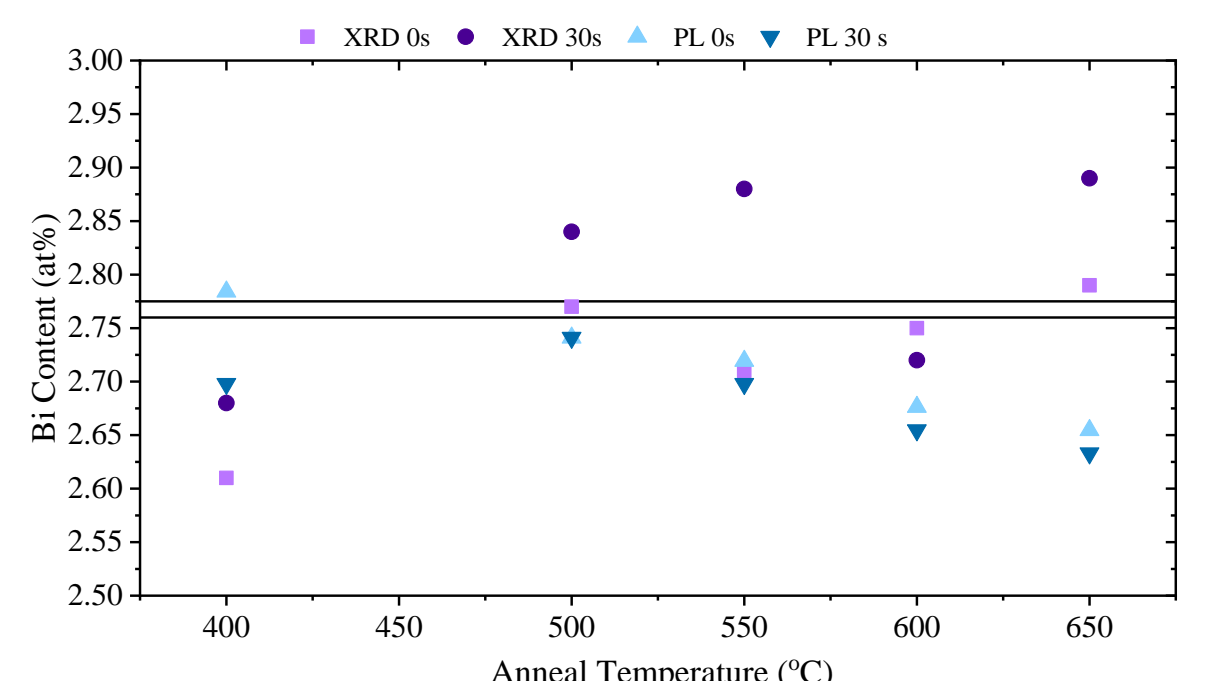
emission remains. This may indicate clusters of lower Bi contents or that the defects which have formed are entirely non radiative as opposed the fractional rates of radiative and non-radiative recombination seen in the previously. Irrespectively of this it indicates the clusters are forming during the AlGaAsBi layer growth. Low temperature measurements at 20 K, shown in Figure 139B, highlight a larger variance in the optical quality across the wafer with an increased PL intensity in the 600 °C and 650 °C sections relative to the control. The increase in theses sections may be the result of flux and temperature uniformity, however it's higher than expected. All of the samples are still lower than the hot capped equivalent so the discrepancy may be due to the cold capping layer and difference in relative positions of the Al, Ga and As fluxes. The transitions to localised states emission are again observed with the low temperature measurements as seen previously in the last chapter. This can be seen by the change in line shape of the AlGaAsBi peak which has an asymmetric shape. This is due to the emission from localised states at lower energies followed by the sharp drop off at the band edge for the AlGaAsBi emission. The mission from the GaAs substrate at 1.42 eV is also supressed in low temperature measurements due to the reduced carrier mobilities which limit recommendation within the upper few 100nms of the sample structures. There exists a slight disparity between the PL and XRD measurements of Bi content however this is within  $\pm$  0.2 at%. This can be partially attributed to the uncertainness in Al content of the Bi layer. This was assumed to be a uniform 5 at% across the samples for the XRD model and PL valence band anti crossing model.

#### 6.2 Annealed Characterisation XRD and PL

Post annealing at the respective temperatures for 30s each cleaved section was reanalysed by a 004 omega 2 theta XRD and PL The raw XRD data with fitting is shown in Figure 140 with PL taken at 297 K and 20 K shown in Figure 142A and B respectively. The fitting achieved to the XRD data is excellent with values of Bi content extracted from the point of peak intensity of the Bi peak in the 297 K PL. The values extracted for the Bi contents from these measurements are shown in Table 13. Figure 141 shows the Bi contents for both analysis technique prior and post the annealing process. The

Sample	Bi Content XRD (at%)	Bi Content PL (at%)
Control	2.79	2.76
400 °C 30s	2.68	2.70
500 °C 30s	2.84	2.74
550 °C 30s	2.88	2.70
600 °C 30s	2.72	2.65
650 °C 30s	2.89	2.63

Table 13 extracted Bi contents post annealing.



Anneal Temperature (°C)
Figure 141 Extracted value of Bi content prior and post annealing extracted by XRD and Pl. Control values indicated by lines.

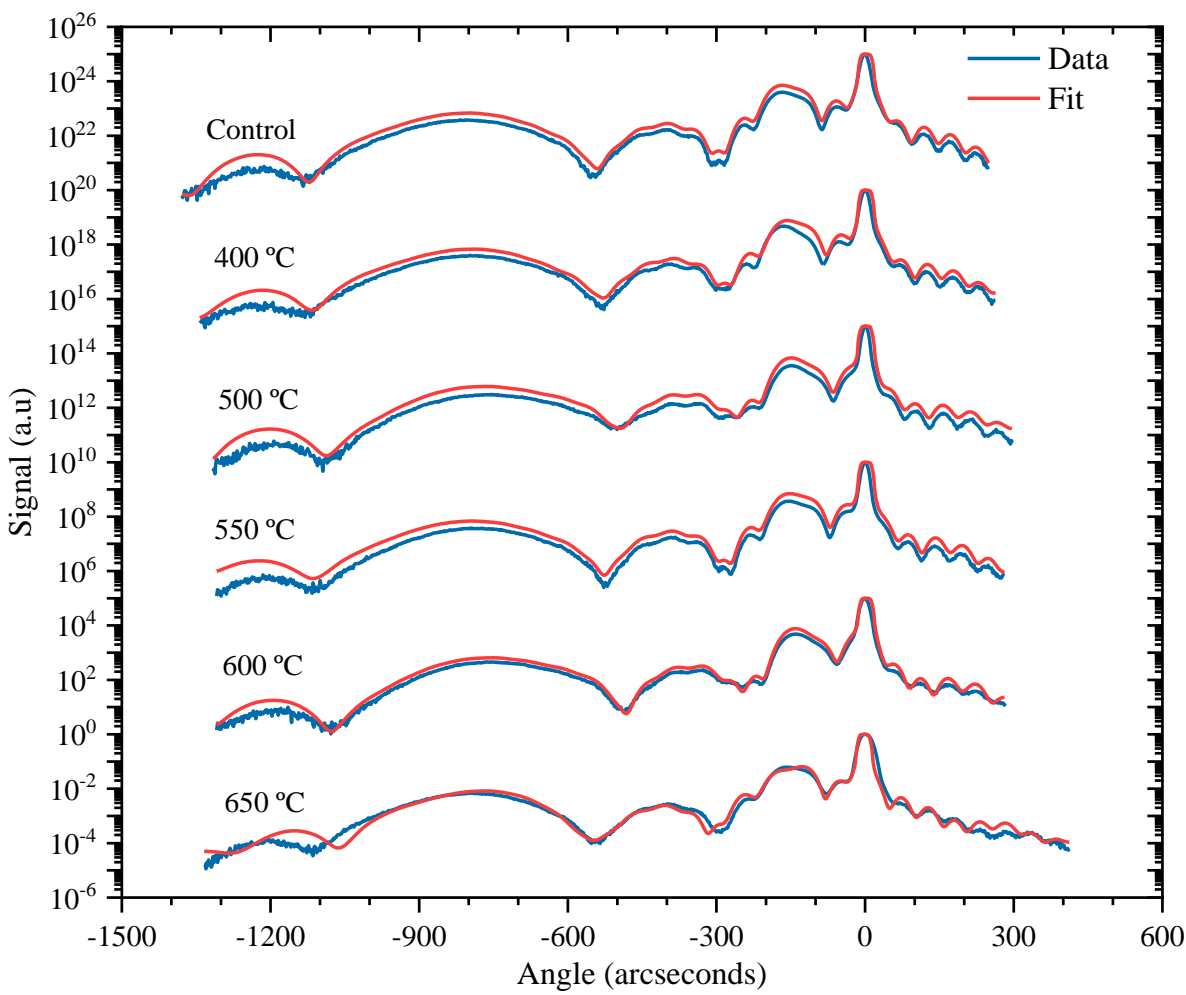


Figure 140 X-ray diffraction for sections of STM 8F post a 30s anneal. Included are the fits to the XRD data used for extracting Bi contents and layer thicknesses.

variance in Bi contents across the series remained steady for PL at 0.13 at% Bi and increased marginally for XRD to 0.21 at% Bi post annealing. The change in the variances falls within run-to-run tolerances for the measurements as quantified by the change in the control sample which varied by 0.03 at% between XRD measurements and 0 at% for PL. The largest change in Bi content observed was for the sample annealed at 550 °C, with an increase in the Bi content of 0.17 at%. The PL for this sample, however, indicates the Bi content remained unchanged from the annealing process. The sample grown at 650 °C also underwent a significant change in composition increasing the apparent Bi content by 0.1 at% post annealing. It is interesting this effect was not observed in the sample between these two annealed at 600 °C. There is evidence of migration of Bi at lower temperatures with the 400 °C showing a slight increase to 2.68 from 2.61 at% Bi by XRD. In all cases except the 600 °C sample annealing marginally increased the Bi content apparent by XRD. RT PL on the hand showed little sensitivity to the annealing process except at 400 °C.

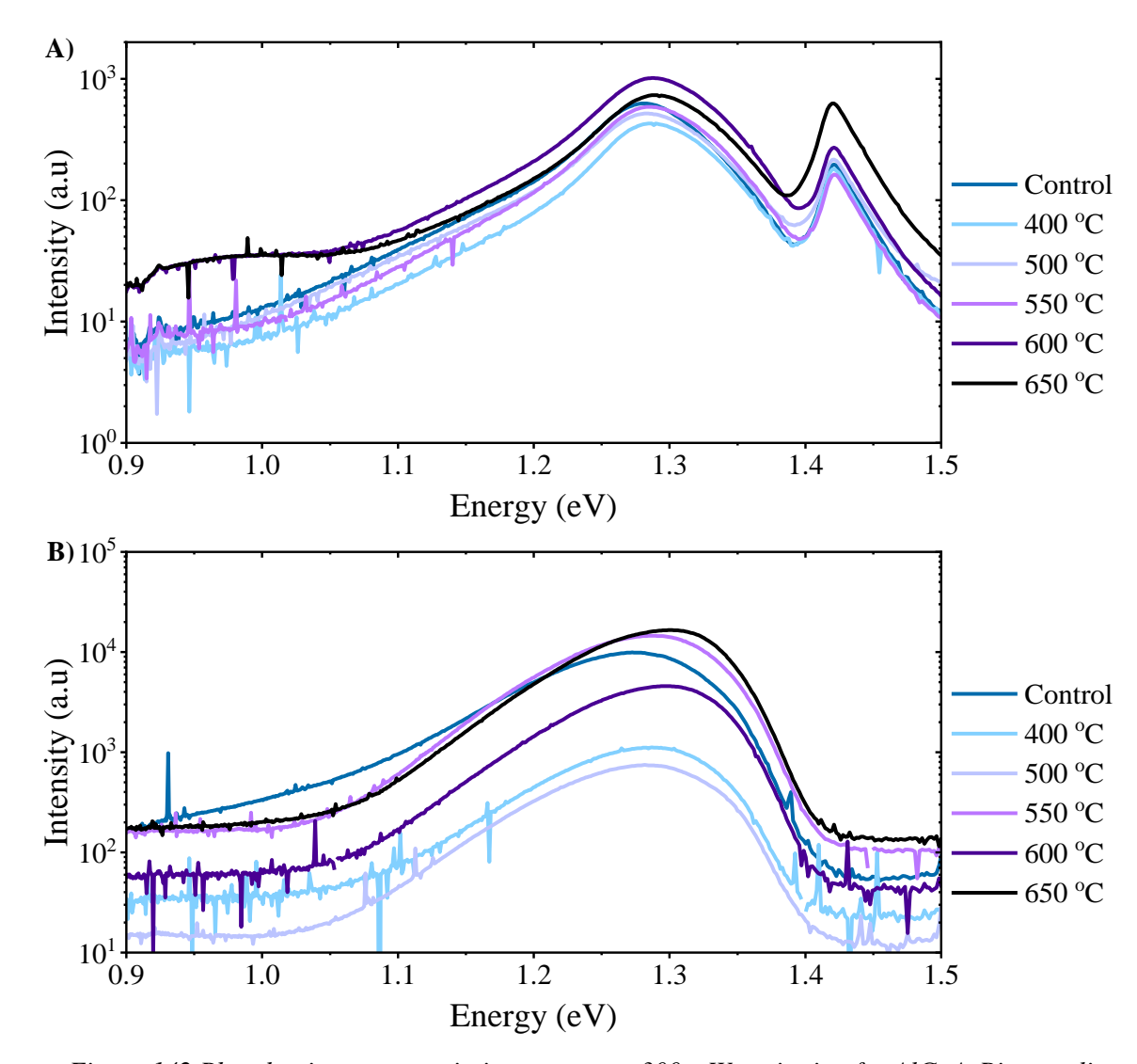


Figure 142 Photoluminescence emission spectra at 300 mW excitation for AlGaAsBi annealing sample sections post a 30 s anneal. Measured at temperatures of A) 297 K and B) 20 K.

Examining the PL measurement at 297 K shown in Figure 142A it can be seen that the samples annealed at  $600\,^{\circ}$ C and  $650\,^{\circ}$ C have developed another emission peak at  $0.9\text{-}1.05\,^{\circ}$ eV. This was not detected prior to annealing indicating it has either formed during annealing or that carriers were previously not able to reach this region. In the  $650\,^{\circ}$ C measurement the relative heights between the substrate peak and Bi peak have also adjusted in favour of the substrate post anneal. This would indicate deteriorating optical quality in the Bi layer relative to the substrate. In the sample annealed at temperatures of  $550\,^{\circ}$ C and below there is no apparent change in line shape relative to the control. The positions of peaks across the series is also very similar post annealing with only the  $400\,^{\circ}$ C annealed sample shifting by more than  $10\,^{\circ}$ meV. The step size of the measurement is 2 meV with realistic determination of the exact peak position  $\pm 4\,^{\circ}$ meV. The measurements at  $20\,^{\circ}$ K are a similar situation with very little shift in the position of the peak. Except for the  $650\,^{\circ}$ C peak which blue shifted by  $25\,^{\circ}$ meV post annealing. This would indicate higher carrier losses post annealing causing recombination to occur closer to the band edge.

Comparing the PL intensities relative to the control prior and post annealing should give some more insight into the overall optical quality of the material. This is shown in Figure 143. It can initially be seen the intensities at 297 K were comparatively similar across the range. Measurements at 20 K before annealing however, showed an increasing intensity in the sections selected for higher temperature annealing. This trend is coincidental with a random sample allocated to each annealing temperature. Post annealing for measurements at 297 K there is a slight increase in intensity of the Bi peak at annealing temperatures of 550 °C and above. This would indicate there has been some reduction in the concentration of non-radiative defects by annealing. However, at s measurement temperature of 20 K the intensity of all samples has decreased, except the 550 °C. The reduction is further exacerbated with

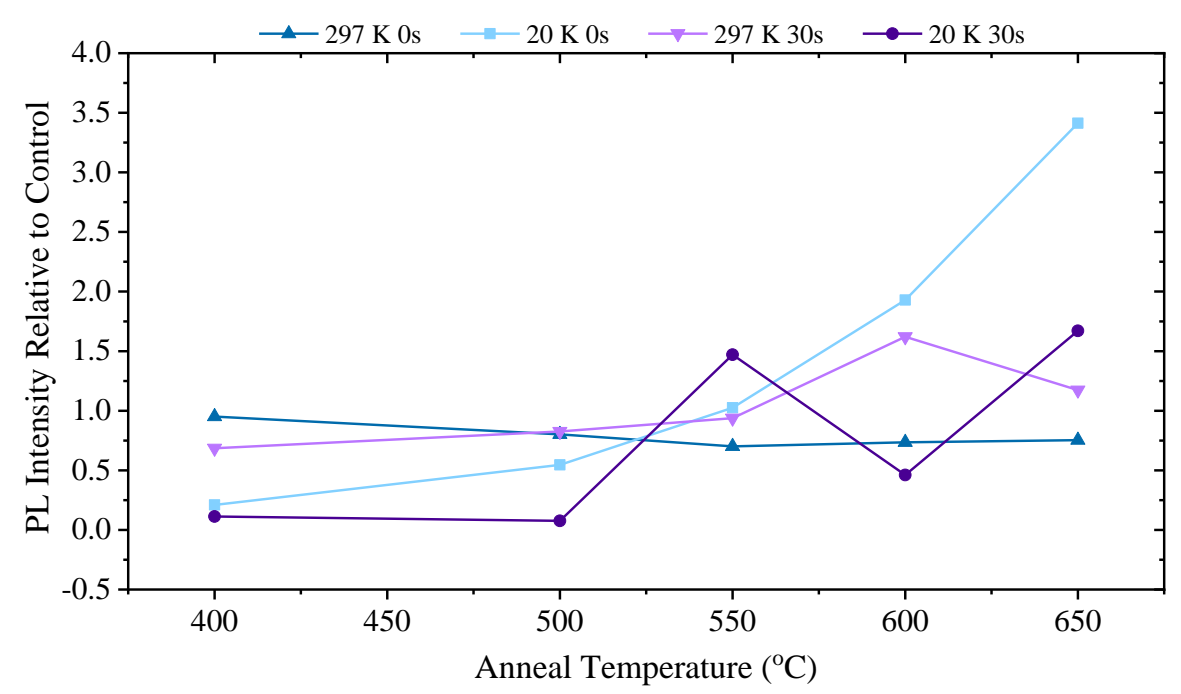


Figure 143 PL Intensities relative to control for measurements at 297K and 20 K prior and post 30 s annealing.

higher annealing temperatures. The gain seen at 20 K in the 550 °C annealed sample and steady state intensity in the 297 K measurement would indicate 550 °C is the sweet spot for annealing. Higher temperature annealing resulted in detriment to optical quality while lower temperatures produced more limited improvements. The detriment seen at higher temperatures may be the result of defects arising from unintentional oxide removal in the absence of an As flux in the rapid thermal annealer (RTA). However, this will not of impacted the underlying Bi containing or AlGaAs cladding layers of the optical structure. It is also hard to quantify how much the starting optical quality hindered or assisted in the annealing process depending on the defect annihilation mechanisms available. This would be a further benefit to simulation the Al<sub>1-x</sub>Ga<sub>x</sub>As<sub>1-y</sub>Bi<sub>y</sub> system to assess the defect compensation mechanisms which form. However, the improvements seen pale in comparison to the respective intensity of the sample grown with the capping layers at 590 °C and 560 °C for AlGaAs and GaAs respectively. This sample comparatively to the control achieved an intensity at 20 K of 10.6, just over 6 times brighter than the optical quality achieved by annealing. This would suggest the defects induced in the capping layers due to the cold growth far outweigh any defect elimination within the Bi layer due to the lack of overgrowth migration of atoms. However, it may still be the case that annealing post growth could yield benefits perhaps in conjunction with a reduced capping temperature to 500 °C. However, to confirm this would require further experimental time and epitaxial growths.

# **6.5 Power Dependent PL**

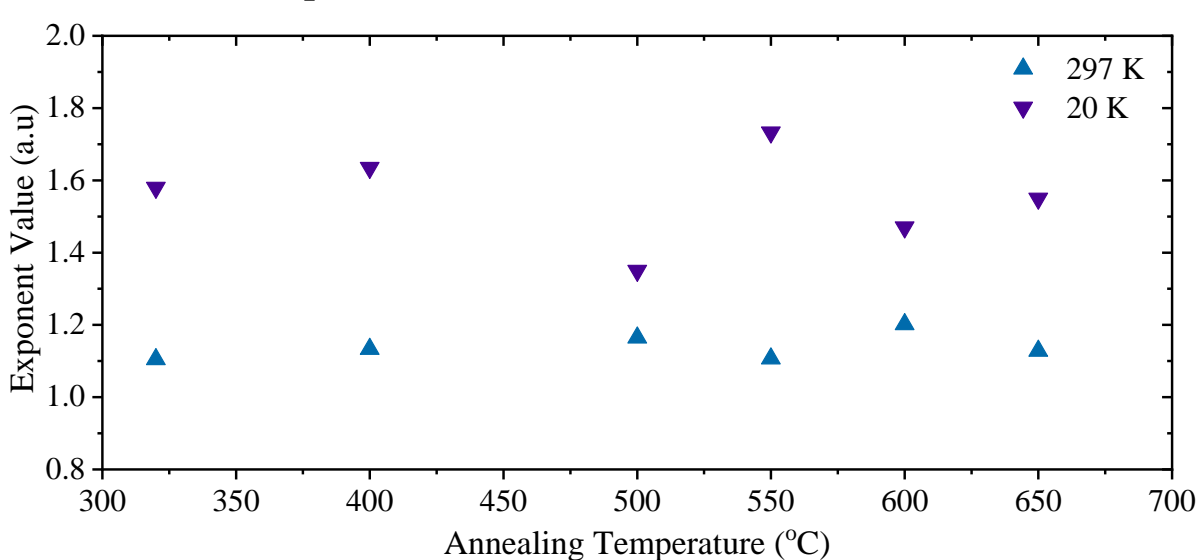


Figure 144 Exponent values extracted from lines of best fit for normalised integrated Photoluminescence vs excitation power at temperatures of 20 K & 297 K for varying annealing temperatures between 400 to 650 °C. The control is also present at the in situ anneal temperature of 320 °C.

The power dependent exponents extracted post annealing are shown in Figure 144 where the control is shown as a 320 °C in situ anneal. These values are extracted from the integrated luminance against optical excitation powers at 20 K and 297 K with the data and fits shown in Figure 145. The PL data was fitted with equation (11) to extract the power exponent. Fitting achieved to the data was reasonable,

however there were indications of strong sample heating above optical excitation power of 50 to 100 mW in the measurements at 20 K. The comparatively lower power at which this is being observed compared with previous PD PL at 20 K can be attributed to the comparatively diminished dimensions

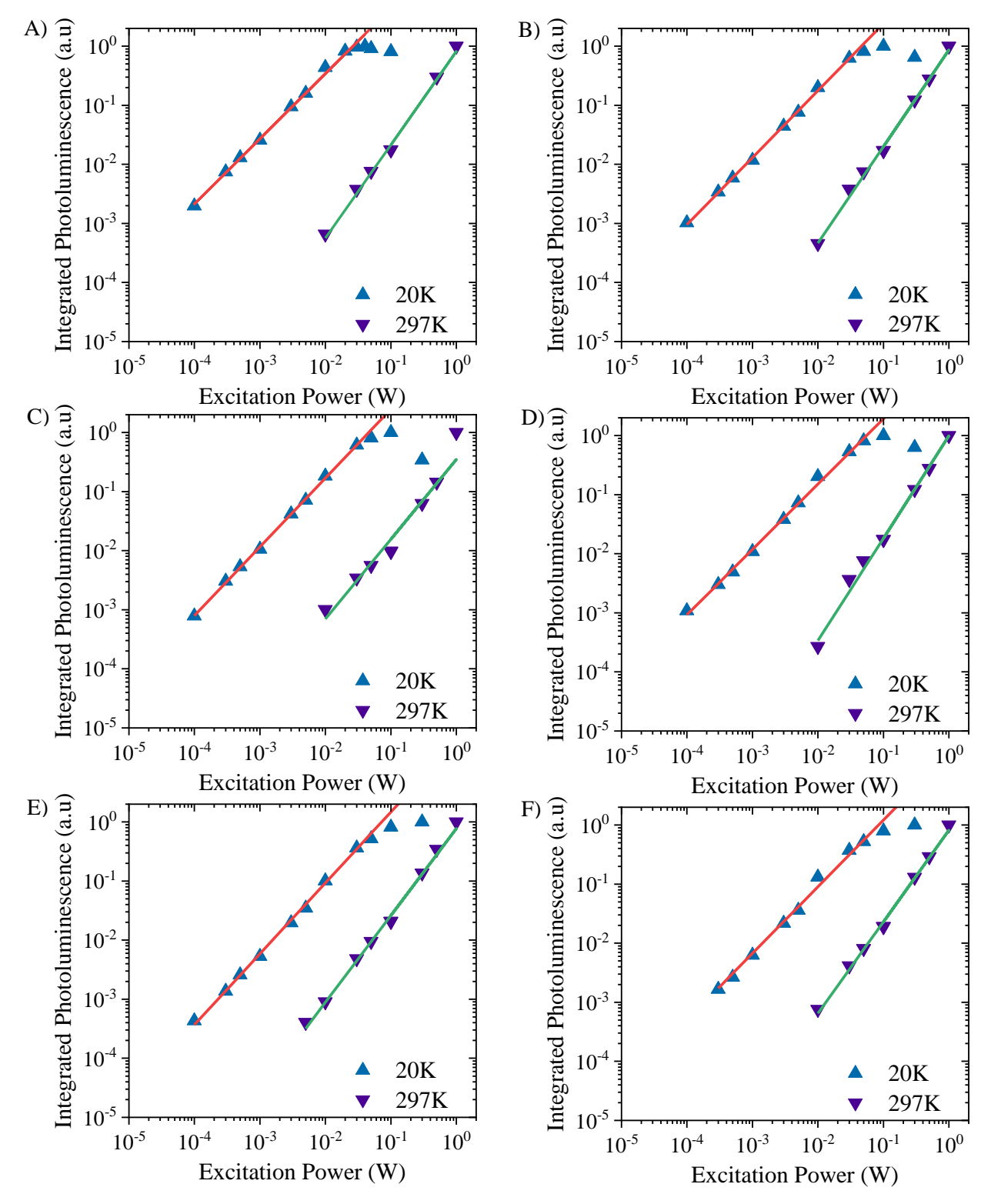


Figure 145 Normalised Integrated Photoluminescence vs excitation power for ex-situ annealing 400 to 650 °C. Where, A) unannealed control, B) 400 °C, C) 500 °C, D) 550 °C E) 600 °C and F) 650 °C.

of cleaved sections. Data where excitation increased the sample temperature was disregarded for the fitting as it deviated from the linear trend due to a disproportionate quantity of traps states becoming active with the increased temperature. The coefficients extracted from measurements at 297 K range between 1.1 to 1.2 with no discernible relation to annealing temperature. Therefore, all samples at room temperature remain defect limited in the radiative recombination with no indication annealing can alter this situation. This is not unexpected with Bi containing materials at room temperature. The low temperature measurements showed a greater variance in the exponents with values between 1.32 to 1.76. In all cases there is still a significant defect limitation in the recombination behaviour across the series, although it remains similar to the 1.6 measured for the previous series control sample grown with a high temperature capping layer. With the exception of the 550 °C sample there is a downward trend in the value of the exponents with increased annealing temperature. Although this is subtle and may fall on the boundary of run-to-run variance. The impact of annealing on the quantum efficiency appears negligible if any impact is indeed present. This may indicate that annealing times were insufficient or the temperature range to limited. However, in light of the results from the previous section it would be more accurate to argue that annealing is not effective in removing the defect compensation mechanisms present in these sample. This would indicate that these compensation mechanisms are thermodynamically stable up to 650 °C and a better approach would be kinetic methods to eliminate the defects.

### **6.6 Ion Beam Analysis**

The ToF ERD and RBS results for the control sample alongside the previous series 5 at% Al control sample grown under identical conditions except for the high temperature capping layers, is shown in Figure 146. In both cases it can be seen that some minor contaminants of O ,C and H are present at the surface in the ToF ERD. This is attributed to water and CO<sub>2</sub> adhesion to the surface. This occurred when samples are removed from the UHV environment and exposed to atmosphere. The concentrations of these contaminants drop sharply with depth indicating the GaAs capping in both cases protected the underlying AlGaAs barrier. Bi contents are comparable between the samples, with RBS reporting 3 at% Bi for the control and 2.56 at% for the hot cap comparison. This fall within standard run to run variance for Bi composition in epitaxial growth.

However, comparing the RBS spectra between the samples and there is a significant deficiency of Ga apparent in the annealing control. This can be seen by the drop in the Ga single between 1.7 to 1.95 MeV and the increase in Al signal between 1.15 to 1.4 MeV. The is most apparent in the AlGaAs buffer layer due to its increased thickness however the disparity would indicate the group III flux ratios have drifted rapidly post calibration. This is likely due to the Ga cell instability as the material source neared complete depletion between flux checks. The last check was conducted 6 days prior to growth with cell depletion occurring 2 days post the growth of the annealing sample. The has resulted in thinner layers

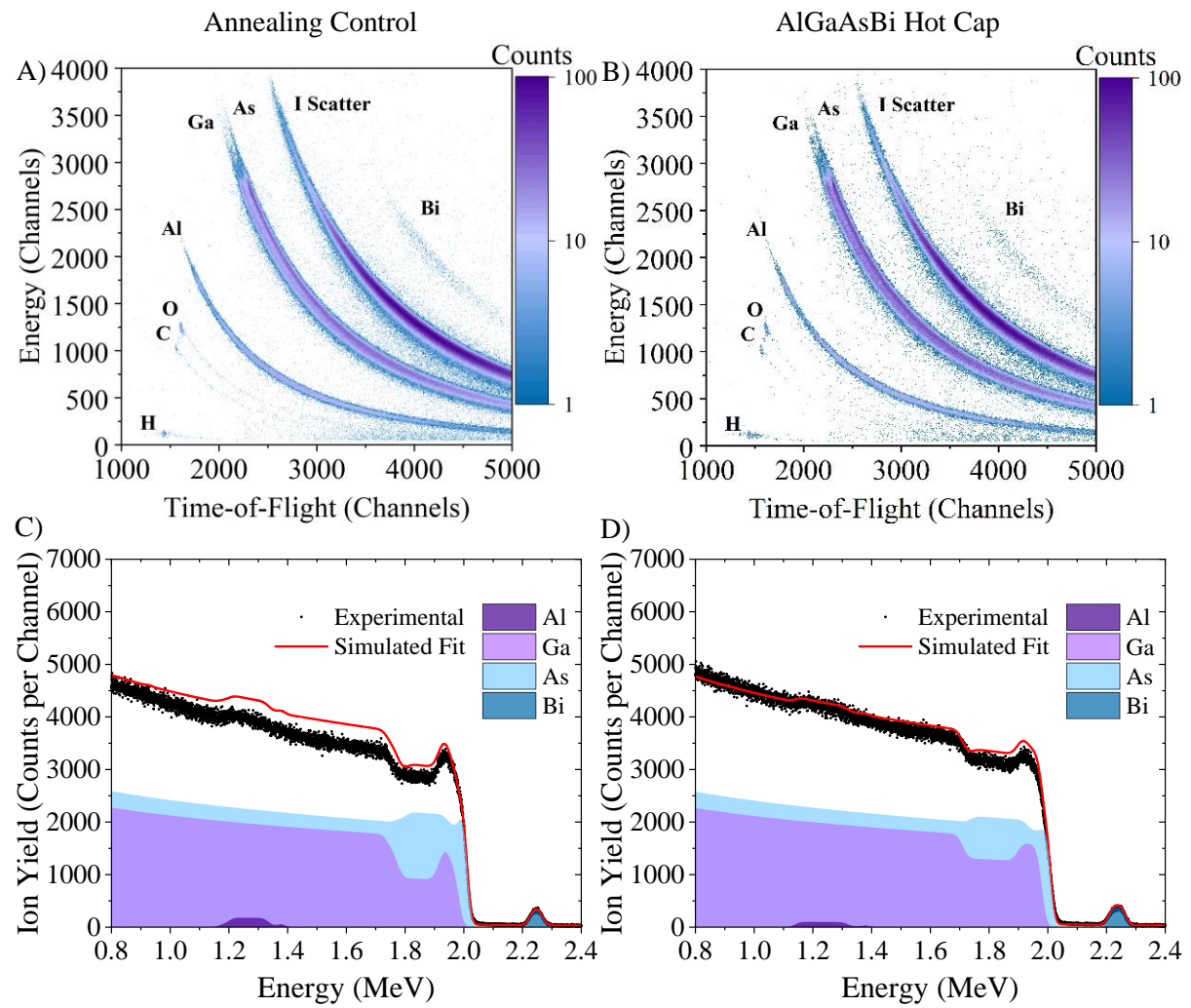


Figure 146 ToF ERD and RBS results for the control sample STM 8FCC and equivalent sample grown with high temperature capping layers, STM 83 Al<sub>0.05</sub>Ga<sub>0.95</sub>As<sub>0.976</sub>Bi<sub>0.24</sub>.

and higher Al content layers than intended for this growth. The reduction equates to an approximately 30 % drop in the output flux of the Ga cell from the targeted values. This was extracted by the comparative reduction in film thickness between the control and the hot cap comparison across all Al containing epilayers. The thicknesses and contents were extracted from MCERD simulations to fit the ToF ERD data shown in Figure 147. MCERD was selected over potku due to its increased accuracy to account for multiple scattering events and straggling ions owing to the poorer crystalline quality of the cold capped sample. The variance in growth rate for these layers equates to a flux reduction of 30.8 to 21 % assuming the Al flux remained constant. There is no indication of any instability in the Al source in flux checks post series completion.

The change in Ga flux altered the group III to As flux ratio and group III to Bi flux ratio. Addressing the III:As flux ratio in the barriers and buffer layer, this will have had a very limited impact on the study. Higher Al contents layers still confine the carriers to the Bi layer of interest, allowing for optical studies. Slight increases in the GaAs/AlGaAs interfacial strain will also be inconsequential in the analysis as the limiting strain remains the Bi containing layer. The layer will however be of reduced

thickness due to the lower growth rate. The buffer layer should still be sufficiently thick to of allowed for recovery of the surface post oxide remove. Disregarding the cause of the previously observed roughness seen at the buffer AlGaAsBi interface. However, the upper cladding region decreased in thickness from 20nm to 16 nm which while borderline from a sample architecture design, luckily this remained sufficiently thick to avoid carrier escape into the GaAs cap. The measured Al contents of the Bi containing layer were higher however at 9.76 at% Al. This is significantly higher than would be expected based on the 30 % Ga flux reduction as indicated by the layer thickness. The value should be approximately 7 at% Al if it aligned to the reduction as indicated by layer thickness.

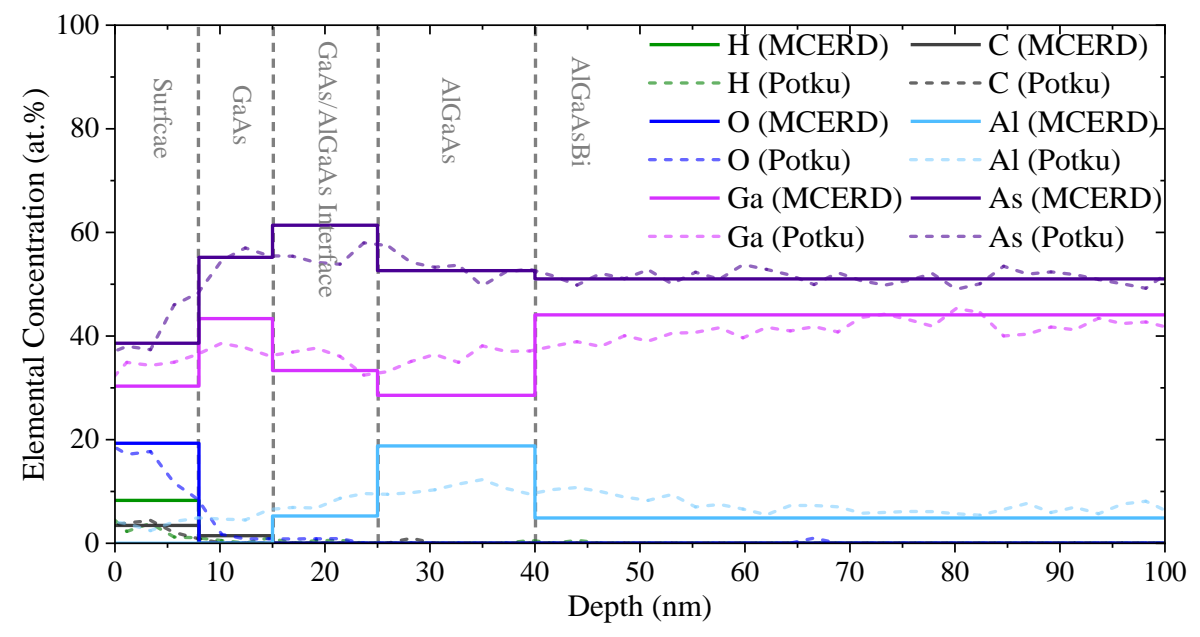


Figure 147 Potku and MCERD simulated composition of the control sample as fitted to the ToF ERD data shown in Figure 146.

Where the impact of this change is significant for this study is within the growth of the Bi containing layer. The reduced growth rate will have adjusted the point of III:As flux unity. Shifting in favour of an oversupply of As. Based on the ToF ERD measurements of layer thicknesses. This will of shifted the flux III:As flux ratio from 1:1.05 to 1:1.31. This would be expected to reduce Bi incorporation efficiency significantly. However, the decreased Ga flux and will also increase the III:Bi flux ratio, effectively increasing the apparent Bi supply. Based on the Bi flux series there is scope for increase Bi flux and higher Bi contents without droplet formation. Equivalating the Bi supply relative to the growth rate 1.4 nA of Bi flux at the reduced growth rate of 0.21 MLs<sup>-1</sup> would approximate 2 nA at targeted growth rate of 0.3MLs<sup>-1</sup>. In terms of the available Bi per monolayer of AlGaAsBi deposited. For 2.2 nA the Bi content was 3.21 at% slightly above the range of Bi contents reported for the control with 2.76 to 3 at% Bi. This may indicate that the sensitivity of Al<sub>1-x</sub>Ga<sub>x</sub>As<sub>1-y</sub>Bi<sub>y</sub> to the III:As flux ratio is less so than for the equivalent GaAsBi sample. This is also likely aided by the reduced growth temperature of 320 °C use for this study. The thinner Al<sub>1-x</sub>Ga<sub>x</sub>As<sub>1-y</sub>Bi<sub>y</sub> layer should also have negligible impact on the optical properties and crystallographic analysis.

While surprising that this deviation from the intended growth went unnoticed in the XRD and PL analysis, this can be accounted for. XRD does not have the sensitivity to distinguish slight changes in Al contents when Bi is also present within the layer as previously discussed. The shift in peak position due to Al is overshadowed by strain induced by Bi. This does however mean the uncertainty in Bi composition is not compromised by the increased Al content. Indeed, when the XRD model is adjusted for the increased Al content of the Bilayer. The value of Bi in the layer changes minorly from 2.79 to 2.76 at% Bi. The sensitivity of XRD fitting for extracting thickness was not sufficient to determine the difference in thickness between 100 to 70nm. This may of be limited by the likely still present rough interfaces between the AlGaAs and AlGaAsBi layers. Altering the PL analysis to account for the increased Al content of the layer dramatically shift the extracted Bi content from 2.76 to 3.95 at%. This is significantly different from both the XRD and RBS values of Bi content. If a value of 7 at% Al is used the Bi content extracted fall to 3.24 at% while still higher this would bring it closer to parity with the XRD and RBS. Therefore, the higher contents of Al measured by ToF ERD would indicate a large concentration of Al interstitials within the Bi layer. For comparison between the annealed series and samples grown with a high temperature capping layers up to now the 5 at% Al form the Al content series has been used. There is an argument to be made that the 10 at% Al would be a fairer comparison. From the previous chapter it can be seen that the Bi incorporation is insensitive of the Al content. I would argue either sample is a fair comparison as the value of Al is between 5-10 at% Al. However, the ToF ERD would seem to off overestimated the Al content base on other available measures.

The MCERD simulations of the ToF ERD shown in Figure 147 also reveal an enhanced As concentration in the cold grown capping layers. This was not present in the high temperature caped equivalent and is not the result of an increased As oversupply. This can be shown as the As content only increased in low temperature layer grown post Bi layer completion. Highlighting one of the key aspects that allows for Bi growth at low temperatures is the improvement in material quality due to the Bi surfactant effect. The cold growth temperatures of 320 °C used for the GaAs and AlGaAs layers in the absence of a Bi surfactant has resulted in capping layers riddled with As antistites. The is a known issue for epitaxially grown GaAs and AlGaAs at low growth temperatures [127]–[129]. The interface region in the upper cladding layer appears particularly problematic with a further enhancement of AsGa antistites with 22.6 at % of the total As sitting interstitially. This is significantly higher than the interstitial quantity of As in the AlGaAs layer which sits at the 5 at% and 10 at% in the GaAs cap. There is further enhancement in concentration of As<sub>Ga</sub> at the interface between the capping layer which may be the result of a lack of growth interrupt while the As flux was changed from AlGaAs to GaAs growth. Due to the capping layer growth rate being target at 0.21 MLs<sup>-1</sup>. However, it was likely closer to 0.15 MLs<sup>-1</sup>. The transition though from a growth rate of 0.237 ML to 0.15 ML under the same As flux shouldn't however lead to a 10 times increase in the concentration of As antistites within the layer. The time elapsed to grow the layer and the interface thickness alongside the flux equilibrations time are also unable to account for this rise in  $As_{Ga}$ . With layer growth of 350 s the flux will have equilibrated within the first 60 s. Therefore, the expected thickness of the enhanced antistites concentrations should be under 5 nm. The measured values are over double at 11 nm. The low growth temperature of the capping can be entirely attributed as the cause of the higher levels of defects present.

Glancing angle RBS has the effect of increasing spatial resolution at the expense of probing depth. This can be used to look at the Bi distribution through the sample in finer detail. Glancing angle RBS of the annealing series control sample is shown in Figure 148. This shows the standard bell-shaped distribution expected, plus a small addition to the peak at energies between 2.23 to 2.27 MeV, as indicated by the green box. This trail off is beyond the typical equilibrium found at the interface between Bi layers. There is a small quantity of Bi present in the AlGaAs and GaAs capping layers ~ 0.2 at% Bi. This was not detected in the sample with the AlGaAs and GaAs grown at 590 °C and 560 °C respectively. It is highly unlikely this is from diffused Bi during the overgrowth at 320 °C. The Bi content of these layers originates from residual Bi remaining on the surface during the growth of these layers. Unlike in high temperature capping situation any remaining Bi will not desorb from the surface at 320 °C. However, the significantly higher As flux will of limited the rate of Bi incorporation such that the residual surface Bi is incorporated slowly at low efficiency over the remaining AlGaAs and GaAs layer growths. This will likely of further deteriorated the quality of the capping material as the Bi layer depleted and became insufficient to provide the surfactant effect post Bi shutter closure. However, it does offer a potential explanation as to why the As antistites concentrations are lower in the AlGaAs layer where the Bi coverage on the surface would have been greater. The unintentional Bi incorporation has not comprised the carrier confinement either due to the higher Al content of the AlGaAs cladding.

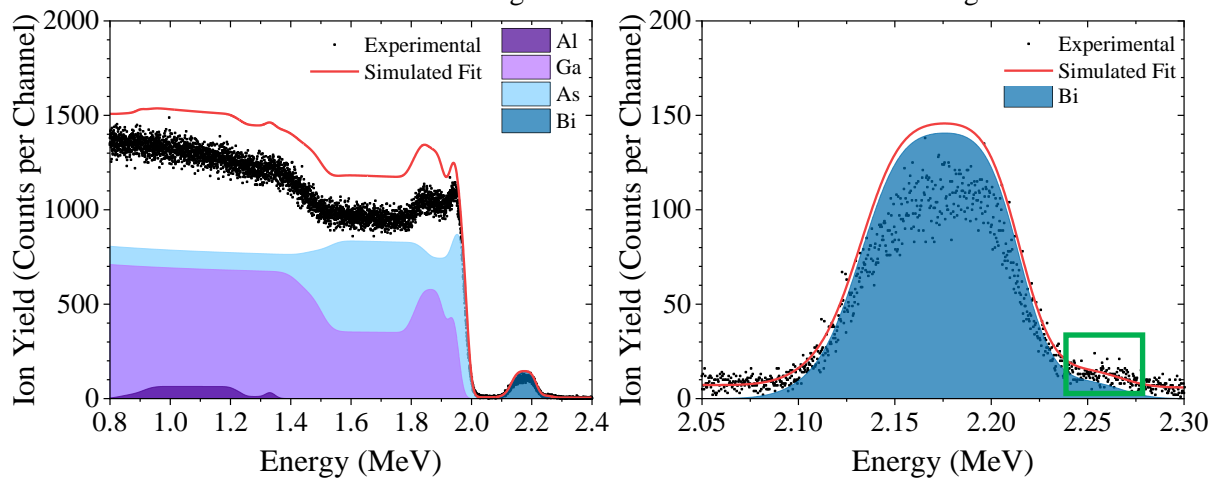


Figure 148 Glancing angle RBS of control sample for annealing series and zoomed in subsection showing the magnified Bi peak.

Having established the characteristics of the base line sample the annealing series can now be considered. Taking the PL and XRD analysis in isolation the sample annealed at 550 °C appeared the most optimal annealing temperature for increasing the optical quality. However, when analysed by ToF ERD a disproportionately high content of contamination was observed. The H, C and O contents were

not only present at the surface but also penetrated through the GaAs and AlGaAs into the AlGaAsBi layer. Previously the H contents at the surface has been up to 40 % of the total composition at the surface, falling to 0% when passing through the GaAs capping layer. For the 550 °C as can be seen in the ToF ERD shown in Figure 149 the impurities penetrate to a far deeper depth and at higher contents. The reported values are 20 % of the total detected atomic fraction in the AlGaAs and AlGaAsBi layer with a content of H, C and O at 11 ,5 and 4 percentage points of total detected atomic fractions respectively. The capping GaAs layer is ever higher with 44 % of the total content measured originating from the impurities. These values far exceed any other values measured across this series and heavily skew the extracted contents of Al, Bi and As. The origin of this additional contamination is unknown. However, as a result the ion beam analysis of the sample annealed at 550 °C must be treated with caution. RBS results of the Bi content were discounted due to the high dechannelling due to the low crystal quality of the capping layers. The trend is most apparent in Figure 150 where the high atomic fractions of impurities, especially in the buried AlGaAs and AlGaAsBi layers can be observed.

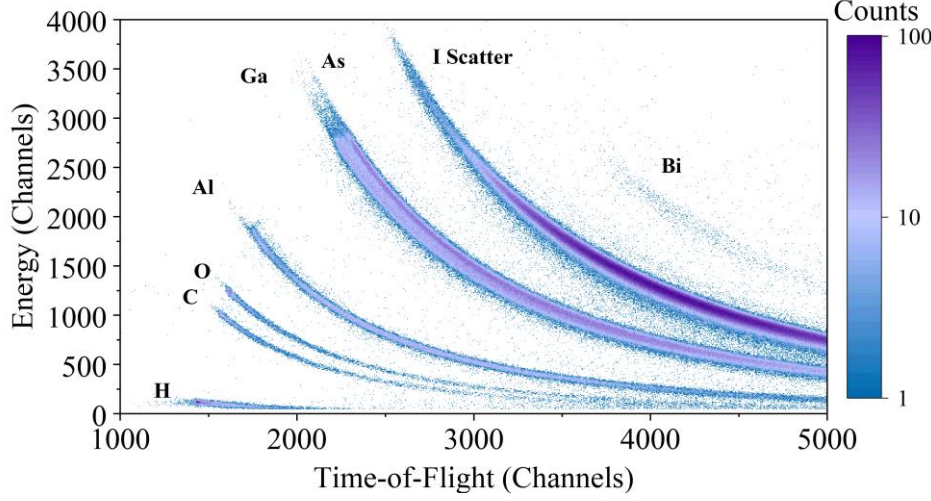


Figure 149 ToF ERD of sample annealed at 550 °C.

The impurity contents across the annealing series are all increased post annealing and significantly higher than in the high temperature capped equivalent samples. The impurities in the annealing control did not penetrate past the GaAs capping layer with the vast majority confined to the surface. This was the situation in all samples grown with high temperature capping layers. Conduction of an ex-situ anneal post growth under a N<sub>2</sub> atmosphere up to 500 °C for 30 s increased the number of impurities at the surface. However this had minimal impact on the underlying layers with the impurities remaining confined to the surface and GaAs capping layer. The 550 °C sample has previously been discussed, but can be summarised as the situation was worsened considerably, with significant quantities of impurities diffusing down to the Al<sub>1-x</sub>Ga<sub>x</sub>As<sub>1-y</sub>Bi<sub>y</sub> layer. The 600 °C sample returned back to more expected levels. However, there was still an increase in impurity contents at the surface and within the GaAs layer. The contents in the GaAs layer were higher than those in the 400 °C and 500 °C sample with the H atomic fraction increasing from 1.72 % and 2 % respectively to 13.7 %. Contents of C and O remained

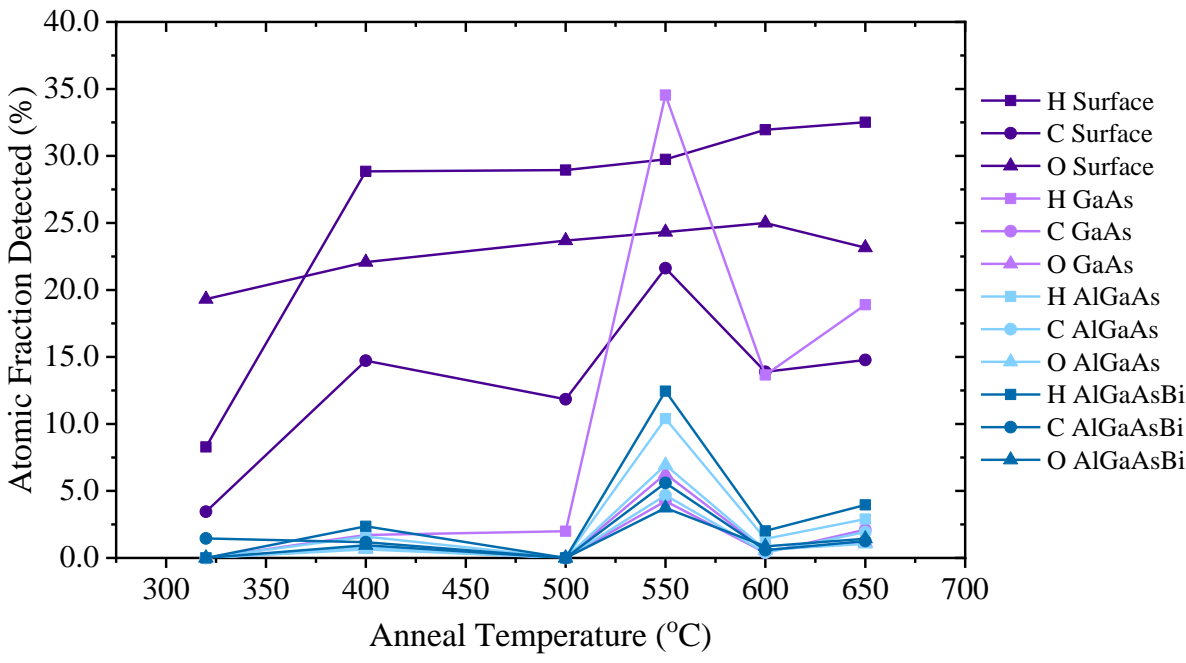


Figure 150 Impurity atomic fractions of H, C and O as detected by ToF ERD in each epitaxial layer for samples annealed between 400 to 650 °C, with the control shown at 320 °C. Layers are colour coded. With each impurity element point differentiated by shape.

unchanged as did the impurities in the AlGaAs layer. The level of impurities reaching the Al<sub>1-x</sub>Ga<sub>x</sub>As<sub>1-y</sub>Bi<sub>y</sub> layer remained consistent with those of the 400 °C sample with atomic fraction for H, C and O at 2.02, 0.58 and 0.86 % respectively. Further increasing the annealing temperature and the contents of all impurities increased in the lower layers while marginally decreasing in at the surface. This is most problematic as within the Al<sub>1-x</sub>Ga<sub>x</sub>As<sub>1-y</sub>Bi<sub>y</sub> layer where the H, C and O atomic fractions detected rose to 3.96, 1.2 and 1.43 % respectively. The detection of impurities in the Al<sub>1-x</sub>Ga<sub>x</sub>As<sub>1-y</sub>Bi<sub>y</sub> layer would account for the lack of improvement optical quality in the 20 K PL. It would also be highly likely this severely deteriorated the electrical properties of the material. Although this may not be an issue for devices with a thicker capping layer. Alternatively, a sample architecture with a sacrificial layer could also be used to mitigates this impurity diffusion. The increasing quantity of defects detected in the annealing process would indicate that the source of contamination is in the RTA itself, likely due to low purity N2 gas. It may be that the cause of the enhanced contamination at 550 °C is due to an increased sputter of impurity from the gas source, although confirming it is not possible. The contamination levels in all the annealed samples further support the argument that growing the capping layer at high temperatures is the better option. Alternatively, if annealing is required then it should be limited to in situ annealing post growth before the sample is removed from the MBE chamber. This would eliminate contamination diffusion into the Bi layer. However, due to the design of this experiment it was not possible to proceed in that manner as the samples required analysing prior to annealing. This does add further uncertainty to the PL results as this dramatically change the defects at play post annealing. It is surprising that any improvement in PL of these annealed samples was observed at all.

One contributing factor to this detriment may be found in analysis of the group III:As ratio of the capping GaAs and AlGaAs layers. If there is a severe disparity from unity in favour of the As this would indicate As<sub>Ga</sub> antistites defects, this is a known issue in cold grown III-Vs [127]–[129]. The III:As ratio as calculated from contents of Ga, Al and As, as measured by ToF ERD are shown in Figure 151. This provides a measurement of the relative abundance of As in each layer. The ideal value would be a unity ratio with the measured group III content. However, some values are slightly reduced by 0.1 to 0.2 at% due to the unintentional presence of Bi in the layers. It can be seen in the GaAs layer prior to annealing the As content is significantly above unity with a ratio between 1:0.77 to 1:0.8, indicating a high quantity of As<sub>Ga</sub> antisite defects. Post annealing between 400 °C to 600 °C the quantity of As decreased indicating the number of As<sub>Ga</sub> also fell accordingly. There drop in As content occurred instantly at 400 °C for a 30 s anneal with a gradual increase in As content with increased annealing temperature. Eventually exceeding the As abundance in the control at the sample annealed at 650 °C. The ratio of the control is close to unity in the AlGaAs suggesting a small population of As antistites in the AlGaAs layer. Excluding the 550 °C point for previously discussed reasons, the atomic ratio showed a gradual decrease with increasing annealing temperatures up to 600 °C. Above this annealing temperature at 650 °C an increase of 0.16 in the ratio was observed. The AlGaAs layer is likely more impactful on the optical properties as it confines the carriers to the  $Al_{1-x}Ga_xAs_{1-y}Bi_y$  layer so any trap states here would be highly detrimental.

PL measurements indicated that at 500 °C, 550 °C and 650 °C a slight increase in PL intensity was observed. Without carrier escape into the GaAs layer the As antistites within the GaAs capping layer do not explain this behaviour. Based on these results it would be expected that 400 °C should produce the highest quality capping layer, however this isn't so. Therefore, there remain other non-radiative

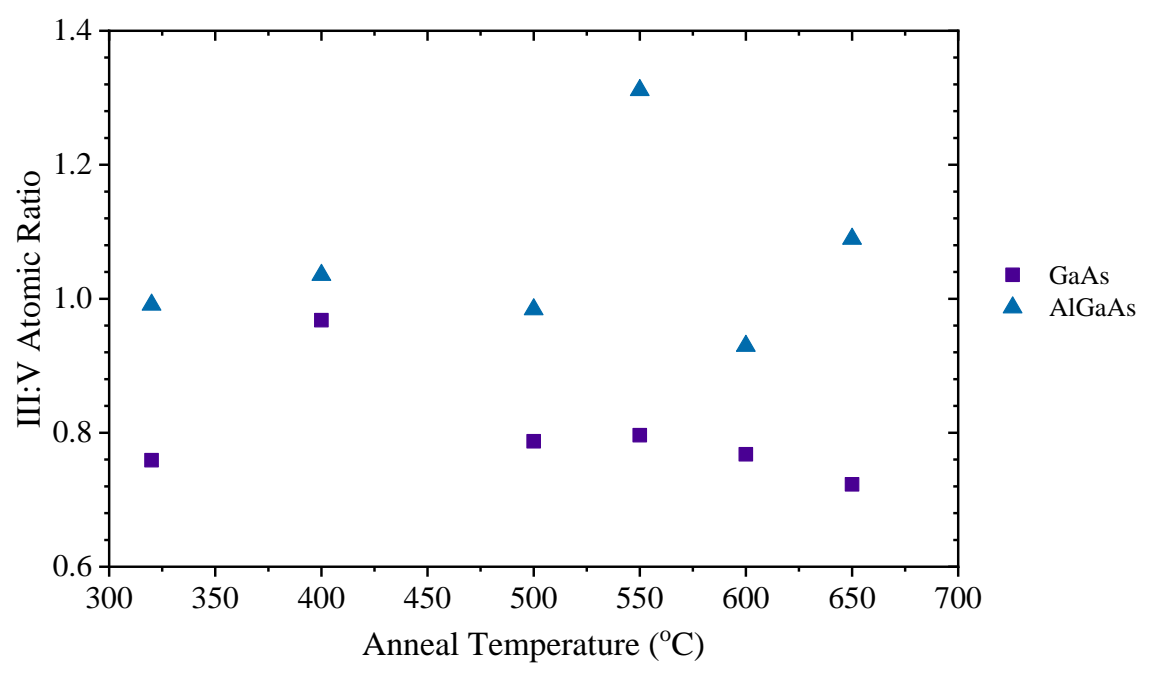


Figure 151 III:V atomic ratio for samples annealed between 400 to 650 °C.

defects within the Al<sub>1-x</sub>Ga<sub>x</sub>As<sub>1-y</sub>Bi<sub>y</sub> layer post annealing. The deterioration of the optical quality of the sample annealed at 650 °C can be explained partially by the loss of As observed in the AlGaAs layer with an increase As content in the GaAs layer. This may suggest As desorption from the surface during the annealing process for this layer. However, in all case the annealing process failed to improve the quality of the cold grown GaAs capping layer. This is a contributing cause to the low optical quality observed across all samples in this series grown with cold grown caping layers. The situation may be improved by using a lower temperature anneal to avoid As desorption over a longer timeframe. However this isn't certain and to confirm would require growth of additional samples.

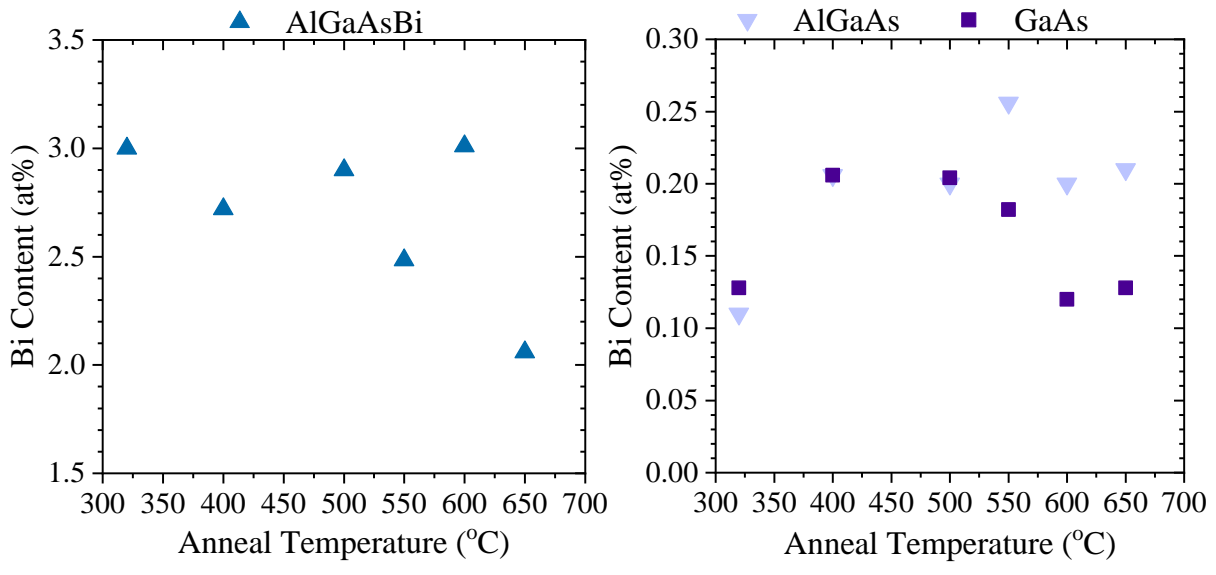


Figure 152 Bi contents as measured by RBS for each epitaxial layer for samples annealed between 400 to 650 °C, with the control shown at 320 °C.

The Bi contents within each layer as measured by RBS are shown in Figure 152. The Bi content within the control sample was 0.24 at% higher than measured by XRD indicating a small proportion of interstitial Bi  $\sim 10\%$ . Within the  $Al_{1-x}Ga_xAs_{1-y}Bi_y$  layer it can be observed that with increasing annealing temperatures the Bi content decreases compared with the control. This would indicate high levels of Bi diffusions out of the Al<sub>1-x</sub>Ga<sub>x</sub>As<sub>1-y</sub>Bi<sub>y</sub> layer. Turning attention to the AlGaAs capping layer it can be seen that post annealing the Bi content initially increased then remained stable at ~0.2 at%. This would indicate some Bi diffusion into the AlGaAs layer is highly likely from the underlying Bi layer. Further this would suggest the same process would occur in the AlGaAs buffer at the other interface to the Al<sub>1-x</sub>Ga<sub>x</sub>As<sub>1-y</sub>Bi<sub>y</sub> layer. However, the RBS shows only a minor interface region between the buffer and Bi layer. Further this region remains at a constant thickness and Bi content across the annealing temperature used. The GaAs capping layer also contained a minor initial quantity of Bi. Annealing seems to initially enhance the content with interlayer diffusion, however past 550 °C the content decreased. It is unlikely the Bi would diffuse back into the AlGaAs or Bi layer due to the similar Bi contents achieved in the lower annealing temperature. It is therefore more likely the Bi is desorbing the surface. The GaAs layer is ultrathin at 7 nm, there is ample time for Bi to move through and reach the surface at which point Bi would rapidly desorb at the temperatures utilised during the annealing.

However, this has not impacted the Al<sub>1-x</sub>Ga<sub>x</sub>As<sub>1-y</sub>Bi<sub>y</sub> layer and there is no indication of Bi diffusing across the AlGaAs and then desorbing. This is deduced based on the constant Bi content within the AlGaAs layer. If the Bi loss from the Al<sub>1-x</sub>Ga<sub>x</sub>As<sub>1-y</sub>Bi<sub>y</sub> layer was transiting across this layer it would be expected that the content detected would also rise with the increased throughput. The Bi peak in the RBS would also skew towards capping layer indicating the diffusion. This however is not observed therefore this process can be ruled out. It does leave the question remaining as to where the Bi has diffused to?

One explanation could be tied to the ion beam analysis itself, which while mirroring the trend in the XRD has an increased range of Bi values reported. The variance in the XRD was 0.2 at% while RBS is reporting 1 at% change across the series. It may be suggested that the loss in crystalline quality in the capping layers is increasing the uncertainty in the RBS measurements. The higher rates of ion dechannelling have made this series particularly challenging to conduct RBS measurement on. This might revive the explanation of Bi desorbing at low rates out through the capping layer at higher Bi contents.

The substitutional percentages of Bi and combined Al and Ga reported reflect the difficulties of the RBS measurements. The measured values are shown in Figure 153. The control sample values are considerably lower than would be expect with a substitutional Bi content of 57 % and Al plus Ga substitutional content of 62 %. The value for substitutional Bi is considerably lower than the previously indicated value of 90% based on the disparity between XRD and RBS measurements of Bi content. This is considerably lower than expected, the nature of these values are attributed to high rates of rechannelling due to low crystalline quality of the capping layers, as seen in the high quantity of As<sub>Ga</sub>. The samples annealed at 500 °C and 550 °C were beyond impractical to measure with the channelling directions eluding the UK National Ion Beam Centre. In their defence the experimental difficulty of

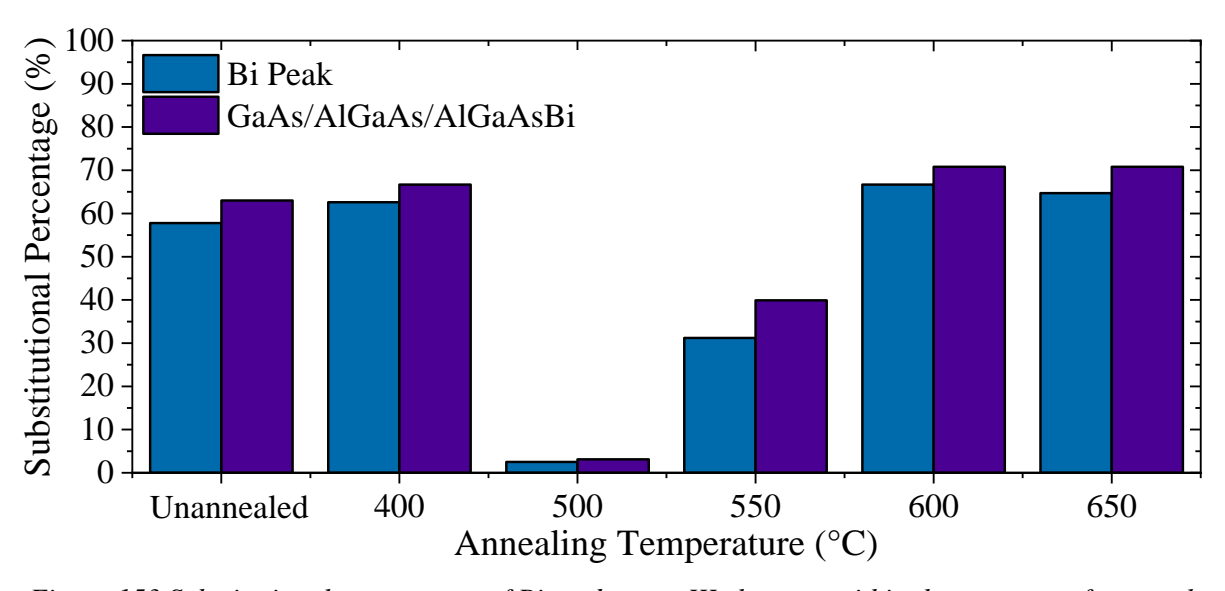


Figure 153 Substitutional percentages of Bi and group III elements within the structures for samples annealed between 400 to 650 °C.

measuring these sample was not in their favour. The high concentrations of defects and impurities in the surface layers combined with diminutive sample dimensions and further exacerbated by high surface roughness at the interfaces. The experimental nature and design and growth quality achieved did not make the task easy. The results of the channelled vs random aligned RBS are severely limited by the As antistites in the GaAs capping layer, with the substitutional percentages never exceeding 70 %. Well below the 76-80 % levels As siting on the group V site as indicated by the contents from the ToF ERD. The trend observed in the Figure 153 ,for samples where the channelling direction was found, matches the III:V atomic ratios of the GaAs layer shown in Figure 151. This further confirms the substantial measurements are being limited by the As contents of the GaAs capping layer. This highlights the issue of growing cold III-V capping layers with the intention of utilising an ex-situ anneal to recover the material quality.

#### **6.7 Conclusions**

The annealing investigation of Al<sub>1-x</sub>Ga<sub>x</sub>As<sub>1-y</sub>Bi<sub>y</sub> has been plagued by issues associated with the cold growth of GaAs and AlGaAs capping layers. The high As<sub>Ga</sub> antistites concentrations as indicated by the group III:As ratio detected by TOF ERD of ~20% remained insensitive to the annealing at all temperatures. For the penalties of the low growth there has been no conclusive indication that the underlying Al<sub>1-x</sub>Ga<sub>x</sub>As<sub>1-y</sub>Bi<sub>y</sub> material is of improved optical or material quality from not undergoing the heat treatment of a high temperature capping layer. The PL intensities support the conclusion that the quality is degraded due to the cold capping. However, this is likely more limited by the poorer-quality capping layers. Ex-situ annealing introduced significant quantities of C, H and O impurities into the epitaxial material. While there was no indication these interfered with the optical properties of the Bi layer it is highly likely they would severely degrade the electronic properties of the material. In addition, the interface regions between the AlGaAs buffer and Al<sub>1-x</sub>Ga<sub>x</sub>As<sub>1-y</sub>Bi<sub>y</sub> layer remained broad and unchanged indicting the same roughness observed in the high temperature capped sample was present and insensitive to the annealing process. The low crystalline quality impacted the RBS studies of the material making it practically infeasible to find channelling vector for certain samples. The drawbacks of the annealing process tested within this chapter far out any miniscule benefits, this is not to dismiss ex-situ annealing as a viable process for this alloy. However, it isn't a practical solution for resolving the high concentrations of defects seen in the  $Al_{1-x}Ga_xAs_{1-y}Bi_y$  material system in the previous chapter. In situ annealing may offer an improved approach as this would eliminate the high impurity content. However, I'd recommend any future attempts to repeat this experiment raise the capping layer temperatures above 480 °C to limit the As<sub>Ga</sub> antistites issue and confine the Bi content within the Al<sub>1-x</sub>Ga<sub>x</sub>As<sub>1-y</sub>Bi<sub>y</sub> layer. It is my opinion that the focus for improving the Al<sub>1-x</sub>Ga<sub>x</sub>As<sub>1-y</sub>Bi<sub>y</sub> alloy quality should remain on exploring the parameter space of the epitaxial growth over ex-situ techniques.

# 7 Final thoughts & Future Works

Within this thesis, I've presented the culmination of 3 years of experimental work. While the samples from which have drawn my conclusions total 23 in number with 11 for chapter 4, 11 for chapter 5 and 1 cleaved into 6 sections for chapter 6. These are the results of 2 and half years of time and effort spent growing and operating an MBE reactor. These represent a fraction of approximately 1500 samples that have been grown in test structures, calibration and diagnosis series in order to produce the series presented here. All of this is in spite of the tendency of the MBE reactor to fully live up to the alternative definition for MBE of mostly broken equipment at least once every 6 months. Further, it has been my privilege to teach 2 other PhD students in the art of III-V epitaxial growth by MBE during this time. In addition to the teaching and training, I've also been involved in throughout my PhD. The output from the project has included 11 presentations and posters at conferences in America, Asia and Europe. 2 Papers have been published to date on materials I have grown during my time on the MBE system with a 3<sup>rd</sup> under review. At least 2 additional papers are planned which includes the first to report on Al<sub>1-x</sub>Ga<sub>x</sub>As<sub>1-y</sub>Bi<sub>y</sub> growth, opening up the quaternary system to the wider scientific community. I would summarise by saying that there has been both hardship but also success from the material output of my work.

The findings of the Bi modified self-assembled InAs QD growth on GaAs highlighted how sensitive the material system is to the starting conditions. Contracting with previous studies and those in the wider literature can provide some insight however there always remains some grey and uncertain areas. The absence of a comprehensive picture as to how Bi was highlighted in this work by the results country to our expectations. Where Bi on the surface during QD formation reversed the trend previously reported in the wider literature. The extensive range of control parameters tuneable during QD growth makes metallic films and subsequent characterisation of the thickness metallic films and subsequent characterisation of the thickness designing a follow up growth study to establish the impact under a significantly wider range of conditions challenging. The number of potential samples to comprehensively map the available parameter space by the previously used growth series construction techniques would be impractically high. Therefore, I would propose an alternative approach to the follow up investigation utilising a larger 3 or 4 inch III-V MBE system.

This would enable the utilisation of the inherent inhomogeneity of the flux profiles present in larger MBE reactors due to relative source positions and distances to positions on the wafer. This is usually countered by rotating the substrate however when using static rotation, it is possible to test a range of flux ratios and growth rates on a single wafer. By accurate characterisation of each induvial flux profile within the reactor by static deposition of metallic films and subsequent characterisation of the thickness. The relative deposition rates for each flux profile for each constituent element at any point can be

calculated prior to the series growth. This then means a range of conditions can be grown simultaneously.

The suggested growth series would require 8 samples grown on 3 or 4-inch insulating GaAs wafers at regular temperature intervals. The recommend range based on the results from this work would be 420, 450, 480, 510 °C. The series is split with 1 control sample and 1 sample exposed to a Bi flux at each temperature. The sample architecture and layer sequence previously used in chapter 4 would be suitable here as well with a buried layer of capped QDs with a subsequent deposition of uncapped surface QDs under identical conditions. The conditions in the centre point of the wafer should be an approximation to an InAs deposition thickness of 2.7 ML at 0.001MLs<sup>-1</sup> based on the findings from Chapter 4. This would allow for comparison to the previous body of work with a common reference point. The static growth on a larger wafer size should provide a broad range of flux profiles across the wafer. Analysis by AFM and PL to map the emission and QD morphology of the 8 wafers will provide a much more extensive overview of how different flux ratios and deposition thicknesses impact the QD formation. This approach while requiring an additional wafer for each element Ga, In, As and Bi to establish the flux profiles initially should yield a much more extensive insight into QD formation. Highlighting the regions where Bi flux control can aid in the morphological control to shift the emission into the O and C telecommunications bands. It could also be further possible to subsequently anneal the wafers post growth and analysis to establish how post-processing changes the morphology and emission under the flux profiles produced to gain additional information into the post-process possibility and under which conditions this would be aid and under which this would lead to a detriment in the properties. From this body of work, it would therefore be possible to define the growth conditions optimal for engineering Bi modified InAs QD devices with or without ex situ annealing. Establishing the ranges of effective operation as well as providing insight into the temperature and flux limitations. Thereby providing answers that slipped beyond the range of the growth series presented within this thesis.

In addressing the questions raised and remaining for chapter 5 it is my main regret that it was not possible to fabricate the grown Al<sub>1-x</sub>Ga<sub>x</sub>As<sub>1-y</sub>Bi<sub>y</sub> into device structures during this body of work. This has left several unanswered questions regarding the achieved ionisation rates within the alloys and untested electronic properties. The latter can be partially inferred in some instances based on the optical properties analysed in this study. However, to take the work further and continue the development of the quaternary alloy the first stage is replicating the growth conditions used within this study to fabricate a device series. It would be recommended to test a least 3 to 5 Al contents between 5-80 at% with 2 to 4 levels of Bi content. The fabrication into simple PIN or NIP devices would allow for the extraction of the ionisation rates, electronic properties and analysing by deep level transient spectroscopy (DLTS). This would however not allow for the analysis of the alloy presented within this work which required thinner capping layer deposition than possible for device fabrication.

Analysis of the device series would provide a measure to allow for quantification of conditions inferred from the body of this work. That extends to the drop in optical quality and if this corresponds to a decrease in the electronic properties to a point where it is detrimental to the device performance. Additionally, The DLTS will provide direct measurements of the defect states that were previously observed in the PL results. This more defended measure of the defect states will enable more accurate attribution to the defect complexes from which they arise. Through simulation of defect clusters and complexes to match the energy more discretely observed energy levels compared to PL. Identification of the complex would be the first stage in reengineering the growth conditions to prevent their formation. From this, it should enable the next stage in development and quantifying the current feasibility of the alloy for APD usage. Any remaining issues with the growth of the alloys would also be highlighted enabling a more targeted approach to their resolution.

Post-process annealing while largely unsuccessful as covered in chapter 6 of this thesis may still prove a usable control technique for the growth of  $Al_{1-x}Ga_xAs_{1-y}Bi_y$  quaternary systems. However, without the conclusion from the further work recommended to answer the open questions raised in Chapter 5. The application of post-process annealing would not be guided and therefore would likely again fail to yield a positive impact. Or if a benefit was found understanding the mechanism of improvement would likely prove frustrating. It is therefore recommended to only apply post-process annealing if the results of the further works for Chapter 5 indicate it as a solution to any issues that may be raised.

While inconclusive or negative results are never the hope of any researcher their inherent value remains. It is my sincerest hope that the complete reports of my studies into Bi modified III-V alloys both good and bad have provided valuable insight. Both with the successful results and synthesis of new quaternary III-V alloys and with the inconclusive or void results where I hope others may learn and avoid the same pitfalls. The further work and experiments I have suggested in this chapter would help continue and answer the remaining questions my work of the last 3 years. Bringing closer the realisable benefits of next generation optoelectronic devices. I will continue to watch keeping a weather eye on how this field continues to evolve and the work that is moving it forward.

# 8 References

- [1] "Bandstructure of gallium arsenide (GaAs)." [Online]. Available: http://lampx.tugraz.at/~hadley/ss1/bands/bandstructures/GaAs/gaas\_bands.html. [Accessed: 26-Jun-2021].
- [2] M. Brozel, "Gallium Arsenide," in *Springer Handbooks*, Springer, 2007, pp. 499–536.
- [3] S. J. Moss and A. Ledwith, "The Chemistry of the semiconductor industry," p. 426, 1987.
- [4] M. Fox, Optical Properties of Solids, Second Edition. Oxford University Press, 2010.
- [5] Charles Kittel, *Introduction to Solid State Physics*, 8th Edition. Wiley, 2018.
- [6] U. K. Mishra and J. Singh, Semiconductor device physics and design. Springer, 2008.
- [7] M. Govoni, I. Marri, and S. Ossicini, "Auger recombination in Si and GaAs semiconductors: Ab initio results," *Phys. Rev. B Condens. Matter Mater. Phys.*, vol. 84, no. 7, 2011.
- [8] M. Usman, C. A. Broderick, A. Lindsay, and E. P. O'reilly, "Tight-binding analysis of the electronic structure of dilute bismide alloys of GaP and GaAs," *Phys. Rev. B*, vol. 84, p. 245202, 2011.
- [9] C. A. Broderick, M. Usman, E P O'Reilly, and S. Sweeney, "Band engineering in dilute nitride and bismide semiconductor lasers," 2012.
- [10] "DoITPoMS TLP Library Introduction to Semiconductors Intrinsic and Extrinsic Semiconductors." [Online]. Available: https://www.doitpoms.ac.uk/tlplib/semiconductors/intrinsic.php. [Accessed: 26-Jun-2021].
- [11] F. Fischer, D. Schuh, M. Bichler, G. Abstreiter, M. Grayson, and K. Neumaier, "Modulating the growth conditions: Si as an acceptor in (110) GaAs for high mobility p -type heterostructures," *Appl. Phys. Lett.*, vol. 86, no. 19, pp. 1–3, 2005.
- [12] H. Ibach and H. Lüth, *Solid-state physics: An introduction to principles of materials science*. Springer Berlin Heidelberg, 2010.
- [13] "Energy bandgap of AlGaAs." [Online]. Available: https://www.batop.de/information/Eg\_AlGaAs.html. [Accessed: 26-Jun-2021].
- [14] "Energy bandgap of InGaAs." [Online]. Available: https://www.batop.de/information/Eg\_InGaAs.html. [Accessed: 26-Jun-2021].
- [15] L. Vegard, "Die Konstitution der Mischkristalle und die Raumfüllung der Atome," *Zeitschrift für Phys.*, vol. 5, no. 1, pp. 17–26, Jan. 1921.

- [16] P. Harrison, Quantum Wells, Wires and Dots: Theoretical and Computational Physics of Semiconductor Nanostructures: Second Edition. 2006.
- [17] O. B. Shchekin and D. G. Deppe, "1.3 μm InAs quantum dot laser with To=161K from 0 to 80°C," *Appl. Phys. Lett.*, vol. 80, no. 18, pp. 3277–3279, May 2002.
- [18] K. W. J. Barnham and G. Duggan, "A new approach to high-efficiency multiband-gap solar cells," *J. Appl. Phys.*, vol. 67, p. 3490, 1990.
- [19] W. Pan, L. Wang, Y. Zhang, W. Lei, and S. Wang, "MBE growth strategy and optimization of GaAsBi quantum well light emitting structure beyond 1.2 μm," *Appl. Phys. Lett*, vol. 114, p. 152102, 2019.
- [20] R. D. Richards, F. Bastiman, D. Walker, R. Beanland, and J. P. R. David, "Growth and structural characterization of GaAsBi/GaAs multiple quantum wells," *Semicond. Sci. Technol.*, vol. 30, no. 9, p. 94013, 2015.
- [21] Y. Arakawa and H. Sakaki, "Multidimensional quantum well laser and temperature dependence of its threshold current," *Appl. Phys. Lett.*, vol. 40, no. 11, pp. 939–941, 1982.
- [22] S. Franchi, G. Trevisi, L. Seravalli, and P. Frigeri, "Quantum dot nanostructures and molecular beam epitaxy," *Progress in Crystal Growth and Characterization of Materials*, vol. 47, no. 2–3. Pergamon, pp. 166–195, 01-Jan-2003.
- [23] I. N. Stranski and L. Krastanow, "Zur Theorie der orientierten Ausscheidung von Ionenkristallen aufeinander," *Monatshefte für Chemie*, vol. 72, no. 1, p. 76, 1939.
- [24] E. Bauer, Bauer, and Ernst, "Phänomenologische Theorie der Kristallabscheidung an Oberflächen. I," ZK, vol. 110, no. 1–6, pp. 372–394, 1958.
- [25] N. Koguchi, S. Takahashi, and T. Chikyow, "New MBE growth method for InSb quantum well boxes," *J. Cryst. Growth*, vol. 111, no. 1–4, pp. 688–692, May 1991.
- [26] J. Wu and J. Peng, "Self-assembly of InAs quantum dots on GaAs(001) by molecular beam epitaxy," *Front. Phys*, vol. 10, p. 108101, 2015.
- [27] J. Grabowski, C. Prohl, B. Höpfner, M. Dähne, and H. Eisele, "Evolution of the InAs wetting layer on GaAs (001) -c (4×4) on the atomic scale," *Appl. Phys. Lett.*, vol. 95, no. 23, p. 233118, Dec. 2009.
- [28] C. Prohl, B. Höpfner, J. Grabowski, M. Dähne, and H. Eisele, "Atomic structure and strain of the InAs wetting layer growing on GaAs(001)-c(4×4)," *J. Vac. Sci. Technol. B*, vol. 28, no. 4, p. C5E13-C5E21, Jul. 2010.

- [29] N. J. Bailey, M. R. Carr, J. P. R. David, and R. D. Richards, "Growth of InAs(Bi)/GaAs Quantum Dots under a Bismuth Surfactant at High and Low Temperature," *J. Nanomater.*, vol. 2022, no. 001, pp. 1–9, 2022.
- [30] I. Kamiya, T. Shirasaka, K. Shimomura, and D. M. Tex, "Influence of in and As fluxes on growth of self-assembled InAs quantum dots on GaAs(0 0 1)," *J. Cryst. Growth*, vol. 323, no. 1, pp. 219–222, 2011.
- [31] D. Leonard, K. Pond, and P. M. Petroff, "Critical layer thickness for self-assembled InAs islands on GaAs," *Phys. Rev. B*, vol. 50, no. 16, pp. 11687–11692, 1994.
- [32] S. L. Portalupi, M. Jetter, and P. Michler, "InAs quantum dots grown on metamorphic buffers as non-classical light sources at telecom C-band: A review," *Semicond. Sci. Technol.*, vol. 34, no. 5, 2019.
- [33] L. Wang *et al.*, "Novel dilute bismide, epitaxy, physical properties and device application," *Crystals*, vol. 7, no. 3, pp. 1–60, 2017.
- [34] C. H. Chiang *et al.*, "Improving the photoluminescence properties of self-assembled InAs surface quantum dots by incorporation of antimony," *Appl. Surf. Sci.*, vol. 257, no. 21, pp. 8784–8787, 2011.
- [35] H. Okamoto *et al.*, "Growth and Characterization of Telecommunication-Wavelength Quantum Dots Using Bi as a Surfactant," *Japanese J. Appl. Phys. To*, vol. 49, pp. 6–7, 2010.
- [36] X. Y. Chen *et al.*, "Growth mechanisms for InAs/GaAs QDs with and without Bi surfactants," *Mater. Res. Express*, vol. 6, no. 1, 2019.
- [37] C. G. Morgan, P. Kratzer, and M. Scheffler, "Arsenic Dimer Dynamics during MBE Growth: Theoretical Evidence for a Novel Chemisorption State of As2 Molecules on GaAs Surfaces," *Phys. Rev. Lett.*, vol. 82, no. 24, p. 4886, Jun. 1999.
- [38] J. R. Arthur, "Gallium Arsenide Surface Structure and Reaction Kinetics: Field Emission Microscopy," *J. Appl. Phys.*, vol. 37, no. 8, pp. 3057–3064, Jul. 1966.
- [39] C. T. Foxon and B. A. Joyce, "Interaction kinetics of As2 and Ga on {100} GaAs surfaces," *Surf. Sci.*, vol. 64, no. 1, pp. 293–304, 1977.
- [40] S. V. Ghaisas and A. Madhukar, "Monte-Carlo simulations of MBE growth of III–V semiconductors: The growth kinetics, mechanism, and consequences for the dynamics of RHEED intensity," *J. Vac. Sci. Technol. B Microelectron. Process. Phenom.*, vol. 3, no. 2, pp. 540–546, Mar. 1985.
- [41] S. V. Ghaisas and A. Madhukar, "Role of Surface Molecular Reactions in Influencing the Page | 210

- Growth Mechanism and the Nature of Nonequilibrium Surfaces: A Monte Carlo Study of Molecular-Beam Epitaxy," *Phys. Rev. Lett.*, vol. 56, no. 10, p. 1066, Mar. 1986.
- [42] S. V. Ghaisas and A. Madhukar, "Surface kinetics and growth interruption in molecular-beam epitaxy of compound semiconductors: A computer simulation study," *J. Appl. Phys.*, vol. 65, no. 10, pp. 3872–3876, May 1989.
- [43] P. Smilauer and D. D. Vvedensky, "Step-edge barriers on GaAs(001)," *Phys. Rev. B*, vol. 48, pp. 15–1993.
- [44] J. Wu, Y. H. Jiao, P. Jin, X. J. Lv, and Z. G. Wang, "Effect of the growth mode on the two-to three-dimensional transition of InAs grown on vicinal GaAs(001) substrates," *Nanotechnology*, vol. 18, no. 26, pp. 14–18, 2007.
- [45] H. Zhang, Y. Chen, G. Zhou, C. Tang, and Z. Wang, "Wetting layer evolution and its temperature dependence during self-assembly of InAs/GaAs quantum dots," *Nanoscale Res. Lett.*, vol. 7, pp. 1–6, 2012.
- [46] C. Heyn and W. Hansen, "Ga/In-intermixing and segregation during InAs quantum dot formation," *J. Cryst. Growth*, vol. 251, no. 1–4, pp. 140–144, Apr. 2003.
- [47] Y. Wang, H. S. Djie, and B. S. Ooi, "Group-III intermixing in InAs/InGaAlAs quantum dots-in-well," *Appl. Phys. Lett.*, vol. 88, no. 11, Mar. 2006.
- [48] S. Yanase *et al.*, "Surfactant effect of Bi on InAs quantum dot laser diode," *Jpn. J. Appl. Phys.*, vol. 61, no. 12, 2022.
- [49] C. Y. Ngo, S. F. Yoon, C. Z. Tong, W. K. Loke, and S. J. Chua, "An investigation of growth temperature on the surface morphology and optical properties of 1.3 μm InAs/InGaAs/GaAs quantum dot structures," *Nanotechnology*, vol. 18, no. 36, 2007.
- [50] V. G. Dubrovskiĭ *et al.*, "Dependence of Structural and Optical Properties of QD Arrays in an InAs/GaAs System on Surface Temperature and Growth Rate," *Semiconductors*, vol. 38, no. 3, pp. 329–334, 2004.
- [51] M. Alduraibi, C. Mitchell, S. Chakraborty, and M. Missous, "Surfactant-mediated growth of InAs-GaAs superlattices and quantum dot structures grown at different temperatures," *Microelectronics J.*, vol. 40, no. 3, pp. 476–478, Mar. 2009.
- [52] Y. Sun, S. F. Cheng, G. Chen, R. F. Hicks, J. G. Cederberg, and R. M. Biefeld, "The effect of antimony in the growth of indium arsenide quantum dots in gallium arsenide (001)," *J. Appl. Phys.*, vol. 97, no. 5, 2005.
- [53] D. Fan *et al.*, "Bismuth surfactant mediated growth of InAs quantum dots by molecular beam Page | 211

- epitaxy."
- [54] Z. Xu *et al.*, "Carrier relaxation and thermal activation of localized excitons in self-organized InAs multilayers grown on GaAs substrates," *Phys. Rev. B Condens. Matter Mater. Phys.*, vol. 54, no. 16, pp. 11528–11531, 1996.
- [55] R. D. Richards *et al.*, "Molecular beam epitaxy growth of GaAsBi using As2 and As4," *J. Cryst. Growth*, vol. 390, pp. 120–124, 2014.
- [56] R. Tait, L. Yan, and J. M. Millunchick, "Droplet induced compositional inhomogeneities in GaAsBi," *J. Appl. Phys.*, vol. 111, p. 215302, 2017.
- [57] J. A. Steele *et al.*, "Surface effects of vapour-liquid-solid driven Bi surface droplets formed during molecular-beam-epitaxy of GaAsBi OPEN," *Nat. Publ. Gr.*, 2016.
- [58] B. A. Carter, V. Caro, L. Yue, C. R. Tait, and J. M. Millunchick, "The effect of III:V ratio on compositional and microstructural properties of GaAs1-xBix (001)," *J. Cryst. Growth*, vol. 548, no. July, 2020.
- [59] J. Puustinen, J. Hilska, and M. Guina, "Analysis of GaAsBi growth regimes in high resolution with respect to As/Ga ratio using stationary MBE growth," *J. Cryst. Growth*, vol. 511, no. December 2018, pp. 33–41, 2019.
- [60] A. J. Ptak *et al.*, "Kinetically limited growth of GaAsBi by molecular-beam epitaxy," *J. Cryst. Growth*, vol. 338, no. 1, pp. 107–110, 2012.
- [61] N. J. Bailey, T. B. O. Rockett, S. Flores, D. F. Reyes, J. P. R. David, and R. D. Richards, "Effect of MBE growth conditions on GaAsBi photoluminescence lineshape and localised state filling," *Sci. Rep.*, vol. 12, no. 1, pp. 1–8, 2022.
- [62] G. Vardar, S. W. Paleg, M. V Warren, M. Kang, S. Jeon, and R. S. Goldman, "Mechanisms of droplet formation and Bi incorporation during molecular beam epitaxy of GaAsBi," *Appl. Phys. Lett*, vol. 102, p. 42106, 2013.
- [63] G. V Rodriguez and J. M. Millunchick, "Predictive modeling of low solubility semiconductor alloys," *J. Appl. Phys.*, vol. 120, no. 12, pp. 215310–4, 2016.
- [64] M. Masnadi-Shirazi, D. A. Beaton, R. B. Lewis, X. Lu, and T. Tiedje, "Surface reconstructions during growth of GaAsBi alloys by molecular beam epitaxy," 2011.
- [65] A. J. Ptak *et al.*, "Kinetically limited growth of GaAsBi by molecular-beam epitaxy," *J. Cryst. Growth*, vol. 338, no. 1, pp. 107–110, 2012.
- [66] M. Ferhat and A. Zaoui, "Structural and electronic properties of III-V bismuth compounds,"

- Phys. Rev. B Condens. Matter Mater. Phys., vol. 73, no. 11, 2006.
- [67] M. Usman *et al.*, "Impact of alloy disorder on the band structure of compressively strained GaBixAs(1-x)," *Phys. Rev. B*, vol. 87, p. 115104, 2013.
- [68] C. Wang *et al.*, "Molecular beam epitaxy growth of AlAs 1-x Bi x," *Semicond. Sci. Technol.*, vol. 34, no. 3, p. 034003, Feb. 2019.
- [69] P. Hess, "Bonding, structure, and mechanical stability of 2D materials: The predictive power of the periodic table," *Nanoscale Horizons*, vol. 6, no. 11, pp. 856–892, 2021.
- [70] A. Y. Cho and J. R. Arthur, "Molecular beam epitaxy," *Prog. Solid State Chem.*, vol. 10, no. PART 3, pp. 157–191, Jan. 1975.
- [71] B. A. Joyce, "Molecular beam epitaxy," *Reports Prog. Phys.*, vol. 48, no. 12, p. 1637, Dec. 1985.
- [72] "News | How does an ion gauge work? Arun Microelectronics." [Online]. Available: https://arunmicro.com/news/how-does-an-ion-gauge-work/. [Accessed: 03-Jan-2024].
- [73] "Kurt J. Lesker Company | Pressure Measurement Technical Notes | Enabling Technology for a Better World." [Online]. Available: https://www.lesker.com/newweb/gauges/gauges\_technicalnotes\_1.cfm. [Accessed: 03-Jan-2024].
- [74] S. Hasegawa, "REFLECTION HIGH-ENERGY ELECTRON DIFFRACTION."
- [75] A. Ichimiya and P. I. Cohen, "Kikuchi and resonance patterns," in *Reflection High-Energy Electron Diffraction*, 2010, pp. 62–76.
- [76] A. Ohtake, "Surface reconstructions on GaAs(001)," *Surface Science Reports*, vol. 63, no. 7. pp. 295–327, 2008.
- [77] K. Barnham and D. Vvedensky, Eds., "Low-Dimensional Semiconductor Structures: Fundamentals and Device Applications," Jul. 2001.
- [78] S. C. Seel, C. V. Thompson, S. J. Hearne, and J. A. Floro, "Tensile stress evolution during deposition of Volmer–Weber thin films," *J. Appl. Phys.*, vol. 88, no. 12, pp. 7079–7088, Dec. 2000.
- [79] J. H. Neave, B. A. Joyce, J. H. Neave, and B. A. Joyce, "Structure and stoichiometry of {100} GaAs surfaces during molecular beam epitaxy," *JCrGr*, vol. 44, no. 4, pp. 387–397, 1978.
- [80] K. Regiński, J. Muszalski, V. V. Preobrazhenskii, and D. I. Lubyshev, "Static phase diagrams of reconstructions for MBE-grown GaAs(001) and AlAs(001) surfaces," *Thin Solid Films*, vol.

- 267, no. 1–2, pp. 54–57, Oct. 1995.
- [81] M. C. Gallagher, R. H. Prince, and R. F. Willis, "On the atomic structure and electronic properties of decapped GaAs(001)(2 × 4) surfaces," *Surf. Sci.*, vol. 275, no. 1–2, pp. 31–40, Sep. 1992.
- [82] William Henry Bragg and William Lawrence Bragg, "The reflection of X-rays by crystals," *Proc. R. Soc. London. Ser. A, Contain. Pap. a Math. Phys. Character*, vol. 88, no. 605, pp. 428–438, Jul. 1913.
- [83] T. B. Pitman, B. C. Jacobs, and J. D. Franson, "Quantum computing using linear optics," *Johns Hopkins APL Tech. Dig. (Applied Phys. Lab.*, vol. 25, no. 2, pp. 84–89, 2004.
- [84] P. W. Shor, "Algorithms for quantum computation: Discrete logarithms and factoring," in *Proceedings Annual IEEE Symposium on Foundations of Computer Science, FOCS*, 1994, pp. 124–134.
- [85] L. K. Grover, "Quantum mechanics helps in searching for a needle in a haystack," *Phys. Rev. Lett.*, vol. 79, no. 2, pp. 325–328, Jul. 1997.
- [86] S. Khalid and F. P. Laussy, "Perfect single-photon sources," *Sci. Rep.*, vol. 14, no. 1, pp. 1–10, 2024.
- [87] D. Huber, M. Reindl, J. Aberl, A. Rastelli, and R. Trotta, "Semiconductor quantum dots as an ideal source of polarization-entangled photon pairs on-demand: A review," *J. Opt. (United Kingdom)*, vol. 20, no. 7, 2018.
- [88] M. Takeshima, "Theory of phonon-assisted Auger recombination in semiconductors," *Phys. Rev. B*, vol. 23, no. 12, pp. 6625–6637, 1981.
- [89] N. Holonyak *et al.*, "Phonon assisted recombination and stimulated emission in quantum well Al," *J. Appl. Phys.*, vol. 51, no. 1980, pp. 1328–1337, 1980.
- [90] P. B. Joyce, E. C. Le Ru, T. J. Krzyzewski, G. R. Bell, R. Murray, and T. S. Jones, "Optical properties of bilayer InAs/GaAs quantum dot structures: Influence of strain and surface morphology," *Phys. Rev. B Condens. Matter Mater. Phys.*, vol. 66, no. 7, pp. 1–8, 2002.
- [91] E. M. Sala, M. Godsland, A. Trapalis, and J. Heffernan, "Effect of Cap Thickness on InAs/InP Quantum Dots Grown by Droplet Epitaxy in Metal—Organic Vapor Phase Epitaxy," *Phys. Status Solidi Rapid Res. Lett.*, vol. 15, no. 9, p. 2100283, Sep. 2021.
- [92] G. Costantini *et al.*, "Interplay between thermodynamics and kinetics in the capping of InAs/GaAs(001) quantum dots," *Phys. Rev. Lett.*, vol. 96, no. 22, p. 226106, Jun. 2006.

- [93] G. Feng, K. Oe, and M. Yoshimoto, "Temperature dependence of Bi behavior in MBE growth of InGaAs/InP," *J. Cryst. Growth*, vol. 301–302, no. SPEC. ISS., pp. 121–124, Apr. 2007.
- [94] H. L. Ho *et al.*, "High-speed 3D imaging using a chaos lidar system," *Eur. Phys. J. Spec. Top.*, vol. 231, no. 3, pp. 435–441, 2022.
- [95] Q. Hao, Y. Tao, J. Cao, and Y. Cheng, "Development of pulsed-laser three-dimensional imaging flash lidar using APD arrays," *Microwave and Optical Technology Letters*, vol. 63, no. 10. pp. 2492–2509, 2021.
- [96] R. J. McINTYRE, "Multiplication Noise in Uniform Avalanche Diodes," *IEEE Trans. Electron Devices*, vol. ED-13, no. 1, pp. 164–168, 1966.
- [97] R. B. Emmons, "Avalanche-Photodiode Frequency Response," *J. Appl. Phys.*, vol. 38, no. 9, pp. 3705–3714, Aug. 1967.
- [98] Hamamatsu, "Si APDs," 2021.
- [99] B. K. Ng, J. P. R. David, G. J. Rees, R. C. Tozer, M. Hopkinson, and R. J. Airey, "Avalanche multiplication and breakdown in AlxGa1-xAs (x < 0.9)," *IEEE Trans. Electron Devices*, vol. 49, no. 12, pp. 2349–2351, Dec. 2002.
- [100] F. Osaka, T. Mikawa, and T. Kaneda, "Impact Ionization Coefficients of Electrons and Holes in (100)-Oriented Ga1-XInXAsYP1-Y," *IEEE J. Quantum Electron.*, vol. 21, no. 9, pp. 1326– 1338, 1985.
- [101] S. Wang *et al.*, "Low-noise impact-ionization-engineered avalanche photodiodes grown on InP substrates," *IEEE Photonics Technol. Lett.*, vol. 14, no. 12, pp. 1722–1724, Dec. 2002.
- [102] M. Ren, S. Maddox, Y. Chen, M. Woodson, J. C. Campbell, and S. Bank, "AlInAsSb/GaSb staircase avalanche photodiode," *Appl. Phys. Lett.*, vol. 108, no. 8, p. 81101, Feb. 2016.
- [103] F. Capasso, W. T. Tsang, and G. F. Williams, "Staircase Solid-State Photomultipliers and Avalanche Photodiodes with Enhanced Ionization Rates Ratio," *IEEE Trans. Electron Devices*, vol. 30, no. 4, pp. 381–390, 1983.
- [104] Y. J. Ma *et al.*, "Enhanced Carrier Multiplication in InAs Quantum Dots for Bulk Avalanche Photodetector Applications," *Adv. Opt. Mater.*, vol. 5, no. 9, p. 1601023, May 2017.
- [105] B. Chen *et al.*, "Low Dark Current High Gain InAs Quantum Dot Avalanche Photodiodes Monolithically Grown on Si," *ACS Photonics*, vol. 7, no. 2, pp. 528–533, Feb. 2020.
- [106] Y. Liu *et al.*, "Valence band engineering of GaAsBi for low noise avalanche photodiodes," *Nat. Commun.*, vol. 12, no. 1, 2021.

- [107] A. R. Mohmad, F. Bastiman, J. S. Ng, S. J. Sweeney, and J. P. R. David, "Photoluminescence investigation of high quality GaAs1-x Bi x on GaAs," *Appl. Phys. Lett.*, vol. 98, no. 12, pp. 1–4, 2011.
- [108] S. J. Sweeney and S. R. Jin, "Bismide-nitride alloys: Promising for efficient light emitting devices in the near- and mid-infrared," *J. Appl. Phys.*, vol. 113, no. 4, p. 43110, Jan. 2013.
- [109] I. H. Oğuzman, Y. Wang, J. Kolník, and K. F. Brennan, "Theoretical study of hole initiated impact ionization in bulk silicon and GaAs using a wave-vector-dependent numerical transition rate formulation within an ensemble Monte Carlo calculation," *J. Appl. Phys.*, vol. 77, no. 1, pp. 225–232, Jan. 1995.
- [110] N. Bailey, "Growth optimisation of III-V semiconductors using bismuth as a surfactant and a constituent," 2022.
- [111] T. Wilson *et al.*, "Assessing the Nature of the Distribution of Localised States in Bulk GaAsBi," *Sci. Rep.*, vol. 8, no. 1, pp. 1–10, 2018.
- [112] P. Laukkanen *et al.*, "Local variation in Bi crystal sites of epitaxial GaAsBi studied by photoelectron spectroscopy and first-principles calculations," *Appl. Surf. Sci.*, vol. 396, pp. 688–694, Feb. 2017.
- [113] G. Luo, S. Yang, G. R. Jenness, Z. Song, T. F. Kuech, and D. Morgan, "Understanding and reducing deleterious defects in the metastable alloy GaAsBi," *NPG Asia Mater.*, vol. 9, no. 1, p. 345, 2017.
- [114] D. Li *et al.*, "First-principles study of the effect of BiGa heteroantisites in GaAs:Bi alloy," *Comput. Mater. Sci.*, vol. 63, pp. 178–181, Oct. 2012.
- [115] S. Adachi, GaAs and Related Materials. WORLD SCIENTIFIC, 1994.
- [116] H. Makhloufi *et al.*, "Molecular beam epitaxy and properties of GaAsBi/GaAs quantum wells grown by molecular beam epitaxy: effect of thermal annealing," *Nanoscale Res. Lett.*, vol. 9, no. 1, pp. 1–5, 2014.
- [117] Y. Mazur *et al.*, "Luminescent properties of GaAsBi/GaAs double quantum well heterostructures," 2017.
- [118] Y. P. Varshni, "Temperature dependence of the energy gap in semiconductors," *Physica*, vol. 34, no. 1, pp. 149–154, 1967.
- [119] R. D. Richards, "Molecular beam epitaxy growth and characterisation of GaAsBi for photovoltaic applications," no. September, p. 197, 2014.

- [120] A. J. Ptak *et al.*, "Kinetically limited growth of GaAsBi by molecular-beam epitaxy," *J. Cryst. Growth*, vol. 338, no. 1, pp. 107–110, 2012.
- [121] B. H. Bononi Dos Santos, G. Gobato, and M. Henini, "Optical and Structural Properties of Emerging Dilute III-V Bismides," *Pap. Appl. Sci. Converg. Technol.*, vol. 23, no. 5, pp. 211– 220, 2014.
- [122] P. C. Grant, D. Fan, and A. Mosleh, "Rapid thermal annealing effect on GaAsBi/ GaAs single quantum wells grown by molecular beam epitaxy ARTICLES YOU MAY BE INTERESTED IN," *J. Vac. Sci. Technol. B*, vol. 32, pp. 2–119, 2014.
- [123] B. O. Alazmi, H. H. H. Althebyani, I. Zaied, H. Fitouri, and A. Rebey, "Thermal annealing effects on the physical properties of GaAsBi/GaAs/GaAs:Si structure," *J. Umm Al-Qura Univ. Appl. Sci.*, vol. 9, no. 2, pp. 164–175, 2023.
- [124] S. Mazzucato *et al.*, "Reduction of defect density by rapid thermal annealing in GaAsBi studied by time-resolved photoluminescence," *Semicond. Sci. Technol.*, vol. 28, no. 2, p. 022001, Jan. 2013.
- [125] Z. Xu *et al.*, "Effect of thermal annealing on structural and optical properties of the GaAs 0.963 Bi 0.037 alloy," *Semicond. Sci. Technol*, vol. 23, p. 4, 2008.
- [126] Z. Chine, H. Fitouri, I. Zaied, A. Rebey, and B. El Jani, "Photoreflectance and photoluminescence study of annealing effects on GaAsBi layers grown by metalorganic vapor phase epitaxy," *Semicond. Sci. Technol.*, vol. 25, no. 6, p. 065009, May 2010.
- [127] R. C. Lutz *et al.*, "analysis in non-stoichiometric GaAs: An annealing study," *Phys. B Condens. Matter*, vol. 273–274, pp. 722–724, 1999.
- [128] X. Liu, A. Prasad, J. Nishio, E. R. Weber, Z. Liliental-Weber, and W. Walukiewicz, "Native point defects in low-temperature-grown GaAs," *Appl. Phys. Lett.*, vol. 67, no. 2, p. 279, Jul. 1995.
- [129] S. U. Dankowski *et al.*, "Above band gap absorption spectra of the arsenic antisite defect in low temperature grown GaAs and AlGaAs," *Appl. Phys. Lett.*, vol. 68, no. 1, pp. 37–39, 1996.